Yong Zhou
Editor

Eco- and Renewable Energy Materials

Science Press
Beijing

Springer

Yong Zhou

Eco- and Renewable Energy Materials

Yong Zhou

Eco- and Renewable Energy Materials

With 130 figures

Science Press
Beijing

Springer

Editor
Yong Zhou
Ecomaterials and Renewable Energy Research
Center (ERERC), Nanjing University
Nanjing, Jiangsu, China
Email:zhouyong1999@nju.edu.cn

ISBN 978-7-03-035260-6
Science Press Beijing

ISBN 978-3-642-33496-2 ISBN 978-3-642-33497-9 (eBook)
Springer Heidelberg New York Dordrecht London

Library of Congress Control Number: 2012947215

Printed on acid-free paper

Springer is part of Springer Science+Business Media (www.springer.com)

Preface

Since the beginning of the 20th century, there have been great improvements in the daily life of human through the use of petroleum as a basic material. However, we now face the problem of petroleum supply and depletion. Meanwhile, global warming, the most threatening problem, stimulates the research towards alternative fuel sources using eco- and renewable energy typically such as solar energy. Material technology plays a particularly important role in the field of energy. Rapid depletion of fossil fuels and growing environmental concerns make energy one of the greatest challenges facing humankind in the 21st century. We need sustainable energy production and efficiently use natural energy to meet socio-economic and environmental targets. To cover various topics in such an interdisciplinary area, it is high time to provide timely review of a number of important developments in this field.

The science of energy-harvesting materials is experiencing phenomenal growth and attracting huge interest. *Eco- and Renewable Energy Materials* showcases the basic principle and the latest developments of the materials technologies, which are related to prevent global warming and secure energy resources from the viewpoint of materials science. Chapter 1 by Chenghui Li provides a concise overview of the development of silicon based photovoltaic materials. With the consideration of the uniqueness of perylenes, Chen Li and Klaus Müllen in Chapter 2 review the development of perylenes in organic photovoltaics. Jianguo Liu et al illustrate carbon corrosion in the electrocatalysts of polymer electrolyte membrane fuel cell in Chapter 3. Chapter 4 by Tingyue Gu and coworkers summarizes various recent advances in bio-fuel cell research using various biomass feed stocks. Yonggang Wang et al in Chapter 5 survey new progress in using nanostructured materials as cathodes and anodes to develop lithium-ion batteries with high energy density, high rate

capability, and excellent cycling stability. In Chapter 6, Dechun Zou et al summarize the updated fabrication and development of flexible solar cells. Chapter 7 by Zhaosheng Li and coworkers introduce history and operating principles of the photoelectrochemical cell for hydrogen generation. In Chapter 8, Huanting Wang et al describe the application of metal-organic frameworks to CO_2 capture. They also review in Chapter 9 recent activities in the development of CO_2 selective separation membranes, focusing on the fabrication and separation performance of current polymeric membranes and their modification, inorganic membranes and mixed-matrix membranes.

In working on this book, I had great pleasure interacting with the authors, and are grateful to all of them for their friendly and competent co-operation. Thanks are due to the financial support from 973 Programs (No. 2011CB933300/2011CB933303) and Jiangsu Provincial Funds for Distinguished Young Scientists (No. BK2012015). I sincerely hope that this book will provide researchers in these fields with newest developments in this rapidly evolving field for advancing research. I also wish to stimulate the next generation of breakthroughs of the eco- and renewable energy, which will further enrich human life.

Yong Zhou
Nanjing,P.R.China
August 24, 2012

Contents

Chapter 1
Silicon Based Photovoltaic Materials

Chenghui Li

State Key Laboratory of Coordination Chemistry, School of Chemistry and Chemical Engineering, Nanjing National Laboratory of Microstructures, Nanjing University, Nanjing 210093, P. R. China

Abstract

Solar energy is an idea renewable energy resource due to its abundance and inexhaustibility. Solar cells, which convert sunlight into electricity, are the most direct devices to use solar energy. Silicon is the most widely used material for solar cells due to its abundance in nature, stability, non-toxicity and well established refining and processing technologies. This chapter, which is divided into five sections, presents a brief review on the research progress of silicon as photovoltaic materials. After a short introduction in section 1, section 2 summarizes the history and current situation of the traditional wafer-based crystalline silicon solar cells. Section 3 draws attention to the development of thin-film silicon solar cells which have the significant advantage in cost reduction. The recently active and compelling nano-structured silicon technologies are reviewed in section 4. Finally, a conclusion and perspective is presented as section 5.

1.1 Introduction

Energy is the lifeblood of modern era. Fossil fuels (coal and oil) are the most important ingredients in producing energy for our lives. But unfortunately, we are facing a global energy crisis with natural reserves of fossil fuels being depleted fast due to over consumption. A possible solution of the global energy crisis is to exploit renewable instead of non-renewable sources of energy. Solar energy is an ideal renewable energy resource due to its abundance and inexhaustibility. By using values for the solar constant and Earth's albedo, it has been found that our Earth receives 1.56×10^{18} kW·h of solar energy per year, which is ~10 000 times

larger than that of current worldwide energy consumption[1]. This means that the Earth receives more solar energy in an hour than the total energy it consumes in an entire year.

We've used the solar energy for drying clothes and food for thousands of years, but only recently have we been able to use it for generating power. Solar cells convert sunlight directly into electricity. When sunlight is absorbed by the semi-conducting materials of the solar cells, the electrons absorb the photons and become liberated from their atoms and flow through the material to produce electricity. This process of converting light (photons) to electricity (voltage) is called the photovoltaic (PV) effect (Figure 1.1).

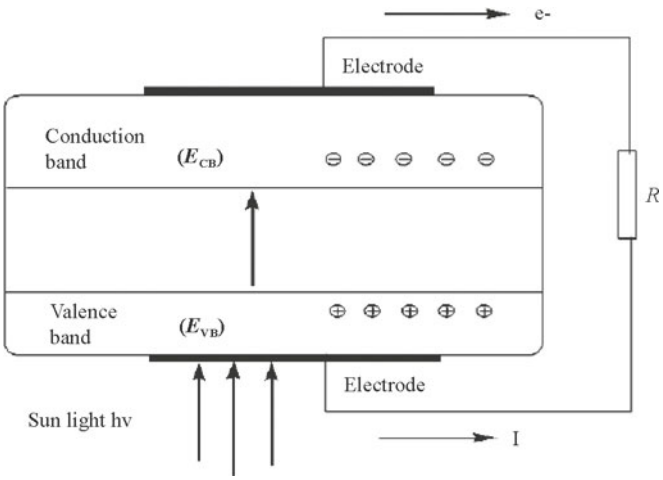

Figure 1.1 The photovoltaic process in a solar cell

Over 95% of all the solar cells produced so far are composed of Silicon. There are several reasons for this. First of all, silicon is a nontoxic element and can be available in sufficient quantity due to its abundance in earth's crust. Secondly, silicon is an ideal semiconductor with good stability and a well-balanced set of electronic, physical and chemical properties. Another reason why silicon cells have been so dominant is that the success of silicon in microelectronics can ensure the supply of high quality silicon wafers for the presently smaller photovoltaic industry.

Most silicon cells have been fabricated using thin wafers cut from large cylindrical ingots. The wafer-based crystalline silicon (c-Si) solar cells yield stable solar cells with good module efficiencies (over 16%) and can be fabricated conveniently by using processing technologies developed for microelectronics industries. However, the wafers have to be sufficiently thick (several hundred

microns) due to the poor optical absorption of crystalline silicon, resulting in the huge consumption of silicon materials. On the other hand, the sawing of ingots into wafers produces significant silicon wastes. To reduce the amount of silicon material required in creating a solar cell, thin-film technology has been developed. In spite of its low photo-conversion efficiency and light induce instability (Staebler–Wronski effect), thin film solar cells have become more and more popular due to the lower costs and other advantages including flexibility, lighter weights, and ease of integration. Recently, nano-structured silicon, with unique electrical and optical properties, has emerged as a new form of silicon for constructing new architecture of solar cells. If the technical challenges including proper surface passivation, shunting, and fabrication of high quality contacts can be solved, nano-structured silicon would be a promising candidate toward low-cost, high-efficiency solar cells.

This chapter intends to provide a concise overview of the development of silicon based photovoltaic materials. Excellent in-depth discussions about historical and ongoing perspective of silicon based photovoltaic materials can be found in the reviews and books list in the reference[2~10].

1.2 Wafer-based crystalline silicon

As the name implies, wafer-based silicon solar cells are fabricated from slices of silicon derived from ingots. Wafer-based crystalline silicon has dominated the photovoltaic materials since the birth of solar PV technology, due to its mature technology and stable photo-conversion efficiency. Despite the numerous attempts at making better solar cells by using new and exotic materials, the reality is that most solar cell manufacturers are currently only equipped to produce wafer-based solar cells. Consequently, a large body of research is being done all over the world aiming to manufacture silicon wafer-based solar cells at lower cost and to increase the conversion efficiencies without an exorbitant increase in production cost.

1.2.1 Mono-crystalline silicon

In mono-crystal silicon, the arrangement of atoms in the material is uniform, and the crystal lattice of the entire sample is continuous and unbroken with no grain boundaries. This uniformity is ideal for transferring electrons efficiently through the material.

The mono-crystalline silicon wafers are generally made from scrap material of microelectronic industry through Czochralski process, Float-zone process or Bridgman techniques[2].The scrap silicon materials are produced in the following way: First, a lower grade of silicon known as “metallurgical grade” is produced by

the reduction of quartzite by carbon. This metallurgical grade silicon is of about 98% purity and is produced in large quantities. The metallurgical grade silicon is then converted to trichlorosilane, which is then purified to 99.9999999% (nine "nines") purity by fractional distillation. The purified trichlorosilane are finally decomposed into silicon in a highly purified form. In this process, electrically heated silicon rods are exposed to a trichlorosilane/hydrogen mixture which reacts on the surface of the rods, depositing silicon onto them. These rods grow with a fine-grain polycrystalline silicon microstructure. After the rod diameter has increased to the required size, the process is stopped and the rods mechanically broken into smaller chunks, which maintain "nine-nines" purity. These chunks then become the starting point for the growth of ingots. In the Czochralski process for growing crystalline ingots, the purified silicon chunks are melted in a quartz crucible. A precisely oriented seed crystal, mounted on a rod, is dipped into the molten silicon. The seed crystal's rod is very slowly pulled upwards and rotated at the same time. By precisely controlling the temperature gradients, rate of pulling and speed of rotation, it is possible to extract a large, single-crystal, cylindrical ingot from the melt. Typically ingots are grown to about 10~15 cm in diameter and 1~2 m in length, weighing 50~100 kg (Figure 1.2(a)). The crystallographic orientation of the seed is transferred to the grown crystal. Generally, for photovoltaic use, the crystal is grown with a preferred orientation so that the wafers which are sliced from the crystal perpendicular to the growth axis have surfaces parallel to {100} crystallographic planes.

Prior to slicing these ingots into wafers, the ingots are generally grinded along the length of the ingot to remove the slight fluctuations in diameter that occur during crystal growth. The ingots are then "squared-off" by sawing off large sections parallel to the growth axis, giving "quasi-square" shape (Figure 1.2(b)). The large pieces of silicon sawn off in this approach are then generally recycled by re-melting as feedstock for the Czochralski growth. The "quasi-square" silicon ingot is then sliced into very thin wafers (Figure 1.2(c)). This is usually done with a diamond saw. This process produces considerable wastage of silicon known as "kerf" loss[2].

Fabrication of solar cells using silicon wafers starts by chemically cleaning and etching their surfaces, generally in a sodium hydroxide etchant, to remove saw damage from the wafers. Crystallographic texturing is then performed using a more dilute solution of sodium hydroxide. The composition and temperature of this solution determines the texturing quality, including the size of the pyramidal features resulting from the texturing and the percentage of wafer surface area successfully covered by such features.

The next major stage of processing is the diffusion of the cell junction. This is generally achieved by spraying or spinning a compound containing phosphorus onto the cell surface, followed by heating at high temperature to allow phosphorus dopant atoms to seep into the cell surface by thermal diffusion. Typically, the depth of diffusion is less than 1 μm. The same thermal diffusion process is widely used in microelectronics but processing for photovoltaics generally involves cruder equipment and techniques, since the aim is to produce cells at the lowest possible cost without unduly sacrificing cell performance.

The screen printing of metal contacts onto the front and rear surfaces is an another step of cell processing. Silver paste consisting of a suspension of fine particles of silver and glass frit in an organic medium together with appropriate binders is squeezed through a patterned screening mesh onto the cell surface. After application, the paste is dried at low temperature and then fired at a higher temperature to drive off the remaining organics and to allow the silver regions to coalesce. The glass frit is important in promoting adhesion to the silicon substrate. Often pastes are doped with phosphorus to help prevent the screened contact from penetrating the thin phosphorus skin that it is intended to contact. The paste for the top surface is printed in a characteristic finger pattern to minimize the resistive losses in the cell while allowing as much light as possible into it. Sometimes the rear contact is also patterned, not to allow light into the cell, but merely to reduce the amount of paste required and hence reduce the cost of this processing step.

A quarter wave antireflection coating can be applied to the cell at this stage. Generally, titanium dioxide is used as the antireflection coating material due to the simplicity of depositing and its almost ideal refractive index for this application. Some manufacturers deposit the antireflection coating before the metal paste-firing step and fire the paste through this coating.

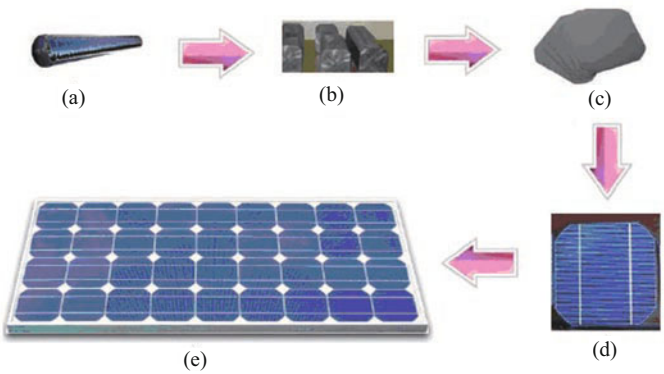

Figure 1.2 The process for fabricating mono-crystalline silicon photovoltaic modules

The as processed solar cells (Figure 1.2(d)) are then packaged and interconnected to form a solar panel (module) (Figure 1.2(e)). The solar panel is used as a component in a larger photovoltaic system to offer electricity for commercial and residential applications. The performance of solar panel is generally determined by that of the worst cell in the module, resulting in large power losses within mismatched modules. Even worse, low output cells can become reverse-biased under some modes of module operation and destroy the module by localized over-heating. Therefore, cells are usually graded based on their short-circuit currents or currents at a nominal operating voltage, e.g., 450 mV, before assembling into modules. Generally, cells are sorted into 5% performance bins. The sorting is important to reduce the amount of mismatch within the completed module.

Commercial single-crystal silicon solar cell with photo-conversion efficiency above 16% has been generally reached in photovoltaic industry. However, this efficiency is still much lower than the theoretical limiting efficiency of 29%[10], indicating there are enormous potential for further efficiency improvement in commercial devices. Part of this potential has been recently realized with the commercialization of solar cells with new structures or processing technology in some world leading company such as Sunpower, Sanyo, BP Solar, Suniva, Suntech Power, Trina Solar, Yingli Solar, JA Solar. In the laboratory in The University of New South Wales, the single crystalline silicon solar cells are approaching the theoretical limiting efficiency (Figure 1.3). If these new technologies can be commercialized in industry without inducing too much additional costs, energy payback period will be significantly shorted.

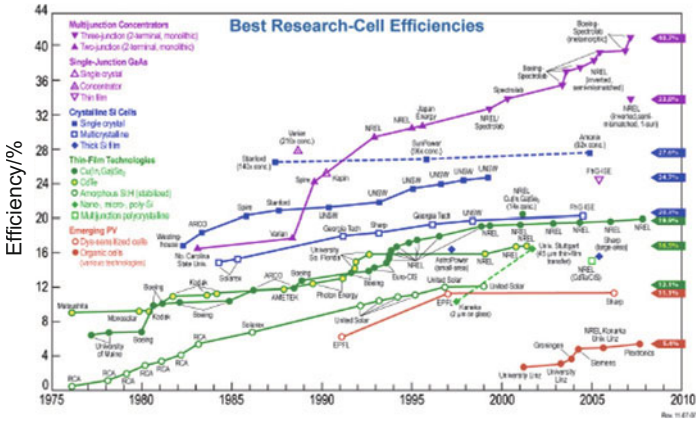

Figure 1.3 The best research-cell efficiencies all over the world
(Source:http://www.nrel.gov/pv/thin_film/docs/kaz_best_research_cells.ppt)

1.2.2 Multi-crystalline silicon

Multi-crystalline silicon, in contrast, consists of numerous smaller crystals or grains, which introduce boundaries. These boundaries impede the flow of electrons and encourage them to recombine with holes to reduce the power output of the solar cell. Therefore, solar cells based on multi-crystalline silicon are generally less efficient. However, multi-crystalline silicon is much less expensive to produce than single-crystalline silicon.

Multi-crystalline silicon is produced using silicon feedstock (Figure 1.4(a)) through casting technology[2] .This technique involves controllably solidifying molten silicon in a suitable container to give silicon ingots with large columnar grains generally growing from the bottom of the crucible upwards. Techniques may differ between different manufacturers in the choice of crucible material, the method of loading silicon into the crucible and the method for controlling the cooling of the melt. Typically, the feedstock made by purification of silicon or by alternative refining methods is charged in a silicon nitride coated quartz crucible and heated until all the silicon is melted. Heat is then extracted from the bottom of the crucible by moving the heat zone up and/or cooling the bottom of the crucible. Therefore, a temperature gradient is created in the melt and the solidification will start at the bottom. Crystals will grow upwards, and grain boundaries will grow parallel to the solidification direction (Figure 1.4(b)). To obtain a directional solidification the heat must be transported through the steadily growing layer of solid silicon. It is necessary to maintain a net heat flux over the solid-liquid interface, and the temperature at the lower part of the crucible must be decreased according to the increase in solid silicon thickness to maintain a steady growth rate. The growth rate is proportional to the temperature gradient difference between the solid and the liquid silicon.

The large ingots are sawn into smaller sections as shown in Figure 1.4(c), eventually to give wafers generally 10~15 cm along the sides (Figure 1.4(d)). These smaller sections can be sawn by the standard inner-diameter or continuous wire sawing processes.

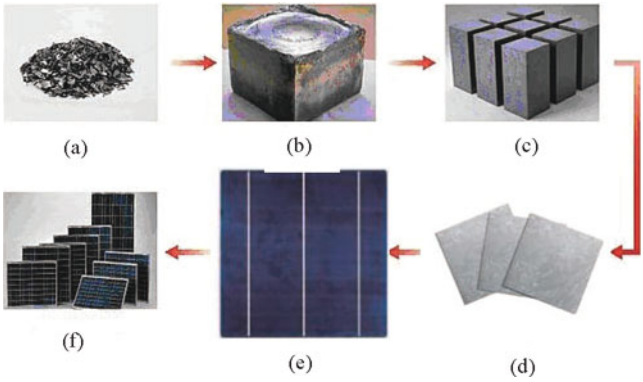

Figure 1.4 (a) Directional solidification of silicon within a mould. (b) sawing of large ingot into smaller sub-sections.

The processing of multi-crystalline silicon wafer is very similar to that of mono-crystalline silicon wafer. The main difference lies in the texturing of wafer surface. Texturing of mono-crystalline silicon is usually done by etching in alkaline solutions. However, these methods are inefficient for multi-crystalline silicon due to the presence of random crystallographic grain orientations and high selectivity of etching along specific directions. There are three different kinds of texturization techniques for multi-crystalline silicon solar cells: ① acid texturization[11,12], ② reactive ion etching[13], and ③ mechanical texturization[14,15] .Each of them has some advantages and drawbacks. The application of etches based on HF-HNO_3 induces irreproducible results due to random distribution of grains of different crystallographic orientation on the surface of multi-crytalline silicon and necessity of precise control of temperature as well as composition of etches. Reactive ion etching creates a needle-like surface, on which screen printing is difficult. Mechanical texturing may be effective, but has some limitations related to textured material. It cannot be applied specially for thin, wraped, and fragile materials.

The resulting multi-crystalline silicon cells are capable of producing cells of about 80% of the performance of a mono-crystalline cell fabricated on a Czochralski wafer. However, because of the higher packing density due to their square or rectangular geometry, this performance difference is largely masked at the module level with multi-crystalline module performance lying in the range demonstrated by modules made from mono-crystalline cells. Therefore, the market share of multi-crystalline silicon (mc-Si) has increased remarkably in recent years due to the reduction of production costs.

1.2.3 Sheet and ribbon silicon

As above mentioned, the silicon ingots have to be sawed into wafers before cell fabrication. This process creates large amounts of micron-sized silicon powder “kerf” which is currently discarded as waste. These “kerf” losses together with contaminated parts near the edges of the ingot that cannot be used for cell processing add up to more than 30% of the silicon starting material. With the rapid increase of silicon based photovoltaic market, the shortage of silicon feedstock will become the bottleneck in restricting the expansion of photovoltaic industry. Therefore, it is important to investigate an alternative way to slicing wafers out of a crystallized ingot while maintaining the well proven processing techniques developed for mc-Si solar cells. In principle, ribbon technology is the most promising one where liquid silicon is directly crystallized in the form of a silicon wafer without the need for sawing. However, the wafer produce from ribbon technology have to reach sufficient material quality and solar cell efficiency to reduce the electricity cost. It was only recently that some of the ribbon technologies, such as in the cases of the edge-defined film-fed growth (EFG) and the string ribbon (SR) technologies, reached maturity and manufactured on megawatt scale[2] .Other technologies such as the silicon film, dendritic web, ribbon growth on substrate (RGS) and rotational solidification techniques are under development at pilot demonstration phases[16].

The typical EFG process involves the pulling of a thin sheet of silicon ribbon from a strip of molten silicon formed by capillary action at the top of a graphite dye (Figure 1.5). The molted silicon is contained in a graphite crucible. Extensive temperature control by radiation shields, cold shoes, and after-heating realizes a maximum temperature gradient where plastic flow is possible, in order to allow for a maximum growth rate. Individual wafers are then cut from the sides of the silicon ribbon, normally by laser scribing wafers from each of the sides[17] .

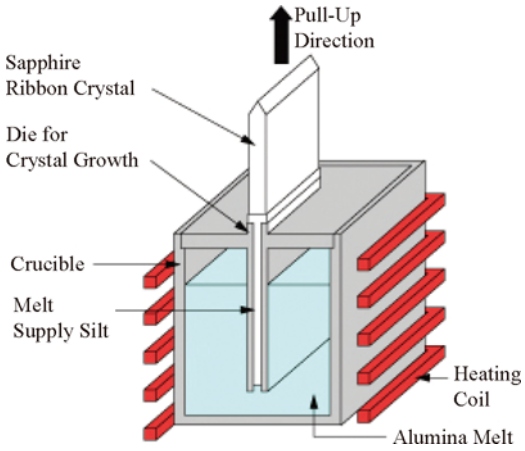

Figure 1.5 A schematic drawing of the EFG process
(Source:http://americas.kyocera.com/kicc/industrial/crystal.html)

The material produced is multi-crystalline with elongated grains and of a similar quality to the standard directionally solidified multi-crystalline material. The solid silicon ribbon is (super)saturated with carbon due to the contact with graphite-containing materials near the liquid–solid interface. Oxygen and transition metals are also presented, although mostly in concentrations not limiting material quality.

Before fabrication of ribbon silicon based solar cells using regular processing techniques adopted for wafers, additional steps of gettering and hydrogenation are implemented to improve the material quality. It was shown that defect structures presented in the as-grown ribbon material can be substantially reduced by gettering and hydrogenation. This is in contrast to the case for mono-crystalline material, where the main task of post-processing is to maintain the high as-grown material quality.

Somewhat related to the above ribbon approaches are other sheet approaches which produce silicon films on substrates from which they are subsequently detached. The most developed version of this technology is the via hole etching for separation of thin film (VEST) technology developed by Mitsubishi[2] .The VEST process is based on the silicon on insulator (SOI) technology. SOI structure is obtained using zone-melting recrystallization (ZMR) method. Large grain polycrystalline silicon thin films on the supporting substrate covered with the silicon dioxide layer can be obtained by ZMR. Via-holes are formed in the silicon film and the silicon dioxide layer is etched away by introducing the hydrofluoric

acid through the via-holes. Thus the silicon film is separated from the supporting substrate, which is reused to form the silicon dioxide layer and the silicon film. If this detached layer is too thin to be self-supporting, it could be transferred to structurally strong components such as the glass layer in a structural superstrate design.

As no kerf losses occur in ribbon and sheet technologies, and almost 100% of the silicon feedstock ends up in the wafer material, a dramatic decrease in wafer costs is available. Apart from the better silicon usage, energy costs are reduced as well, as time and energy-consuming ingot growth is eliminated. Therefore, a significantly reduced energy payback time (i.e., the time required for the photovoltaic solar module to 'pay back') for the PV module can be expected. However, the cells made from ribbon silicon are generally less efficient than mono-crystalline silicon. Promising efficiencies over 16% have been obtained from this approach for substrates that are only 60~70 μm in thickness, but are still self-supporting. On the other hand, the advantages of ribbon and sheet silicon based wafer technologies in consuming less silicon has been surpassed by the more economic thin film technology. Ribbon silicon solar cells have to improve their efficiency and stability in the future to maintain their cost-effectiveness.

1.3 Thin-film silicon

Thin-film silicon solar cells require a far lower amount of silicon material than the 'classical' wafer based crystalline silicon solar cells, indicating that they have, on a medium-term time scale, a more pronounced cost reduction potential. Furthermore, the energy payback time, which may be a decisive item in the long run, is at least a factor of two lower in the case of thin-film silicon solar cells than for wafer-based crystalline silicon solar cells. Therefore, thin film solar cell industry in recent years been rapidly developed.

There are two forms of thin-film silicon materials that can be used for constituting such a solar cell: hydrogenated amorphous silicon (a-Si:H) and hydrogenated microcrystalline silicon (mc-Si:H).

1.3.1 Hydrogenated amorphous silicon (a-Si:H)

Amorphous solids, like common glass, are materials whose atoms are not arranged in any particular order. They don't form crystalline structures at all, and they contain large numbers of structural and bonding defects, such as dangling bonds (Figure 1.6). Dangling bonds provide places for electrons to recombine with holes, but they may be neutralized somewhat with hydrogen.

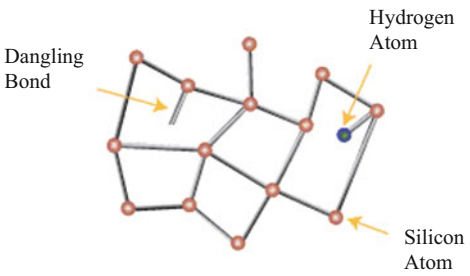

Figure 1.6 Structure model of amorphous silicon
(Source:http://www.eere.energy.gov/basics/renewable_energy/types_silicon.html)

Amorphous silicon (a-Si:H) layers were first deposited by Chittick[18] .He was experimenting with silane (SiH_4) plasmas and accidentally obtained a-Si:H layers in a remote part of his plasma reactor. Chittick's results were taken up by Spear and co-workers at Dundee University[19], who published the first systematic study on plasma-enhanced chemical vapour deposition (PECVD) with silane plus (optional) doping gases. Their results show that doping of a significant percentage of hydrogen atoms bonded into the amorphous silicon structure is essential to the improvement of the electronic properties of the plasma-deposited material[20]. As a consequence, the improved form of amorphous silicon has generally been known as hydrogenated amorphous silicon (or, more briefly, a-Si:H). In recent years, many researchers have used the term amorphous silicon to refer to the hydrogenated form, which acknowledges that the unhydrogenated forms of amorphous silicon are only infrequently studied today.

The bandgap of amorphous silicon depends on the species and concentration of doping atoms and can range from 1.4 to 1.8 eV, which is considerably larger than that for c-Si (1.1 eV). One may concluded that a-Si:H would absorb less photos than c-Si by comparing their bandgaps. However, the real situation is: the "selection rules" in "indirect bandgap" semiconductors that greatly reduce optical absorption in c-Si do not apply to a-Si. The structural disorder present in a-Si 'relaxes' the quantum mechanical selection rules. Amorphous silicon absorbs solar radiation 40 times more efficiently than singce-crystal silicon does, so a film only about 1 micrometer—or one-millionth of a meter—thick can absorb 90% of the usable light energy shining on it. This is one of the chief reasons that amorphous silicon could reduce the cost of photovoltaics since less silicon are needed.

After the first report of amorphous silicon solar cells in 1976 by Carlson and Wronski[21], extensive efforts have been devoted to a-Si:H based photovoltaic

technologies. For doped a-Si:H, it turns out that minority photocarriers (holes in n-type a-Si:H, electrons in p-type a-Si:H) do not move very far (around 0-1 μm, while over 200 μm in crystalline silicon), and so a p-n structure would only collect photocarriers from photons generated in an extremely thin layer of doped a-Si:H. Because of this reason p-i-n diodes are always used for a-Si:H solar cells. The fundamental photodiode inside an amorphous silicon–based solar cell has three layers deposited in either the p-i-n (Figure 1.7) or the n-i-p sequence. The three layers are a very thin (typically 20 nm) p-type layer, a much thicker (typically a few hundred nanometer) undoped intrinsic (i) layer, and a very thin n-type layer. In such a p-i-n cell the main part of light absorption and photogeneration of carriers will take place in the intrinsic (i) part of the solar cell.

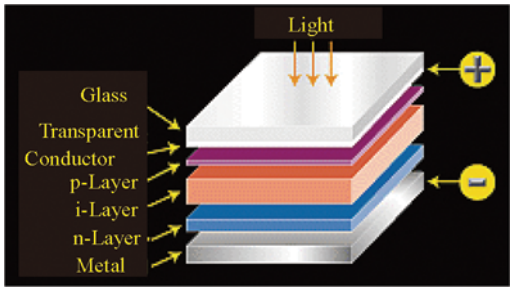

Figure 1.7 The typical amorphous silicon cell employs a p-i-n structure
(Sources:http://www.usc.edu/dept/architecture/mbs/tools/thermal/controls_activesolar.html)

In the following years after their introduction[22], p-i-n-type amorphous silicon solar cells made rapid progress in reaching higher efficiencies. By 1982, a-Si:H solar cells with (initial) efficiencies over 10% had been obtained[23]. However, a-Si:H solar cells suffer from a light-induced degradation effect (the so-called Staebler–Wronski effect)[24]. The electrical output of a-Si:H solar cells decreases over a period of time when first exposed to sunlight. Eventually, however, the electrical output stabilizes. This effect can result in up to a 20% loss in output before the material stabilizes.

Considering that amorphous silicon has a higher optical absorption coefficient for photons with energies greater than 2 eV, while lower optical absorption coefficient for photons with energies lower than 2 eV compared to microcrystalline silicon (Figure 1.8), recent researches have been focus on multi-junction thin-film silicon solar cells with aim to better exploit the solar spectrum. The multi-junction thin-film silicon solar cells consist in stacking two (tandem) or even three (triple) junction structures on top of each other, the different subcells being connected in

series. Taken a tandem solar cell made from a-Si:H (top) and mc-Si:H (bottom) for example, the a-Si:H solar cell can effectively use the high energy photons. The longer wavelength photons, which are not absorbed in the a-Si:H solar cell, get absorbed in mc-Si:H and thus achieving high efficiency.

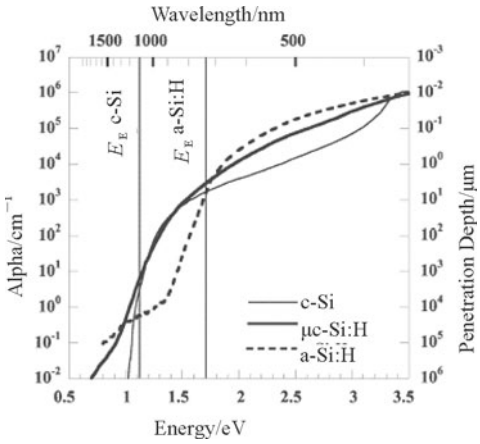

Figure 1.8 Curves for the optical absorption coefficient α and the penetration depth $d\lambda = 1/\alpha$ of monochromatic light with photon energy $h\nu$ and wavelength λ, for wafer-type crystalline silicon (c-Si) and typical device-quality a-Si:H and mc-Si:H layers on glass. [8]
(Reprinted with permission of John Wiley&Sons,Inc)

1.3.2 Hydrogenated microcrystalline silicon (c-Si:H)

Hydrogenated microcrystalline silicon (c-Si:H) is a mixed phase material, containing a crystalline silicon fraction and an amorphous silicon fraction. The crystallites are generally only a few nanometers to a few tens of nanometers in diameters, and are present in "bunches" or "conglomerates" in the layers. These conglomerates are much larger than the crystallites themselves, up to a micron or even larger. Because the crystallites are in the nanometer range, microcrystalline silicon is often referred to as "nano-crystalline silicon". The two names are nowadays used interchangeably. Like amorphous silicon, microcrystalline Si contains a lot of hydrogen (several percents), which is incorporated in situ during deposition and ensures passivation of most defects in the layers. The term "microcrystalline Si" covers, in fact, a whole range of materials, ranging from amorphous silicon with a few percents of crystalline phase to a material with only a few percents of amorphous silicon. The properties of the materials at the two extremes are quite different. In practice, the best devices are obtained with material

close to the edge between microcrystalline and amorphous Si, so most recent papers refer to this type of material, which contains a large amorphous fraction. The development of thin-film polycrystalline silicon (polysilicon) for solar cells can be seen as the continuation of this trend towards higher crystallinity. Thin film polysilicon is a material with grain size in the range 1 μm to 1 mm. In contrast to microcrystalline silicon, this material does not contain any amorphous tissue, or only a very small amount (well below 1%). One could think that the border between microcrystalline and polycrystalline silicon is not very sharp. In practice, there is a very clear distinction between the two materials because polysilicon is very far from the amorphous-to-crystalline transition, and always involves much higher temperatures than those used for microcrystalline silicon. Thin-film polysilicon solar cells have active layers that are usually thinner than 5 μm, often about only 2 μm. The technology is more recent and less mature than amorphous and microcrystalline silicon, but progress in the last few years has been very fast.

Microcrystalline silicon (mc-Si:H) layers were first produced by Veprek and Marecek in 1968 in Prague by a low-temperature plasma-assisted deposition process[25]. The bandgap of microcrystalline Si depends on the fraction of amorphous silicon in the material. Layers with a substantial crystalline fraction have a bandgap close to that of mono-crystalline silicon (1.1 eV). The apparent higher absorption (Figure 1.8) for such microcrystalline layers compared to mono-crystalline silicon has been demonstrated to be caused by light scattering at the layer surfaces. The absorption below the bandgap is much higher than that for crystalline silicon, and is caused by defects within the bandgap.

The device structure of microcrystalline silicon solar cells is very similar to that of amorphous silicon solar cells. As with amorphous silicon, both superstrate (p-i-n) and substrate (n-i-p) configurations are possible. The optimal thickness of the i-layer is much larger than that for amorphous Si cells, from 1 to 2 μm. This is related with the weaker absorption by the microcrystalline silicon. The mc-Si:H solar cells generally do not suffer from a pronounced Staebler–Wronski effect. However, recent work shows that mc-Si:H, if deposited at deposition conditions very near to the microcrystalline/amorphous transition, may indeed show a considerable amount of light-induced degradation.[30]

1.4 Nano-structured silicon

Nano-structured silicon is expected to possess significantly different optical properties from their bulk-length counterparts because they are smaller than the wavelength of visible light. The low optical reflection from ordered arrays of nano-structured silicon could be exploited to improve the photon absorption efficiency

of solar cells. Moreover, solar cells made from nano-structured silicon may offer a mechanically flexible alternative to Si wafers for photovoltaics. In this section, we will focus on the recent progress in synthesis, characterization, and fabrication of nano-structured silicon based solar cells.

1.4.1 Silicon nanowire

As early as 1964, Wagner and Ellis firstly reported the growth of silicon whiskers.[31]Later Givargizov elucidated the growth mechanism of silicon whiskers in 1975[32]. Subsequently, there were extensive investigations carried out on the synthesis, physical properties, and device fabrication and application of Silicon nano-wires (SiNWs). It has been showed that the energy gap of SiNWs was found to increase with decreasing SiNW diameter from 1.1 eV for 7 nm to 3.5 eV for 1.3 nm in diameter, in agreement with previous theoretical predictions[33,34] . Many other structure parameters i.e. growth directions, cross section, may also affect band structure and thus physical properties of SiNWs, especially for ultra tiny SiNWs[35,36]. Kelzenberg [37] reported that the diffusion length in Si NWs can be as long as 2 μm, which corresponds to a minority carrier lifetime of ~15 ns. All these results show that silicon nano-wire may have great advantages over their bulk-length counterparts in future design of high efficiency solar cells.

In order to fabricate solar cells based on SiNWs, the basic issue is to realize controllable synthesis of large-scale high quality SiNWs. The well-known vapour-liquid-solid (VLS) reaction have been used to grown SiNWs for a long time[38]. In the VLS reaction, metal particles, for example gold particles on Si substrate, are generally used as the mediating solvent to direct the growth of SiNWs. Some other methods, such as oxygen-assisted-growth (OAG)[39,40], vapor-solid-solid (VSS)[41,42] and electroless etching methods[43~46], have also been developed to synthesize SiNWs in largescale. Usually SiNWs grown by using VLS or VSS techniques have been proved to be obviously advantageous compared with OAG and electroless etching techniques in terms of well-defined surface and well-controlled diameter. Moreover, the VLS and VSS techniques can prepare ordered vertically standing epitaxial nanowires on single crystal substrate with better control of growth direction as a device platform, avoiding pick-and-place approaches or nano-manipulations in the fabrication of nano-devices. Unfortunately, metals especially gold and copper using as catalyst to direct the growth of SiNWs by VLS or VSS techniques may induce deep levels in SiNWs, which would trap electrons and holes in Si, and then depress the optical and electronic properties of the nanowires. Indeed much effort has already been made to solve this problem by altering metal catalysts such as Al[47]. At present, most of the SiNWs used in solar cells are

synthesized with VLS and VSS methods.

To get uniform doping in SiNWs is also a key issue to fabricate high performance SiNWs-based soalr cells. At the present time, the doping methods of SiNWs mainly include thermal diffusion, ion implantation and in-situ doping during growth process by co-flowing doping gas with silane or tetrachlorosilane. These methods have some disadvantages such as inducing defects and doping fluctuation especially for high level doping. Precise doping of semiconductor nano-materials remains as a challenge to be solved.

SiNWs solar cells have many kinds of structures. Their heterojunctions may be aligned in axes or radius. But typical structure of SiNWs solar cells is core-shell p-type/instinct/n-type (p-i-n) or p-type/n-type(p-n) configuration, namely, radial junctions[47~49]. By orthogonalizing the direction of light absorption and carrier collection, radial junctions can enable efficient carrier collection in optically thick nano-wire arrays, even when minority carrier diffusion lengths are shorter than the optical absorption length. The schematic drawing of the radial p-n junction cell is shown in Figure 1.9. This design has the potential to enable energy-conversion efficiency approaching that of wafer-based crystalline Si solar cells but competitive with thin film technologies at costs. Tiam et al[47]. fabricated single SiNWs solar cell of this structure to drive ultralow power devices, yielding a maximum power output of 200 pW per single nanowire device and an energy efficiency of 3.4%. Atwater[48] created a new type of flexible solar cell using arrays of long, thin silicon wires embedded in a polymer substrate. The silicon-wire arrays absorb up to 96% of incident sunlight at a single wavelength and 85% of total collectible sunlight. In addition to its high performance in absorbing lights, this kind of solar cell only use a fraction of the expensive silicon materials required by conventional solar cells. It would be expected that more and more efforts will be devoted to the novel SiNWs based solar cells in future in spite that the experiment efficiency of solar cells based on SiNWs is still far less from the academic calculation (15%~18%)[50].

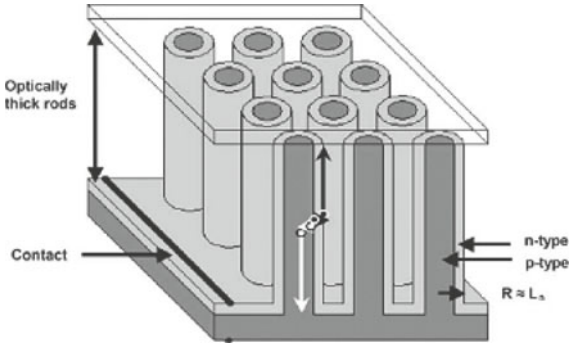

Figure 1.9 Schematics of a radial p-n junction nanorod solar cell [52]
(Reprinted with permission of American Institute of physics)

1.4.2 Silicon quantum dots

Given the spectrum of photons received from the Sun, there exists an optimum bandgap for a semiconductor absorber in a single-junction conventional photovoltaic device. As the bandgap increases, less energy is absorbed, but less of that absorbed energy is lost as heat due to rapid intra-band thermalization. The optimum bandgap for a single bandgap solar cell is between about 1.0 and 1.6 eV. The upper theoretical power conversion efficiency limit is 33.7% and is referred to as the Shockley–Queisser (SQ) limit [51]. Recently, Hanna and Nozik point out that photo-conversion efficiencies exceeding the SQ limit are possible for single junction devices by means of quantum dots.

When a normal photovoltaic material captures a photon of sunlight, it produces a negatively charged electron, which leaves behind a positively charged "hole" in the material. Under the solar cell's electrical field, the two charge carriers migrate to the terminals of the cell and produce a current. But quantum dots produce "excitons," consisting of electrons loosely bound to positive holes. Photons with energy equal to n times the bandgap can potentially produce n excitons at the bandgap, where n is an integer, in accordance with energy conservation. If the excitons can be effectively dissociated into electrons and holes and then migrate to the cell terminals without recombination, photo-conversion efficiencies higher than SQ limit would be expected. Hanna and Nozik's calculations show that a power conversion efficiency of 44% is possible under unconcentrated AM1.5G light for solar cells based on a single junction multiple exciton generation (MEG) absorber with a bandgap of 0.7 eV. Under full light concentration, this limit rises to 66% [52] .

To use the incipient free energy after MEG occurs, it is important to find materials with quantum yields for exciton generation greater than 100%. Currently, efficient MEG has been observed in silicon, making it possible to fabricate solar cells based on silicon quantum dots [53~55]. More recently, tandem solar cells formed by combination of silicon quantum dot and crystalline silicon wafers has been demonstrated [56]. This result is an encouraging step towards the realization of high efficiency solar cells based on silicon quantum dot materials.

1.5 Conclusion and perspective

Silicon wafer based solar cells is and will be the main focus of photovoltaic manufactures due to its stable efficiency and mature technologies in large scale production. However, the wafers will be more and more thinner in the future. Improved processing sequences, such as the buried contact and HIT approaches, now both in pilot production, will come to the fore as wafer thickness decreases and material quality increases. The trends in producing higher efficient solar cells with thinner wafer result in that fabrication technique, such as surface passivation of both front and rear surfaces, will become more and more important.

A laboratory scientist, however, may have more interest in the low-cost, thin-film silicon technology. It would be expected that the commercial product based on this technology should be mature in the near future, with energy conversion efficiency approaching that of its wafer counterpart. The present bottlenecks of thin-film silicon solar cell technology are the relatively high temperature and low deposition rates. The high temperature results in the difficulty in fabricating solar cells on organic substrates which is the fundamental requirement for flexible photovoltaic devices. The low deposition rates induce long deposition time and high energy consumption. If these problems can be tackled, thin-film solar cell will be the most promising technology toward low-cost, high-efficiency solar cells.

Nano-structured silicon materials, including silicon nanowires and quantum dots, show great potential for future solar cell devices. However,extensive efforts, such as improving the materials parameters (resistivity, size, purity, etc.) and optimizing device fabrication process, are required to improve their photovoltaic performances. Success in nano-structured silicon solar cells may lead to greatest leap in the efficiency improvement in silicon based solar cells.

References

[1] Markvart T. Solar Electricity (2nd edition). Chichester: John Wiley and Sons, 2000.

[2] Green M A. Solar Cells: Operating Principles, Technology and System Applications. New Jersey: Prentice-Hall, 1982.

[3] Green M A. The future of crystalline silicon solar cells. Progress in Photovoltaics: Research and Applications, 2000, 8(1): 127~139.

[4] Pizzini S. Bulk solar grade silicon: How chemistry and physics play to get a benevolent microstructured material. Applied Physics A: Materials Science and Processing, 2009, 96(1): 171~188.

[5] Poortmans J, Arkhipov V. Thin Film Solar Cells: Fabrication, Characterization and Applications. New York: John Wiley and Sons, 2006.

[6] Hamakawa Y. Thin-Films Solar Cells. Berlin Heidelberg: Springer-Verlag, 2004.

[7] Schropp R E I, Carius R, Beaucarne G. Amorphous silicon, microcrystalline silicon, and thin-film polycrystalline silicon solar cells. Materials Research Society Bulletin, 2007, 32(3): 219~224.

[8] Shah A V, Schade H, Vanecek M, et al. Thin-film silicon solar cell technology. Progress in Photovoltaics: Research and Applications, 2004, 12(23): 113~142.

[9] Wan Y, Sha J, Chen B, et al. Nanodevices based on silicon nanowires. Recent Patents on Nanotechnology, 2009, 3(1):1~9.

[10] Green M A. Third generation photovoltaics: Solar cells for 2020 and beyond. Physica E: Low-dimensional Systems and Nanostructures, 2002, 14(1~2): 65~70.

[11] Panek P, Lipiski M, Dutkiewicz J. Texturization of multicrystalline silicon by wet chemical etching for silicon solar cells. Journal of Material Science, 2005, 40(6):1459~1463.

[12] Yerokhov V Y, Hezel R, Lipinski M, et al. Cost-effective methods of texturing for silicon solar cells. Solar Energy Materials and Solar Cells, 2002, 72(1~4): 291~298.

[13] Fukui K, Inomata Y, Shirasawa K. Surface texturing using reactive ion etching for multicrystalline silicon solar cell// Proceedings of the 26th IEEE Photovoltaic Specialists Conference, PVSC'97, Anaheim, 1997: 47~50.

[14] Fath P, Marckmann C, Bucher E, et al. Multicrystalline silicon solar cells using a new high throughput mechanical texturization technology and a roller printing metallization technique// Proceedings of the 13th European PV Solar Energy Conference, Nice, 1995: 29~32.

[15] Gerhards C, Marckmann C, Tolle R, et al. Mechanically V-textured low cost multicrystalline silicon solar cells with a novel printing metallization// Proceedings of the 26th IEEE Photovoltaic Specialists Conference, PVSC'97, Anaheim, 1997: 43~46.

[16] Hahn G, Schönecker A. New crystalline silicon ribbon materials for photovoltaics. Journal of Physics: Condensed Matter, 2004, 16: R1615~R1648.

[17] Schmidt W, Woesten B, Kalejs J P. Manufacturing technology for ribbon silicon (EFG) wafers and solar cells. Progress in Photovoltaics: Research and Applications, 2002, 10(2): 129~140.

[18] Chittick R C, Alexande J H, Sterling H F. The preparation and properties of amorphous silicon. Journal of the Electrochemical Society, 1969, 116: 77~81.

[19] Spear W E, Lecomber P G. Properties of substitutionally doped amorphous Si and Ge. Philosophical Magazine, 1976, 33: 935~949.

[20] Fritzsche H. Early research on amorphous silicon: Errors and missed opportunities. Materials Research Society Symposium Proceedings. 2001, 609: 1~12.

[21] Carlson D E, Wronski C R. Amorphous silicon solar cells. Applied Physics Letters, 1976, 28(11): 671~673.

[22] Carlson D E, Wronski C R, Pankove J I. Properties of amorphous silicon and a-Si solar cells. RCA Review, 1977, 38: 211~225.

[23] Catalano A, D'Aiello R, Dresner J, et al. Attainment of 10% conversion efficiency in amorphous silicon solar cells// Proceedings of the 16th IEEE Photovoltaic Specialists Conference, San Diego, 1982, 1421~1422.

[24] Staebler D L, Wronski C R. Reversible conductivity changes in discharge-produced amorphous silicon. Applied Physics Letters, 1977, 31(4): 292~294.

[25] Vepřek S, Mareček V. The preparation of thin layers of Ge and Si by chemical hydrogen plasma transport. Solid State Electronics, 1968, 11(7): 683~684.

[26] Klein S, Finger F, Carius R, et al. Intrinsic microcrystalline silicon prepared by hot-wire chemical vapour deposition for thin film solar cells. Thin Solid Films 2003, 430(1~2): 202~207.

[27] Fonrodona M, Soler D, Asensi J M, et al. Influence of the crystalline fraction on the stability of nanocrystalline silicon solar cells// Proceedings of the 3rd World Conference on PVSEC, Osaka, 2003: 11~18.

[28] Ahn J Y, Jun K H, Lim K S. Stable protocrystalline silicon and unstable

microcrystalline silicon at the onset of a microcrystalline regime. Applied Physics Letters, 2003, 82(11): 1718~1720.

[29] Beck N, Torres P, Fric J, et al. Optical and electrical properties of undoped microcrystalline silicon deposited by the VHF-GD with different dilutions of silane in hydrogen. Proceedings of the Materials Research Society Symposium, 1997, 452: 761~766.

[30] Poruba A, Fejfar A, Remes Z, et al. Optical absorption and light scattering in microcrystalline silicon thin films and solar cells. Journal of Applied Physics, 2000, 88(1): 148~160.

[31] Wagner R S, Ellis W C. Vapor-liquid-solid mechanism of single crystal growth. Applied Physics Letters, 1964, 4(5): 89~90.

[32] Givargizov E I. Fundamental aspects of VLS growth. Journal of Crystal Growth, 1975, 31(1): 20~30.

[33] Ma D D D, Lee C S, Au F C K, et al. Small-diameter silicon nanowire surfaces. Science, 2003, 299: 1874~1877.

[34] Read A J, Needs R J, Nash K J, et al. First-principles calculations of the electronic properties of silicon quantum wires. Physical Review Letters, 1992, 69(8): 1232~1235.

[35] Vo T, Williamson A J, Galli G. First principles simulations of the structural and electronic properties of silicon nanowires. Physical Review B, 2006, 74(4): 045116.

[36] Migas D B, Borisenko V E. Tailoring the character of the band-gap in < 011 >-, < 111 >- and < 112 >-oriented silicon nanowires. Nanotechnology, 2007, 18: 375703.

[37] Kelzenberg M D, Turner-Evans D B, Kayes B M, et al. Photovoltaic measurements in single-nanowire silicon solar cells. Nano Letters, 2008, 8(2): 710~714.

[38] Wagner R S, Ellis W C. Vapor-liquid-solid mechanism of single crystal growth. Applied Physics Letters, 1964, 4(5): 89~90.

[39] Zhang R Q, Lifshitz Y, Lee S T. Oxide-assisted growth of semiconducting nanowires. Advanced Materials, 2003, 15(7~8): 635~640.

[40] Li C P, Lee C S, Ma X L, et al. Growth direction and cross-sectional study of silicon nanowires. Advanced Materials, 2003, 15(7~8): 607~609.

[41] Garnett E C, Liang W J, Yang P D. Growth and electrical characteristics of platinum-nanoparticle-catalyzed silicon nanowires. Advanced Materials, 2007, 19(19): 2946~2950.

[42] Wang Y W, Schmidt V, Senz S, et al. Epitaxial growth of silicon nanowires using an aluminium catalyst. Nature Nanotechnology, 2006, 1(3): 186~189.

[43] Peng K Q, Yan Y J, Gao S P, et al. Synthesis of large-area silicon nanowire arrays via self-assembling nanoelectrochemistry. Advanced Materials, 2002, 14(16): 1164~1167.

[44] Peng K Q, Yan Y J, Gao S P, et al. Dendrite-assisted growth of silicon nanowires in electroless metal deposition. Advanced Functional Materials, 2003, 13(2): 127~132.

[45] Peng K Q, Hu J J, Yan Y J, et al. Fabrication of single-crystalline silicon nanowires by scratching a silicon surface with catalytic metal particles. Advanced Functional Materials, 2006, 16(3): 387~394.

[46] Peng K Q, Fang H, Hu J J, et al, Metal-particle-induced, highly localized site-specific etching of Si and formation of single-crystalline Si nanowires in aqueous fluoride solution. Chemistry-A European Journal, 2006, 12(30): 7942~7947.

[47] Tian B, Zheng X, Kempa T J, et al. Coaxial silicon nanowires as solar cells and nanoelectronic power sources. Nature, 2007, 449: 885~890.

[48] Kayes B M, Lewis N S, Atwater H A. Comparison of the device physics principles of planar and radial p-n junction nanorod solar cells. Journal of Applied Physics, 2005, 97(11): 114302~114311.

[49] Garnett E C, Yang P D. Silicon nanowire radial p-n junction solar cells. Journal of the American Chemical Society, 2008, 130(29): 9224~9225.

[50] Kelzenberg M D, Boettcher S W, Petykiewicz J A, et al. Enhanced absorption and carrier collection in Si wire arrays for photovoltaic applications. Nature Materials, 2010, 9(3): 239~244.

[51] Shockley W, Queisser H J. Detailed balance limit of efficiency of p-n junction solar cells. Journal of Applied Physics, 1961, 32(3): 510~519.

[52] Hanna M C, Nozik A J. Solar conversion efficiency of photovoltaic and photoelectrolysis cells with carrier multiplication absorbers. Journal of Applied Physics, 2006, 100(7): 074510.

[53] Schaller R D, Klimov V I. High efficiency carrier multiplication in PbSe nanocrystals: Implications for solar energy conversion. Physical Review Letters, 2004, 92(18): 186601.

[54] Ellingson R J, Beard M C, Johnson J C, et al. Highly efficient multiple exciton generation in colloidal PbSe and PbS quantum dots. Nano Letters, 2005, 5(5): 865~871.

[55] Nozik A J. Multiple exciton generation in semiconductor quantum dots. Chemical Physics Letters, 2008, 457(1~3): 3~11.

[56] Cho E C, Park S, Hao X, et al. Silicon quantum dot/crystalline silicon solar cells. Nanotechnology, 2008, 19(24): 245201.

Chapter 2
Perylenes in Organic Photovoltaics

Chen Li, Klaus Müllen

Max Planck Institute for Polymer Research, Ackermannweg 10, D-55128 Mainz, Germany

Abstract

As metal-free dyes, perylene derivatives have been widely applied in various optical devices owing to their outstanding chemical, thermal and photochemical stability and non-toxicity. Moreover, the exploitation of perylene dyes for organic solar cells can be traced back to the first efficient organic photovoltaic cell fabricated by Tang where phthalocyanine and perylenedibenzimidazole were applied as active materials with a reasonable power conversion efficiency of up to 1%. Their tunable solubilities as well as optical and electronic properties render perylene dyes available for all kinds of organic solar cells, including organic heterojunction and hybrid solar cells. Because of their outstanding π-conjugated planar core with imide or amidine groups, perylene compounds have high electron affinities and can thus accept electrons from most donor compounds. Soluble perylene dyes have been widely used in solution-processable polymer solar cells, whereas perylene pigments can be employed in bilayer heterojunction solar cells via sublimation. Perylene compounds can also couple to other electron-donating groups to form donor-acceptor oligomers or polymers for photovoltaic applications. Using the anhydride or carboxylic acid groups as anchors, perylene molecules are able to be applied in dye-sensitized solar cells as well. With the consideration of the uniqueness of perylenes, the present article reviews the development of perylenes in organic photovoltaics.

2.1 Introduction

Since Kardos patented the first perylenediimide (PDI) in 1912[1], perylenes have been intensively developed and many papers about perylene have been

then appeared. Especially, there are more than a thousand publications regarding perylene each year from 2002. The extraordinary chemical, thermal and photochemical stability of perylene has attracted the attention of many scientists and engineers . Nowadays, perylenes and their derivatives are not only used in colorant field, but also applied in many high-tech applications, for instance, organic electronic devices[2~6], dye lasers[7], bio-labels[8] and sensors[9, 10].

Generally, the solubility, optical and electrochemical behaviors of perylenes can be efficiently tuned by using a variety of synthetic procedures, which include the functionalization in either bay or peri positions of perylene core (Figure 2.1)[11~13]. The industry production of perylenes starts with perylenediimide (1) which can be saponified to form a important commercialized product perylenedianhydride (2, PDA). Tetra-chlorinated or di-brominated PDAs (compounds 5 and 3, respectively) are able to be prepared via the halogenation of compound 2. The anhydrides 2, 3 and 5 can be converted to corresponding imides (PDIs) 1, 4 and 6, which represent useful building blocks for the synthesis of water-soluble, push-pull and core-expanded perylene derivatives. Quite recently, some direct functionalization of PDI 1 was described in the literatures, for example, 2,5,8,11-functionalized PDI can be achieved via the Murai reaction by using PDI 1 as the starting material[14~16].

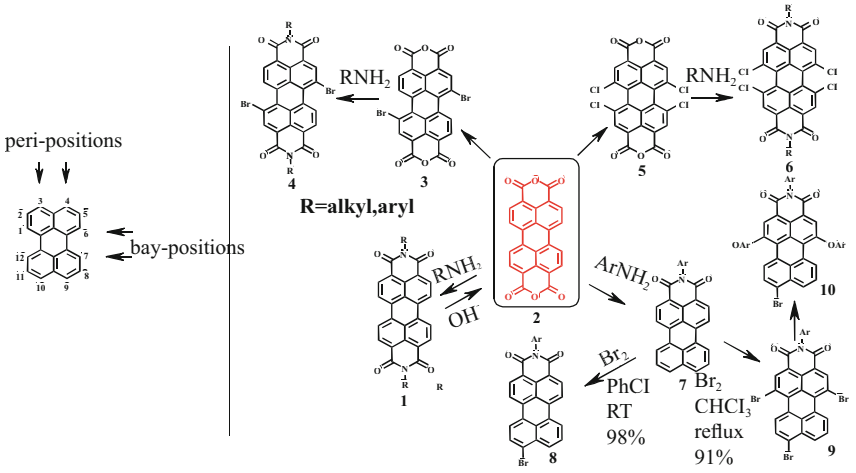

Figure 2.1 Perylene structure and synthesis of perylene imides

Alternatively, one-pot imidization-decarboxylation of compound 2 affords perylenemonoimide (7, PMI), which can be either monobrominated or tribrominated in high yield depending on different reaction temperature and

solvents[11]. The brominated products 8 and 9 are the basic building blocks for the extension of the perylene core and the introduction of donor groups.

Based on the above mentioned facile molecular decoration methods, the photovoltatic application of perylenes and their derivatives covers all types of organic solar cells, including molecule, polymer and dye-sensitized solar cells. In this chapter, we summarize perylenes used in organic photovoltaics (OPV).

2.2 Perylene pigments in solar cells

In 1986, Tang published the first efficient organic solar cell. The device was fabricated in a sandwich structure, which contained a two-active-layer structure of perylenedibenzimidazole (PTCBI) and copper phthalocyanine (CuPc)[17]. The active organic layers are located between the indium tin oxide (ITO) and the metal electrode. As shown in Figure 2.2, the donor (CuPc) and the acceptor (PTCBI) compounds are deposited on the ITO-coated substrate (glass) layer by layer. On top of the acceptor layer, the metal electrode is deposited also under vacuum. When light shines on the device, photons absorbed by donor and acceptor materials (the active layer) lead to the formation of electronic excited states, where the electrons and holes are bound by Coulombic forces. These Coulomb-correlated electron-hole pairs are properly described as excitons. Subsequently, the excitons diffuse to the interface of donor-acceptor materials where charge separation occurs. There the excitons dissociate into electrons and holes. Finally, the free charge carriers move to their corresponding electrodes (holes to ITO and electrons to metal electrode) with the help of the internal electric field.

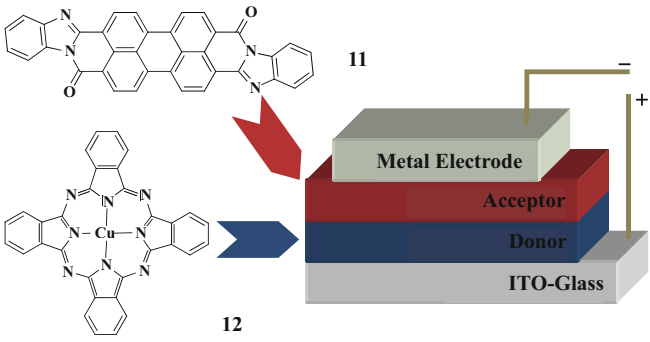

Figure 2.2 Perylenedibenzimidazole (11, PTCBI), copper phthalocyanine (12, CuPc) and the device structure of the first efficient organic solar cell

With the above mentioned solar cell device structure, the first organic solar

cell with a reasonable power conversion efficiency of 1% was demonstrated. This discovery opens up the development of organic photovoltaics. After that, many other perylene pigments (13~19) were synthesized for the application of organic solar cells[18~28]. Most of the perylene compounds have poor solubility and can be sublimed. Because of their outstanding π-conjugated planar structure with two imide or amidine groups, perylene compounds have high electron affinities and can thus accept electrons from most donor compounds. A vast number of studies have been devoted to improving photovoltaic performance by introducing different derivatives of perylenes as electron-acceptors and metal phthalocyanines or conjugated polymers as electron-donors. However, the highest efficiency reported so far for this kind of cell is 2.7% and the materials used in the devices are still PTCBI 11 and CuPc 12[29].

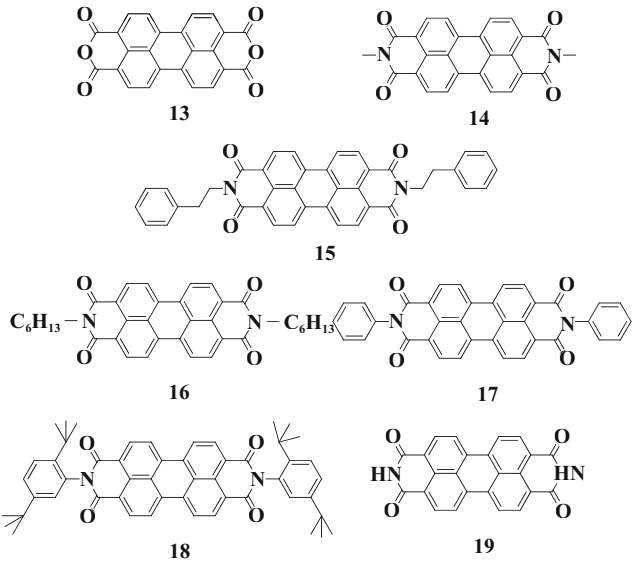

2.3 Perylene dyes in solar cells

Different from the perylene pigments based organic solar cells, the perylene dyes based organic photovoltaics can be fabricated via solution processed printing techniques, including spin-coating, doctor-blading, screen-printing, and drop-casting[30]. One can dissolve the donor and acceptor molecules in a common solvent, and then print the materials on the substrates. Consequently, in the so-called bulk-heterojunction formation, where the donor phase is intimately

intermixed with the acceptor phase, the excitons can more easily access the donor-acceptor interface and subsequently dissociate to holes and electrons at the donor-acceptor interface. The free charge carriers will then move to the corresponding electrodes by following the continuous route of either donors or acceptors. Using this strategy, well-soluble N,N'-Bis(1-ethylpropyl)-3,4:9,10-perylenediimide (20, PDI), hexa(alkylphenyl)- subsitutued hexabenzocoronene (21, HBC) was mixed in chloroform[3]. The solution of 8 and 9 (with a weight distribution ratio of 40:60) was spin-coated on ITO substrates and produced thin films with vertically segregated domains with a large interfacial surface area. When Al was used as counter electrode, the devices exhibited an incident photon-to-current conversion efficiency (IPCE) of 34% at 490 nm. This result demonstrated that efficient exciton generation and dissociation was achieved upon using these components. Under monochromatic illumination at 490 nm (0.47 mW/cm^2), the solar cell containing 20 and 21 showed a power conversion efficiency of 1.95% with a short circuit current of 33.5 μA/cm^2, an open circuit voltage of 0.69 V, and a fill factor of 40%. (Figure 2.3)The photovoltaic performance of these devices under standard solar irradiation, however, was limited by the weak absorption of compound 21 in the solar spectrum.

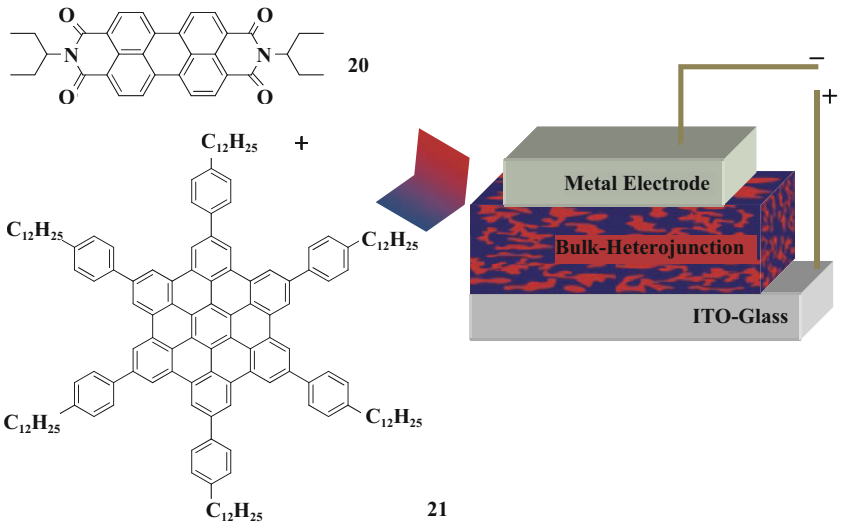

Figure 2.3 *N,N'*-Bis(1-ethylpropyl)-3,4:9,10-perylenediimide (20, PDI), hexa(alkylphenyl)-substituted hexabenzocoronene (21, HBC) and the device structure of the bulk-heterojunction solar cell

Due to its outstanding solubility, PDI 20 was also used as acceptor in polymer solar cells where poly(N-alkyl-2,7-carbazole) was applied as donor[31]. However in polymer photovoltaics, 1-[3-(methoxycarbonyl)propyl]-1-phenyl-(6,6)-C61 (PCBM) is the most promising electron accepter. Therefore, to compare the properties of acceptor materials (PDI and PCBM), the solar cell devices containing PCBM and 22 were also tested. In terms of light absorption, 20 compensates the absorption of 22 more efficiently than PCBM does. The photovoltaic devices were fabricated from the blend of 20:22 or PCBM:22 at a donor-acceptor ratio of 1:1. The IPCE spectrum of the device using PCBM exhibited an IPCE maxium at 400 nm with a value of 2.5%. In contrast, the device using PDI 20 revealed a broad IPCE spectrum with two strong peaks showing IPCE values of 3.4% at 420 nm and 3.8% at 500 nm, corresponding to the absorption of 22 and PDI 20, respectively. The compounds 22 and PDI 20 (1:1) blend solar cells exhibited a power conversion efficiency which is three-fold of the efficiency of 22 and PCBM based solar cells under the same light irradiation. The blend containing 20 wt% of 22 and 80 wt% of 20 (1:4) gave an overall efficiency of 0.63% (under 10 mW/cm^2 sunlight intensity), and a maximum IPCE of 15.7 % at 495 nm.

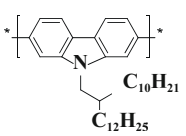

22

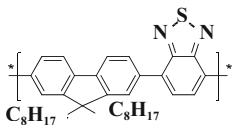

23

The PDI 20 gave a better photovoltaic performance than that of PCBM in polycarbazole 22 based solar cells, however, in most cases of polymer solar cells, PCBM and its derivatives are the most promising acceptors for organic solar cells, for instance, the polymer solar cells with P3HT:PCBM as active materials have a highest power conversion efficiency up to 5%[32,33], but the P3HT:PDI 20 based devices only exhibit low efficiencies[31].Especially, the reported quantum efficiency of devices utilizing perylene derivatives has not exceeded roughly 30%. Compounds 20 and 23 were used to investigate the cause of this low quantum efficiency[34]. The relaxation of excitons into stabilized, and essentially immobile, intermolecular states on the PDI was considered as a loss mechanism. These stabilized states lead to a long-lived red-shifted emission and are typically formed rapidly (on the time scale of 100 ps) after photoexcitation. It is concluded that ① the formation of stable, neutral, intermolecular states on PDI before charge transfer occurs must be avoided; ② small domains of PDI that allow excitons to

quickly reach a heterojunction are favored; ③ the bimolecular recombination is very fast in the blend. Therefore, for the red-absorbing electron-acceptor PDI to realize its potential in organic solar cells, the rate of formation of intermolecular states on the PDI must be suppressed by disrupting the π-π stacking of PDI compounds.

To minimize the aggregation of PDI compounds, Sharma and Mikroyannidis et al. developed diphenoxylated PDI acceptors for organic solar cells[35~37]. A blend of 24 with small molecule 25 or polymer 26 exhibited power conversion efficiencies up to 2.85% with a short circuit current of 6.8 mA/cm^2, an open circuit voltage of 0.88 V and a fill factor of 0.47. Additionally, the incorporation of a thin annealed ZnO layer between the bulk-heterojucntion of 27 and 28 and the top Al electrode, resulted in a PCE of 3.17%. These results opened a new design of perylene based bichromophores as acceptors in organic solar cells. The pyrene or anthracene groups in 24 and 27 enable additional intramolecular energy transfer to perylenediimide, improving on one hand the light-harvesting ability of the dye, and on the other hand enhancing the communication between the perylene acceptor and the donor compounds in devices.

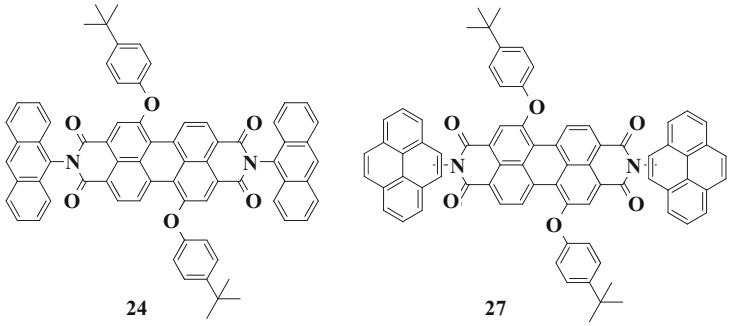

24

27

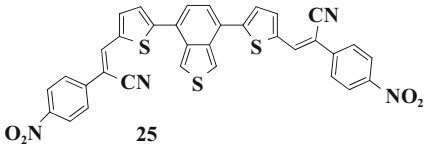

25

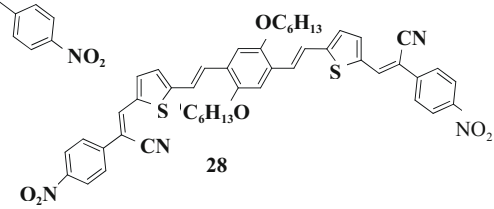

28

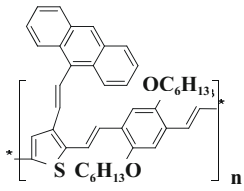

26

2.4 Perylene contained polymers/oligomers in solar cells

In bulk-heterojunction solar cells with donor-acceptor mixture, the charge transport and collection in a disordered nanoscale blend may be hindered by phase boundaries and discontinuities. Covalent connection of donor and acceptor in a single polymer or oligomer chain can overcome these drawbacks. Perylene dyes have therefore been linked to other electron-donating groups to form donor-acceptor oligomers or polymers for photovoltaic applications. The intramolecular donor-acceptor combination can enhance the photoinduced energy and electron transfer between donor and acceptor moieties. Therefore, many perylene copolymers have been developed. There are three types of covalently linked donor-acceptor polymers: ① semiconducting polymers as a donor with pendant acceptor groups; ② alternative (random or regular) donor-acceptor copolymers; ③extended donor and acceptor units arranged in diblock copolymers. Because of the strong inter- and intramolecular interactions between donor and acceptor moieties, the latter two strategies may have important advantages. The intrinsic tendency of each segment in block copolymers to aggregate in an individual phase provides a means to create a well-ordered nanoscale morphology.

2.4.1 Perylene contained heterojunction solar cells

The combination of perylene dyes with structurally defined oligothiophenes was firstly reported by Bäuerle et al[38~40] They designed and synthesized a series of N-(2,6-diisopropylphenyl)-perylene-3,4-dicarboximides (Perylenemonoimide (PMI), as acceptor) substituted by oligo(3-hexylthiophenes) (as donors) in the 9-position of the perylene core (compounds 29~40). The typical charge transport and self-assembling properties of oligiothiophene in the solid state was preserved by this type of π-donor-acceptor dyad molecule, whereas the perylene unit should provide high absorptivity in the visible region as well as electron-accepting properties. When the oligothiophene length increased, the intensity of the emission bands and the quantum yields progressively decreased due to the enhanced intramolecular charge transfer. Excitation at wavelengths corresponding to the oligothiophene absorption resulted in complete fluorescence quenching in the oligothiophene part, and the fluorescent spectra only showed the emission of the perylene compounds. An energy transfer from the oligothiophene to the perlyene moiety is indicated by these aspects. HOMO/LUMO energies were determined via cyclic voltammetry in dichloromethane. It was clearly observed that the HOMO-LUMO bandgap decreases with increasing chain length of the oligothiophene unit, which is mainly due to the fact that the constant raise of the HOMO energy level as the LUMO level remains more or less unchanged. These compounds were tested for solar cells with the device

structure of ITO/PEDOT:PSS/perylene-oligothiophene:PCBM/LiF/Al. In the donor-acceptor series, 34 gave the best photovoltaic performance with a V_{oc} of 0.94 V and a power conversion efficiency of 0.48%. With the acceptor-donor-acceptor structure, the 35 based solar cells exhibited a V_{oc} of 0.68 V and a η of 0.2%. The perylene-oligothiophene compound 39 showed a V_{oc} of 0.60 V and a power conversion efficiency of 0.25% in a solar cell device. From these results it can be concluded that the device performance has been greatly affected by the structural tuning. Completely different behaviors were shown in these compounds with the same perylene and oligothiophene moieties in different combinations. To further improve the structure of the compounds for better photovoltaic performance, more focus should be placed on the perylene moiety, e.g. changing from an isopropylphenyl imide substituent to an alkyl imide in order to enhance the self-organization ability of the whole molecule. As shown here, the best photovoltaic performance of these three structural classes comes from the donor-acceptor structure, where the oligothiophenes play a very important role in the film formation resulting in the best photovoltaic performance. A detailed investigation of the morphology of the devices should help in improving such systems.

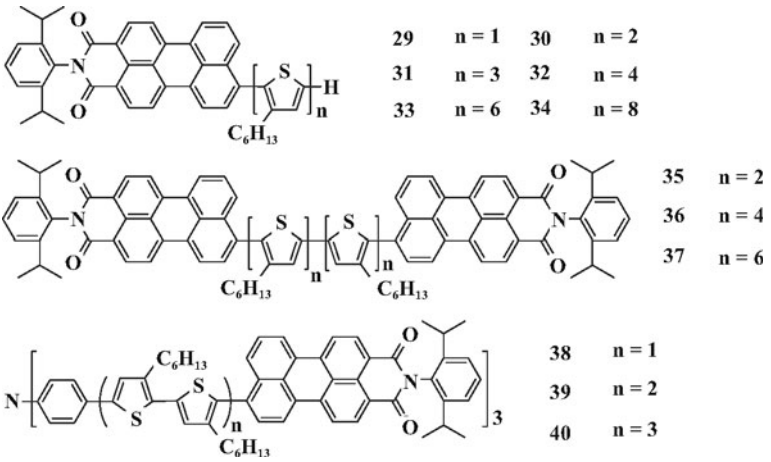

Besides perylene-thiophene oligomers, many copolymers containing perylene and thiophene derivatives have been developed. Via the Stille coupling, compound 41 was synthesized with a dithienothiophene scaffold[41~43]. This polymer has good solubility in most organic solvents and exhibits charge carrier mobilities of up to 1.3×10^{-2} $cm^2/V\cdot s$ characterized in an OFET geometry under nitrogen atmosphere. To investigate the potential of 41 for photovoltaic applications, an

all-polymer solar cell was fabricated, with 41 as the electron acceptor and 42 as the electron donor. With the device structure ITO/PEDOT:PSS/41:42(1:1)/Al, a power conversion efficiency of 1.5% was achieved from the cell with a V_{oc} of 0.63 V, a I_{sc} 4.2 mA/ cm^2 and a FF of 0.39. Like other low bandgap polymers, polymer 41 was also designed under the concept of the donor-acceptor construction to lower the polymer bandgap. Therefore, a broad absorption band over the whole visible region and into the near infrared is shown. Within the given donor-acceptor structure, the donor part in the polymer main chain can be easily varied, as the perylene moiety remained unchanged. In this way, the energy gap of such polymers can be well tuned.

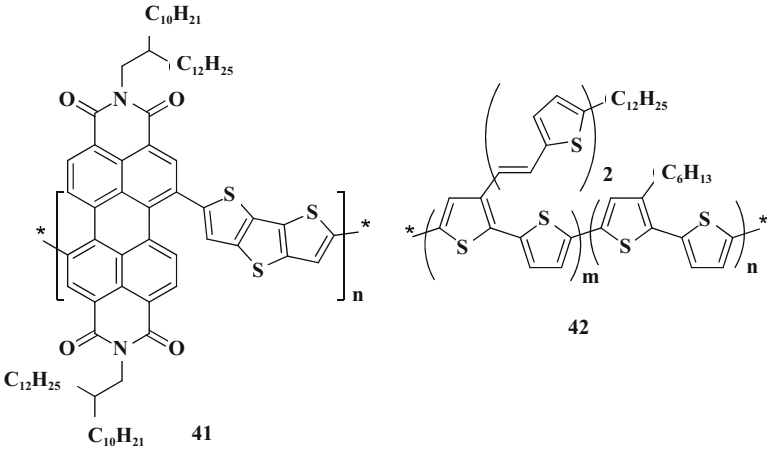

2.4.2 Perylene contained single-molecular solar cells

Janssen and his coworkers first reported copolymers based on oligophenylenevinylene and perylenediimide.44 A solution of 43 and 44 in chloroform was spin-coated on ITO glass covered with a layer of PEDOT:PSS. A LiF/Al top electrode was deposited by vacuum. With an ITO/PEDOT:PSS/polymer/LiF/Al structure, the devices exhibited high V_{oc} values (1~1.2 V), but extremely low short circuit current densities (0.008~0.012 mA/ cm^2). The low current was resulted from the fast geminate recombination (more than 80% recombination within 1 ns) and poor transport characteristics due to face-to-face orientations of the perylenediimide and oligophenylenevinylene segments in alternating stacks in the polymer films. These results showed, that in order to overcome the intrinsic tendency of donor and acceptor segments giving alternating

stacks, stronger antagonistic interactions directing the microscopic morphology should be introduced.

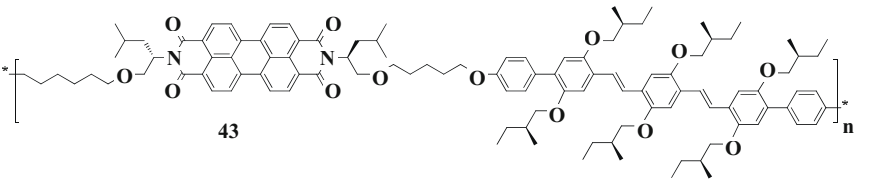

43

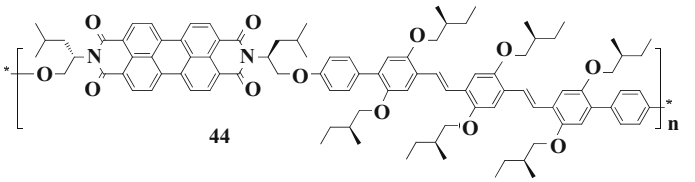

44

The copolymerization of perylenediimides and donor groups via the bay positions of the core was reported by Zhu and his coworkers in 2005 for the first time.45 In comparison to pure 1,7-diphenoxy-perylenediimide, which shows an absorption maximum at 526 nm, the absorption maxima of 45 and 46 are red-shifted by 10 and 13 nm, respectively. The solar cell devices based on 45 and 46 were fabricated under the structure of ITO/PEDOT:PSS/polymer/Ca/Al. A solar cell with polymer 45 exhibited a short circuit current of 0.45 mA/ cm^2, an open circuit voltage of 0.3 V and a fill factor of 36%. However, the solar cell with 46 gave a much lower I_{sc} of 0.0167 mA/ cm^2, a higher V_{oc} of 0.42 V, and a lower FF of 28%. The authors claimed that the much higher content of perylene in 45 than that in 46 resulted in the higher I_{sc} of the 45 cell. The absorber in the two copolymers should mainly be the perylene units, since the stilbene or triphenylamine is almost transparent in the visible region. The content of perylene units in the copolymers, therefore, played an important role in the photovoltaic performance.

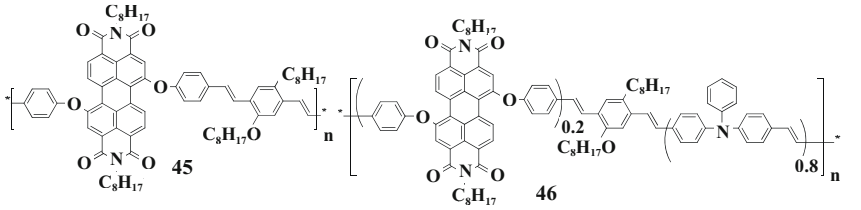

45

46

Another method to introduce perylenes into polymers, where the perylene moiety is not directly in the polymer backbone, was first realized by Hua et al.[46], who synthesized a highly soluble polymer based on polyphenylenevinylene, triphenylamine, and tetraphenoxy perylenediimide. The photovoltaic performance observed for ITO/PEDOT:PSS/polymer 47/Ba/Al solar cells presented that the PCE reached only values of 0.0005%. According to the authors, the cell's poor performance was ascribed to the face that the majority of the absorbed energy by the polyphenylenevinylene backbone was promptly conveyed to the perylene's lowest singlet excited state, leaving only a very small portion of absorbed light to contribute effectively to the photocurrent. Additionally, the fluorescence quantum yield of polymer 47 is only around 0.1 which is much lower than that of perylenediimide (~1). Therefore, the unexpected low fluorescence indicated strong photoinduced electron transfer instead of energy transfer from triphenylamine moiety to perylenediimide in the polymers.

Thelakkat and his coworkers reported a diblock copolymer bearing perylenediimide without bay functionalization to further optimize the nanostructured bulk-heterojuctions[47~49]. These block copolymers 48~50 can self-assemble into a nanostructure, which provides charge-separation interfaces on the nanometer scale. With an ITO/PEDOT:PSS/polymer/Al configuration, the cells based on these polymers demonstrated a much better photovoltaic performance than the device based on the monomer blend. By using 49 as a single-active-layer, a top PCE of 0.3% with an I_{sc} of 1.14 mA/ cm^2, a V_{oc} 0f 0.69 V, and a FF of 0.32 could be achieved. Based on these results, an elegant and promising solution for overcoming the short exciton diffusion length in organic semiconductors seems to be the use of a block copolymer with suitable electronic properties.

Recently, Bu and his coworkers demonstrated monodisperse conjugated oligomers 51~53 which are characterized by a uniform chemical structure as well as a tunable molecular length around 10 nm[50]. Different from the compounds which Bäuerle group reported, compounds 51~53 contain perylenediimide with hexyl functionalized imide, which renders the compounds strong segregation ability. The UV-Vis absorption spectra of the oligomers indicate that the perylenediimide units are face-to-face stacked (H-aggregation) in films, exhibiting highly ordered alternating donor-acceptor lamellar nanostructures. Under the construction of ITO/PEDOT:PSS (50 nm)/oligomers (70 nm)/PDI 20 (3 nm)/LiF (1 nm)/Al (100 nm), oligomer 53 gave the best device performance, with a power conversion efficiency of 1.5%, an open circuit voltage of 0.87 V, a short circuit current of 4.49 mA/ cm^2 and a fill factor of 0.38. In the photovoltaic devices, the PDI 20 was functionalized as a hole-blocking layer and resulted in the higher fill

factor and short circuit current density. Up to now, this is the best result of organic single molecular solar cells.

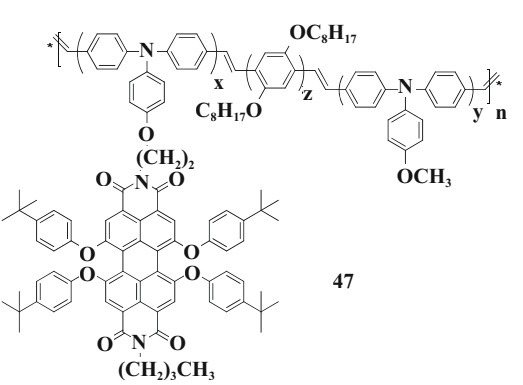

47

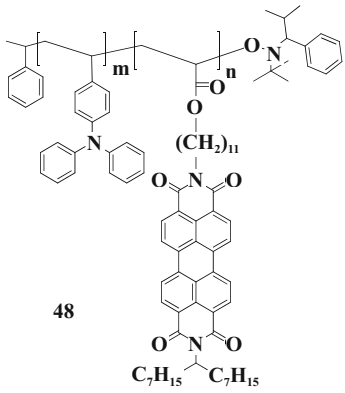

48

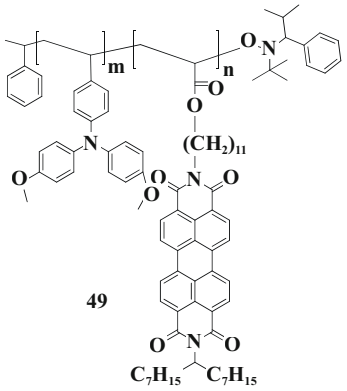

49

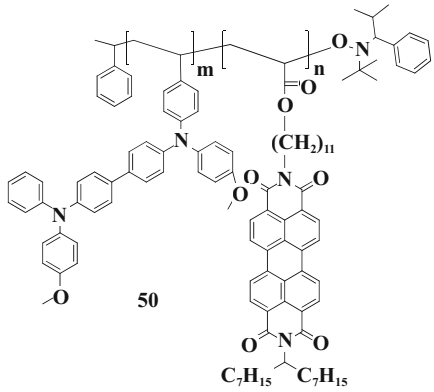

50

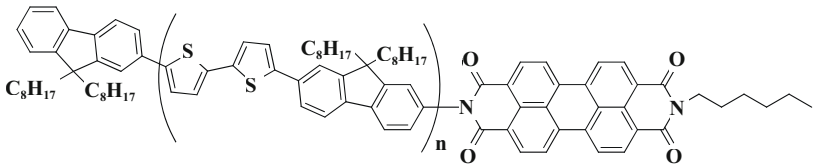

51 n = 4 52 n = 5 53 n = 6

In the heterojunction solar cells, perylenes can be used as electron-acceptors, they can also be copolymerized with electron rich units, to achieve materials functioning as donors or alone as D-A systems for single-system devices. With all these features, perylenes are seemly desirable materials for heterojunction solar cells.

2.5 Perylenes in Grätzel solar cells

Complementary to their use in heterojunction solar cells, perylenes have also been applied as sensitizers in dye-sensitized solar cells[51] (also named as Grätzel cells which was first published by Grätzel and O'Regan in 1991) since they can be easily functionalized with carboxylic acid or anhydride groups which serve as anchor groups for attachment onto inorganic semiconductor surfaces. Research into perylene sensitizers started in 1996, when Burfeindt reported an electron injection rate of 190 fs for 2,5-bis(tert-butly)-9-methylphosphonic acid perylene adsorbed on nanocrystalline TiO_2[52].

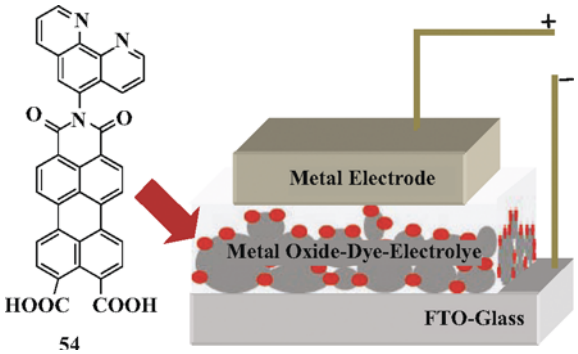

Figure 2.4 One of the first perylene sensitizers (54) and the device structure of the dye-sensitized solar cell.

2.5.1 The derivatives of perylenediimides

The application of perylenes as sensitizers began in 1997, when Gregg et al. introduced a sensitizing dye-semiconductor system comprising of perylene 54~56 with a carboxylic acid groups on SnO_2[53]. These perylenes are highly emissive, facilitating time-correlated emission experiments employed to measure charge injection rates. The cells had a 2.5 μm thick nanoporous SnO_2 film on FTO glass and contained an electrolyte solution of 0.5 M LiBr, 0.05 M Br_2, and 0.2 M 4-tert-butylpyridine in 80:20 (v:v) ethylene carbonate:propylene carbonate. The counter electrode was a platinum-coated F-SnO_2 glass substrate. With such a device structure, the maximum IPCE value of the cell based on 55 was approximately 30% for the wavelength region 458~488 nm, and an overall power conversion efficiency of 0.89% was achieved.

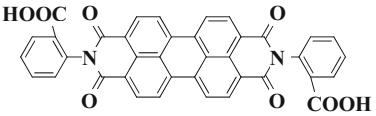

55

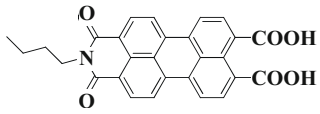

57

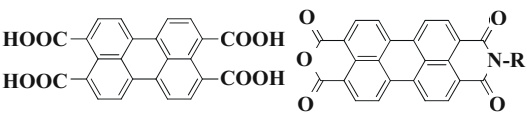

56

58 R=1-Pentyl-hexyl

59 1-Isobutyl-3-methyl-butyl

60 2-Ethyl-hexyl

61 2,6-Diisopropyl-phenyl

62 Cyclohexyl

In 2002, Li et al. reported TiO_2 nanocrystalline films sensitized by perylene 56 and 57[54]. Via bromine-doping of TiO_2 nanocrystalline film, the maximum IPCE of the perylene dye 56 was improved up to 40% for the wavelength region from 440 to 530 nm.

Many perylene sensitizers have been developed by using anchoring groups such as anhydride which reacts chemically with inorganic semiconductors, for instance TiO_2[55]. Icli et al. studied the influence of the substituents in the imide groups of perylene monoimide monoanhydride on the photovoltaic performance in DSCs.55 It was found that higher device efficiencies were achieved by the dyes with longer and branched alkyl chains. In this series of dyes, 58 exhibited the highest efficiency of 1.61% under AM 1.5 solar light.

To further improve the efficiency of perylene sensitizers, Shibano et al. introduced pyrrolidines as electron-donating groups in the 1, 6-positions of perylene core[56]. It was claimed that such structures have the following advantages: ① the pyrrolidine groups exhibit strong electron donation at the perylene core and shift the first oxidation potential considerably in the negative direction. Therefore, it could be expected that a more exothermic electron injection from the excited singlet state to the conduction band of TiO_2 electrode would take place. Also, the light-harvesting ability in the red-to-NIR region could be improved by such substitution. ② Further, the *bay*-substituents suppress the dye aggregation on the TiO_2 surface and consequently the intermolecular charge recombination can be hindered. The cells were built under typical procedures using 13 μm TiO_2 and I-/I3- electrolyte. The highest efficiency of 2.6% was obtained using 63 as the sensitizer.

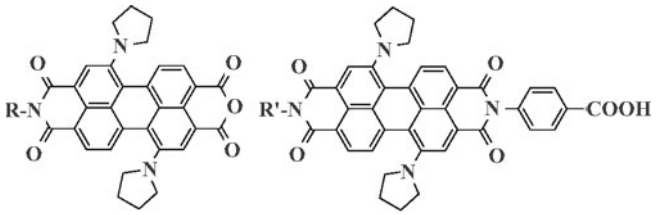

63 R=2,6-diisopropylphenyl 65 R'=2,6-diisopropylphenyl
64 R=cyclohexyl 66 R'=cyclohexyl

Similar to the research of Fortage et al. reported the effect of ① the nature of electron-donating substituents (phenoxy or piperidine) on the perylene core, ② the position of the anchoring groups, ③ the presence of a fused benzimidazole moiety on the performance of DSCs[57]. Efficiencies ranging from 0.2% to 2.3% were shown by these dyes 67~74. It was noted that the electron injection efficiency can be controlled by the position of the anchoring groups. The presence of the four phenoxy groups in the perylene bay position led to effects similar to those of the two piperidine groups, but with a lower propensity to aggregation and a slightly higher photovoltaic performance. It is effective to functionalize perylene with a benzimidazole moiety to extend the absorption spectrum into the red: but owing to the rather electron-rich nature of benzimidazole, it should be placed at the opposite side of the anchoring group.

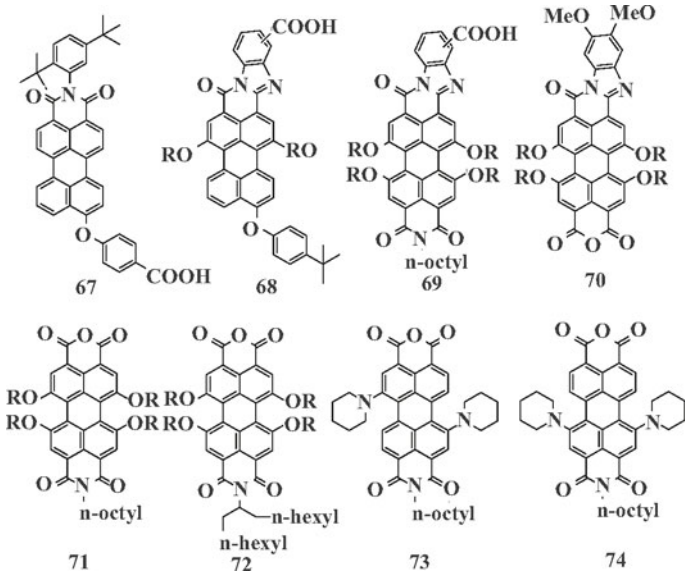

67 68 69 70

71 72 73 74

As a further development of piperidine-substituted perylene sensitizers, Planells et al. presented a perylene sensitizer 75, which contains a complexing unit and is capable of selectively binding lithium ions in DSCs[58]. Compared to the 76-sensitized solar cells, the devices of 75 yielded higher voltages but lower photocurrents under simulated sunlight. This indicated a shift in the TiO_2 conduction band edge due to the complexation of Li with the azacrown ether, which may induce the formation of a dipole at the nanoparticle surface.

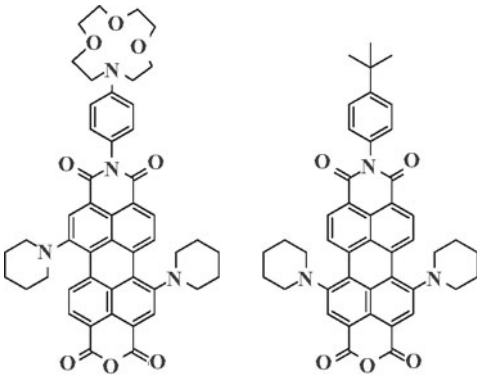

75 76

2.5.2 The derivatives of perylenemonoimides

In 2001, push-pull type perylenes 77~81 were developed by Ferrere and Gregg[59,60]. They improved the device efficiency through exposing the cell to ultraviolet (UV) light[61]. The short circuit photocurrent improvements ranged from three- to more than 100-fold. A positive shift of the conduction band of TiO_2 appears to be the primary mechanism[61]. The cells were constructed by using 6~7 μm thick TiO_2 layers and an electrolyte which contained 0.5 M tetra-n-butylammonium iodide, 0.05 M I_2, and 0.2 M 4-tert-butylpyridine in 3-methoxyproprionitrile solution. After UV treatment, perylene 78 based cells presented a highest power efficiency of 1.92%, while an efficiency of 4.4% was shown by cells sensitized by the N3 ruthenium complex (cis-di(thiocyanato)-bis(2,2'-bipyridyl-4,4'-dicarboxylate)- ruthenium(II)) under the same condition.

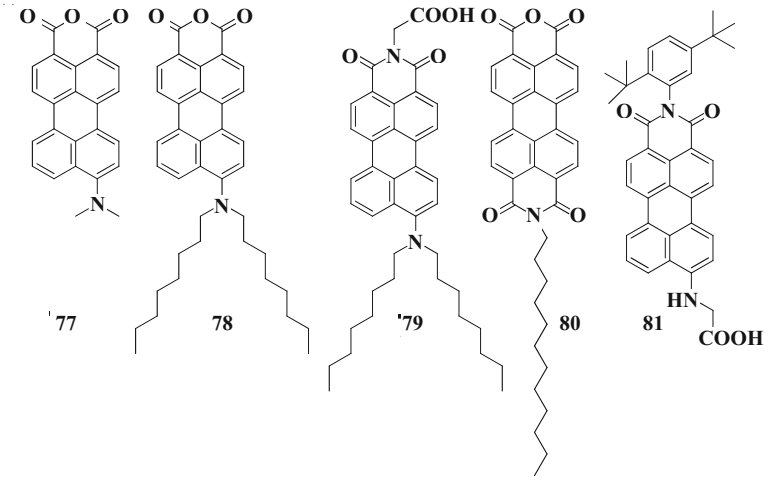

After the research of Ferrere and Gregg using similar structure concept Matsui et al. reported a series of 9-substituted perlyene monoanhydrides 82~87 for dye-sensitized ZnO solar cells[62]. Among these compounds, the 9-bromo perylene monoanhydride 83 showed the highest overall power efficiency of 0.52%, however, with no improvement compared to previous examples. Obviously, the poor photovoltaic performance of these dyes is ascribed to the lack of strong donor substituents in 9-position of perylene.

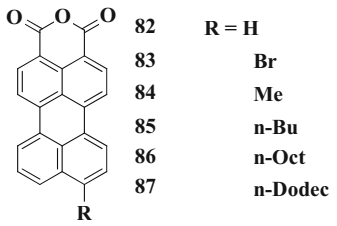

In the field of dye-sensitized solar cells, most organic metal-free sensitizers possess push-pull structures with donor-acceptor functionalization[63]. With this molecular design principle, our group constructed a family of perylene dyes covering the entire visible region. Their optical and electrochemical properties were thereby tunable via the introduction of electron-donating or electron-withdrawing groups in the 1, 6-positions of perylenemonoimide and additional electron-donating groups in the 9-position of perylenemonoimide to form push pull structures with controllable properties[64]. These push-pull type perylenes 88~92

can be synthesized simply and their optical and electrochemical properties can be tuned in a facile way. Moreover, these perylenes display a rainbow of colors and absorption maxima modifiable throughout the whole visible region. Furthermore, due to the strong electron-donating groups in the 9-position, intramolecular charge transfer and favorable orbital partitioning (which occurs when on the donor part of the molecule the HOMO coefficients are high, while on the acceptor part of the same molecule the coefficients of the LUMO are high), necessary for DSC, are achieved.

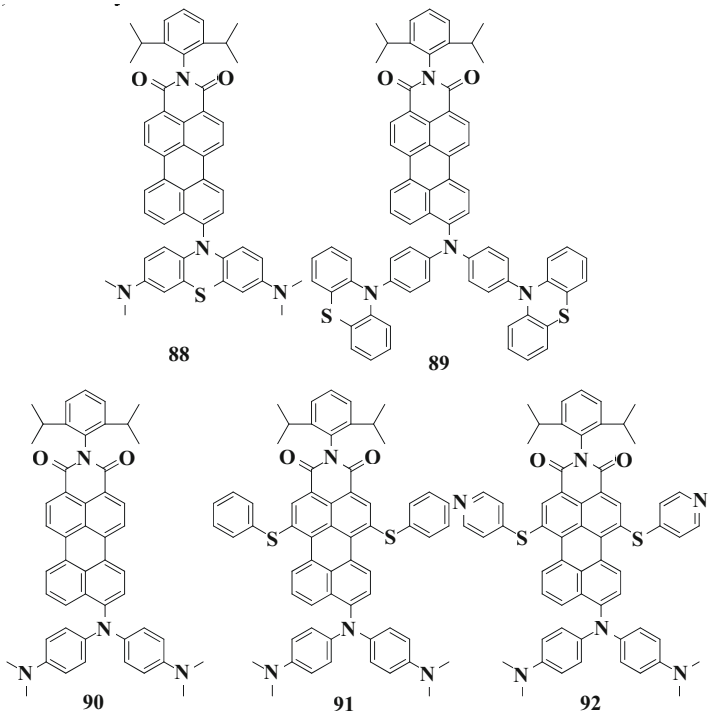

Taking advantage of these properties, many perylene sensitizers have been synthesized[65~67]. A monotonic increase of the absorption maximum in dichloromethane was observed ranging from perylene 93 to 96 due to increasing donor strength, which also induced a dipole moment increase of the compounds as well as an improvement of the intramolecular charge transfer. Consequently, the power efficiencies of perylene 93~96 sensitized TiO_2 were from 1.4% → 2.0% → 2.4% → 3.2%, corresponding to the trend of the intramolecular charge transfer values[65].

Via the introduction of different substituents into the 1, 6-positions of the perylene core, three push-pull type perylene sensitizers 97~99 with different molecular sizes, but similar spectroscopic and electrochemical properties, were made to investigate the relationship between the photovoltaic performance and the size of the sensitizers[67]. It was found that sensitizers with a smaller size showed better performance at low light intensities. However, at higher light intensities, the efficiencies for the cells with larger dyes approached those of the smaller dyes, despite much less adsorption on TiO_2. It is suggested by the results that dye morphology plays an important role in device performance, with specific regard to aggregation and recombination.

It should be noted that a breakthrough in perylene sensitizers was the discovery that the introduction of two phenylthio groups in the 1,6-position of perylene core could tune the HOMO and LUMO energies as well as the absorption wavelength of the dyes (especially on TiO_2)[66]. As a result, compound 100 exhibited an unprecedented IPCE of 87% and yielded an efficiency of 6.8% under standard AM 1.5 solar conditions.

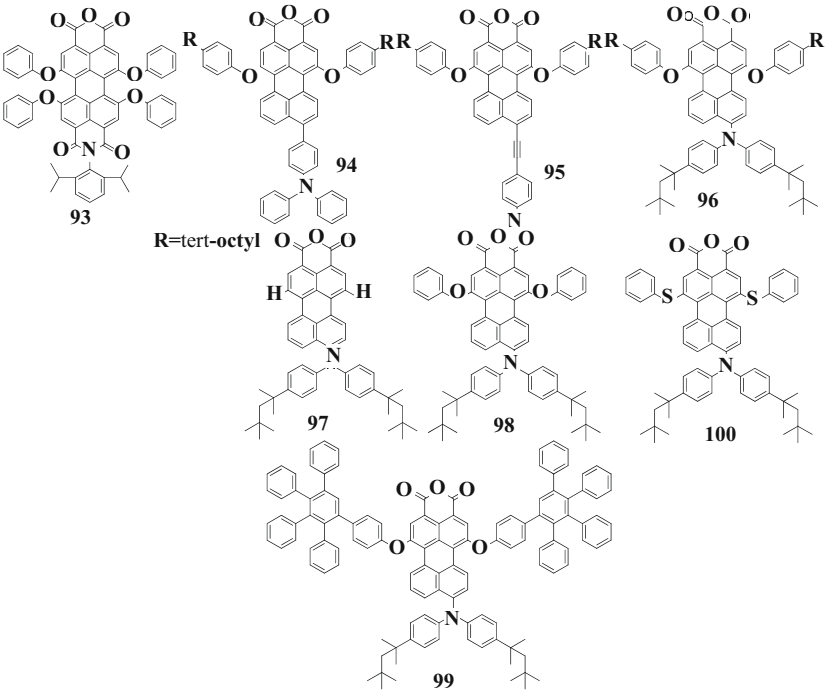

2.5.3 Perylene based multichromophores

With the aim of improving the absorption properties of ruthenium complexes, Liu et al. introduced naphthalene or perylene moieties into the ligand of ruthenium compounds[68]. However, the intramolecular charge transfer properties are affected by the strong electron-withdrawing nature of the imide groups, which leads to low efficiencies of these dyes in DSCs. The highest efficiency of 3.08% was achieved by using 101 as the sensitizer.

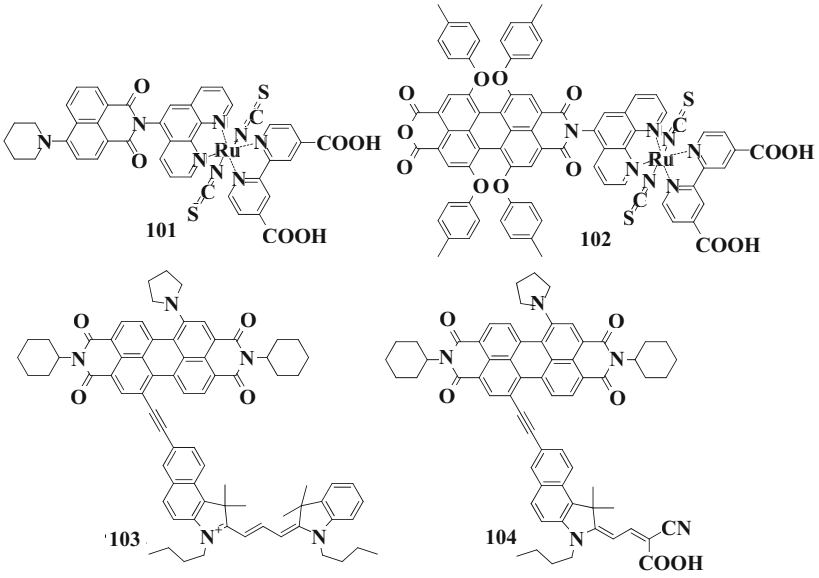

Meng et al. designed and synthesized another kind of bichromophore which contained perylene and benzo[e]indole units[69]. Wide absorption bands with high molar absorption coefficients over the entire visible spectrum were shown by these dyes. However, both compounds 103 and 104 exhibited low efficiencies, 0.34% and 1.38%, respectively, under irradiation with 75 mW/ cm^2 light illumination. According to the authors, these lower conversion efficiencies were ascribed to the imide group whose strong electron-withdrawing nature influenced the polarity of the whole molecule with a result of an unfavorable transfer direction of photo-generated electrons and consequently the decrease of the overall photocurrent performance.

2.6 Conclusion and outlook

Since the first efficient organic solar cell was reported by Tang, perylenes and their derivatives have been intensively used in the field of organic photovoltaics not only due to their various simple synthesis and functionalization methods, but also to their tunable solubility, optical and electrochemical properties. Their extraordinary photo-, thermo- and chemical stability as well as high electron affinity qualifies them as the promising materials for all kinds of organic solar cells, including molecule, polymer and dye-sensitized solar cells.

In this review, we have overviewed the state of the art design and development of perylenes in organic solar cells. Despite significant progress in this field, there is still plenty of room to improve the photovoltaic performance of perylenes.

(1) Perylenes as acceptor materials in molecule solar cells: the LUMO energy levels tuning of perylene pigments should be developed in order to achieve better electron injection from donors to perylenes.

(2) Perylenes as acceptor compounds in polymer solar cells: it is necessary to minimize the bimolecular recombination by additional side groups to suppress the aggregation of perylenes.

(3) Perylene polymers in single molecular solar cells: the design of block polymers or oligomers to control the morphology for a better exciton dissociation is very important.

(4) Perylenes as sensitizers in Grätzel solar cells: the energy levels variation of perylene dyes should be further investigated to obtain better perylene absorbers.

Our review indicates that perylenes and their derivatives will still be important candidates for organic solar cells.

Acknowledgements

We acknowledge the financial support of the Deutsche Forschungsgemeinschaft (DFG) priority program (SPP 1355) Elementary Processes of Organic Photovoltaics, the BMBF (Bundesministerium für Bildung und Forschung), and BASF SE.

References

[1] Kardos M. In Deutsches Reichspatent, 1913, Vol. 276357.

[2] Peumans P, Uchida S, Forrest, S R. Efficient bulk heterojunction photovoltaic cells using small-molecular-weight organic thin films. Nature,

2003, 425: 158~162.

[3] Schmidt-Mende L, Fechtenkotter A, Müllen K, et al. Self-organized discotic liquid crystals for high-efficiency organic photovoltaics.Science,2001, 293: 1119~1122.

[4] Jones B A, Ahrens M J, Yoon M H, et al. High-mobility air-stable n-type semiconductors with processing versatility:Dicyanoperylene-3,4 : 9,10-bis(dicarboximides).Angewandte Chemie-International Edition, 2004, 43: 6363~6366.

[5] Piliego C, Jarzab D, Gigli G,et al. High electron mobility and ambient stability in solution-processed perylene-based organic field-effect transistors.Advanced Materials, 2009, 21: 1573~1576.

[6] Tang M L, Oh J H, Devi Reichardt A,et al. Chlorination: A general route toward electron transport in organic semiconductors. Journal of the American Chemical Society, 2009, 131: 3733~3740.

[7] Sadrai M, Hadel L, Sauers R R,et al. Lasing action in a family of perylene derivatives: Singlet absorption and emission spectra, triplet absorption and oxygen quenching constants, and molecular mechanics and semiempirical molecular orbital calculations. Journal of Physical Chemistry, 1992, 96: 7988~7996.

[8] Peneva K, Mihov G, Nolde F,et al. Water-soluble monofunctional perylene and terrylene dyes: Powerful labels for single-enzyme tracking.Angewandte Chemie, International Edition, 2008, 47: 3372~3375.

[9] Zhang X, Rehm S, Safont-Sempere M M,et al. Vesicular perylene dye nanocapsules as supramolecular fluorescent pH sensor systems. Nature Chemistry, 2009, 1: 623~629.

[10] Chandrasekharan N, Kelly L A. A dual fluorescence temperature sensor based on perylene/exciplex interconversion. Journal of the American Chemical Society, 2001, 123: 9898~9899.

[11] Avlasevich Y, Li C, Müllen K. Synthesis and applications of core-enlarged perylene dyes. Journal of Material Chemistry, 2010, 20: 3814~3826.

[12] Herrmann A, Müllen K. From industrial colorants to single photon sources and biolabels: The fascination and function of rylene dyes. Chemistry Letters, 2006, 35:978~985.

[13] Würthner F. Perylene bisimide dyes as versatile building blocks for functional supramolecular architecture. Chemical Communication, 2004: 1564~1579.

[14] Bullock J E, Vagnini M T, Ramanan C,et al. Photophysics and redox properties of rylene imide and diimide dyes alkylated ortho to the Imide

Groups. Journal of Physical Chemistry B, 2010, 114: 1794~1802.

[15] Nakazono S, Easwaramoorthi S, Kim D,et al. Synthesis of arylated perylene bisimides through C-H Bond cleavage under ruthenium catalysis. Organic Letters, 2009, 11: 5426~5429.

[16] Nakazono S, Imazaki Y, Yoo H,et al. Regioselective ru-catalyzed direct 2,5,8,11-Alkylation of perylene bisimides. Chemstry-A European Journal, 2009, 15: 7530~7533.

[17] Tang C W. 2-Layer organic photovoltaic cell. Applied Physics Letters, 1986, 48: 183~185.

[18] Al-Mohamad A, Soukieh M. Solar cells and high efficiency photo-diodes having metal-organic thin film-semiconductor structures. Thin Solid Films ,1995, 271: 132~137.

[19] Derouiche H, Bernede J C, L'Hyver J. Optimization of the properties of bulk heterojunctions obtained by coevaporation of Zn-phthalocyanine/ perylene. Dyes amd Pigments 2004, 63: 277~289.

[20] Dittmer J J, Petritsch K, Marseglia E A,et al. Photovoltaic properties of MEH-PPV/PPEI blend devices. Synthetic Metals, 1999, 102: 879~880.

[21] Gregg B A. Bilayer molecular solar cells on spin-coated TiO_2 substrates. Chemical Physics Letters, 1996, 258: 376~380.

[22] Haensel H, Zettl H, Krausch G, et al. Optical and electronic contributions in double-heterojunction organic thin-film solar cells. Advanced Materials, 2003, 15: 2056~2060.

[23] Halls J J M, Friend R H. The photovoltaic effect in a poly(p-phenylenevinylene)/perylene heterojunction. Synthetic Metals, 1997, 85: 1307~1308.

[24] Hiramoto M, Fujiwara H, Yokoyama M. 3-Layered organic solar-cell with a photoactive interlayer of codeposited pigments. Applied Physics Letters, 1991, 58: 1062~1064.

[25] Kim I, Haverinen H M, Wang Z,et al. Effect of molecular packing on interfacial recombination of organic solar cells based on palladium phthalocyanine and perylene derivatives. Applied Physics Letters, 2009, 95: 1.

[26] Rim S B, Fink R F, Schoneboom J C,et al. Effect of molecular packing on the exciton diffusion length in organic solar cells. Applied Physics Letters, 2007, 91: 173504/1.

[27] Sylvester-Hvid K O. Two-dimensional simulations of CuPc-PCTDA solar cells: The importance of mobility and molecular pi stacking. Journal of Physical Chemistry B, 2006, 110: 2618~2627.

[28] Triyana K, Yasuda T, Fujita K,et al. Tandem-type organic solar cells by

stacking different heterojunction materials. Thin Solid Films, 2005, 477: 198~202.

[29] Peumans P, Bulovic V, Forrest S R. Efficient photon harvesting at high optical intensities in ultrathin organic double-heterostructure photovoltaic diodes. Applied Physics Letters, 2000, 76: 2650~2652.

[30] Brabec C, Scherf U, Dyakonov V, et al.Organic Photovoltaics: Materials, Device Physics, and Manufacturing Technologies. Chichester: John Wiley and Sons ,2008.

[31] Li J, Dierschke F, Wu J,et al. Poly(2,7-carbazole) and perylene tetracarboxydiimide: A promising donor/acceptor pair for polymer solar cells. Journal of Materials Chemistry, 2006, 16: 96~100.

[32] Kim J Y, Kim S H, Lee H H,et al. New architecture for high-efficiency polymer photovoltaic cells using solution-based titanium oxide as an optical spacer. Advanced Materials, 2006, 18: 572~576.

[33] Ma W, Yang C, Gong X,et al. Thermally stable, efficient polymer solar cells with nanoscale control of the interpenetrating network morphology. Advanced Functional Materials, 2005, 15: 1617~1622.

[34] Howard I A, Laquai F, Keivanidis P E,et al. Perylene tetracarboxydiimide as an electron acceptor in organic solar cells: A study of charge generation and recombination. Journal of Physical Chemistry C, 2009, 113: 21225~21232.

[35] Mikroyannidis J A, Stylianakis M M, Suresh P,et al. Efficient hybrid bulk heterojunction solar cells based on phenylenevinylene copolymer, perylene bisimide and TiO_2. Solar Energy Materials and Solar Cells, 2009, 93: 1792~1800.

[36] Sharma G D, Balraju P, Mikroyannidis J A,et al. Bulk heterojunction organic photovoltaic devices based on low band gap small molecule BTD-TNP and perylene-anthracene diimide. Solar Energy Materials and Solar Cells, 2009, 93: 2025~2028.

[37] Sharma G D, Suresh P, Mikroyannidis J A,et al. Efficient bulk heterojunction devices based on phenylenevinylene small molecule and perylene–pyrene bisimide. Journal of Materials Chemistry, 2009, 20: 561~567.

[38] Cremer J, Baeuerle P. Perylene-oligothiophene-perylene triads for photovoltaic applications. European Journal of Organic Chemistry, 2005, 17: 3715~3723.

[39] Cremer J, Baeuerle P. Star-shaped perylene–oligothiophene–triphenylamine hybrid systems for photovoltaic applications. Journal of Materials Chemistry, 2006, 16: 874~884.

[40] Cremer J, Mena-Osteritz E, Pschierer N G,et al. Dye-functionalized head-to-tail coupled oligo(3-hexylthiophenes) - perylene-oligothiophene dyads for photovoltaic applications. Organic and Biomolecular Chemistry, 2005, 3: 985~995.

[41] Zha X, Tan Z, Domercq B,et al. A high-mobility electron-transport polymer with broad absorption and its use in field-effect transistors and all-polymer solar cells. Journal of the American Chemical Society, 2007, 129: 7246~7247.

[42] Tan Z, Zhou E, Zhan X, et al. Efficient all-polymer solar cells based on blend of tris(thienylenevinylene)-substituted polythiophene and poly[perylene diimide-alt-bis(dithienothiophene)]. Applied Physics Letters, 2008, 93: 073309/1.

[43] Zhan X, Tan Z, Zhou E,et al. Copolymers of perylene diimide with dithienothiophene and dithienopyrrole as electron-transport materials for all-polymer solar cells and field-effect transistors. Journal of Materials Chemistry, 2009, 19: 5794~5803.

[44] Neuteboom E E, Meskers S C J, Van Hal P A,et al. Alternating oligo(p-phenylene vinylene)−perylene bisimide copolymers:Synthesis, photophysics, and photovoltaic properties of a new class of donor−acceptor materials. Journal of the American Chemical Society, 2003, 125: 8625~8638.

[45] Liu Y, Yang C, Li Y,et al. Synthesis and photovoltaic characteristics of novel copolymers containing poly(phenylenevinylene) and triphenylamine moieties connected at 1,7 bay positions of perylene bisimide. Macromolecules, 2005, 38: 716~721.

[46] Hua J, Meng F, Li J,et al. Synthesis and characterization of new highly soluble and thermal-stable perylene–PPV copolymers containing triphenylamine moiety. European Polymer Journal, 2006, 42: 2686~2694.

[47] Sommer M, Lindner S M, Thelakkat M. Microphase-separated donor-acceptor diblock copolymers: Influence of HOMO energy levels and morphology on polymer solar cells.Advanced Functional Materials,2007, 17: 1493~1500.

[48] Sommer M, Thelakkat M. Synthesis, characterization and application of donor-acceptor block copolymers in nanostructured bulk heterojunction solar cells. European Physical Journal-Applied Physics, 2006, 36: 245~249.

[49] Lindner S M, Huettner S, Chiche A,et al. Charge separation at self-assembled nanostructured bulk interface in block copolymers. Angewandte Chemie-International Edition 2006, 45: 3364~3368.

[50] Bu L, Guo X, Yu B,et al. Monodisperse co-oligomer approach toward nanostructured films with alternating donor−acceptor lamellae. Journal of the American Chemical Society, 2009, 131: 13242~13243.

[51] O'Regan B, Grätzel M. A low-cost, high-efficiency solar cell based on dye-sensitized colloidal TiO_2 films. Nature, 1991, 353: 737~740.

[52] Burfeindt B, Hannappel T, Storck W,et al. Measurement of temperature-independent femtosecond interfacial electron transfer from an anchored molecular electron donor to a semiconductor as acceptor. Journal of Physical Chemistry, 1996, 100: 16463~16465.

[53] Ferrere S, Zaban A, Gregg B A. Dye sensitization of nanocrystalline tin oxide by perylene derivatives. Journal of Physical Chemistry B, 1997, 101: 4490~4493.

[54] Wang S, Li Y, Du C,et al. Dye sensitization of nanocrystalline TiO_2 by perylene derivatives. Synthetic Metals, 2002, 128: 299~304.

[55] Zafer C, Kus M, Turkmen G,et al. New perylene derivative dyes for dye-sensitized solar cells. Solar Energy Materials and Solar Cells, 2007, 91: 427~431.

[56] Shibano Y, Umeyama T, Matano Y,et al. Electron-donating perylene tetracarboxylic acids for dye-sensitized solar cells. Organic Letters, 2007, 9: 1971~1974.

[57] Fortage J, Severac M, Houarner-Rassin C,et al. Synthesis of new perylene imide dyes and their photovoltaic performances in nanocrystalline TiO_2 dye-sensitized solar cells. Journal of Photochem Photobio A, 2008, 197: 156~169.

[58] Planells M, Cespedes-Guirao F J, Goncalves L,et al. Supramolecular interactions in dye-sensitised solar cells. Journal of Material Chemistry, 2009, 19: 5818~5825.

[59] Ferrere S, Gregg B A. Development of new dyes for the dye sensitized solar cell. Proceedings - Electrochemical Society 2001,10: 161~172.

[60] Ferrere S, Gregg B A. New perylenes for dye sensitization of TiO_2. New Journal of Chemistry, 2002, 26: 1155~1160.

[61] Ferrere S, Gregg B A. Large increases in photocurrents and solar conversion efficiencies by UV illumination of dye sensitized solar cells. Journal of Physical Chemistry B, 2001, 105: 7602~7605.

[62] Osasa T, Matsui Y, Matsumura T,et al. Determination of photo-active region in organic thin film solar cells with an organic heterojunction. Solar Energy Materials and. Solar Cells 2006, 90: 3136~3142.

[63] Mishra A, Fischer M K R, Baüerle P. Metal-free organic dyes for dye-

sensitized solar cells: From structure property relationships to design rules. Angewandte Chemie-International Edition, 2009, 48: 2474~2499.

[64] Li C, Schöneboom J, Liu Z,et al. Rainbow perylene monoimides: Easy control of optical properties. Chemistry--A European Journal, 2009, 15: 878~884.

[65] Edvinsson T, Li C, Pschirer N,et al. Intramolecular charge-transfer tuning of perylenes: Spectroscopic features and performance in dye-sensitized solar cells. Journal of Physical Chemistry C, 2007, 111: 15137~15140.

[66] Li C, Yum J H, Moon S J,et al. An improved perylene sensitizer for solar cell applications. Chem Sus Chem, 2008, 1: 615~618.

[67] Li C, Liu Z, Schöneboom J,et al. Perylenes as sensitizers in hybrid solar cells: How molecular size influences performance. Journal of Materials Chemistry, 2009, 19: 5405~5415.

[68] Liu B, Zhu W, Wu W,et al. Hybridized ruthenium(II) complexes with high molar extinction coefficient unit: Effect of energy band and adsorption on photovoltaic performances. Journal of Photochemistry and Photobiology A: Chemistry, 2008, 194: 268~274.

[69] Jin Y, Hua J, Wu W,et al. Synthesis, characterization and photovoltaic properties of two novel near-infrared absorbing perylene dyes containing benzo[e]indole for dye-sensitized solar cells. Synthetic Metals, 2008, 158: 64~71.

Chapter 3
Carbon Corrosion in Polymer Electrolyte Membrane Fuel Cell Catalysts and its Mitigation Strategies

Jianguo Liu[1], Zhongjun Hou[2]

1 Department of Materials Science and Engineering, Nanjing University, 22 Hankou Road, Nanjing, China

2 Sunrise Power Co LTD, Dalian, Liaoning, China

Abstract

Carbon corrosion in the electrocatalysts of polymer electrolyte membrane fuel cell (PEMFC) has a critical effect on its lifetime and becomes one of the main obstacles to its commercialization. The corrosion of supporting materials can be serious because of the appearance of the high voltage (>0.9V) when PEMFC operates in start/stop cycles or encounters local hydrogen starvation. One solution is a system strategy using existing materials by a voltage-limitation device to minimize the single cell voltage. The ultimate solution is the development of alternative corrosion-resistant supporting materials for Pt. Carbon nanotube is one of the most promising materials among all carbon forms. Nevertheless, non-carbon materials resistant to corrode under high voltage are still highly desired.

3.1 Introduction

Polymer electrolyte membrane fuel cell (PEMFC), with the advantage of low temperature operation (80^{o}C), quick response and high efficiency, is considered as a promising candidate for the application of transportation such as electric vehicle since 1980's [1].

The core component of PEMFC is membrane & electrode assembly (MEA), in which the electrochemical reactions occur. As showed in Figure 3.1, the state-of-the-art MEA is normally composed of gas diffusion layer, catalyst layer and Nafion membrane. The role of gas diffusion layer is to transport the reactants

and products into and out of the reactive sites in the catalyst layer. The catalyst layer which is attached directly to the membrane, will mainly response for the electrochemical reactions of oxidation and reduction in the anode and the cathode. The membrane is called polytetrafluoroethylene, or Nafion® made by Du Pont, in which proton can migrate from the anode to the cathode so that the whole reaction in the equation((3.1)～(3.3))can be finished.

$$\text{Anode reaction: } 2H_2 \rightarrow 4H^+ + 4e^- \quad Eo=0 \text{ V (vs. RHE)} \tag{3.1}$$

$$\text{Cathode reaction: } O_2 + 4H^+ + 4e^- \rightarrow 2H_2O \quad Eo=1.229 \text{ V (vs. RHE)} \tag{3.2}$$

$$\text{Overall reaction: } 2H_2 + O_2 \rightarrow 2H_2O \quad \Delta E=1.229 \text{ V (vs. RHE)} \tag{3.3}$$

There are many demonstrations of electric cars and buses based on PEMFC technologies around the world under the development of automobile companies and research institutes in the last two decades. The results of demonstrations indicate that one of primary factors that impede the large-scale commercialization of PMEFC is inadequate durability [2]. The lifetime of real application for cars and buses should reach 5 000 h and 20 000 h, respectively, which are not fully reached till now [3]. The durability of MEA has been investigated in real PEMFC from a thousand hour to tens of thousands hours [4～5]. One of challenges during such a long-term operation is the stability of the supporting material for Pt catalyst, i.e. carbon stability [6].

Reactions3.1～3.4 at low temperature (below 80°C) require noble metal like platinum as effective electrocatalysts to be accomplished, so it should achieve a high utilization of Pt to minimize the cost. Up to now, the platinum loading in the electrode is reduced to 0.4 mg/cm^2 or less from initial 4 mg/cm^2 (in the early space shuttle) in 1960's. The decrease of Pt loading is obtained by dispersing nano catalyst particles on a low-cost support material with a large surface area as showed in Figure3.2. The most common materials used one to date is carbon black, which has high electrical and thermal conductivity, high surface area and low-cost. Despite widespread usage of carbon, especially XC-72 from Cobat Corp., the support in PEMFC electrodes is susceptible to corrosive conditions, which include low pH (< 1), elevated temperature (50～90°C), high potential (>0.6V), certain humidification and oxygen concentration. When carbon corrodes, some Pt particles will peel from the electrode, resulting in weak interaction between Pt and the support. Yu reports that a corrosion of 5%～10% of carbon support leads to a dramatic performance loss [7].

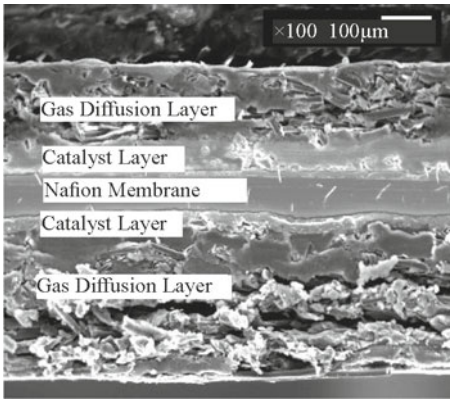

Figure 3.1 Scanning electron microcopy (SEM) image of membrane & electrode assembly (MEA)

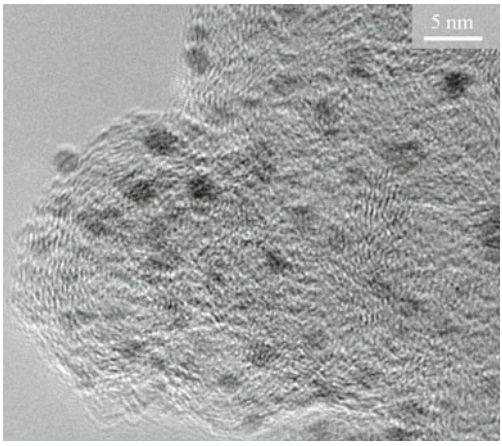

Figure 3.2 Transmission electron microscope (TEM) image of Pt supported XC-72 carbon black

3.2 Carbon corrosion

3.2.1 The reasons and consequences

The standard potential for carbon corrosion to carbon dioxide is 0.207V as showed in equation (3.4), which is much lower than the usual cathode potential of fuel cells (normally 0.6～1.2V).

$$C+2H_2O \rightarrow CO_2+4H^++4e^- \quad E^o=0.207\ V\ (vs.\ RHE) \tag{3.4}$$

Although thermodynamics of carbon is unstable, the kinetics of carbon corrosion under 0.8V vs. RHE is quite slow [8]. Actually, UTC Fuel Cells has demonstrated more than 200 units of phosphoric acid fuel cell (PAFC) as

stationary power sources in the world wide with an accumulation of 7 million hours field experience since the last decade [9]. Recently, they reported another progress of Purecell 400 running smoothly for more than 100 000 hours (ten years lifetime) [10]. As we know, PAFC works at much higher temperature (200°C), so it can be concluded that similar achievement can be made in PEMFC. However, PEMFC with solid electrolyte applied in the electric vehicles suffers different degradation situations.

Frequent startups and shutdowns during the real application of transportation are unavoidable, which will not happen a lot once the PAFC was started as stationary power sources. Over the life of a vehicle, around 20 000 startup/shutdown cycles as well as 1 000 000 low to high power cycles are expected [7]. Before the startup of fuel cell based vehicle, both the anode and the cathode are full of air due to the leakage from outside and crossover through Nafion membrane. When hydrogen is introduced into the anode chamber of fuel cell during startup, a condition is present that only part of the anode is occupied by hydrogen. The air/fuel boundary can generate a higher interfacial voltage of 1.4V at the cathode, which will definitely accelerate the rate of carbon corrosion as showed in Figure3.3. This is because membrane potential in the air-covered area can be reduced to −0.593V to maintain the oxygen reduction according to the reverse-current mechanism as mentioned in the model presented by Reicer [11]. Accordingly, the interfacial potential of the cathode will increase to 1.4 V, which will lead to serious carbon corrosion and oxygen evolution from water electrolysis as shown in equation (3.4) and (3.5). This mechanism is further confirmed by a dual cell configuration and a large area MEA experiment with a hydrogen and inert gas flow configuration. The cell performance under the higher interfacial potential suffers a significant drop. The results of ECA of corresponding Pt at the cathode was decreased from approximately 43 m^2/g to 39, 32, 22 every 1 h. The electron microprobe analysis (EMPA) results shows that the cathode catalyst layer was thinned, which was also reported by Gasteiger[12]. The thinner cathode means the collapse of the initially highly porous electrode structure (60%～65%), and leads to a dramatic performance loss [13]. Similar phenomena of reverse-current will also be generated due to partial hydrogen coverage when fuel cell is shut down.

$$2H_2O \rightarrow O_2+4H^++4e^- \quad (3.5)$$

Yu et al. test the degradation of cell performance after cycles of startup/shutdown at 0.2 A/cm^2, 80 °C and 66/66% inlet relative humidity [7]. Losses greater than 100mV are observed only after 200 startup/shutdown cycles. After 100 startup/shutdown cycles, the collapse of carbon support results in the failure of discharging at 1.5 A/cm^2, which can initially discharge at 0.5V.

Recently, Schneider reports that in-plane current due to the voltage gradient between channel and land areas in a polymer electrolyte fuel cell can be clearly observed using submillimeter segmentations during start/stop experiments [14]. A faster change of cell voltage can be seen, and the inplane current is higher by a factor of 2 in the startup process compared to the shutdown procedure.

The air/fuel boundary due to partial hydrogen coverage can also be caused when a fuel channel at the anode is blocked or fuel starvation [15]. To extend the maximum driving distance of electric vehicles based on fuel cell, it is necessary to improve the utilization of hydrogen stored onboard. Normally, the stoichiometry of hydrogen at the anode is between 1 and 2, which might lead to the non-uniform distribution of fuel in a large area active cell. Additionally, the speed of shearing on the surface of the anode is so low that some of the channel might be blocked by liquid water in such a low stoichiometry. In that case, hydrogen cannot transfer to the catalytic sites, thus leading to fuel starvation. Another way to result in fuel starvation is due to transient operation in the transportation. Transient discharging at large current might suddenly consume most of fuel in the channel, which would generate more liquid water and reduce the ability to remove of liquid water, so some parts or channels can be blocked.

In the whole fuel cell stack, the current will pass through each cell during discharging. Once hydrogen oxidation cannot provide enough current, carbon would be oxidized at the anode instead. This is a little different from the carbon corrosion as indicated in Figure.3.3, which happens at the cathode. Usually, the carbon corrosion at the anode will not be serious.

Fuller et al. developed a two-dimension model of carbon corrosion induced by partial coverage of hydrogen on the anode [16]. They conclude that the following conditions can accelerate the carbon corrosion on the cathode:

(1) Higher cell potential.

(2) Lower conductivity of the ionomer.

(3) Larger region of partial hydrogen coverage.

(4) More rapid kinetic for carbon corrosion.

(5) Greater permeability of oxygen through the separator.

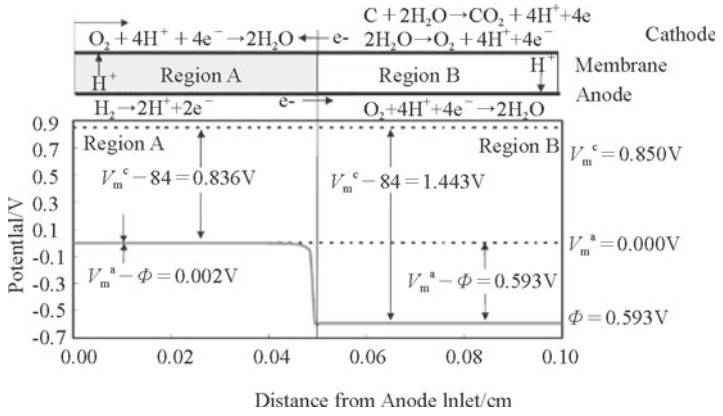

Figure 3.3 A reverse-current decay mechanism due to the air/H_2 boundary presented by [11]

3.2.2 Mechanism of carbon corrosion

As mentioned above, the thermodynamic potential of carbon oxidation to CO_2 is only 0.207 V vs. RHE. Oxygen atoms being generated by nano Pt particles will definitely react with carbon atoms to produce the oxides on the surface of carbon black. At the elevated temperature and high local potential during the startup and shutdown of fuel cell, gaseous products such as CO and CO_2 can be detected [17]. Surface oxide generation in acid condition involves the step of carbon oxidation in the lattice structure (3.6), followed by hydrolysis (3.7) and gasification of oxidized carbon to CO_2 (3.8) [18], where s denotes surface species.

$$C_s \rightarrow C_s^+ + e^- \tag{3.6}$$

$$C_s^+ + \frac{1}{2}H_2O \rightarrow C_sO + H^+ \tag{3.7}$$

$$C_sO + H_2O \rightarrow CO_2(g) + 2H^+ + e^- \tag{3.8}$$

Although there is no widely accepted mechanism for the whole carbon oxidation to CO_2, one proposed generic stepwise mechanism as follows:

$$R\text{-}C_s\text{-}H \rightarrow R\text{-}C_s\text{-}OH \rightarrow R\text{-}C_s{=}O \rightarrow R\text{-}C_sOOH \rightarrow R\text{-}H + CO_2 \tag{3.9}$$

Liu et al. employ in-situ TEM to observe the carbon oxidation in 50% Pt/C under thermal and electrochemical conditions [19]. It can be found the carbon corrosion rate is much quick at the beginning and decreases asymptotically with time. The initial quick rate of carbon corrosion is due to the formation of carbon oxidation, which will not play a detrimental role on the electrode porosity or structural framework. However, once the carbon is further oxidized to carbon dioxide or carbon monoxide, the cell performance will dramatically be influenced.

It is interesting to mention about XC-72 that an inside-out corrosion mode

results in the center-hollowed morphology whether by a gas-phase oxidation by air [20], liquid oxidation by HNO_3 [21] or electrochemical oxidation [22]. It indicates that the core of XC-72 is less organized than the outer shell. Also, the structure and the sources of carbon have a critical effect on carbon corrosion. Cherstiouk et al. compared the corrosion current at 1.2V vs. RHE of carbons from hydrolysis of hydrocarbon, XC-72 (furnace carbon) and carbon filament, and concluded that current densities normalized to the surface area depended strongly on the microstructure and increased with the proportion of the grain boundaries between quasi-graphitic crystallite [23]. Wang et al. explored the electrochemical behavior of the Pt supported on BP-2000 and XC-72 under simulated PEMFC condition [24]. The BET surface area for BP-2000 and XC-72 are 1487 m^2/g and 235 m^2/g. It is found that almost 2-fold degradation rate of electrochemical active area (EAS) happens for BP-2000 compared with XC-72. It indicates that high surface area of carbon suffer more serious corrosion in PEMFC condition.

Yu et al. reported that MEAs with graphitized carbon support show a higher resistance to carbon corrosion by a factor of 35 compared to conventional MEAs at the point of a 5% carbon weight loss. The startup/shutdown durability based on graphitized carbon kinetic parameters can be improved 5-fold at 10% carbon weight loss [7].

Stevens and Dahn studied effect of Pt's existence on the carbon corrosion in the gas phase reaction with air [25]. No weight loss happened for BP2000 carbon at 195°C after 3000 h. However, significant weight loss can be found even at 125°C when Pt supported on BP-2000. The weight loss increased as the temperature and Pt loading increased. It indicates that Pt will accelerate the corrosion rate of carbon as a catalyst for the combustion of carbon with oxygen. The more active the Pt/C is, the greater carbon corrosion rate will be.

3.2.3 Test methods and characterization

To check the durability of PEMFC in real application for transportation, full cell test in a long-term operation is the most direct method to understand the details of the degradation including carbon corrosion [26,27]. Nevertheless, the test of constant current discharging is time-consuming and not available for each lab. Furthermore, the effect of carbon corrosion on fuel cell performance degradation can be overlapped together with Pt particle sintering, ionomer decomposition and the change of hydrophobicity of gas diffusion layer. Since the carbon corrosion is mostly created by the high voltage at the cathode [28], some researchers try to directly apply high voltage on carbon in-situ or ex-situ to understand the mechanism and consequences of carbon corrosion of elctrocatalyst in fuel cell.

By this method, carbon corrosion can be studied independently. Also, the rate of carbon corrosion can be accelerated by the high voltage, which will reduce the time of evaluation of new material as a promising support for Pt catalyst [29].

Besides the cell performance degradation and morphological observation of carbon support by TEM or SEM before and after acceleration tests, the rate of carbon corrosion can be obtained by the concentrations of CO_2 and CO in the cathode output gas using FTIR [17], temperature programmed oxidation (TPO) [30] and mass spectrometry [31]. Recently, in-situ electrochemical quartz crystal microbalance (EQCM) has been used to evaluate the stability of various carbons [32]. Figure3.4 shows the EQCM results during the CV scan of XC-72 and graphitized XC-72 in deaerated 0.5M H_2SO_4 at 298K. It indicates that EQCM can distinguish the tiny difference of various carbons corrosion. Therefore, EQCM coupled with CV can be a simple and time-effective tool to investigate the corrosion behavior.

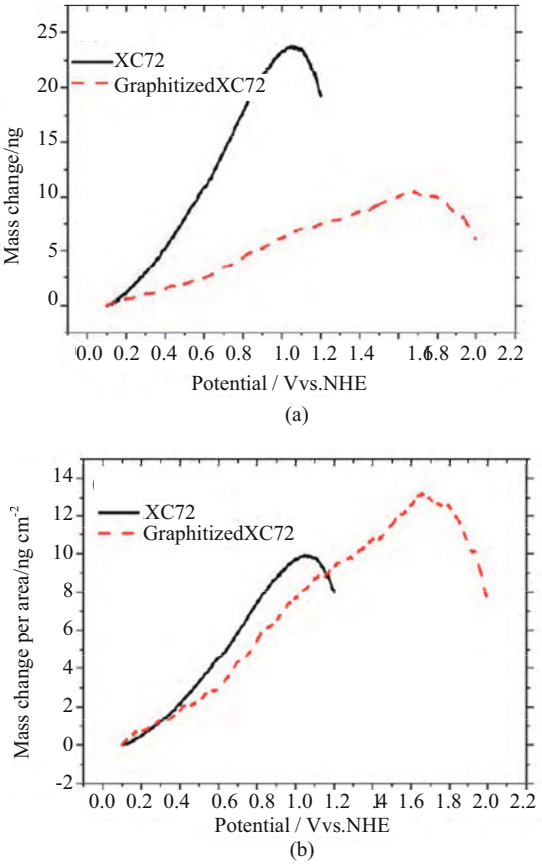

Figure 3.4 EQCM mass change vs. positive CV, (a) the original and (b) normalized by BET surface area for XC-72 and graphitized XC-72 [32]

The long-term stability of carbon support can also be determined by an experimental simulation under high temperature oxidation. Stevens et al. proposed to hold platinum-loaded carbon at elevated temperature (125°C and 150 °C) under dry or humidified air [8]. The rate of carbon combustion under humidified air can be increased significantly due to a possible water-gas reaction. Cai et al. suggested that the stability of carbon in Pt/C can be evaluated by heat treatment at 250 °C in 0.7% oxygen and 8 % water [33]. Furthermore, the correlation between the accelerated hydrogen absorption area loss due to the thermal treatment and that observed during electrochemical cycling was given.

3.3 Mitigation strategies to carbon corrosion

3.3.1 System strategy

Since high voltage is the key effect on carbon corrosion during start-up and shut-down, the limitation of cell voltage can maintain the carbon stability in the catalyst layer. The researchers from UTC Power proposed to use a voltage-limitation device (VLD) to mitigate start/stop loss [34]. A voltage sensor is connected with the stack coupled with a dummy load, so the cell voltage during fuel-filling or fuel-purging can be limited to a pre-set voltage such as tens of mill voltages instead of exceeding 0.9 V. Figure 3.5 shows the voltage degradations in a 20-cell stack with and without voltage control [34]. These tests reveal that the average cell voltage significantly drops after hundreds of start/stop cycles. On the contrary, the stack with VLD gives the steady voltage even after 12 000 start/stop cycles.

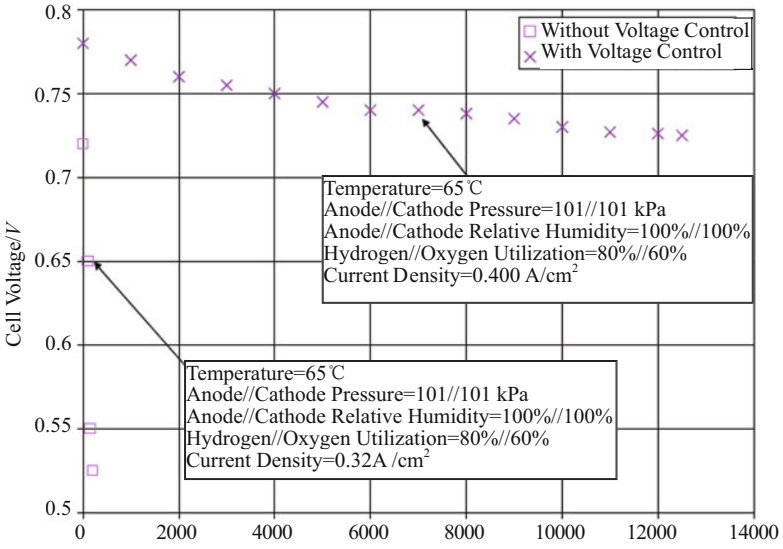

Figure 3.5 Effect of voltage control during fuel introduction on performance loss [34]

In the fuel cell stack without well-designed start/stop strategies, local or gross fuel starvation during normal operation will cause the serious decay under some circumstances [35]. One effective method to eliminate the local hydrogen starvation is to use fuel recycle. A fuel-cycle loop can make hydrogen flow in a high velocity through the anode and avoid the appearance of hydrogen starvation. Nevertheless, the good design of fuel manifold still play critical roles in the uniform distribution of hydrogen in order to avoid negative voltages under high fuel utilization and fast transients.

3.3.2 Corrosion-resistant catalyst support

The ultimate solution to degradation of catalyst supports in fuel cell is to develop corrosion-resistant one. At least, supporting materials with less corrosion is highly needed.

3.3.2.1 Modification of carbon black

Since the graphite is one of the most stable states of carbon, the easiest way to promote the stability of catalyst support is to graphitize widely-used XC-72 carbon black. Graphitized carbon does show better durability in fuel cell tests, but the surface area of the catalyst has been dramatically reduced due to the prolonged treatment under high temperature [36~38]. It can result in low electrochemical performance of the electrocatalysts. In order to eliminate the effect of low surface area of XC-72 carbon during graphitization, graphitic mesoporous carbon [39], high surface area graphite [30] and nanoscale graphite particles [40] have been reported. They possess the graphitized structure as well as the large surface area. Nevertheless, the high-temperature treatment around 2 800 ^{o}C will definitely increase the whole manufacture cost of electrocatalysts.

Nitrogen-doped carbon is very common way to modify carbon surface and structure. Nitrogen can be introduced to carbon by ammonia treatment under certain temperature [41, 42], or by a nitrogen-rich precursor such as polypyrrole [43], polyaniline [44]. N-doped carbon was found to be more stable during accelerated stress test (AST). It also should be mentioned that the graphitic and pyridinic nitrogen doped on carbon can be an active site for oxygen reduction reaction, which make it a hybrid catalyst [45]. Besides nitrogen, boron is also employed to increase the interaction between Pt and carbon support [46]. The results indicated that boron-doped carbon support is more resistant to carbon corrosion when compared with conventional carbon.

Metal oxide can also be used to improve the stability of carbon support. Liu et al. [47] present that TiO_2 can reduce the Pt agglomerate and prevent carbon corrosion due to the interaction between Pt and TiO_2. Thirty percent improvement

of electrochemical active area of Pt/TiO_2/C can be observed after accelerating aging test compared with Pt/C. Jung and Kim added 2 wt% IrO_2 to the catalyst layer in the cathode to prevent the electrochemical carbon corrosion [48]. After 30min corrosion test by holding the cathode voltage at 1.6V vs. NHE, IrO_2 modified cathode shows the decrease of carbon corrosion by 76% compared with a commercial Pt/C. The IrO_2 in the cathode behaved as a water electrolysis, which is essential to avoid carbon corrosion.

3.3.2.2 Novel carbon materials

Carbon nanotubes (CNT) with more graphite component than carbon black and high electron conductivity, has been considered as a promising support material for fuel cells and studied for almost ten years [49]. The surface area of carbon nanotubes is around 100 m^2/g, which is only half of XC-72carbon black (220 m^2/g), and the results suggests that CNT as catalyst support doesn't improve the activity of Pt in comparison to Vulcan carbon black [50]. However, Pt/CNT under both accelerated stress test (AST) in half cell and real fuel cell condition shows much better stability than Pt/C. Figure 3.6 shows the change of normalized ESA of both Pt/CNT and Pt/C as a function of hold time at 1.2V [51]. Less degradation after 200 h AST can be noticed while Pt/C shows a significant EAS drop after only 50 h AST. Li and Xing [52] compared the corrosive behavior of carbon black and CNT at 80 °C and concludes that the intact graphite planes of CNT are corrosive resistant while the amorphous of carbon black tends to be in-depth corrosion. Single-walled and multi-walled carbon nanotubes were also evaluated under potentiostatic condtions [53]. It indicates that MWNTs exhibit higher electrochemical stability than SWNTs. The reason was attributed to larger surface area and smaller tube diameter of SWNTs, in which local strain energy will accelerate the corrosive rate.

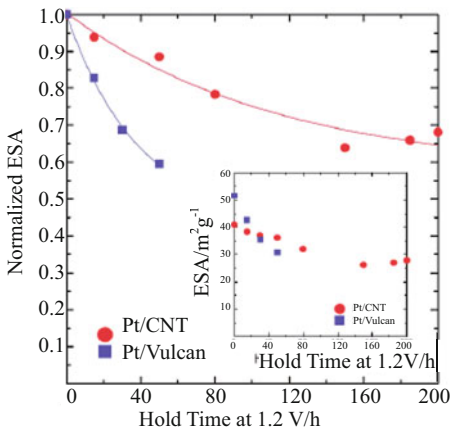

Figure 3.6 Normalized electrochemical surface area for Pt/CNT and Pt/Vulcan as a function of hold time at 1.2V [51]

Other morphologies of carbon such as fullerenes [54], nanospheres [37] and nanofibers [38] are investigated under the stimulated condition of fuel cell cathode with a constant potential holding. Among them, high surface area core/shell diamond with boron-doped ultrananocrystalline (B-UNCD) shows a good stability [55]. Figure 3.7 illustrates thermograms and derivative thermograms for (A) bare B-UNCD-D and Vulcan XC-72 and (B) Pt-BUNCD-D and Pt-(XC-72) with a 20% Pt/C loading. Although bare Vulcan is more resistant to oxidation than bare diamond, Pt-BUNCD-D shows higher onset oxidation temperature than Pt-(XC-72). It indicates that B-doped diamond is more resistant to gas oxidation than carbon black under the existence of Pt nanoparticles.

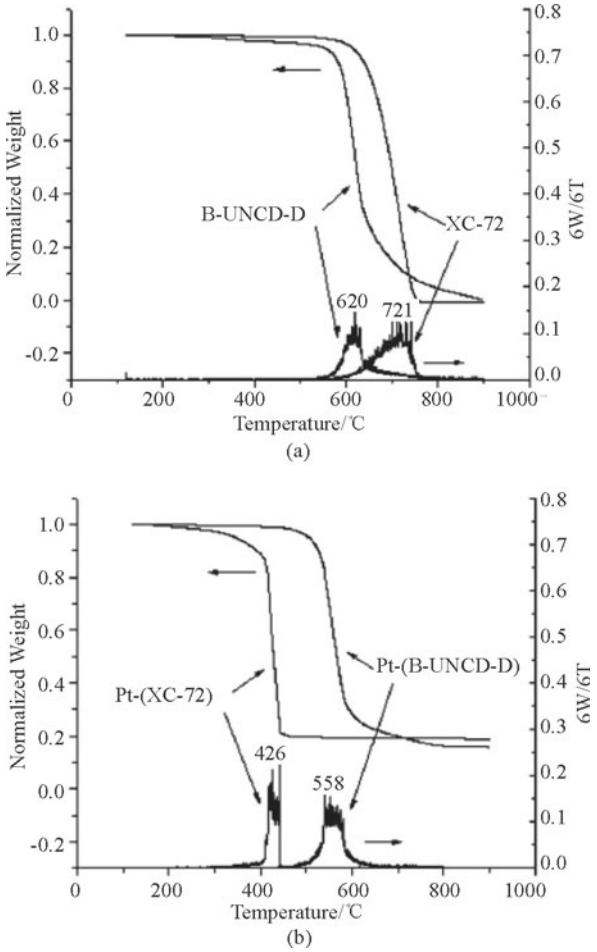

Figure 3.7 Normalized weight and derivative profiles as a function of temperature for (a) bare B-UNCD-D and Vulcan XC-72 and (b) Pt-(B-UNCD-D) and Pt-(XC-72) with a loading of 20% [55]

Graphene, emerging as a 2-dimensional carbon material, has attracted strong scientific and technological interests of fuel cells in the past several years due to its unique physicochemical properties such as high surface area (theoretically 2630 m^2/g for single-layer graphene), excellent electric conductivity, and strong mechanical strength [56]. Since 2009, there have been many studies reported on graphene supported platinum (Pt/G) catalysts for fuel cells, which aim to improve their electrocatalytic activities and durability compared to commercialized carbon supported platinum catalyst [57]. Guo et al. demonstrated a new type of graphene/bimetallic nanodendrite hybrids [58]. Jafri et al. presented a hybrid nanomaterial that nanostructured platinum dispersed on functionalized graphene and functionalized multiwalled carbon nanotube [59]. Shao et al. reported the platinum nanoparticles deposited on poly (diallyldimethylammonium chloride) (PDDA)-coated graphene nanoplatelets [60]. Xin et al. revealed the optimization of Pt/G catalyst by means of the thermal treatment [61]. Since the graphene in those reports was chemically reduced from the graphene oxide (GO), which was prepared by a modification of Hummers and Offenman's method [62], there are lots of defects in the center and brink of graphene plane. The defects can be easily oxidized in a high voltage and results in the structure failure of graphite. That is the reason that no advanced stability of graphene than XC-72 has been reported until now. More works to reduce the oxygen-containing species in the chemically-synthesized graphene should be done.

Both the modified carbon black by graphitization and novel carbon materials cannot prevent carbon corrosion thoroughly, although it will decrease the corrosive rate in the fuel cell configuration. Therefore, non-carbon supporting materials were studied.

3.3.2.3 Other supporting materials

Inorganic metal oxides have been investigated whether they can employ to be good corrosion-resistant supports. Although Pt supported on TiO_2 [63], WO_3 [64], Indium tin oxide (ITO) [65] show better stability under high voltage than carbon materials, the poor essential electrical conductivity of metal oxides still limit its real application in fuel cells. However, it should be pointed out that some metal oxides such as doped TiO_2 [66] reveals promising properties of electrical conductivity. About all kinds of ceramic materials as catalyst supporting materials, Antolini and Gonzalez gave a wonderful review [67].

Recently, nanoporous metals have been studied extensively because of its bicontinuous structure of pore and bulk metal [68] Erlebacher J. is the first one who apply nanoporous gold (NPG) as the supporting material for Pt catalyst in fuel

cell as showed in Figure 3.8 [69]. The Pt loading in Pt-NPG is far low than that of commercial Pt/C. As we know, gold has a great electrical conductivity and stability far higher than carbon. However, the porous structure might be not very constant during electrochemical scanning. Recently, Ge et al. studied the effect of annealing temperature on the morphologies of Pt-NPG and concluded that layers of Pt on the NPG can significantly improve its structure [70]. It indicates that NPG might be one of the promising supporting materials for Pt catalyst since its porous structure and good conductivity.

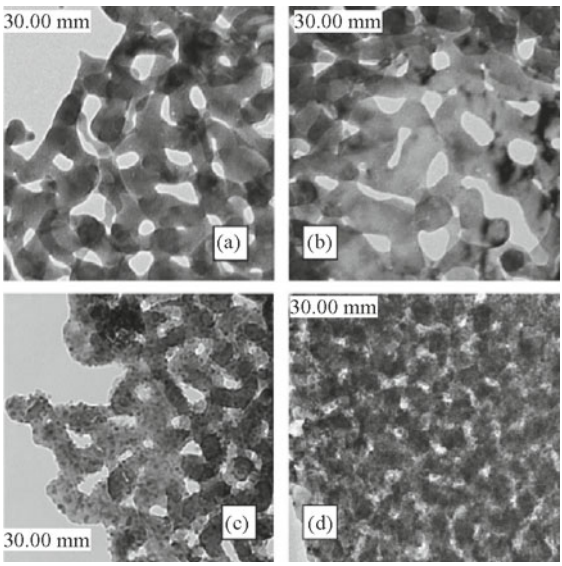

Figure 3.8 Transmission electron micrographs of Pt-Nanoporous membranes. The Pt loading from a to d: 0.01 mg/cm^2 to 0.05 mg/cm^2 [69]

Acknowledgements

This work was supported by National Basic Research Program of China (2007CB613300), National High Technology Research and Development Program of China (2011AA11A271), and Natural Science Foundation of China (20906045).

References

[1] Costamagna P, Srinivasan S. Quantum jumps in the PEMFC science and technology from the 1960s to the year 2000: Part I. fundamental scientific aspects. Journal of Power Sources, 2001, 102: 242～252.

[2] Wu J F, Yuan X Z, Martin J J, et al. A review of PEM fuel cell durability: Degradation mechanisms and mitigation strategies. Journal of Power Sources, 2008, 184: 104～119.

[3] Ishigami Y, Takada K, Yano H, et al. Corrosion of carbon supports at cathode during hydrogen/air replacement at anode studied by visualization of oxygen partial pressures in a PEFC—Start-up/shut-down simulation. Journal of Power Sources, 2011, 196: 3003～3008.

[4] Cheng X, Chen L, Peng C, et al. Catalyst microstructure examination of PEMFC membrane electrode assemblies vs. time. Journal of the Electrochemical Society, 2004, 151: A48～A52.

[5] Cleghorn S J C, Mayfield D K, Moore D A, et al. A polymer electrolyte fuel cell life test: 3 years of continuous operation. Journal of Power Sources, 2006, 158: 446～454.

[6] Shao Y Y, Yin G P, Wang Z B, et al. Proton exchange membrane fuel cell from low temperature to high temperature: Material challenges. Journal of Power Sources, 2007, 167: 235～242.

[7] Yu P T, Gu W B, Makharia R, et al. The impact of carbon stability on PEM fuel cell startup and shutdown voltage degradation. ECS Transactions, 2006, 3: 797～809.

[8] Stevens D A, Hicks M T, Haugen G M, et al. Ex Situ and in Situ stability studies of PEMFC catalysts. Journal of the Electrochemical Society, 2005, 152: A2309～A2315.

[9] Fuller T F, Perry M, Reiser C. Applying the lessons learned from PAFC to PEM Fuel Cells. ECS Transactions, 2006, 1: 337～344.

[10] http://www.utcpower.com/

[11] Reiser C A, Bregoli L, Patterson T W, et al. A reverse-current decay mechanism for fuel cells. Electrochemical and Solid-State Letters, 2005, 8: A273～A276.

[12] Gasteiger H A, Gu W B, Makharia R,et al. Catalyst degradation mechanism in PEM and direct methanol fuel cells. Mini-micro Fuel Cells, 2008, 25～233.

[13] Gasteiger H A, Gu W, Makharia R,et al. Beginning-of-Life MEA performance – efficiency loss contributions//Vielstich W, Lamm A,Gasteiger HA. Handbook of Fuel Cells. New York: Wiley, 2003, 593～610.

[14] Schneider I A,Dahlen S.Start-stop phenomena in channel and land areas of a polymer electrolyte fuel cell. Electrochemical and Solid-State Letters, 2011, 14: B30～B33.

[15] Baumgartner W R, Wallnofer E, Schaffer T, et al. Electrocatalytic corrosion

of carbon support in PEMFC at fuel starvation. ECS Transactions, 2006, 3, 811.

[16] Fuller T F,Gray G, Carbon corrosion induced by partial hydrogen coverage. ECS Transactions, 2006, 1: 345～353.

[17] Maass S, Finsterwalder F, Frank G, et al. Carbon support oxidation in PEM fuel cell cathodes. Journal of Power Sources, 2008, 176: 444～451.

[18] Binder H, Kohling A, Richter K, et al. Über die anodische oxydation von aktivkohlen in wässrigen elektrolyten. Electrochimica Acta, 1964, 9, 255～274.

[19] Liu Z Y, Brady B K, Carter R N, et al. Characterization of carbon corrosion-induced structural damage of PEM fuel cell cathode electrodes caused by local fuel starvation. Journal of the Electrochemical Society, 2008, 155: B979～B984.

[20] Heckman F A, Harling D F. Progressive oxidation of selected particles of carbon black: Further evidence for a new microstructural model. Rubber Chemistry and Technology, 1966, 39: 1～13.

[21] Donnet J B, Bouland J C. Revue Generale du Caoutchouc et des Plastiques, 1964, 41: 407.

[22] Gruver G A. The corrosion of carbon black in phosphoric acid. Journal of the Electrochemical Society, 1978, 125: 1719～1720.

[23] Cherstiouk O V, Simonov A N, Moseva N S, et al. Microstructure effects on the electrochemical corrosion of carbon materials and carbon-supported Pt catalysts. Electrochimica Acta, 2010, 55: 8453～8460.

[24] Wang J J, Yin G P, Shao Y Y, et al. Effect of carbon black support corrosion on the durability of Pt/C catalyst. Journal of Power Sources, 2007, 171: 331～339.

[25] Stevens D A, Dahn J R. Thermal degradation of the support in carbon-supported platinum electrocatalysts for PEM fuel cells. Carbon, 2005, 43: 179～188.

[26] Janssen G J M, Sitters E F,Pfrang A. Proton-exchange-membrane fuel cells durability evaluated by load-on/off cycling. Journal of Power Sources, 2009, 191: 501～509.

[27] Wu J F, Yuan X Z, Martin J J, et al. Proton exchange membrane fuel cell degradation under close to open-circuit conditions: Part I: In situ diagnosis. Journal of Power Sources, 2010, 195: 1171～1176.

[28] Tang H, Qi Z G, Ramani M, et al. PEM fuel cell cathode carbon corrosion due to the formation of air/fuel boundary at the anode. Journal of Power Sources, 2006, 158: 1306～1312.

[29] Liu Z Y, Zhang J L, Yu P T, et al. Transmission electron microscopy observation of corrosion behaviors of platinized carbon blacks under thermal and electrochemical conditions. Journal of the Electrochemical Society, 2010, 157:B906～B913.

[30] Ferreira-Aparicio P, Folgado M A,Daza L. High surface area graphite as alternative support for proton exchange membrane fuel cell catalysts. Journal of Power Sources, 2009, 192: 57～62.

[31] Oh S H, Oh J G, Haam S, et al. On-line mass spectrometry study of carbon corrosion in polymer electrolyte membrane fuel cells. Electrochemistry Communications, 2008, 10: 1048～1051.

[32] Hung C C, Lim P Y, Chen J R, et al. Corrosion of carbon support for PEM fuel cells by electrochemical quartz crystal microbalance. Journal of Power Sources, 2011, 196: 140～146.

[33] Cai M, Ruthkosky M S, Merzougui B, et al. Investigation of thermal and electrochemical degradation of fuel cell catalysts. Journal of Power Sources, 2006, 160: 977～986.

[34] Perry M L, Patterson T W,Reiser C. Systems strategies to mitigate carbon corrosion in fuel cells. ECS Transactions, 2006, 3: 783～795.

[35] Takagi Y,Takakuwa Y. Effect of shutoff sequence of hydrogen and air on performance degradation in PEFC. ECS Transactions, 2006, 3: 855～860.

[36] Luo X, Hou Z J, Ming P W, et al. Effect of graphitic carbon on stability of Pt/C catalysts for proton exchange membrane fuel cells. Chinese Journal of Catalysis, 2008, 29: 330～334.

[37] Miyazaki K, Shirakata H, Abe T, et al. Novel graphitised carbonaceous materials for use as a highly corrosion-tolerant catalyst support in polymer electrolyte fuel cells. Fuel Cells, 2010, 10: 960～965.

[38] Ko Y J, Oh H S, Kim H. Effect of heat-treatment temperature on carbon corrosion in polymer electrolyte membrane fuel cells. Journal of Power Sources, 2010, 195: 2623～2627.

[39] Shanahan P V, Xu L B, Liang C D, et al. Graphitic mesoporous carbon as a durable fuel cell catalyst support. Journal of Power Sources, 2008, 185: 423～427.

[40] Wang M X, Xu F, Sun H F, et al. Nanoscale graphite-supported Pt catalysts for oxygen reduction reactions in fuel cells. Electrochimica Acta, 2011, 56: 2566～2573.

[41] Wang X, Lee J S, Zhu Q, et al. Ammonia-treated ordered mesoporous carbons as catalytic materials for oxygen reduction reaction. Chemistry of Materials, 2010, 22: 2178～2180.

[42] Biniak S, Szymanski G, Sieldlewski J, et al. The characterization of activated carbons with oxygen and nitrogen surface groups. Carbon, 1997, 35: 1799～1810.

[43] Fuertes A B, Centeno T A. Mesoporous carbons with graphitic structures fabricated by using porous silica materials as templates and iron-impregnated polypyrrole as precursor. Journal of Materials Chemistry, 2005, 15: 1079～1083.

[44] Vinu A, Srinivasu P, Mori T, et al. Novel hexagonally ordered nitrogen-doped mesoporous carbon from SBA-15/Polyaniline nanocomposite. Chemistry Letter, 2007, 36: 770～772.

[45] Yang C M, Weidenthaler C, Spliethoff B, et al. Facile template synthesis of ordered mesoporous carbon with polypyrrole as carbon precursor. Chemistry of Materials. 2005, 17: 355～358.

[46] Acharya C K, Li W, Liu Z F, et al. Effect of boron doping in the carbon support on platinum nanoparticles and carbon corrosion. Journal of Power Sources, 2009, 192: 324～329.

[47] Liu X, Chen J, Liu G, et al. Enhanced long-term durability of proton exchange membrane fuel cell cathode by employing $Pt/TiO_2/C$ catalysts. Journal of Power Sources, 2010, 195: 4098～4103.

[48] Jung S E , Kim HS. Effect of water electrolysis catalysts on carbon corrosion in polymer electrolyte membrane fuel cells. Journal of the American Chemical Society, 2010, 132: 14700～14701.

[49] Wang X, Li W Z, Chen Z W, et al. Durability investigation of carbon nanotube as catalyst support for proton exchange membrane fuel cell. Journal of Power Sources, 2006, 158: 154～159.

[50] Hasche F, Oezaslam M,Strasser P. Activity, stability and degradation of multi walled carbon nanotube (MWCNT) supported Pt fuel cell electrocatalysts. Physical Chemistry Chemical Physics, 2010, 12, 15251～15258.

[51] Park S, Shao Y Y, Kou R, et al. Polarization losses under accelerated stress test using multiwalled carbon nanotube supported Pt catalyst in PEM fuel cells. Journal of the Electrochemical Society, 2011, 158: B297～B302.

[52] Li L,Xing Y C. Electrochemical durability of carbon nanotubes at 80 ℃. Journal of Power Sources, 2008, 178: 75～79.

[53] Wang J J, Yin G P, Shao Y Y, et al. Electrochemical durability investigation of single-walled and multi-walled carbon nanotubes under potentiostatic conditions. Journal of Power Sources, 2008, 176: 128～131.

[54] Gabriel M A, Genovese L, Krosnicki G, et al. Metallofullerenes as fuel cell

electrocatalysts: A theoretical investigation of adsorbates on $C_{59}Pt$. Physical Chemistry Chemical Physics, 2010, 12: 9406～9412.

[55] Guo L, Swope V M, Merzougui B, et al. Oxidation resistance of bare and Pt-Coated electrically conducting diamond powder as assessed by thermogravimetric analysis. Journal of the Electrochemical Society, 2010, 157: A19～A25.

[56] Novoselov K S, Geim A K, Morozov S V, et al. Electric field effect in atomically thin carbon films. Science, 2004, 306: 666～669.

[57] Yoo E J, Okata T, Akita T, et al. Enhanced electrocatalytic activity of Pt subnanoclusters on graphene nanosheet surface. Nano Letters, 2009, 9: 2255～2259.

[58] Guo S J, Dong S J, Wang E K, Three-dimensional Pt-on-Pd bimetallic nanodendrites supported on graphene nanosheet: Facile synthesis and used as an advanced nanoelectrocatalyst for methanol oxidation. ACS Nano, 2010, 4: 547～555.

[59] Jafri R I, Arockiados T, Rajalakshmi N, et al. Nanostructured Pt dispersed on graphene-multiwalled carbon nanotube hybrid nanomaterials as electrocatalyst for PEMFC. Journal of the Electrochemical Society, 2010, 157: B874～B879.

[60] Shao Y Y, Kou R, Wang D H, et al. Enhanced activity and stability of Pt catalysts on functionalized graphene sheets for electrocatalytic oxygen reduction. Electrochemistry Communications, 2009, 11: 954～957.

[61] Xin Y C, Liu J G, Zhou Y, et al. Preparation and characterization of Pt supported on graphene with enhanced electrocatalytic activity in fuel cell. Journal of Power Sources, 2011, 196: 1012～1018.

[62] Hummers W S, Offenman R E. Preparation of graphitic oxide. Journal of the American Chemical Society, 1958, 80: 1339.

[63] Huang S Y, Ganesan P, Popov B N. Titania supported platinum catalyst with high electrocatalytic activity and stability for polymer electrolyte membrane fuel cell. Applied Catalysis B: Environmental, 2011, 102: 71～77.

[64] Ye J L, Liu J G, Zou Z G, et al. Preparation of Pt supported on WO_3–C with enhanced catalytic activity by microwave-pyrolysis method. Journal of Power Sources, 2010, 195: 2633～2637.

[65] Chhina H, Campell S, Kesler O. An oxidation-resistant indium tin oxide catalyst support for proton exchange membrane fuel cells. Journal of Power Sources, 2006, 161: 893～900.

[66] Huang S Y, Ganesan P, Popov B N. Electrocatalytic activity and stability of niobium-doped titanium oxide supported platinum catalyst for polymer

electrolyte membrane fuel cells. Applied Catalysis B: Environmental, 2010, 96: 224～231.

[67] Antolini E, Gonzalez E R. Ceramic materials as supports for low-temperature fuel cell catalysts. Solid State Ionics, 2009, 180: 746～763.

[68] Erlebacher J. An atomistic description of dealloying. Journal of the Electrochemical Society, 2005, 151: C614～C626.

[69] Zeis R, Mathur A, Fritz G, et al. Platinum-plated nanoporous gold: An efficient, low Pt loading electrocatalyst for PEM fuel cells. Journal of Power Sources, 2007, 165: 65～72.

[70] Ge X B, Yan X L, Wang R Y, et al. Tailoring the structure and property of Pt-Decorated nanoporous gold by thermal annealing. Journal of Physical Chemistry: C, 2009, 113: 7379～7394.

Chapter 4
Converting Low-grade Biomass to Produce Energy Using Bio-fuel Cells

Meng Tong[1], Zhuwei Du[2] and Tingyue Gu[3]

1 National Analysis and Testing Centre for Iron and Steel, China Iron & Steel Research Institute Group, Beijing 100081, People's Republic of China

2 National Key Laboratory of Biochemical Engineering, Institute of Process Engineering, Chinese Academy of Sciences, Beijing 100190, People's Republic of China

3 Department of Chemical and Biomolecular Engineering, Ohio University, Athens, Ohio 45701, USA

Abstract

Aerobic and anaerobic respiration of microorganisms involves redox reactions that provide energy for cell growth or maintenance. The energy comes from breaking up chemical bonds during the oxidation of organic carbons by the microorganisms. The electrons released from the oxidation are taken up by the reduction of an oxidant such oxygen, sulfate, nitrate, etc. If the oxidation and reduction reactions occur at the same place, for example, the cytoplasm of microbial cells, no electricity is produced. The energy produced will be used for cell growth or maintenance. The rest will be released as low-grade heat that cannot be harvested cost-effectively. Electrochemically, digestion of organic carbons can be split into anodic (organic carbon oxidation) and cathodic (proton reduction) reactions to produce an electric current that can be harvested when electrons from the oxidation reaction is donated to the anode and flow through an external circuit before be utilized by the reduction reaction at the cathode. Bio-fuel cells are classified into two different categories. One is the so-called microbial fuel cell (MFC) that relies on a microbial biofilm to provide enzyme catalysis to the anodic reaction while the other utilizes a cell-free enzyme system for catalysis. The recent energy crisis and concerns over global warming have reinvigorated interests in

bio-fuel cells because their potential applications in electricity generation and biohydrogen production from renewable sources that are often low-cost or zero-cost wastes. Currently, the bottleneck of real-world applications of bio-fuel cells in harnessing energy lies in their low power density and high costs, thus limiting their uses to powering small sensors or devices that require very little power. Numerous interesting and innovative approaches have been reported to increase the performances and to reduce reactor construction and operating costs of bio-fuel cells. Although significant hurdles remain ahead, new progresses are making bio-fuel cells closer to eventual practical applications utilizing low-grade biomass. This book chapter reviews various recent advances in bio-fuel cell research using various biomass feed stocks.

4.1 Introduction

The conflict between the rapid growth in global energy consumption and the depletion of the traditional non-renewable fossil fuels has drawn much academic and industrial research efforts to find alternate renewable methods of providing power from biomass, wind and photovoltaic sources that is collectively known as green energy. Bio-fuel cells, as a suborder of fuel cells, have a special nitch due to their efficiency and ability to sustain consistent power production by consumption of renewable biomass sources that are often considered worthless wastes. Microbial fuel cells (MFCs) and enzymatic fuel cells (EFCs) are two main types of bio-fuel cells reported in the literature[1~3]. The former employ whole microorganisms as biocatalysts and the latter accomplish electrochemical energy conversion via enzymes isolated from them. The parallel uses of both types of catalysts are natural extensions of immobilized-cell and immobilized enzyme catalysis in non-electrochemical processes. The development of bio-fuel cells started in 1910 with an English botanist Potter who obtained a small current (0.2 mA) from *Escherichia coli* and *Saccharomyces* cultures using platinum electrodes[4]. In the early 1960s the initial boom in space research ushered in a general interest in bio-energy. EFCs were first developed by Kimble and coworkers in 1964. They constructed three different bio-fuel cells using glucose oxidase, amino acid oxidase, alcohol dehydrogenase enzymes, respectively in the anodic chamber and then compared the their performances[5]. However, research of bio-fuel cells declined after 1965 as a result of Lewis and Austin's less-than-optimistic conclusion that up to that time no successful biochemical fuel cell applications had been demonstrated[6]. In recent years, the interest in bio-fuel cells was rekindled by a growing awareness of a shortage in the world oil supplies and the need for energy diversification including expanded use of green energy. Researchers were

encouraged by the demonstrated ability of electron mediators in enhancing bio-fuel cell's performance in the late 1970s and the early 1980s[6]. And breakthroughs in MFCs and EFCs were both made in the late 1990s when researchers observed that some microbes were able to transfer electrons directly to the anode[7, 8] and an enzymatic cascade consisting of alcohol dehydrogenase, formaldehyde dehydrogenase, and formate dehydrogenase was used to convert methanol to carbon dioxide[9]. Today, bio-fuel cell research has become a promising research area bridging several disciplines that may contribute to the overall energy supply technology strategy of the future.

The relative advantages and disadvantages of whole-cell catalysts vs. enzymes are continually debated. Whole organisms are very attractive as multi-enzyme reactors that are capable of completing oxidation of a wide variety of fuels. And the regeneration ability of the living biocatalysts makes MFCs stable over long period of operation[10]. Continuous running of MFCs over five years has been reported[11]. But the limitation on the use of whole microorganisms in bio-fuel cells still comes from the barrier to electron transport which is presented by the cell walls and membranes of microorganisms. Hence they have low power densities in W/cm^2[5]. By contrast, Enzymatic fuel cells possess orders of magnitude higher power densities. However, limitations including incomplete oxidation of fuels and short lifetimes due to enzyme loss and inactivation plague these systems[10]. Because only a limited number of enzymes are employed, a feed that contains a large array of organic carbons from simple volatile fatty acids such as acetate to complicated polysaccharides such as cellulose in wastewater cannot possibly be processed by an EFC. In the following sections, the recent progresses in bio-fuel cells research using various biomass sources are discussed.

4.2 Theoretical principles of bio-fuel cells

From the electrochemical point of view, an electrochemical reaction consists of two half reactions: an oxidation reaction at the anode and a reduction reaction at the cathode. This split is necessary to prevent the direct oxidation of the fuel substrates. Biocatalyst can be used to accelerate either the anodic or the cathodic reaction, or both. Accelerating anodic reaction has attracted greater attention, because degradation of biomass in the anodic chamber is thermodynamically favorable but kinetically retarded without biocatalysis. Because this work deals with bio-fuel cells with a bioanode, the bio-fuel cell may be formally represented as

$$\text{anode} \mid \text{substrate} + \text{biocatalyst} \,\vdots\, O_2 \text{ or substitute} \mid \text{cathode} \tag{4.1}$$

Bio-fuel cells can use biocatalysts (either enzymes or whole cell organisms) in two different ways[6]: ① Indirect bio-fuel cells, in which the biocatalysts, by

biocatalytic transformation or a metabolic process, convert the fuel substrates to a secondary fuel utilized at the electrode. For example, *Clostridium butyricum* yields hydrogen and formic acid as the secondary fuel that can be oxidized to carbon dioxide on the electrode surface in the anodic compartment and oxygen is reduced on the electrode surface in the cathodic compartment[12,13]. Other microorganisms such as *Desulfovibrio desulfuricans* were reported to yield sulfide ions that in turn were oxidized at the anode[14, 15]. ② Direct bio-fuel cells[7, 8], employ biocatalysts that are either microorganisms or redox-enzymes to facilitate the electron transfer chain between substrates and electrode surfaces.

EFCs are similar to chemical fuel cells especially polymer eleectrolyte fuel cells. Generally speaking, the system works with continuous recycling of the enzyme catalyst. If the enzyme acts with a cofactor, it is usually the reduced form of the cofactor that fuels the electrode reaction. Electrochemical coupling of the enzyme/co-enzyme system can be made more effective with the aid of an electron mediator.

In whole-cell microbial systems, i.e. MFCs, the cofactor resides in the cell cytoplasm. During normal bacterial metabolism, the substrate undergoes degradation via an oxidative process and supplies energy to drive biochemical reactions of assimilation or for cell maintenance. Electrons extracted from the substrate (or from secondary products) are transferred to cofactors such as FAD (flavin adenine dinucleotide), NAD(P)H (nicotinamide adenine dinucleotide, or its phosphorylated derivative), PQQ (pyrroloquinoline quinone)[6], etc. Reaction (4.2) shows the case for metabolism of glucose.

$$C_6H_{12}O_6 + 6H_2O \rightarrow 6CO_2 + 24H^+ + 24e^- \text{ (to NADH)} \quad (4.2)$$

Consumption of H^+ occurs in a reaction with oxygen at a terminal cytochrome site of the respiratory chain:

$$6O_2 + 24H^+ + 24e^- \rightarrow 12H_2O \quad (4.3)$$

Reactions (4.2) and (4.3) together give the overall biochemical reaction for aerobic respiration (Reaction (4.4)) with ATP production, which stores energy within the microorganism.

$$C_6H_{12}O_6 + 6O_2 \rightarrow 6CO_2 + 6H_2O \quad (4.4)$$

It is generally acknowledged that the terminal reactions described by Reactions (4.2) and (4.3) in the process of biological energy generation take place at separate electron-donor and electron-acceptor sites in microorganisms. In MFCs the electrodes, locating in different compartments, are analogous to the electron-donor and electron-acceptor in microorganisms. Anode and cathode are at opposite ends of the respiratory chain of the microorganisms and reactions like Reactions (4.2)

and (4.3) occur at the electrode surfaces. Under normal conditions a respiring organism derives energy as electrical charge flows through the respiratory chain to eventually reduce oxygen at a cytochrome center, but in the anaerobic environment of an MFC's anodic chamber. The electrons released by the organic carbon oxidation reaction are donated to the anode. They flow through an external to drive a load before returning to the cathode to participate in the reduction reaction.

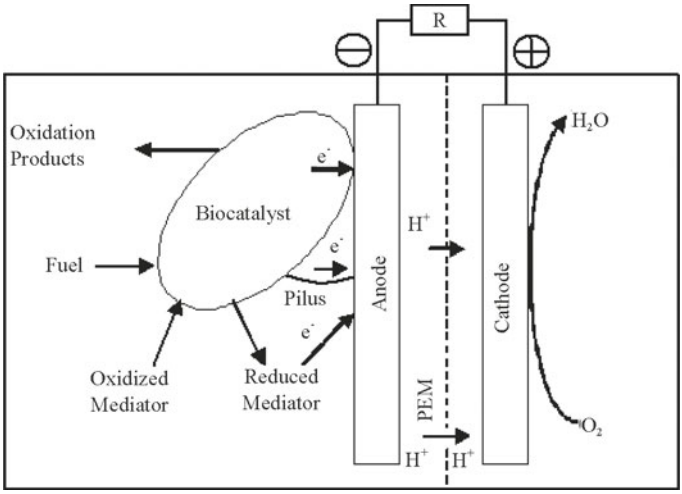

Figure 4.1 Schematic of a typical bio-fuel cell producing electricity

Figure 4.1 illustrates how a bio-fuel cell produces electricity from a substrate (fuel). Three electron transfer routes are depicted although only one or two may be present in an actual system. The anodic and cathodic chambers are partitioned by a proton exchange membrane (PEM) that allows proton diffusion to maintain electro-neutrality while preventing oxygen diffusion[16, 17]. Biodegradation of organics is split into anodic (organic carbon oxidation) and cathodic (oxygen reduction) reactions to produce an electric current that can be harvested. Bio-catalyzed oxidation occurs at the anode and oxygen reduction at the cathode in a bio-fuel cell. As a renewable biomass that is derived originally from the ecosystem via photosynthesis approaches the anodic surface, it is electrochemically oxidized and this generates protons that enter the electrolyte and migrate toward the cathode, where oxygen is reduced to water. Inside a bio-fuel cell, the electricity flows from the anode to the cathode in the form of proton migration, while externally, the electricity flow is represented by the flow of electrons from anode to cathode. The essential feature of the bio-fuel cell is that the electron source of the bio-system is connected to the electrode via a suitable electron-transfer pathway, with

a current flow through the external circuit providing electric energy. Figure 4.1 shows direct electron transfer and mediator electron transfer. Pili grown by microbes are conductive nanowires that also transfer electrons between cells and an anode.

In addition, examples have been reported to exploit biocatalysis by micro-organimism for renewable H_2 production[18, 19]. Photoelectrocatalytic H_2 production and electroanalytic H_2 production are the two feasible routes, with the former successfully demonstrated in enzymatic fuel cells[20, 21]. In EFCs, H^+ reduction enzyme should be used at cathode in most cases. NAD^+-dependent – glucose-dehydrogenase (anode) / NADH-dependent - hydrogenase (cathode) and NAD^+-dependent-glucose-dehydrogenase / Mg-chlorophyll - a are examples of biocatalysis couples for H_2 production from glucose[22]. Besides, the [FeFe]-hydrogenase from *Clostridium acetobutylicum* is a very good catalyst for H^+ reduction[23]. Microbial electrolysis cells (MECs) that are a modified version of MFCs can be used to produce high purity hydrogen gas in the cathodic chamber. Electrons donated by the anode from oxidizing an organic substrate in the anodic chamber flows through an external circuit to the cathode where they reduce the protons that diffused through a PEM from the anodic chamber to the cathodic chamber to produce hydrogen. An externally applied voltage is needed to make the reactions thermodynamically favorable. The hydrogen evolution reaction $2H^+ + 2e^- \rightarrow H_2$ in biological systems requires a voltage of -0.41V, while the microbial biofilm on the anodic surface degrades a organic substrate that typically has a reduction potential around -0.30V because the reduction potentials for $2CO_2$/acetate, NAD+/NADH, FAD/FADH are -0.29, -0.32 and -0.28V, respectively[21, 24]. Thus, theoretically, an external voltage of roughly only 0.1V is needed to make renewable H_2 production thermodynamically feasible in a MEC. Compared to the 1.2V required for direct electrolysis of water at neutral pH, 0.1V is much lower because the anodic degradation of the organic substrate produces energy. Another advantage for hydrogen production using MECs is that MECs can reach a yield of about 8～9 mol H_2/mol glucose compared to the typical 4 mol H_2/mol glucose yield from conventional fermentation[25]. Because the cathodic chamber is anaerobic during biohydrogen using MECs, oxygen leak to the anodic chamber is no longer an issue, and this enhances MEC efficiency. MECs produce higher purity hydrogen gas with reduced separation costs because the cathodic chamber does not involve complicated gas mixtures that are in the fermentation off gas. Hydrogen produced from MECs can be accumulated and then used to drive larger loads that cannot be driven by an online MFC due to its low power output. Some researchers foresee that biohydrogen produced from organic wastes from MECs can contribute to a future hydrogen economy[26] .

4.3 Designs for scaling up

Up to now, many miniature configurations for implantable applications or powering small sensors of devices have been reported[27, 28]. The focus here is on the designs suitable for scale-up that are necessary for bio-fuel cells to become a practicable energy supply alternative. Two-compartment bio-fuel cells are more difficult and costly (e.g., high cost of the membrane) to scale up due to their complex designs. The simple one-compartment design of bio-fuel cells as shown in Figure 4.2 offers cost savings. The common point for one-compartment MFC design is to expose the cathode directly to the air. However, the PEM are still necessary to keep the anode anaerobic. Single chamber EFCs can follow the design as that of MFCs. In addition, if proper enzymes with good selectivity and stabilities are employed, the anode and the cathode of EFCs can be positioned in one chamber as in membrane-less EFCs[29]. A membrane-less up-flow mode MFC is especially suitable for scaling up in wastewater treatment. Figure 4.3 shows an example. The continuous feed stream is fed from the bottom where the anode is. The scream flows upward and exits at the top where the cathode is[30]. There are no separate anolyte and catholyte solutions. The distance between the anode and cathode presents a diffusion barrier that forms an oxygen (DO) gradient to avoid direct oxidation of organic carbon at the anode. Upward flow is better than horizontal or downward flow in prevent oxygen from entering the anode area. The convective flow from anode to cathode allows fast proton migration, thus greatly reduces internal resistance. Membrane-less is gaining popularity in MFC designs.

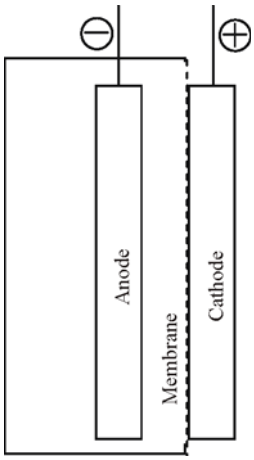

Figure 4.2 Schematic of a bio-fuel cell with the cathode directly exposed to the air

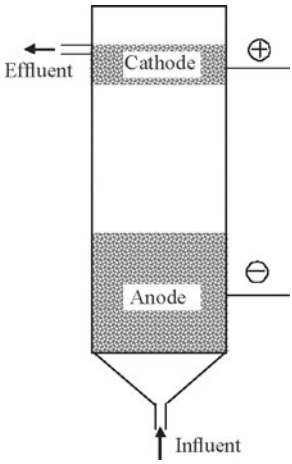

Figure 4.3 Schematic diagram of membrane-less up-flow mode MFC

4.4 Materials in bio-fuel cells

4.4.1 Fuels

Many organic chemicals can serve as both energy-sources and starting materials or intermediates for chemical syntheses. These fuels deserve special considerations because they are the forms in which energy can be stored economically for very long periods[31] and some of them are present in organic wastes. The versatilities of the biocatalysts used in bio-fuel cells make it possible for bio-fuel cells to utilize a large variety of substrates from simple compounds to complicated mixtures of organic matters in wastewater. MFCs especially those using mixed culture biofilm consortia, compared with EFCs, have much a stronger capacity in utilizing complex low-grade biomass, offering the possibility of generating electricity from a wide range of substrates. Furthermore, substrates can be thoroughly oxidized to form CO_2 and H_2O in MFCs. It is difficult to compare substrate influence on bio-fuel cell performances, due to different cell configures, operating conditions, and different electrode materials and biocatalysts involved. Generally, low-grade biomass in wastewater has relatively low performance, but they are cheaper and often come without cost. Some popular substrates and their basic features are discussed below.

1. Pure compounds

Glucose is the most commonly used substrate for research in bio-fuel cells,

especially in EFCs[32~34]. It is abundant in nature as a common source of carbon and energy source for microbial metabolism of many species. Its important metabolic intermediate is aldohexose carbohydrate involved in the glycolysis metabolic pathway, in which it is oxidized to pyruvate before entering the citric acid cycle. Glucose eventually is oxidized to form CO_2 and water after a series of biochemical transformations with a release of energy using either enzyme catalysis or biofilm catalysis[10, 35]. Other sugars including monosaccharides such as fructose and xylose, disaccharides such as lactose, cellobiose, maltose and sucrose, polysaccharides such as cellulose and starch[35~37] can also be digested by bio-fuel cells. However, only fructose, lactose and cellobiose are commonly reported as fuels in EFCs[37].

Organic acids are another fuel choice often for electricity generation in MFCs. Acetate is the end product of fermentation and methanogenesis for higher order carbon sources. MFCs fueled by acetate often achieve higher Coulombic efficiency than other microbial conversions at room temperature[38]. Other organic acids include fumarate, cysteine, glucuronic acid, lactate, propionate and pyruvate[36]. Aliphatic alcohols are often used in EFCs. Methanol, ethanol and glycerol are renewable fuels from biomass. They can also be potentially substrates in EFCs used in future distributed power systems[37]. In comparison with the three alcohols, sugar alcohols such as arabitol, mannitol, ribitol, sorbitol, xylitol, galactitol have more complex molecular structures and they have been used in MFCs[39]. Even some industrial chemicals, such as phenol, 1,2-dichloroethane, usually toxic to microorganisms are also possible substrates in MFCs, but they have lower power output[40, 41].

2. Mixtures

Low-grade biomass containing a huge variety of organic compounds can fuel MFCs. Municipal wastewater, food processing wastewater, lignocellulosic biomass, landfill leachate and marine sediments have been tested as substrates in MFCs[35, 36]. MFCs are attractive for wastewater treatment because they can reduce solids by 50 to 90% while potentially halve the energy needed in a conventional treatment process for aeration[26, 30]. Mixed-culture biofilms are especially suitable for energy recovery from low-grade biomass. Up to 80% removal of COD (chemical oxygen demand)[42, 43] and a Coulombic efficiency as high as 80% have been reported in the literature[44].

4.4.2 Biocatalysts

Theoretically, any biochemical process that involves oxidation and reduction

can be potentially used in a bio-fuel cell if the two reactions can be split up. Therefore many different biocatalysts are used in bio-fuel cells for electricity production including single enzyme (with or without co-factors), enzyme cascades and whole cells. The significance of microbes is that they contain molecular assemblies capable of catalyzing reactions under moderate conditions with efficiencies rarely matched by synthetic systems[31]. Bio-fuel cells attempt to make use of these properties either by employing whole cells or their enzymes. If a biocatalyst is capable of transferring electrons between the electrode and the biocatalyst, the process is termed Direct Electron Transfer (DET)[1]. Otherwise, mediators aiding electron transportation from an biocatalyst to the electrode are needed in the bio-fuel cells and the process is called Mediated Electron Transfer (MET)[1].

Among over 1000 redox enzymes, less than 10% can carry out DET[45] .Catalytic centers are usually buried fairly deeply in the proteins, and achieving efficient electron transfer at an electrode is a challenge for EFCs[37]. MFCs have a similar situation. Though theoretically almost all bacteria can be used for electricity generation, not many of them can directly transfer electrons to the anode. Mediators can help those that are incapable of DET[35]. In the cyclic process of MET, mediators should react readily with the electron source and be electrochemically active at the electrode surface in a bio-fuel cell. In order not to lose energy in the MET step, the formal redox potential of the mediator should be close to that of the redox couple providing the reducing action[6]. Recently, with the progress in immobilization technology mediators might again draw the attention of the researchers. Worth noting is that mediators of low solubility which were considered not meeting the criteria for practical mediators in early studies have advantages for designs using a mediator-modified electrode. Mediators can be secreted by anodophiles in a biofilm or by synergistic microbes in the same biofilm consortium. This is probably one reason why mixed-culture biofilms tend to perform better.

4.4.3 Enzymes in EFCs

Typical biocatalysts employed at EFC anodes are glucose oxidases and dehydrogenases which differ in their cofactors and physiological electron acceptors. Most glucose-oxidizing enzymes target the C1 hydroxyl group of glucose forming gluconolactone which spontaneously hydrolyses to gluconate[5]. Oxidases using O_2 as the electron acceptor can be isolated from many microorganisms. For example, fungal glucose oxidases come from *Aspergillus niger and Penicillium amagasakiense*[20]. The glucose oxidase from A. *niger* is widely used. It has a mean molecular mass of 160 kDa, and

an isoelectric point of about 4.2[46]. Its redox co-factor FAD is buried in the protein resulting in a very sluggish DET with an electrode[37]. Dehydrogenases, also widely used in enzymatic fuel cell applications, have three cofactors for bioelectrocatalysis including quinone, flavin, or NAD^+[5]. Glucose dehydrogenase from *Acinetobacter calcoaceticus* is a quinoprotein-dehydrogenase that is a dimer with identical subunits (ca. 50 kDa). It can oxidize a wide range of aldose sugars to the lactones with the hydride carrier PQQ as the catalytic center. Some classes of enzymes that catalyze oxidation of alcohol functionalities in sugars also oxidize simple primary alcohols such as methanol and ethanol[47]. Alcohol oxidizing enzymes are usually suitable as anode catalysts in membrane-less EFCs as they are not damaged by O_2[20]. Table 4.1 lists the selected enzymes for typical substrate employed in EFCs together with their co-factors.

Table 4.1 Typical substrates and enzymes used in enzymatic bio-fuel cells[5, 20, 37]

Enzyme	Co-factor	Substrate	Anodic Reaction
Glucose oxidase	FAD	glucose	glucose → glucono-1,5-lactone + $2H^+$ + $2e^-$
Glucose dehydrognenase	PQQ	glucose	glucose → glucono-1,5-lactone + $2H^+$ + $2e^-$
Glucose dehydrognenase	NAD(P)	glucose	glucose → glucono-1,5-lactone + $2H^+$ + $2e^-$
Alcohol dehydrogenase	NAD(P)	ethanol	ethanol →acetaldehyde + $2H^+$ + $2e^-$
Alcohol dehydrogenase	PQQ	ethanol	ethanol →acetaldehyde + $2H^+$ + $2e^-$
Methanol dehydrogenase	PQQ	methanol	methanol→formaldehyde + $2H^+$ + $2e^-$
Fructose dehydrogenase	FAD	fructose	fructose →5-dehydrofructose + $2H^+$ + $2e^-$
Glycerol dehydrogenase	NAD	glycerol	glycerol →dihydroxyacetone + $2H^+$ + $2e^-$
Glycerol dehydrogenase	PQQ	glycerol	glycerol →dihydroxyacetone + $2H^+$ + $2e^-$

In anodic systems using a single enzyme catalyzed partial oxidation of the fuel limits the number of electrons recovered. The biocatalyzed reaction likely breaks only one chemical bond. However, for EFCs using enzyme cascades, the complete oxidation of the fuels to CO_2 can be achieved to harvest more electrons to increase the current density[10].

4.4.4 Microbes used in MFCs

Many microorganisms can be used in MFCs to generate electricity as seen in Table 4.2. Not all of them have the ability to transfer the electrons from substrate oxidation to the anode directly. MET to the anode is possible via electroactive metabolites, such as anthraquinone, the oxyanions of sulphur (sulphate and thiosulphate) or with the addition of non-natural (chemical) redox mediators such as dyes[48, 49]. Cell surface structures in microorganisms vary widely, but the main features for bacteria are an out-layer containing peptidoglycan, a chain-like disaccharide heteripolymer glycan with peptide substituents, and the cytoplasmic membrane consisting primarily of phospholipids. Lipid-bilayer membranes generally contain about 50% proteins with varied and specific catalytic/carrier functions, but about 30% of the phospholid component may be relatively pure. The fluid properties are affected by the aqueous content, and the electrical resistance of the bilayer is 102 ~ 105 ohms[6]. For many bacteria, the non-conductive cell surface hinders the direct electron transfer to the anode[50]. Mediators are required for those microbes that are incapable of DET. Mediators shuttle between the anode and the microbe to transport electrons. In the anodic chamber, they take up the electrons from substrate oxidation by microbes and then release them at the anodic surface. *Actinobacillus succinogenes*[51], *D. desulfuricans*[15, 49], *E. coli*[52], *Proteus mirabilis*[53], *Proteus vulgaris*[54] need extraneous mediators, but some microorganisms secrete their own mediators. For example, pyocyanin molecules secreted by *Pseudomonas aeruginosa*[55] are electron shuttles.

DET from microbes to a typical carbon-based anode via extracellular cytochromes or conductive microbial *pili* (electrically conductive nanowires) have also been observed[7, 8]. Generally dissimilatory metal reducing microorganisms are anodophiles. They produce biologically useful energy from the dissimilatory reduction of metal oxides anaerobically in soils and sediments. The electrons are transferred to terminal electron acceptors such as Fe_2O_3 through DET between the mineral oxides and the metal reducing microorganisms[56, 57]. In a mediator-less MFC, metal reducing bacteria such as those from the families of *Shewanella*, *Rhodoferax*, and *Geobacter* use the anode as terminal electron acceptor in the dissimilatory respiratory metabolism of the biofilm as if they were metal oxides. In lab experiments, these microbes yielded high Coulombic efficiencies[8, 58]. *Shewanella putrefaciens*[59], *Geobacteraceae sulferreducens*[60], *Geobacter metallireducens*[61] and *Rhodoferax ferrireducens*[8] have all been found to be operationally stable because these bio-electrochemically active microbes readily form a biofilm on the anode surface and DET is carried out by conductance through the cell membrane. These microorganisms have been isolated from fresh water, wastewater and

marine sediments, as well as activated sludge[62]. So far almost all of mediator-less MFCs used dissimilatory metal reducing microorganisms with the exception of *Clostridium butyricum*[63, 64]. Although mediator-less MFCs can run without mediators because they anodophilic biofilms, anodes containing electron mediators such as Mn^{4+} or neutral red have shown enhancement of the performance of MFCs using anodophile *Shewanella. putrefaciens*[65].

Table 4.2 Microbes used in MFCs

Microbes	Electron Transfer Mechanisms
Actinobacillus succinogenes	MET/Neutral red or thionin as electron mediator[51, 66]
Aeromonas hydrophila	DET/anodophile[67]
Alcaligenes faecalis,	MET/Self-mediate[55]
Enterococcus gallinarum	MET/Self-mediate[55]
Desulfovibrio desulfuricans	MET/Sulphate-sulphide as mediator[49, 15]
Erwinia dissolven	MET/Ferric chelate complex as mediators[34]
Escherichia coli	MET/methylene blue as mediator[49, 52]
Geobacter metallireducens	DET/anodophile[61]
Geobacter sulfurreducens	DET/anodophile[60, 68]
Gluconobacter oxydans	MET/HNQ, resazurin or thionine as mediator[69]
Klebsiella pneumoniae	MET/HNQ as mediator[70, 71]
Lactobacillus plantarum	MET/Ferric chelate complex as mediators[34]
Proteus mirabilis	MET/Thionin as mediator[53]
Proteus vulgaris	MET/Thionin as mediator[54]
Pseudomonas aeruginosa	MET/Self-mediate[55]
Rhodoferax ferrireducens	DET/anodophile[8]
Shewanella oneidensis	MET/AQDS as mediator[72]
Shewanella putrefaciens	DET/anodophile[7, 65]
Streptococcus lactis	MET/Ferric chelate complex as mediators[34]

Apart from pure cultures, MFCs can also use mixed culture biofilms such as those enriched from marine sediments and anaerobic sludge. These biofilms tend to have better stability and also performances due to microbial synergy. One example of synergy in an anodic biofilm consortium is that one microbe secretes mediators for the other microbe both will benefit bioenergetically from the enhanced degradation of organic matters in the anodic chamber. Because there are many microbes in a single biofilm, a much wider range of substrates can be digested. Electrophiles and anodophiles in a anodic biofilm consortium with the help of locally secreted mediators can work together to digest the various organic substrates present in a wastewater stream.

4.4.5 Oxidants

Dissolved oxygen is a widely used oxidant for the cathodic reaction in bio-fuel cells. In two-compartment bio-fuel cells, pure oxygen (in lab tests) or air can

be sparged through the catholyte solution. Due to the low solubility of oxygen in water, power output of a bio-fuel cell can be strongly affected by the dissolved oxygen level because the driving force for mass transfer of oxygen from the bulk solution to the cytoplasm can be insufficient[37]. Single-chamber bio-fuel cells with an air-cathode rely on oxygen in the air to dissolve in the web liquid film covering the cathode. Other oxidants used in MFCs include hydrogen peroxide and potassium ferricyanide. These highly reactive oxidants are toxic and their practical applications will be very limited or impossible[73]. Biocathodes using anaerobic microbes can use oxidants that are already present in wastewater streams. They include sulfate, nitrate and nitrite that are common in agricultural runoffs. MFCs with bioanodes and biocathodes can process one wastewater stream in a membrane-less MFC or two different streams in an MFC with its two chambers partitioned by a membrane.

4.4.6 Electrode materials

Though bio-fuel cells possess some attractive features, they are still not widely employed at all. One major bottleneck is the slow electron transfer between catalysts and the electrodes. New electrode materials including composite or alloyed electrodes can help solve this problem. Because the redox units are buried in the 3-D enzyme protein structures shielded by a thick carbohydrate shell, many biofilms undergo a much lower metabolic rate in MFCs than that of their normal state[74]. Therefore, modification of electrodes is a key issue. Many metals are toxic toward biocatalysts. Pt and some other precious metals are an exception under anaerobic condition, but they are cost-prohibitive for any large-scale applications.

The anode in bio-fuel cells must facilitate electron transfer. Mediators tend to be very helpful in achieving electrical communication. However, involving mediators in the system also brings the problems associated with mediator diffusion or leaching. Their cost can also be prohibitive for practical applications. Immobilization of enzymes and mediators is a possible solution to increasing current densities, enhancing enzyme stability, and improving electron transfer kinetics[75]. Immobilization techniques can be classified into four well known categories: physical adsorption, covalent binding, cross-linking and entrapment in polymeric materials. Typical enzymatic electrodes include architectures with or without electron transfer mediators. Crosslinking is a common and simple way for immobilization. However, activity reduction of the enzymes in the process of crosslinking is not acceptable for enzymatic bio-fuel cells, because of the present low catalytic activity of the enzyme[5]. Figure 4.4 shows four typical anode assemblies.

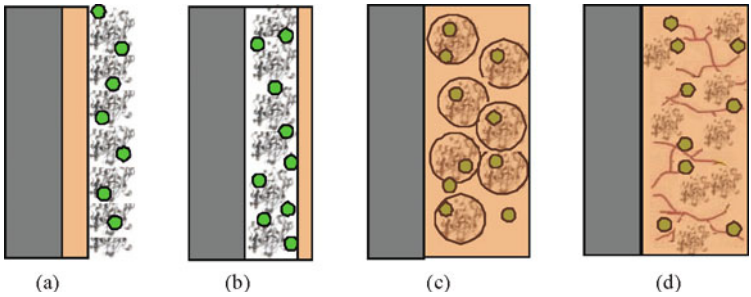

Figure 4.4 Typical anode assemblies (a) an initial matrix layer followed by enzyme and mediator adsorption or covalent. (b) an out-layer entrapping the enzyme. (c) the physical entrapment of an enzyme by microencapsulation. (d) immobilizing enzymes and mediators by physical entrapping or chemically binding in redox hydrogels (Figure redrawn after References [5] and [37] with modifications)

Compared with an enzymatic anode without a mediator, mediator based bioanodes are more commonly used in enzymatic fuel cells. For practical purposes, mediators should be immobilized to minimize mediator cost. Three-dimensional matrices like polymers, lipids and carbon nanotubes or their combinations are used to incorporate enzyme and mediators in various states[76]. Adsorption and covalent binding are the two popular ways in fabrication of enzymatic electrode composites. Many systems have employed an initial matrix layer, followed by enzyme and mediator adsorption or covalent binding, but this simple method increases the distance from the enzyme catalytic site to the electrode surface. Entrapment by polymer coating, microencapsulation or gelation can entrap an enzyme in pores or matrices at the electrode surface[5, 76]. Employing an out-layer to entrap the enzyme has the effect of adding an extra mass transfer barrier between fuel molecules and the catalytic sites of the enzyme in the system. Microencapsulation is the physical entrapment of an enzyme in pores or matrices of a membrane at the electrode surface. Modified Nafion without the destructive acidity and chitosan are suitable for this purpose[5]. Immobilizing enzymes and mediators by physical entrapping or chemically binding in redox hydrogels has drawn much attention. The matrix provides a pathway for electrons to reach the redox centers attached to the polymer and can greatly enhance bio-fuel cell life expectancy and performance[37]. Bio-fuel cells based on redox hydrogels have shown good characteristics for immobilization of GOx and other enzymes[77, 78].

The first electrodes for MFCs were made from platinum[4] but it was gradually substituted by other much less expensive materials. Nowadays, Graphite is commonly used for electrodes in MFC designs. There are also various types of relatively inexpensive carbon cloths and felts that have become commercially

available, and have proven very suitable for use in MFCs. They are cheaper and provide an electrode with a greater surface area. However, these materials are less electroactive than platinum, supporting lower exchange-current densities. Biofilm catalysis and mediators help to overcome this shortcoming. Large electrodes are feasible using such cheap materials. Non-porous graphite providing a large specific surface area as high as 1 m^2/g has been reported[6].

To improve electron transfer between the microorganisms and the electrode, electrode modification is actively being investigated to improve MFC performances. Graphite anode with immobilized mediators can greatly increase the current output compared to the graphite anode alone[65, 79]. Anode modifications including immobilization of AQDS, NR or 1,4-naphthoquinone (NQ) and doping metal elements of Mn(II) , Mn(IV) , Ni(II), Fe(III) have shown improvements in electricity generation[51, 66, 80]. The principle for their catalytic activity is the same as that of electron shuttles. Electrode modifiers of conductive polymers such as fluorinated polyanilines poly(2-fluoroaniline) and poly(2,3,5,6-tetrafluoroaniline) also serve as immobilzed mediators thanks to their structural similarities to conventional redox mediators[52, 81, 82]. From this point of view, proper electrode assemblies similar to enzymatic anodes may also be promising in anode design for MFCs. Cost will remain a factor in the success of any of the modifications.

4.4.7 Power output in bio-fuel cells

The electric power output from a bio-fuel cell depends on metabolic and electrochemical processes[83]. The biological reactions in a bio-fuel cell are slower than the chemical reactions in a conventional chemical fuel cell. In a bio-fuel cell, the following factors influence the biological process: the amount of biocatalysts (microbial cell densities or concentrations of cell-free enzymes) and their bioactivities and reaction kinetics, the organic carbon loading rate and mass transfer[83].

In the electrochemical process, a bio-fuel cell's output power P is the product of cell voltage V and the current I, i.e., $P=I\times V$. The open circuit potential that provides the maximum cell voltage (E_0) (usually between 750 to 800 mV) drops significantly when an external load is used to close the electrical loop. This is primarily because of overpotential, the potential losses owing to charge transfer resistance at the electrodes and internal resistance. A membrane-less bio-fuel cell has much smaller internal resistance, because convective flow of protons is possible. The cell configuration and operating conditions also impact the internal resistance significantly[83~85]. The cell voltage V can be calculated using the following equation[83]

$$V = E_0 - \eta_a - \eta_c - I \times R \quad (4.5)$$

in which η_a and η_c represent the overpotential losses at the anode and cathode, respectively, and R the overall internal cell resistance.

The output power densities of bio-fuel cells, especially MFCs, are much lower than that for chemical fuel cells. Chemical fuel cells can provide $10^6 \sim 10^7$ mW/m^2[86−89]. The power densities of several chemical fuel cells and bio-fuel cells are listed in Table 4.3. Obviously, in order to use bio-fuel cells to generate electricity to power larger devices, more research is needed to improve both the chemical and electrochemical processes in bio-fuel cells. However, it is unrealistic and unfair to expect bio-fuel cells to become comparable with chemical fuel cells in terms of power densities simply because the fuels used by the former have much a lower energy density and biological reactions are slower than the chemical reactions in the latter. One distinct advantage for bio-fuel cells is obviously that they use low-grade energy sources, often wastes that are low cost or zero cost. In some cases, a source may even come with subsidy.

Table 4.3 Comparison of power densities of chemical fuel cells and bio-fuel cells

Fuel Cell Types	Power Density/ (mW/m^2)	References
Proton exchange membrane fuel cell (PEMFC)	2.5×10^7	[86]
Direct methanol fuel cell (DMFC)	2.1×10^6	[87]
Solid oxide fuel cell (SOFC)	8.8×10^6	[88]
Phosphoric acid fuel cell (PAFC)	5.6×10^6	[89]
Microbial fuel cell (MFC)	5.6×10^2	[90]
Microbial fuel cell (MFC)	2.63×10^2	[91]
Microbial fuel cell (MFC)	7.2×10^3	[92]
Microbial fuel cell (MFC)	4.31×10^3	[52]
Enzymatic bio-fuel cell (EFC)	9.3×10^3	[93]
Enzymatic bio-fuel cell (EFC)	1.32×10^4	[94]
Enzymatic bio-fuel cell (EFC)	4.6×10^3	[95]
Enzymatic bio-fuel cell (EFC)	2.5×10^3	[96]

4.5 Concluding remarks

In view of the progresses and the limited successes so far obtained for producing energy, bio-fuel cells appear to be competitive on the basis of Coulombic efficiency and the ability to use cheap low-grade wastes. However, the performances are still low on the basis of current or power density, especially for MFCs. Recent studies suggest that higher current and energy densities can be expected to accompany improvements in reactor design. Further improvements

in charge transfer and mass transfer are needed, so that the full reducing power of the biocatalysts can be delivered. “Super bugs” may be available in the future from wild-type selection, mutagenesis or even genetic engineering. Ideal super bugs can bind with an electrode tenaciously with a high surface density. They also exibit hyperpilation that increases electron flow from a single cell to the anode and enable more than one layer of electron donating cells through massive networking by pili. Membrane-less bio-fuel cells are probably the only option for large-scale applications because of the high costs associated with membranes and their easy fouling.

Regarding the biocatalysts, a large variety of enzymes and microorganisms have been investigated by researchers, but a clear trend is to use enzyme cascades and mixed-culture microorganisms. EFCs yield higher power densities than MFCs. However, they are easily contaminated by microbes when they are fed complicated organic wastes such as wastewater because such wastes contain a large number of microbes. EFCs also lack the ability to digest the large array of organic carbons in a waste stream. Furthermore, EFCs cannot recover from the inevitable enzyme loss or attrition because it is not a living system. Regardless of these drawbacks, EFCs has an edge over MFCs in powering implanted medical devices, because EFCs can operate in a sterile environment. Because the demand for small-scale power sources and miniature devices will likely increase in the future, bio-fuel cells are promising in serving as distributed power systems for local uses and for powering miniature devices (especially remote sensors) for long term operations. Many underdeveloped regions in the world could make better use of readily available low-grade biomass. Bio-fuel cells offer alternatives to conventional routes of harnessing energy from various biomass. The potential for harnessing energy from bio-fuel cell systems should not be overlooked, but the full realization of this potential depends on socio-economic factors (such as energy costs and the push for green energy) as well as advances in scientific research and technological development. Relatively large-scale practical bio-fuel cells probably will first be practical in niche applications. One example is for wastewater treatment on remote US military forward operation bases such as those currently in Afghanistan, where there is a need for sustainable wastewater treatment processes with low energy input because the local fuel cost is 10 times than normal.

References

[1] Bullen R A, Arnot T C, Lakeman J B, et al. Bio-fuel cells and their development. Biosens Bioelectron, 2006, 21, 2015～2045.

[2] Zhao F, Slade R C T, Varcoe J R. Techniques for the study and development of microbial fuel cells: An electrochemical perspective. Chem Soc Rev, 2009, 38, 1926～1939.

[3] Logan B E, Hamelers B, Rozendal R, et al. Microbial fuel cells: methodology and technology. Environ Sci Technol, 2006, 40(17), 5181～5192.

[4] Potter M C. Electrical effects accompanying the decomposition of organic compounds. Proc R Soc Ser B, 1912, 84, 260～276.

[5] Moehlenbrock M J, Minteer S D. Extended lifetime bio-fuel cells. Chem Soc Rev, 2008, 37, 1188～1196.

[6] Bennetto H P. Microbial fuel cells. Life Chemistry Reports, 1984, 2, 363～453.

[7] Kim B H, Kim H J, Hyun M S, et al. Direct electrode reaction of Fe(III)-reducing bacterium, *Shewanella putrifaciens*. J Microbiol Biotechnol, 1999, 9, 127～131.

[8] Chaudhuri S K, Lovley D R. Electricity generation by direct oxidation of glucose in mediatorless microbial fuel cells. Nat Biotechnol, 2003, 21, 1229～1232.

[9] Palmore G T R, Bertschy H, Bergens S H, et al. J Electroanal Chem, 1998, 443, 155～161.

[10] Minteer S D, Liaw B Y, Cooney M J. Enzyme-based bio-fuel cells. Curr Opin Biotech, 2007, 18, 228～234.

[11] Kim B H, Chang I S, Gil G C, et al. Novel BOD (biological oxygen demand) sensor using mediator-less microbial fuel cell. Biotechnol Lett, 2003, 25, 541～545.

[12] Karube I, Matsunaga T, Mitsuda S, et al. Microbial electrode BOD sensors. Biotechnol Bioeng, 1977, 19, 1535～1547.

[13] Karube I, Matsunaga T, Tsuru S, et al. Biochemical fuel cell utilizing immobilized cells of *Clostridium butyricum*. Biotechnol Bioeng, 1977, 19, 1727～1733.

[14] Park D H, Kim B H, Moore B, et al. Electrode reaction of *Desulfovibrio desulfuricans* modified with organic conductive compounds. Biotechnol Tech, 1997, 11, 145～148.

[15] Zhang L, Schryver P D, Gusseme B D, et al. Chemical and biological

technologies for hydrogen sulfide emission control in sewer systems: A review. Water Research, 2008, 42, 1～12.

[16] Wilkinson S. “Gastrobots” - Benefits and challenges of microbial fuel cells in food powered robot applications. Auton Robot, 2000, 9, 99～111.

[17] Gil G C, Chang I S, Kim B H, et al, Operational parameters affecting the performance of a mediator-less microbial fuel cell. Biosens Bioelectron, 2003, 18, 327～334.

[18] Cheng S, Logan B E. Sustainable and efficient biohydrogen production via electrohydrogenesis. PNAS, 2007, 104(47), 18871～18873.

[19] Oh S E, Logan B E. Hydrogen and electricity production from a food processing wastewater using fermentation and microbial fuel cell technologies. Water Res, 2005, 39, 4673～4682.

[20] Cracknell J A, Vincent K A, Armstrong F A. Enzymes as Working or Inspirational Electrocatalysts for Fuel Cells and Electrolysis. Chem Rev 2008, 108, 2439～2461.

[21] Wagner R C, Regan J M, Oh S E, et al. hydrogen and methane production from swine wastewater using microbial electrolysis cells. Water Res, 2009, 43, 1480～1488.

[22] Pothukuchy A, Mano N, Georgiou G, et al. A potentially insect-implantable trehalose electrooxidizing anode. Biosens Bioelectron, 2006, 22, 678～684.

[23] Hambourger M, Gervaldo M, Svedruzic D, et al. J Am Chem Soc, 2008, 130, 2015～2022.

[24] Campbell W H. Nitrate reductase structure, function and regulation: bridging the gap between biochemistry and physiology. Annu Rev Plant Physiol Plant Mol Biol, 1999, 50,277～303.

[25] Liu H, Grot S, Logan B E. Electrochemically assisted microbial production of hydrogen from acetate. Environ Sci Tchnol, 2005, 4317～4320.

[26] Holzman D C. Microbe power. Environ Health Persp 2005, 113, A754～A757.

[27] Kerzenmacher S, Ducree J, Zengerle R, et al. Energy harvesting by implantable abiotically catalyzed glucose fuel cells. J Power Sources, 2008, 182, 1～17.

[28] Ringeisen B R, Ray R, Little B. A miniature microbial fuel cell operating with an aerobic anode chamber. J Power Sources, 2007, 165, 591～597.

[29] Coman V, Vaz-Dominguez C, Ludwig R, et al. A membrane-, mediator-, cofactor-less glucose/oxygen bio-fuel cell. Phys Chem Chem Phys, 2008, 10, 6093～6096.

[30] Jang J K, Pham T H, Chang I S, et al. Construction and operation of a novel

mediator- and membrane-less microbial fuel cell. Process Biochem, 2004, 39, 1007～1012.

[31] Higgins I J, Hill H A O. Microbial generation and interconversion of energy sources, in Microbial Technology: Current State, Future Prospects, eds. Bull A T, Ellwood D C, Ratledge C, Cambridge University Press, Cambridge, 1979, 359～377

[32] Gao F, Courjean O, Mano Ni. An improved glucose/O_2 membrane-less bio-fuel cell through glucose oxidase purification. Biosens Bioelectron, 2009, 25, 356～361.

[33] Kavanagh P, Boland S, Jenkins P, et al. Performance of aGlucose/O_2 Enzymatic Bio-fuel cell Containing a Mediated *Melanocarpus albomyces* Laccase Cathode in a Physiological Buffer. Fuel Cells, 2009, 1, 79～84.

[34] Vega C A, Fernandez I. Mediating effect of ferric chelate compounds in microbial fuel cells with *Lactobacillus plantarum*, *Streptococcus* lactis, and *Erwinia dissolvens*. Bioelectrochem Bioenerg, 1987, 17, 217～222.

[35] Du Z, Li H, Gu T. A state of the art review on microbial fuel cells: A promising technology for wastewater treatment and bioenergy. Biotechnol Adv, 2007, 25, 464～482.

[36] Pant D, Bogaert G V, Diels L, et al. A review of the substrates used in microbial fuel cells (MFCs) for sustainable energy production. Bioresource Technol, 2010, 101, 1533～1543.

[37] Ivanov I, Vidakovic-Koch T, Sundmacher K. Recent advances in enzymatic fuel cells: Experiments and modeling. Energies, 2010, 3, 803～846.

[38] Logan B E, Cheng S, Watson V, et al. Graphite fiber brush anodes for increased power production in air-cathode microbial fuel cells. Environ Sc. Technol, 2007, 41, 3341～3346.

[39] Catal T, Xu S, Li K, et al. Electricity production from polyalcohols in single-chamber microbial fuel cells. Biosens Bioelectron, 2008, 24, 855～860.

[40] Luo H, Liu G, Jin S. Phenol degradation in microbial fuel cells. Chem Eng J, 2009, 147, 259～264.

[41] Pham H, Boon N, Marzorati M, et al. Enhanced removal of 1,2-dichloroethane by anodophilic microbial consortia. Water Res, 2009, 43, 2936～2946.

[42] Liu H, Logan B E. Electricity generation using an air-cathode single chamber microbial fuel cell in the presence and absence of a proton exchange membrane. Environ Sci Technol, 2004, 38, 4040～4046.

[43] Min B, Kim J R, Oh S E, et al. Electricity generation from swine wastewater

using microbial fuel cells. Water Res, 2005, 39, 4961～4968.

[44] Kim J R, Min B, Logan B E. Evaluation of procedures to acclimate a microbial fuel cell for electricity production. Appl Microbiol Biotechnol, 2005, 68, 23～30.

[45] Ramanavicius A, Ramanaviciene A. Hemoproteins in design of bio-fuel cells. Fuel Cells, 2009, 9, 25～36.

[46] Wilson R, Turner A P F. Glucose-oxidase - An ideal enzyme. Biosens Bioelectron, 1992, 7, 165～185.

[47] Guven G, Prodanovic R, Schwaneberg U. Protein Engineering – An Option for Enzymatic Bio-fuel cell Design. Electroanal, 2010, 22, 765～775.

[48] Stams A J M, de Bok F A M, Plugge C M, et al. Exocellular electron transfer in anaerobic microbial communities. Environ Microbiol, 2006, 8, 371～382.

[49] Ieropoulos I A, Greenman J, Melhuish C, et al. Comparative study of three types of microbial fuel cell. Enzyme Microb Tech, 2005, 37, 238～245.

[50] Davis F, Higson S P J. Bio-fuel cells - Recent advances and applications. Biosens Bioelectron, 2007, 22, 1224～1235

[51] Park D H, Zeikus J G. Electricity generation in microbial fuel cells using neutral red as an electronophore. Appl Environ Microb, 2000, 66, 1292～1297.

[52] Schroder U, Nieben J, Scholz F. A generation of microbial fuel cells with current outputs boosted by more than on e order of magnitude. Angew Chem Int Ed, 2003, 42, 2880～2883.

[53] Choi Y, Jung E, Kim S, et al. Membrane fluidity sensoring microbial fuel cell. Bioelectrochemistry, 2003, 59, 121～127.

[54] Thurston C F, Bennetto H P, Delaney G M, et al. Glucose metabolism in a microbial fuel cell. Stoichiometry of product formation in a thionine-mediated *Proteus vulgaris* fuel cell and its relation to Coulombic yields. J Gen Microbiol 1985, 131, 1393～1401.

[55] Rabaey K, Boon N, Siciliano S D, et al. Bio-fuel cells select for microbial consortia that self-mediate electron transfer. Appl Environ Microb, 2004, 70, 5373～5382.

[56] Lovley D R, Holmes D E, Nevin K P. Dissimilatory Fe(III) and Mn(IV) reduction. Adv Microb Physiol, 2004, 49, 219～286.

[57] Vargas M, Kashefi K, Blunt-Harris E L, et al. Microbiological evidence for Fe(III) reduction on early earth. Nature, 1998, 395, 65～70.

[58] Scholz F, Schroder U. Bacterial batteries. Nat Biotechnol, 2003, 21, 1151～1152.

[59] Kim H J, Park H S, Hyun M S, et al. A mediator-less microbial fuel cell using a metal reducing bacterium, *Shewanella putrefaciens*. Enzyme Microb Tech, 2002, 30, 145～152.

[60] Bond D R, Lovley D R. Electricity production by Geobacter sulfurreducens attached to electrodes. Appl Environ Microbiol 2003, 69, 1548～1555.

[61] Min B, Cheng S, Logan B E. Electricity generation using membrane and salt bridge microbial fuel cells. Water Res, 2005, 39, 1675～1686.

[62] Niessen J, Harnisch F, Rosenbaum M, et al. Heat treated soil as convenient and versatile source of bacterial communities for microbial electricity generation. Electrochem Commun, 2006, 8, 869～873.

[63] Oh S E, Logan B E. Proton exchange membrane and electrode surface areas as factors that affect power generation in microbial fuel cells. Appl Microbiol Biotechnol, 2006, 70, 162～169.

[64] Park H S, Kim B H, Kim H S, et al. A novel electrochemically active and Fe(III)-reducing bacterium phylogenetically related to Clostridium *butyricum* isolated from a microbial fuel cell. Anaerobe, 2001, 7, 297～306.

[65] Park D H, Zeikus J G. Impact of electrode composition on electricity generation in a single-compartment fuel cell suing *Shewanella putrefaciens*. Appl Microbiol Biotechnol, 2002, 59, 58～61.

[66] Park D H, Zeikus J G. Utilization of electrically reduced neutral red by *Actinobacillus succinogenes*: Physiological function of neutral red in membrane-driven fumarate reduction and energy conservation. J Bacteriol, 1999, 181, 2403～2410.

[67] Pham C A, Jung S J, Phung N T, et al. A novel electrochemically active and Fe(III)-reducing bacterium phylogenetically related to *Aeromonas hydrophila*, isolated from a microbial fuel cell. FEMS Microbiol Lett, 2003, 223, 129～134.

[68] Bond D R, Holmes D E, Tender L M, et al. Electrode-reducing microorganisms that harvest energy from marine sediments. Science, 2002, 295, 483～485.

[69] Lee S A, Choi Y, Jung S, et al. Effect of initial carbon sources on the electrochemical detection of glucose by *Gluconobacter oxydans*. Bioelectrochemistry, 2002, 57, 173～178.

[70] Rhoads A, Beyenal H, Lewandowshi Z. Microbial fuel cell using anaerobic respiration as an anodic reaction and biomineralized manganese as a cathodic reactant. Environ Sci Technol, 2005, 39, 4666～4671.

[71] Menicucci J, Beyenal H, Marsili E, et al. Procedure for determining maximum sustainable power generated by microbial fuel cells. Environ Sci

Technol, 2006, 40, 1062～1068.
[72] Ringeisen B R, Henderson E, Wu P K, et al. High power density from a miniature microbial fuel cell using *Shewanella oneidensis* DSP10. Environ Sci Technol, 2006, 40, 2629～2634.
[73] Willner I, Katz E, Patolsky F, et al. Bio-fuel cell based on glucose oxidase and microperoxidase-11 monolayer-fundionalized electrodes. J Chem Soc, Perkin Trans, 1998, 2, 1817～1822.
[74] Holmes D E, Bond D R, O' Neil R A, et al. Microbial communities associated with electrodes harvesting electricity from a variety of aquatic sediments. Microbial Ecol, 2004, 48, 178～190.
[75] Willner I, Yan Y M, Willner B, et al. Integrated Enzyme-Based Bio-fuel cells–A Review. Fuel Cells, 2009, 7～24.
[76] Sarma A K, Vatsyayan P, Goswami P, et al. Recent advances in material science for developing enzyme electrodes. Biosens Bioelectron, 2009, 24, 2313～2322.
[77] Barriere F, Ferry Y, Rochefort D, et al. Targetting redox polymers as mediators for laccase oxygen reduction in a membrane-less bio-fuel cell. Electrochem Commun, 2004, 6, 237～241.
[78] Tasca F, Gorton L, Harreither W, et al. Highly efficient and versatile anodes for bio-fuel cells based on cellobiose dehydrogenase from *Myriococcum thermophilum*. J Phys Chem C, 2008, 112, 13668～13673.
[79] Park D H, Zeikus J G. Improved fuel cell and electrode designs for producing electricity from microbial degradation. Biotechnol Bioeng, 2003, 81, 348～355.
[80] Lowy D A, Tender L M, Zeikus J G, et al. Harvesting energy from the marine sediment-water interface II kinetic activity of anode materials. Biosens Bioelectron, 2006, 21, 2058～2063.
[81] Niessen J, Schroder U, Rosenbaum M, et al. Fluorinated polyanilines as superior materials for electrocatalytic anodes in bacterial fuel cells. Electrochem Commun, 2004, 6, 571～575.
[82] Niessen J, Harnisch F, Rosenbaum M, et al. Heat treated soil as convenient and versatile source of bacterial communities for microbial electricity generation. Electrochem Commun, 2006, 8, 869～873.
[83] Rabaey K, Verstraete W. Microbial fuel cells: Novel biotechnology for energy generation. Trends Biotechnol. 2005, 23, 291～298.
[84] James L, Andrew D, (2003) Fuel cell systems explained (2nd Edition), John, Wiley and Sons.
[85] Aswin K M, Florian M. The internal resistance of a microbial fuel cell and

its dependence on cell design and operating conditions. Electrochimica Acta. 2005, 54, 1664～1670.

[86] Oliver J M, G.Duncan H, David J M. High power density proton-exchange membrane fuel cells. J Power Source. 1994, 47, 353～368.

[87] Lim C, Wang C Y. Development of high-power electrodes for a liquid-feed direct methanol fuel cell. J Power Source. 2003, 113, 145～150.

[88] Ramakrishna P A, Yang S, Sohn C H. Innovative design to improve the power density of a solid oxide fuel cell. J Power Source. 2006, 158, 378～384.

[89] Neergat M, Shukla A K. A high-performance phosphoric acid fuel cell. J Power Source. 2001, 102, 317～321.

[90] Moon H, Chang I S, Kim B H. Continuous electricity production from artificial wastewater using a mediator-less microbial fuel cell. Biosenource Technol. 2006, 97, 621～627.

[91] Mohan Y, Manoj-Muthu-Kumar S, Das D. Electricity generation using microbial fuel cells. Int J Hydrogen Energy. 2008, 33, 423～426.

[92] Oh SE, Min B, Logan B E. Cathode performance as a factor in electricity generation in microbial fuel cells. Environ Sci Technol. 2004, 38, 4900～4904.

[93] Sokic-Lazic D, Minteer S D. Pyruvate/air enzymatic biofuel cell capable of complete oxidation. Electrochem. Solid-State Lett. 2009, 12, 26～28.

[94] Arechederra R L, Minteer S D. Complete oxidation of glycerol in an enzymatic biofuel cell. Fuel Cells 2009, 9, 63～69.

[95] Sabina T, Shelley D M. Development of a membraneless ethanol/oxygen biofuel cell. Electrochim. Acta. 2006, 51, 2168～2172.

[96] Zhang X C, Ranta A, Halme A. Direct methanol biocatalytic fuel cell-Considerations of restraints on electron transfer. Biosens Bioelectron. 2006, 21, 2052～2057.

Chapter 5
Nanostructured Electrode Materials for Lithium-ion Battery

Ping He[2], Yonggang Wang[1]*

1 Chemistry Department, Fudan University, Shanghai 200433, People's Republic of China

2 College of Modern Engineering and Applied Science, Nanjing University, Nanjing 210093,People's Republic of China

* Email: ygwang@fudan.edu.cn

Abstract

Owing to the limited oil storage and the global warming threat, it has been a worldwide topic to build the low carbon society which is based on the sustainable energy, such as wind and solar energy. As an effective energy storage device for the sustainable energy, lithium-ion battery plays a more and more important role in human's life. Future generations of lithium-ion batteries are required to store electricity from sustainable energy source and power not only the portable electronic devices (cellphones, laptop computer etc.) but also electric vehicles (EVs). In order to increase energy and power density to meet the future challenges of energy storage, many efforts have been made to develop nanosturctured electrode materials for lithium-ion battery. Herein, we review some new progress in using these nanostructured materials as cathodes and anodes to develop lithium-ion batteries with high energy density, high rate capability, and excellent cycling stability.

5.1 Introduction

It is now generally considered that flue gas emissions from fossil fuel combustion are not only polluting the air of large, modern cities but also bringing a global warming with alarming consequences. Accordingly, to build the low carbon society, which is based on the clean and sustainable energy, has been a worldwide

topic. Solar radiation, wind, and waves represent typical clean and sustainable energy sources, whereas they are variable in time and diffuse in space, and thus need effective energy storage. Thereby, energy storage is more important today than at any time in human history. The rechargeable battery provides the portability of stored chemical energy with the ability to deliver this energy as electrical energy with high conversion efficiency and no gaseous exhaust. Moreover, the alternative energy sources, mentioned above, are preferably converted to d. c. electrical energy well-matched to store as chemical energy in a battery. Future generations of rechargeable batteries are required to store electricity from clean and sustainable energy source and power both the portable electronic devices and electric vehicles (EVs).

A short list of these available rechargeable batteries could include Lead-acid, Ni-MH and Lithium-ion batteries. Owing to their higher operating voltage and energy density compared with Lead-acid and Ni-MH batteries, lithium-ion batteries were quickly developed, and thus occupied the main market of battery devices. This explains why lithium-ion batteries receive most attention at both fundamental and applied levels [1, 2]. Lithium-ion battery, which is based on a graphite anode and a $LiCoO_2$ cathode, was first successfully commercialized by Sony in 1991. Since then, lithium-ion battery has been widely used to power various portable devices, such as cellular phones, cameras, laptop PC, etc. In order to improve driveline efficiency and/or to provide for the use of energy sources other than petroleum for road transportation, large scale lithium-ion battery powered vehicles are being developed by auto companies.

The typical commercial lithium-ion battery commonly does not contain lithium metal. It is a lithium-ion device, comprising a graphite negative electrode (anode), a non-aqueous liquid electrolyte, and a positive electrode (cathode) formed from layered $LiCoO_2$ (Figure 5.1). During charge process, lithium ions are deintercalated from the layered $LiCoO_2$ intercalation host, pass across the electrolyte, and are intercalated between the graphite layers in the anode. Discharge process reverses the charging process. The electrons pass around the external circuit. The schematic representation of a lithium-ion battery, shown in Figure 5.1, is only a typical example for present lithium-ion battery established by SONY in 1991. During the past decades, various alternative materials for graphite or $LiCoO_2$ have been developed to form lithium-ion batteries. This will be further introduced in section 2 and 3, respectively.

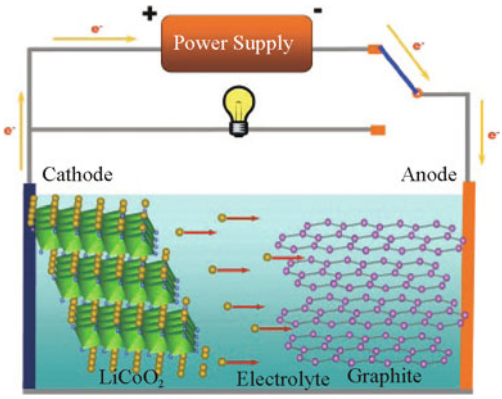

Figure 5.1 Representative sketch of operating mechanism for lithium-ion battery

To achieve the goal of new rechargeable lithium-ion batteries for increasing markets, lithium-ion intercalation electrode materials need to possess the excellent rate capability which is associated with the electronic conduction and the diffusion of lithium-ion insertion/extraction process in intercalation compound. The lithium-ion diffusion in host electrode materials is associated with the lithium-ion diffusion coefficient and the diffusion length. The characteristic time for diffusion can be represented as followed:

$$\tau = L^2/D_{\mathrm{Li}} \tag{5.1}$$

Where L is lithium diffusion length, which is relevant to size of the intercalation compound particle. D_{Li} is the Li^+ diffusion coefficients. As we know, the lithium-ion diffusion coefficient depends on the instinct of host materials. It is worth mentioning that the values estimated in most previous literatures are apparent diffusion coefficient and are determined as function of electrode potential. The time τ for intercalation increases with the square of the diffusion length. Therefore, minimizing the particle size to shorten the lithium-ion diffusion length is an effective strategy for enhancing the rate capability of electrode materials. This is just one of advantages that arise from the use of nanosturctured electrode materials. In addition to the advantage of reduced diffusion length, many other merits of the nanostructured materials have also been proposed, such as new reaction mechanisms; enhancing electron transport; realizing a high lithium-ion flux across the interface; change of electrode potential; transforming the phases of solid solution and so on.

The goal of this chapter is to review some new progress in using these nanostructured materials as cathodes and anodes to develop lithium-ion batteries with high energy density, high rate capability, and excellent cycling stability.

5.2 Nanostructured anode

In the early period of research, primary lithium batteries have been developed. In this kind of battery, metallic lithium was used as anode, coupling with the cathode material of transition metal oxide or sulfide. However, as the anode materials, metallic lithium suffer from security issue which resulted from formation of dendritic lithium during the process of charge and discharge. The dendritic lithium can lead to cell shorting. After that, it was found graphite with treatment can deliver high reversible capacity at a low oprating potential. In 1991, SONY combined the graphite anode with a $LiCoO_2$ cathode to make the first successful lithium-ion battery, which now dominates the lithium battery marcket. The carbon anode, which forms the compound LiC_6 on reaction with lithium, makes a much safe battery. Up to the present, graphite is still the dominant anode material for lithium-ion battery.

However, the theoretical specific capacity of graphite is 372 mAh/g, which is still much lower than that of metallic lithium (3860 mAh/g). Furthermore, the volumetric energy density of graphite is limited by its inherent low tap density. Thereby, extensive research efforts are focused on seeking for carbon alternatives anode materials with both larger capacities and large density. Such an effort resulted in the find of a number of metal and metal-metalloid materials with large capacity, such as Si, Ge, Bi and Sn. However, these materials always suffer from poor cycle performance due to the large crystal volume expand/contract. Fortunately, nanosturcture provide an effective solution for this drawback. Furthuremore, in recent years, a series of nano-sized transition metal oxides (MO, where M is Co, Ni, Cu or Fe) were proposed to use as anode materials [3]. On the other hand, lithium titanium oxides ($Li_4Ti_5O_{12}$) and titanium oxides (TiO_2), with the Ti^{4+}/Ti^{3+} redox couple working at approximately 1.5 V versus Li/Li^+, were also adopted as anode materials of large-scale lithium-ion battery for EVs [4].

In this section, a series of alternative materials for graphite are described respectively. In particular, the development and merits of these alternative materials in nanoscale are also emphasized.

5.2.1 Nanostructured Si

Si is an alternative of graphite for Li-ion batteries because it has a lager density and the highest known theoretical charge capacity (4200 mAh/g). Although this is more than ten times higher than existing graphite anodes [5], Si anodes have limited applications because volume changes by 400% upon lithium alloying/dealloying. This phenomenon results in electrode disintegration and a loss of electrical contact between particles, and thus leads capacity fading[6]. Fortunately, nanostructured

electrode materials can absorb this large volume expansion/contraction, preserving the integrity of the electrode and leading to stable cycle performance. Based on this strategy, Si-based nanostructures such as nanoparticles, thin films, nanowires, and nanotubes have been studied[7 – 13].

The applications of nanostructured Si-based anode materials indeed enhanced the cycling stability of lithium-ion battery significantly compared with bulk Si. For example, Cho and Cui prepared Si nanotubes by reductive decomposition of a silicon precursor in the alumina template and etching. (Figure 5.2) Their experimental data suggested that the prepared Si nanotubes had very high reversible charge capacity of 3247 mAh/g and also demonstrated superior capacity retention. They also demonstrated the capacity in lithium-ion full cell consisting of cathode $LiCoO_2$ and anode Si nanotube displayed 10 times higher capacity than commercially available graphite even after 200 cycles [7].

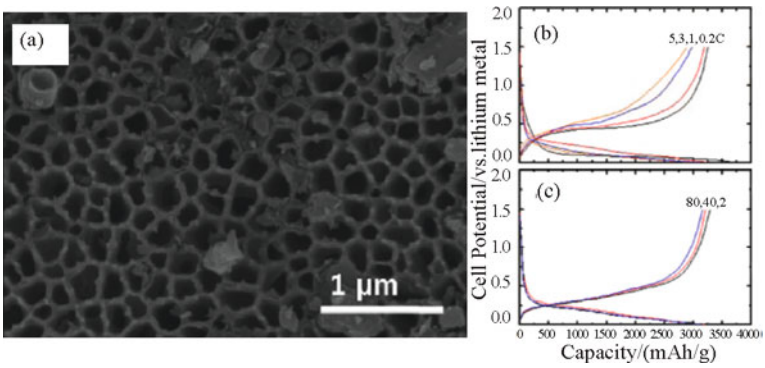

Figure 5.2 (a) SEM image of cycled Si nanotubes. Cells for (b) used a fixed 1C rate during all the discharge cycles and were tested with increasing rates from 0.2C to 5C (15 A/g) during the charge cycles. Cells for (c) were cycled at a rate of 1C between 0 and 1.5 V and voltage profiles were plotted after the 2nd, 40th, and 80th cycles [7]

Si/Carbon composite is also considered as a viable solution to overcome the above issues. It can further provide the buffer layer needed for Si expansion and allow for fast transport of Lithium ions, and carbon will allow the improved solid/electrolyte interface formation, structural integrity and high electrical conductivity. Herein, the Si/Carbon composite is divided into two categories. One is Si/carbon-coating anodes, where Si is coated with carbon layer[14, 15]. For instance, Cho and his co-workers prepared mesoporous Si@carbon core-shell nanowires for a lithium-ion battery anode material. (Figure 5.3) Their results demonstrated that nanostructured Si with carbon coating can achieve both lager capacity and

excellent capacity retention.

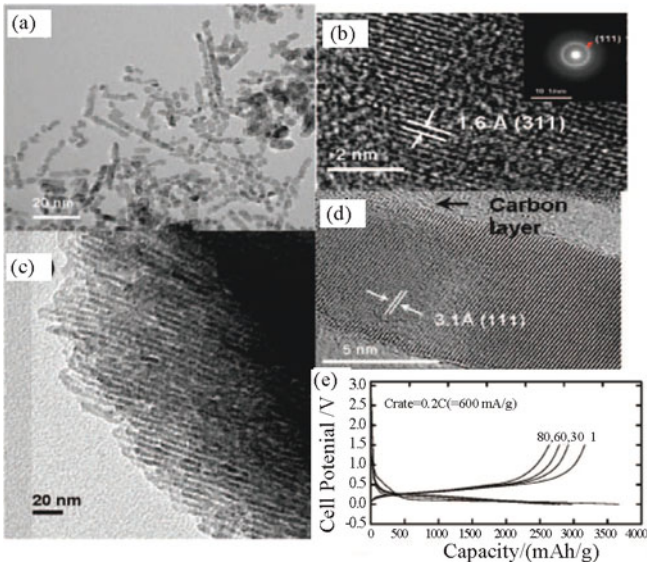

Figure 5.3 (a) TEM image of the Si@carbon core-shell nanorods obtained from first impregnation. (b) Expanded TEM image of (a) (inset is SADP of (b)). (c) TEM image of the Si@carbon core-shell nanowires obtained from fourth impregnation. (d) Expanded TEM image of (c) and (e) Voltage profiles of the Si@carbon core-shell nanowire electrode after 1, 30, 60, and 80 cycles at a rate of 0.2 C between 1.5 and 0 V in coin-type half-cells[14]

(Copyright 2008, American Chemical Society)

The other is Si/carbon-matrix anodes, where Si material is loaded on carbon supporter. The carbon-matrix involves carbon nanotubes, annealed carbon black, carbon nanofibers[16~18]. For example, Cui's group developed a novel design of carbon-silicon core-shell nanowires. (Figure 5.4) Amorphous silicon was loaded onto carbon nanofibers to form a core-shell structure and the resulted core-shell nanowires have a high charge storage capacity of 2000 mAh/g and good cycling life [18]. Several other groups synthesized various kinds of Si/carbon-matrix anodes. They all alleged that carbon has a much smaller capacity compared to silicon, the carbon core experiences less structural stress or damage during lithium cycling and can function as a mechanical support and an efficient electron conducting pathway[16~18] . Actually, other nanostructured materials with high conductivity, such as $TiSi_2$ nanonets, can also be used as the structural support as well as the component to facilitate effective charge transport [19].

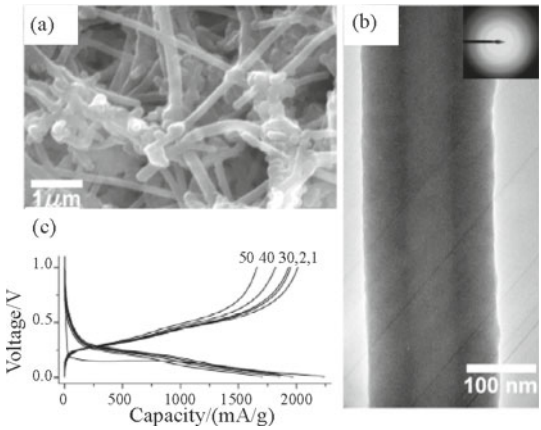

Figure 5.4 (a) SEM image of Si coated CNFs. (b) TEM and SAED images (inset) of a C-Si core-shell NW. (c) Voltage profile of the half cell for Si coated CNFs[18]
(Copyright 2009, American Chemical Society)

5.2.2 Nano-sized transition-metal oxides

Transition-metal oxides were ever considered as cathode in the early period of the development of lithium battery. In 2000, Tarascon JM et al. first demonstrated that nanoparticles of transition-metal oxides (MO, where M is Co, Ni, Cu, or Fe) can be used as anode materials for lithium-ion batteries. The mechanism of Li reactivity differs from the classical Li insertion/deinsertion or Li-alloying processes, and involves the formation and decomposition of Li_2O, accompanying the reduction and oxidation of metal nanoparticles (in the range 1～5 nanometres) respectively. This mechanism can be summarized as following reaction:

$$M_xO_y + 2yLi \rightarrow xM + yLi_2O \quad (5.2)$$

After Morales et al.'s report, the transition-metal oxides (M_xO_y, where M is Co, Ni, Cu or Fe) have attracted extensively attentions [3, 20～22].

Among transition-metal oxide nanostructures, cobalt oxides (Co_xO_y, namely, CoO and Co_3O_4) have received considerable attention due to the high Li-storage capacities about three times larger than those of graphite. However, the large irreversible capacity in the first cycle and poor capacity retention during charge and discharge cycling restrict their practical applications[23～26]. Now, most studies have been focused on their preparation in various forms (e.g., nanotubes, nanowires, nanowalls, thin films and nano composite) in order to enhance their electrochemical performances[25, 27～32]. For example, Chen, C. H. et al. prepared carbon-free CoO-Li_2O composite films with a novel reticular morphology

supported on a conducting nickel-foam substrate which has been prepared by the ESD technique.(Figure 5.5) The initial discharge capacity of a CoO-Li_2O film (Li/Co 1:1) reaches 903 mAh/g with a first-cycle capacity loss of only 16.4%. They believe that the Li_2O component in the composite play a threefold role: as a prohibitor for the CoO particle growth during synthesis, as an oxidizer for the conversion of Co^{2+} to Co^{3+}, and as a structural buffer[33].

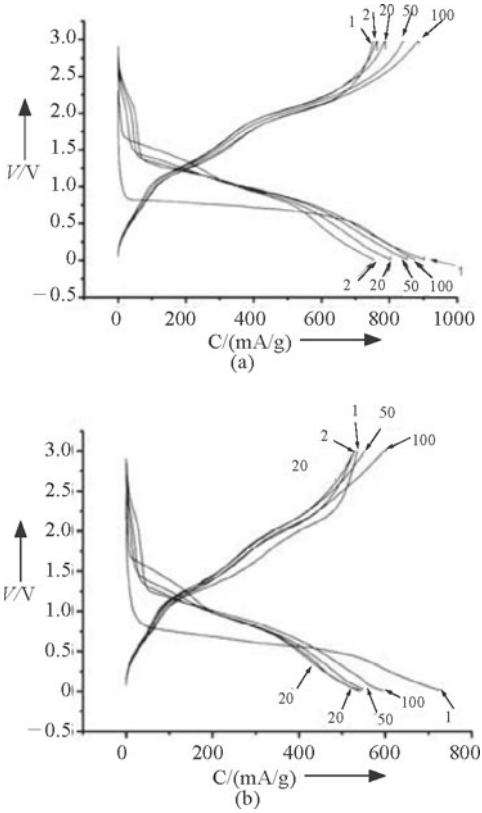

Figure 5.5 The electrochemical performance of the CoO-Li_2O thin-film electrodes cycled between 0.01 V and 3 V vs. Li^+/Li. (a), (b) Plots of the voltage–capacity curves of a reticular (a) and a dense (b)[33] (Copyright 2005, Wiley-VCH)

Besides cobalt oxides anode materials, Fe_2O_3 reacts with six Li per formula unit, exhibiting capacities higher than 1000 mAh/g, through a conversion reaction where the oxide turns into metallic iron and Li_2O nanoparticles. Iron oxides with large particles have been considered too difficult to be used as negative electrode materials for lithium-ion batteries due to their irreversible phase transformation

during the reaction. There have been reports on the effects of particle size on the lithium intercalation reaction with alpha-Fe_2O_3, showing that nano alpha -Fe_2O_3 has better electrochemical performance than micro-sized alpha-Fe_2O_3[34～38]. Chou et al. prepared hollow-structured alpha-Fe_2O_3/carbon (HIOC) nanocomposite with a high surface area by a one-step[37]. As seen in Figure 5.6, their experimental data showed the improved electrochemical performance in terms of high capacity (1210 mAh/g at 0.1 C), enhanced rate capability and excellent cycle stability with 720 mAh/g～at 2 C up to 220 cycles. They ascribed the high performance to the novel high-surface-area carbon composite structure which can facilitate the contact between active materials and the electrolyte, enhance lithium and electron transport, and accommodate the volume change.

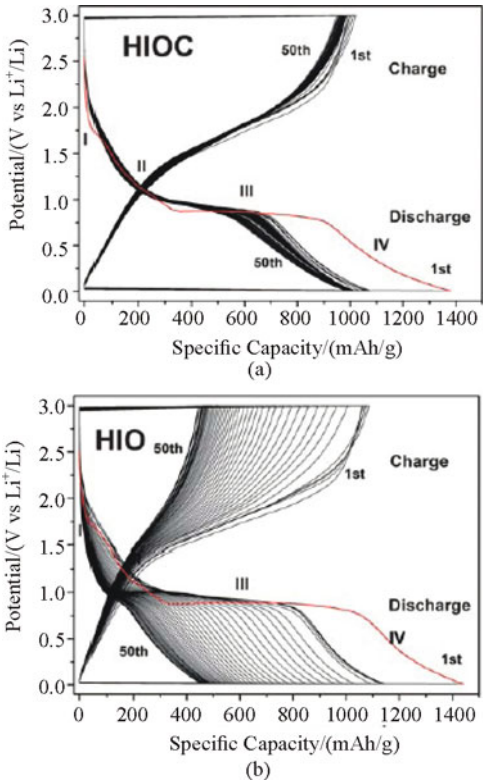

Figure 5.6 Typical charge-discharge curves of HIOC nanocomposite electrode (a) and HIO electrode (b). The current densities were 50 mAh/g (0.05 C) for the first five cycles and 100 mAh/g (0.1 C) for the following cycles[37]

In addition to cobalt oxides and iron oxide, cupper oxides were also widely studied as the anode materials for lithium-ion batteries. To improve the coulombic efficiency and cycling life, nanostructured CuO with various morphology and structures and CuO based composites have been widely investigated. Such as film [39], spheres [40~42], nanotubes [43, 44], nanoribbons [45], nanowires [46]. Zheng et al. developed a simple solution method for large-scale synthesis of self-assembled CuO-CNT nanomicrospheres. (Figure 5.7) The results show that the capacity retention and rate capability of the CuO-CNT composite are significantly improved. They believe the 3D network of CNTs acts as not only a 3D current collector network for both CuO nanomicrospheres and CuO nanoplates in individual sphere, but also as an elastic buffer to relieve the strain during Li uptake-release [42].

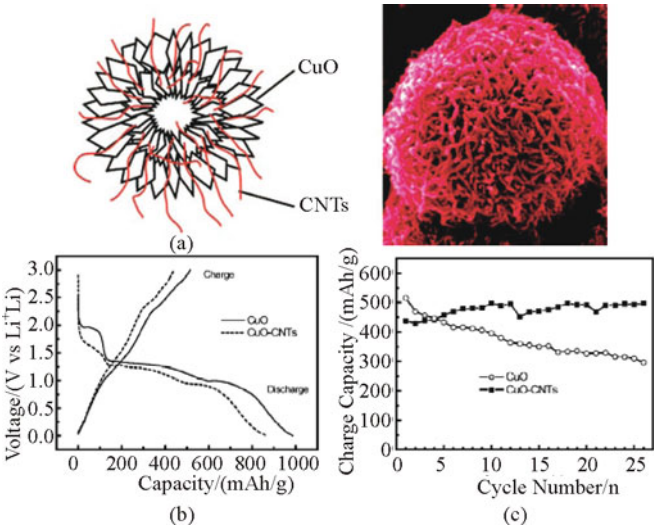

Figure 5.7 (a) Schematic illustration and SEM image of CuO-CNT nanomicrosphere. (b) Initial charge-discharge voltage profiles of Cu and CuO-CNT nanomicrospheres at a rate of C/10. (c) Variation of charge capacity versus cycle number for Cu and CuO-CNT nanomicrospheres at a rate of C/10 [42] (Copyright 2008, American Chemical Society)

5.2.3 Nanostructured Sn alloy and oxide

Metallic Tin (Sn) deserves special attention as they offer a promising alternative to carbon as a anode material due to its high theoretical capacity of 994 mAh/g and inherent high density. However, the volume variation on lithium alloying/dealloying much limits the cycle performance of Sn anode, which is similar with Si anode. In order to overcome this problem, an effective strategy is to

prepare composite compounds (M1M2) which consist of an inactive phase M1 that does not react with lithium, an active phase M2 that reacts with lithium. Carbon matrix can be adopted as component M1 acting as an inactive confining buffer. Kim et al. first report a Sn-C composite that can enhance the electrochemical property of Sn electrode [47]. However, contained Sn particles of 200 nm, these probably are too large a size to assure full mechanical integrity and a long cycle life. Scrosati, B. and his co-workers synthesized nanostructured Sn-C composite formed by tin particles of on average 30 nm size embedded in a carbon matrix. (Figure 5.8). Their results show that the Sn-C composite electrode can operate in a lithium cell at constant capacity levels as high as 500 mAh/g for several hundreds of cycles and that it can be cycled at rates exceeding 5 C still recovering 40% of its total capacity [48].

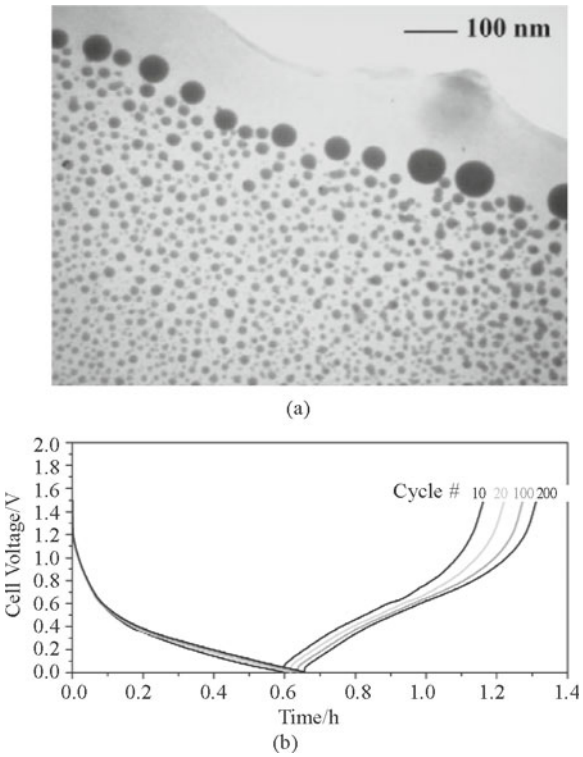

Figure 5.8 (a) TEM image of a Sn-C composite material. (b) Voltage profiles at a 0.8 C rate of a Sn-C composite electrode in an electrochemical cell having lithium metal as a counter electrode and a LiPF6-EC:DMC electrolyte[48]

On the other hand, metal that does not act with lithium also can be employed as an electrochemically inactive matrix to buffer the volume variation during the lithium alloying/dealloying process. This strategy has attracted more attention and a series of tin-based intermetallics electrode have been proposed, such as Cu_6Sn_5 [49], SnSb [50], CoSn [51], Cu_2Sb [52], SnMn [53], Sn-Fe [54], Ni_3Sn_4 [55]. In 2009, Xia and his co-work proposed a strategy combining both intermetallics and carbon to improve the cycling life of Sn-based electrode. (Figure 5.9) They prepared a core-shell-structure nanoscale Cu_6Sn_5–carbon composite. Their data shows a low initial coulombic efficiency, but exhibits an excellent electrochemical performance with a reversible capacity of 437 mAh/g and no obvious fading after 50 cycles. The improvement in the cycling stability could be attributed to the fact that the well-coated carbon layer can effectively prevent aggregation and pulverization of nano-sized Cu_6Sn_5 alloy particles during charge/discharge cycling [56].

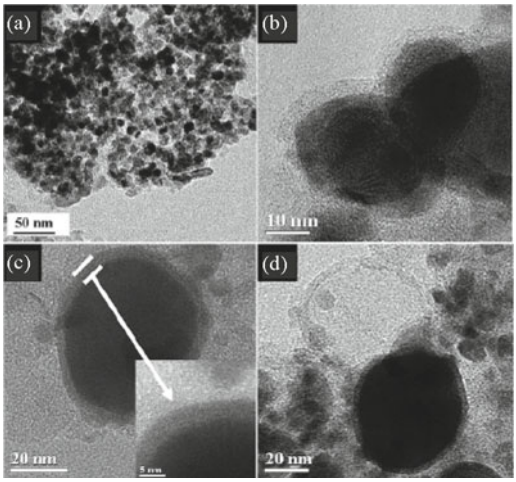

Figure 5.9 TEM images of a final product, core–shell carbon-coated nanosizedCu_6Sn_5. Inset in (c) is an HRTEM image of the carbon layer [56]
(Copyright 2009, RCS Publishing)

Besides description above, metalloid Si also can be introduced to form Sn-based intermetallics. Kwon and his co-workers proposed $Sn_{0.9}Si_{0.1}$ core/carbon shell nanoparticles showed excellent initial capacity and capacity retention up to 50 cycles [57]. The carbon shell acts as a buffer layer to prevent the aggregation between nanoparticles(Figure 5.10).

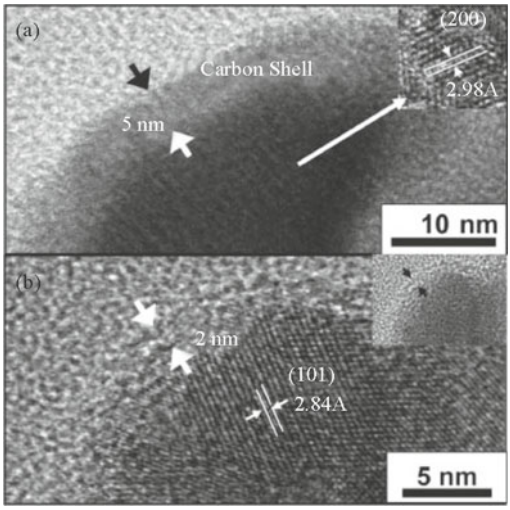

Figure 5.10 Magnified high-resolution TEM images of $Sn_{0.9}Si_{0.1}$ core/carbon shell nanoparticles [57] (Copyright 2007, American Chemical Society)

In addition to these tin based anode materials mentioned above, Ti oxide (SnO_2) is also considered as a promising anode material because of high theoretical capacity. In theory, the discharge process of SnO_2 anode includes a conversion reaction and lithium alloying reaction. These can be summarized as following:

$$SnO_2 + 4Li^+ + 4e^- \rightarrow Sn + 2Li_2O \text{ (conversion reaction)} \quad (5.3)$$

$$Sn + xLi^+ + xe^- \rightarrow Li_xSn \quad \text{(alloying reaction)} \quad (5.4)$$

Charge process of SnO_2 reverses the discharge. Although the combination of conversion reaction and lithium alloying/dealloyging reaction lead the high theoretical capacity, SnO_2 anode still suffers from large initial irreversible capacity and poor cycle performance. The large initial irreversible capacity is often ascribed to the irreversible reaction that forms Li_2O at conversion reaction. The poor capacity retention found in SnO_2 has been widely speculated to arise from the large volume changes in the electrode materials created by lithium alloying/dealloying process. Accordingly, multifarious SnO_2 nanostructures, such as nanoparticles (0D), nanowires and nanorods (1D), and 3D hollow and core/ shell structures, have been developed. Some of these nanostructures also showed enhanced reversible capacities in lithium ion batteries [58~61]. Yin and his co-workers reported a simple template-free route to prepare hierarchical SnO_2 nanostructures with hollow interiors [62]. (Figure 5.11) These high porous architectures, with the diameter about 200 nm, were assembled by nanosheets. Their electrochemical results showed that

the sample exhibited both high capacity and excellent cyclability, when utilized as the negative electrode for lithium ion batteries.

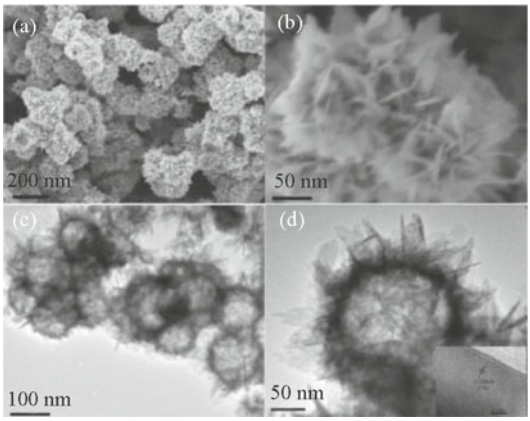

Figure 5.11 (a) SEM image of the hierarchical SnO_2. (b) Magnified image of the structure. (c) TEM image of the hierarchical SnO_2. (d) Magnified TEM image of the structure with HRTEM in the inset [62] (Copyright 2010, American Chemical Society)

Besides optimizing the nanostructure of anode materials, it has also been suggested that carbon coating can improve the cycling performance of noncarbonaceous anode materials [63 ~ 65]. It is hypothesized that the carbon coating layer plays an important role as structural buffering layer to mitigate the mechanical stress caused by large volume change. For example, Lou and his co-works synthesized nearly monodisperse carbon-coated SnO_2 nanocolloids in gram scale by a simple hydrothermal method followed by carbonization [66] (Figure 5.12). Their result clearly demonstrated that carbon nanocoating can be an effective way for improving cycling performance compared to SnO_2 nanospheres.

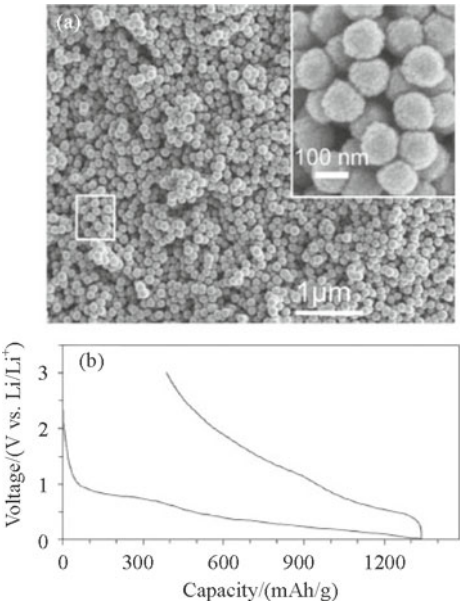

Figure 5.12 (a) Carbon-coated SnO_2 nanocolloids obtained after carbonization of particles. inset is a magnified FESEM image from the area indicated by rectangle. (b) First-cycle discharge-charge voltage profile of carbon-coated SnO_2 nanocolloids[66]
(Copyright 2009, American Chemical Society)

5.2.4 Nanostructured lithium titanium oxides and titanium oxides

Recently, lithium-ion battery technologies have been progressing in terms of power, safety, life, light weight and compactness for large-scale applications such as hybrid electric vehicles (HEVs), pure electric vehicles (EVs), and clean energy storage. An increase in the charge/discharge rate of lithium-ion batteries of more than one order of magnitude is required to meet the demands of future EVs and clean energy storage. One of the safety issues in present lithium-ion batteries would arise from the dendritic lithium growth on the anode surface at over charge process, which is owing to that the Li-insertion potential of conventional graphite anode is less than 100 mV vs. Li/Li^+. A fundamental solution is replacement of carbon materials by other materials with higher Li-insertion potential. Thereby, spinel $Li_4Ti_5O_{12}$ (denoted as LTO) has been considered as one of promising alternative materials to carbon anodes because its Li-insertion process operates at about 1.5 V (vs. Li/Li^+), providing an electrode system with much better safety characteristics. Furthermore, spinel $Li_4Ti_5O_{12}$ shows a very small volume variation during the charge-discharge process, consequently resulting in excellent cycle

stability [4]. Last but not least, the 2 V class Li-ion battery system in an average voltage range of 2.2 to 2.5 V with a combination of the LTO anode and some 4 V class cathodes such as $LiCoO_2$, $LiNi1/3Mn_1/3Co_1/3O_2$, and $LiMn_2O_4$ is a very promising candidate for HEVs, EVs, and industrial applications [67–69].

However, because of the low conductivity of this material, $Li_4Ti_5O_{12}$ has a poor rate electrochemical performance, which needs to be overcome before its realization for practical applications. To enhance the rate performance, various nanostructures of $Li_4Ti_5O_{12}$ were synthesized and displayed an improved rate electrochemical performance resulting from the shorter diffusion distances for Li-ion and electron [70]. For example, Li et al. have shown improved performance with one-dimensional (1D) LTO nanostructures, namely, nanotubes/nanowires synthesized by hydrothermal method [71]. Tang et al. have reported nanosheets of flower like LTO synthesized by a hydrothermal route in the presence of glycol solution that delivers high capacity even at very high charge-discharge rates [72]. Sorensen et al. have reported 3D-ordered macroporous LTO with thin wall thickness which could deliver excellent high-rate capacities [73]. Jiang have reported the synthesis of hollow spheres of LTO by a sol-gel method using carbon spheres as templates that exhibit high-rate performance [74].

Recently, nanostructure combining with surface carbon coating was employed to further improve the performance of $Li_4Ti_5O_{12}$. Wang et al. introduced a facile method to prepare $Li_4Ti_5O_{12}$, through which both tailored particle size and double surface conductive surface modification based on Ti(III) and carbon can be achieved simultaneously.(Figure 5.13) In this method, polyaniline (PANI) coated TiO_2 particles and a lithium salt were used as precursors to prepare $Li_4Ti_5O_{12}$. The carbonization of PANI not only effectively restricted the particle-size growth of $Li_4Ti_5O_{12}$, but also reduced the surface Ti(III) into Ti(III). The surface modification combined with tailored particle size can improve the surface conductivity, shorten the Li-ion diffusion path and increase the equilibrium solid solution that is beneficial for lithium-ion mobility [75].

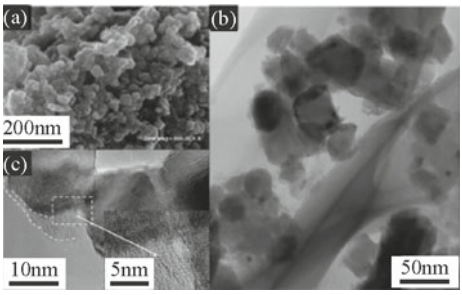

Figure 5.13 Characterization of the prepared $Li_4Ti_5O_{12}$-carbon composite: (a) SEM image. (b), (c) TEM images with different magnifications [75]

Cheng et al. paid continuous attention to improve the electrochemical property of $Li_4Ti_5O_{12}$. They prepared carbon coating bulk $Li_4Ti_5O_{12}$ electrode through a CVD process [76] and proposed a simple approach to synthesize nanostructured $Li_4Ti_5O_{12}$ spinel materials with different morphologies (nanorods, hollow spheres and nanoparticles), in which the TiO_2 precursor is first coated with a conductive carbon layer by the chemical vapor decomposition (CVD) method [77]. Their results indicate that, by employing the carbon pre-coating process, the carbon-coated nanostructured $Li_4Ti_5O_{12}$ can maintain the initial morphologies of the TiO_2 precursors and also show significant improvement in the rate capability for lithium-ion intercalation due to both good electronic conductivity and the short lithium-ion diffusion path. (Figure 5.14)

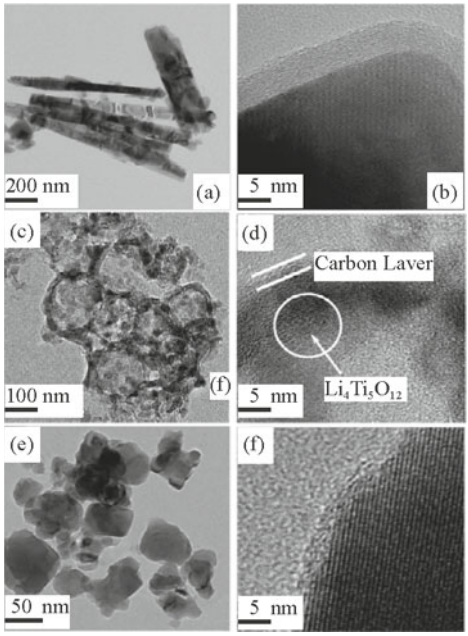

Figure 5.14 TEM images of carbon-coated $Li_4Ti_5O_{12}$ with various morphology: (a),(b) $Li_4Ti_5O_{12}$ nanorod materials. (c),(d) $Li_4Ti_5O_{12}$ hollow spheres. (e),(f) $Li_4Ti_5O_{12}$ nanoparticles[77]
(Copyright 2009, RCS Publishing)

Besides the carbon-coating method, thermal nitridation also was adopted to modify $Li_4Ti_5O_{12}$ to make it electronically more conductive. The author believed that the mixed-valent intermediate phase, $Li_{4+\delta}Ti_5O_{12}$, and the TiN layer may fully trigger the electrochemical reactions, thus the rate capability was enhanced [78].

TiO_2 polymorphs have also received significant attention as possible

materials to replace graphite due to its advantages that are similar with $Li_4Ti_5O_{12}$. In principle, TiO_2 electrodes would offer about twice capacity of $Li_4Ti_5O_{12}$ if they could be discharged to the rock salt composition $LiTiO_2$, at which all the titanium ions would be trivalent (335 mAh/g). Among various TiO_2 polymorphs, rutile, anatase, brookite and TiO_2(B) are considered as the most efficient materials. Lithium insertion into bulk TiO_2 is difficult because transport is very slow in the ab-planes, restricting Lithium ions from easily reaching the thermodynamically favorable octahedral sites and limiting Li in the c-channels. Furthermore, repulsive Li-Li interactions in c-channels together with trapped lithium-ion pairs in the ab-planes may block the c-channels and restrict insertion well below its theoretical limit [79]. The capacity stability and improved rate capability can be achieved by the use of nanostructured titania materials. Nanostructured TiO_2 with Various morphology have been synthesized, such as nanoparticles [80], nanowires [81~83], Mesoporous [84, 85], nanotubes [86], nanofilm [87] and nanonet [88].

These nanomaterials have attracted significant attention in the energy storage and conversion field owing to their specific features that enhance the electrochemical activity so that full lithium ion reversibility can be achieved. Nevertheless, in addition to low volumetric energy density, the need for the large-scale production of nanomaterials can be argued to be disadvantageous for lithium-ion batteries. Recently, in order to circumvent above problems, nanodomains of $Li_4Ti_5O_1$ [89] or TiO_2 embedded in large micrometer-size particles have been proposed [90, 91]. For instance, Amine et al. prepared a new LTO structure with higher packing density: micron-size (0.5～2 μ m) secondary particles composed of nanometer-size (<10 nm) primary particles (MSNP-LTO). (Figure 5.15) This synthesized MSNP-LTO materials shows perfect electrochemical performance.

Pol and his co-workers reported an anhydrous autogenic technique for synthesizing electronically interconnected, carbonencapsulated, nanoparticulate anatase anode materials (TiO_2-C) for lithium-ion batteries [91]. (Figure 5.16) The TiO_2-C nanoparticles forming oval- and spherical-shaped secondary particles provide a reversible capacity of ~200mAh/g, which exceeds the theoretical capacity of the commercially attractive spinel anode, $Li_4Ti_5O_{12}$ (175mAh/g) and is competitive with the capacity reported for other TiO_2 products.

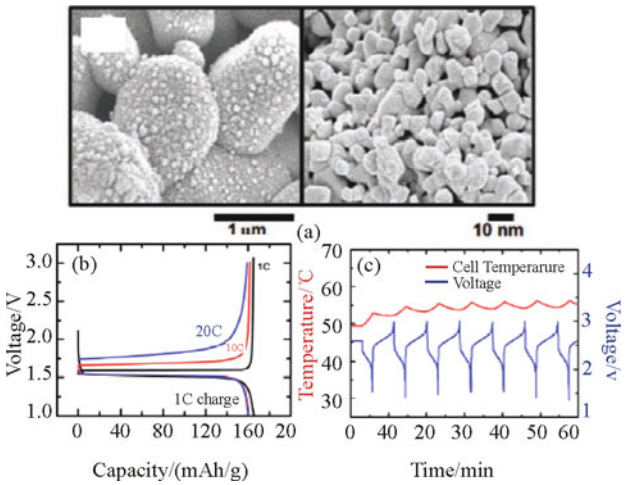

Figure 5.15 (a) Scanning electron microscopy under low and high magnification of MSNP-LTO, showing secondary and primary particles. (b) Charge and discharge curves of micronsize MSNP-LTO. (c) Cell skin temperature change during 10-C charge and 20-C discharge of MSNP-LTO/LMO cells[89]

(Copyright 2010, Wiley-VCH)

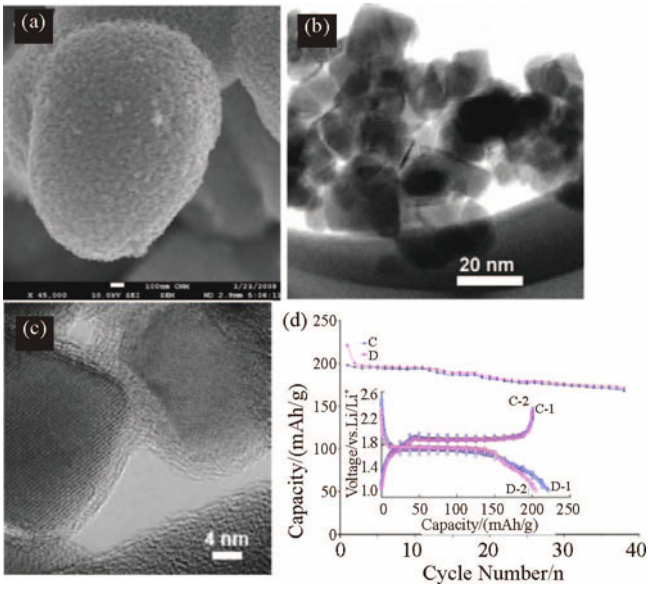

Figure 5.16 (a) Field emission scanning electron microscope images of TiO_2-C. (b),(c) high-resolution TEM of TiO_2-C at different magnifications. (d) Cycling behavior of Li/TiO_2-C half cells (1.1-2.5 V, 16.3 mA/g, C/17 rate) [91]

(Copyright 2010, Elsevier)

5.3 Nanostructured cathode

Since the idea of a rechargeable lithium battery based Li intercalation reactions was initiated in the early 1970s, numerous lithium intercalation electrodes have been proposed to date [92]. The earliest configuration of rechargeable lithium batteries used metallic lithium or Li-Al alloys as the negative electrode, with a variety of chalcogenides (TiS_2, MoS_2, etc.), as the positive electrode in several prototypes and commercial products [93, 94]. Later, manganese and vanadium oxides were utilized as cathode materials for rechargeable lithium batteries. However, the combination between oxide cathode and metallic anode was ultimately rejected because dendrite growth on the metal surface after repeated Li plating that led to internal short circuits. In 1980, Mizushima et al. recognized that $LiCoO_2$ had a structure similar to the layered structures of the dichalcogenides and showed that the lithium could be removed electrochemically, thus making it a viable cathode material [95]. Until 1991, SONY combined the $LiCoO_2$ cathode with a carbon anode to make the first successful lithium-ion battery, which now dominates the lithium battery market. The commercial Graphite-$LiCoO_2$ battery is built in the discharged state. It thus must be charged before use. The theoretical capacity of the $LiCoO_2$ cell is relatively low at around 130 mAh/g because only around 0.5 Li/Co can be reversibly cycled without causing cell capacity loss due to changes in the $LiCoO_2$ structure [94]. In these years, Layered lithium transition metal oxides arguably represent the most successful category of cathode, comprising compounds with formula of $LiMO_2$ (M: Co, Mn, and Ni) that crystallize in a layered structure. Besides these layered lithium transition metal oxides, spinel lithium intercalation compounds, the spinel cathode $LiMn_2O_4$, originally proposed by Thackeray et al. in 1983, also attracted much attention as the cathodes of high-power lithium-ion batteries for HEVs and EVs [94, 96]. On the other hand, considerable interest in a new class of transition metal phosphate materials was sparked by the introduction of $LiFePO_4$ as a cathode material about 10 years ago [97]. Details on the cathode materials for lithium-ion battery has been reviewed by Whittingham in 2004 [94]. In this section, we mainly summarize the recent development of nanostructured cathode materials for rechargeable lithium-ion battery.

5.3.1 Nanostructured metal oxides

5.3.1.1 Nanostructured vanadium oxides

Vanadium pentoxide,V_2O_5, has been investigated for 30 years[98]; it has a layered structure with weak vanadium-oxygen bonds between the layers and is now known to react by an intercalation mechanism [94, 98]: $xLi + V_2O_5 = Li_xV_2O_5$.

During the past years, vanadium pentoxide and its derivatives have attracted wide attention. For Li-ion intercalation applications, vanadium oxides offer the essential advantages of low cost, an abundant source, easy synthesis, and high energy densities.

In recent years, Nanostructured V_xO_y materials with ultrahigh surface area have been reported with much enhanced capacity. As reported by Sudant et al [99], nanofiber-like V_2O_5 aerogels with a surface area higher than 100 m^2/g can exhibit a large capacity near 400 mAh/g and allow high rates of discharge. And their derivative nanotextured VO_2 (B) aerogels even delivered a higher capacity over 500 mAh/g [100]. In view of the large surface area of this nanotextured VO_2 (B) (185 m^2/g), it is reasonable to assume that the surface/near surface storage might play an important role in such a large capacity. Other 1-dimentional (1D) nanostructures such as nanowires [101, 102], nanorods [103, 104] , nanobelts [105] have been well documented for vanadium-based cathode materials. Lee and Cao reported the synthesis and electrochemical properties of V_2O_5 films with nanosized features[106]. In their report, platelet- and fibrillar-structured V_2O_5 films were prepared by solution methods, and the discharge capacities and cyclic performance of these films were compared with those of the conventional plain structured film. The initial discharge capacities of platelet and fibrillar structured V_2O_5 films are1240 and 720mAh/g, respectively, which are far larger than the initial discharge value (260mAh/ g) of the conventional plain-structure film. They believe that such large discharge capacity values are ascribed to the combined effects of the reduced Li^+ diffusion distance, which prevents concentration polarization of Li^+ in the V_2O_5 electrode and poor interlayered cross-linking offering more Li^+ intercalation. However, platelet- and fibrillar-structured V_2O_5 films were easily degraded during electrochemical cyclic tests.

In addition to 1D nanostructures mentioned moved, 3D nano/micro hierarchical structures are more attractive since they can combine both the advantages of nano and micro. The nanometer-sized building blocks of the hierarchical structure can provide short lithium-ion diffusion lengths, additional surface storage and possible new Li storage mechanisms, thus are favorable for electrode kinetics and high capacities; while the micro-assemblies guarantee good stability and easy of fabrication[94]. Recently, Liu et al. developed a nanothron VO_2 (B) hollow microsphere by a facile one-step hydrothermal method [107] . As shown in Figure 5.17 , the hollow microspheres about 1 μm in diameter were self-assembled by well-defined VO_2(B) nanothorn single-crystals (10 nm in width and several tens nanometers in length) growing

perpendicularly onto the sphere surface. When used as the cathode material for a lithium-ion battery, this VO_2 (B) material can provide inner and outer wall surface of contact sites between electrode material and electrolyte, porous tunnels for electrolyte penetrating, short lithium diffusion length within the tiny nanothrons, and 3D rigid structure to prevent the nanothrons from agglomeration. A large discharge capacity of 450 mAh/g can be obtained at the current density of 10 mA/g. Similarly, improved Li storage properties have also been found by Cao et al. for V_2O_5 by fabricating hollow microspheres with uniform hedgehog-like morphology [108].

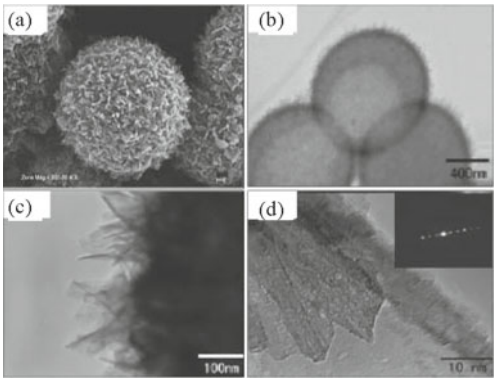

Figure 5.17 Panoramic SEM graph (a) and TEM graph (b) of the synthesized nanothorn VO_2 (B) hollow microspheres by hydrothermal method. details of the hollow sphere surface (c) and individual nanothron building block (d) by TEM at high magnitude[107]
(Copyright 2009, RCS Publishing)

5.3.1.2 Nanostructured manganese oxides

Manganese dioxide (MnO_2) has been largely studied for use as cathode materials for Li primary and secondary batteries due to its low cost, environmental merit and easy preparation [109, 110]. MnO_2 exists in various forms (with tunnels, layers, and spinel structures) when the structural units (MnO_6 octahedra) are linked in different ways [109, 111]. The crystallographic structure and morphology strongly affect its electrode performance since intercalation or extraction of lithium-ion into or from MnO_2 lattice determines the kinetics of electrode reaction [109 ~ 112].

In recent years, nanostructured MnO_2 of different crystallographic types and morphologies has been synthesized through solution routes and investigated as lithium-ion battery cathode materials [113 ~ 116]. To evaluate the influence of crystal structure and morphology on electrochemical properties, Cheng et al. prepared α,βand γ-MnO_2 nanowires by simple hydrothermal treatment of Mn(II) species

without any template [114], and compared their electrochemical performance as the cathode materials for lithium battery (Figure 5.18). Their results clearly show that electrochemical performance of nanostructures is superior to that of comparative bulk form. For instance, the γ-MnO_2 nanowires deliver a high discharge capacity of 210 mAh/g which is much higher than the achieved capacity (180 mAh/g) of the bulk γ-MnO_2 (Figure 5.18).

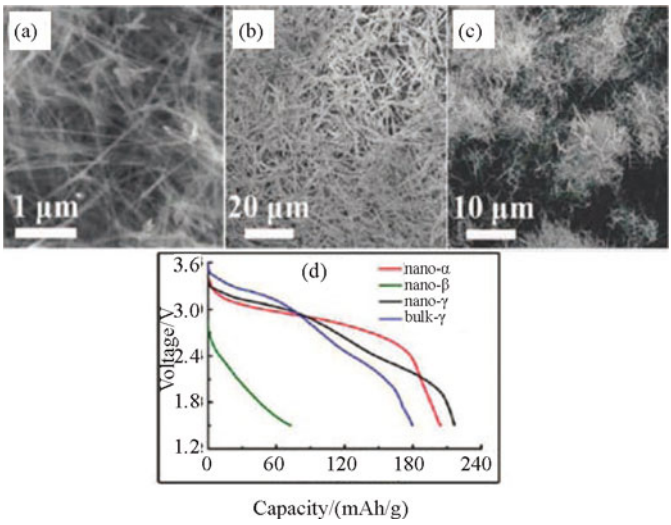

Figure 5.18 SEM images of nanowires of α-MnO_2 (a), β-MnO_2 (b) and γ-MnO_2 (c). the discharge curves of bulk and nanosructured MnO_2 in Li-Mn battery[114]
(Copyright 2006, American Chemical Society)

Furthermore, in their report, β-MnO_2 nanowires display poor electrochemical performance in term of low capacity and potential, while γ-MnO_2 or α-MnO_2 nanowires demonstrate favorable electrochemical performance. Among the three phases, β-MnO_2 possesses only narrow (1× 1) tunnels, which unfavorable for lithium-ion diffusion; whereas the large (1× 2) or (2×2) tunnels present in γ-MnO_2 or α-MnO_2 favor the insertion and transfer of ions in the lattice framework, leading to the high activity [109, 112]. A recent work by Xia and his co-workers reported a highly electrochemical reaction of lithium in the template-prepared mesoporous β-MnO_2, which has been generally believed to exhibit poor electrode performance due to the highly crystallinity and crystal structure with narrow channels [117]. In their report, the ordered mesoporous β-MnO_2 was successfully synthesized using mesoporous silica KIT-6 as a template (Figure 5.19). Electrochemical measurements showed that the as-prepared ordered mesoporous β-MnO_2

electrode exhibits high initial capacity, excellent high rate discharge performance,

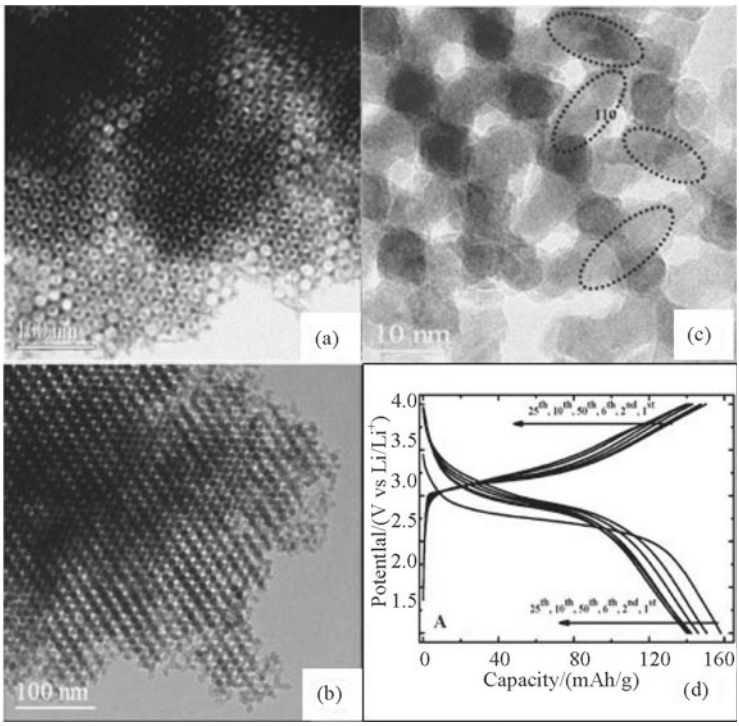

Figure 5.19 TEM image of mesoporous β-MnO_2 viewed down the (a) [111] and (b) [210] Zone axis. (c) high-resolution TEM image of mesoporous β-MnO_2 viewed from [210] direction. (d) Charge and discharge profiles of mesoporous β-MnO_2 for the 1st, 2nd, 6th, 10th, 25th, and 50th cycles at a current rate of 0.4 mA/cm^2 [117]

(Copyright 2006, American Chemical Society)

and supreme cycling reversibility. The designed mesoporous structure can provide larger specific surface area leading to higher current density and a thin pore wall reducing the lithium ion diffusion path. In addition, the mesoporous structure facilitates the fast transport of electrolyte with lithium ion and can also act as a buffer layer to alleviate the volume expansion of the electrode materials during lithiation/delithiation. Therefore, the ordered mesoporous β-MnO_2 can be a promising cathode material in rechargeable lithium-ion batteries. The significantly enhanced electrochemical performance of templated mesoporous β-MnO_2 over the bulk crystalline counterparts has been confirmed by Jiao and Bruce [118]. On the basis of their report, the template-directed β-MnO_2 with a highly ordered pore structure and highly crystalline walls can accommodate reversibly a large amount

of Li (Li: Mn = 0.92:1) on intercalation, with more than 80% capacity retention after cycling at a high rate of 300 mA/g for 50 cycles.

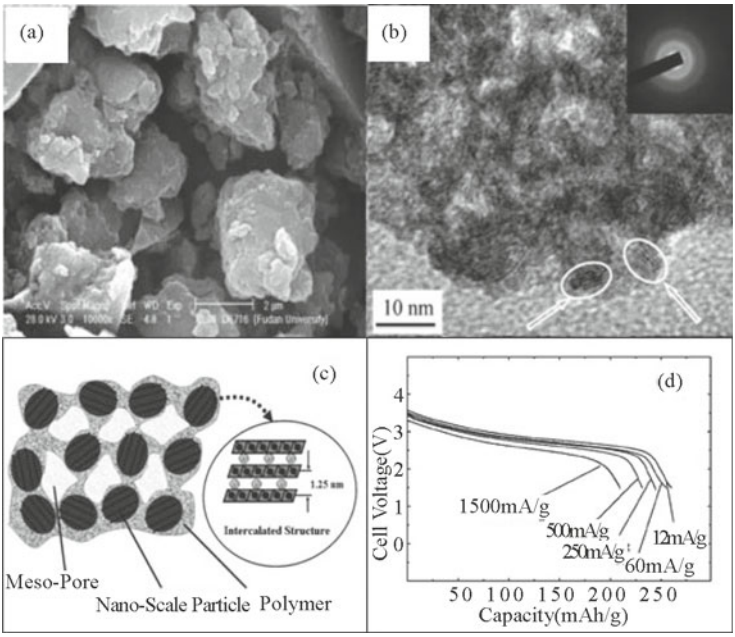

Figure 5.20 SEM image (a) and TEM image (b) of prepared intercalated layered MnO_2;(c)Schematic structure of the prepared intercalated layered MnO_2;(d)discharge curves of the prepared intercalated layered MnO_2 at different current densities [119]
(Copyright 2008, Wiley-VCH)

In addition to α,γ,β-MnO_2, layered manganese oxides have also received increasing attention as cathode materials used in lithium-ion batteries. Recently, Wang et al. developed a facile method to prepare polyaniline (PANI)-intercalated layered manganese oxides, and reported its primary performance as the cathode material for lithium battery [119]. In their preparation process, the PANI was in-situ intercalated into the layered manganese oxide at an aqueous/ organic interface in which the aniline was dissolved in an organic solvent (CCl4) and the oxidant, potassium permanganate, was dissolved in an aqueous solution (pH 7). The chemical oxidation polymerization of aniline occurred at the aqueous/organic interface. At the same time the oxidant, MnO_4^-, was reduced to form a manganese oxide precipitate. By continuous diffusion of aniline from the organic to the aqueous solution, layer-by-layer assembly of the layered manganese oxide and polymer is realized. As shown in Figure 5.20, the prepared composite has five novel characteristics: swelled

layered structure, a uniform mesoporous structure, typical nanosize, a high surface area, and a crystalline phase coated by amorphous phase, which suggest its possible use as an electrode with both high power and high energy densities. The swelled layered structure can improve the diffusion rate of lithium ions within the bulk of the prepared materials; the nanoscale size (5～10 nm) can greatly reduce the diffusion length over which the lithium ions must transfer during the discharge process; the 4 nm uniform mesoporous structure can be filled with electrolyte solution during use to provide electrolyte and lithium ion pathways throughout the material; the amorphous polymer coating on the outer surface of the intercalated composite can provide a buffer layer at high discharge rate. In addition, the high surface area of the prepared materials can reduce the effective specific current density. The electrochemical measurement also demonstrated that the prepared polymer-intercalated layered manganese oxide processes both high power and high energy density.

5.3.2 Lithium transition metal oxides

The most common cathode active materials that are being researched and commercially used in lithium ion batteries are the lithium transition metal oxides such as $LiCoO_2$, $LiNiO_2$, $LiMn_2O_4$, and the doped counterparts [94, 120～122]. It is well known that the rate-determining step in the electrodes of lithium ion batteries is supposed to be a solid state diffusion. To improve the intercalation-deintercalation kinetics of the material, it is necessary to downsize the material to achieve short diffusion distance and large surface area.

There have been several recent reports on the synthesis and electrochemical properties of nanostructured lithium metal oxides. For example, Li et al.[122] successfully prepared $LiCoO_2$, $LiNi_{0.8}Co_{0.2}O_2$, and $LiMn_2O_4$ nanotubes by thermal decomposition of sol-gel precursors within the template of porous anodic aluminum oxide (Figure 5.21), and reported their high electrochemical performance as the cathode materials for lithium-ion battery. They believe the thickness of the tubes (20～30 nm) is much less than the radii of the corresponding commercial spheres or nanocrytallines, resulting in a higher diffusion rate and significantly faster electronic kinetics. Furthermore, the high specific surface areas of hollow tubular structures offer more active positions for lithium ion

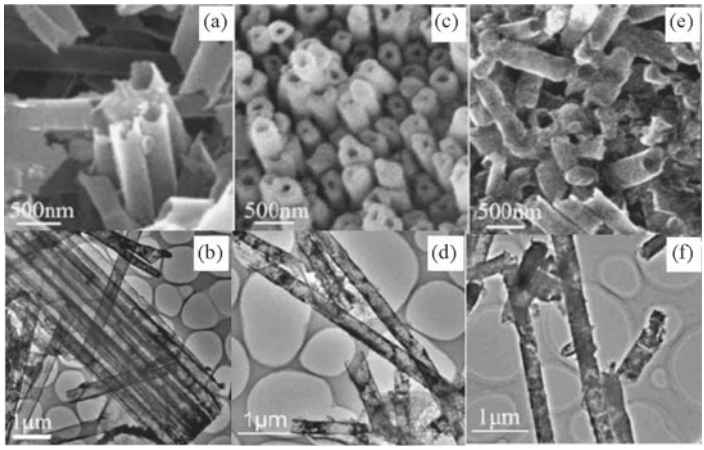

Figure 5.21 SEM images of nanotubes of (a) $LiCoO_2$, (c) $LiNi_{0.8}Co_{0.2}O_2$ and (e) $LiMn_2O_4$. TEM images of nanotubes of (b) $LiCoO_2$, (d) $LiNi_{0.8}Co_{0.2}O_2$ and (f) $LiMn_2O_4$ [122]
(Copyright 2005, American Chemical Society)

intercalating/deintercalating and lower the real current density. In addition to this template method, Bruce and his collaborators reported the synthesis of mesoporous low-temperature $LiCoO_2$ by a post-templating reaction [123]. In their synthesis process, mesoporous Co_3O_4 was first prepared with hard template of SBA-15 or KIT-6, and then the prepared Co_3O_4 was coupled with LiOH to form mesoporous $LiCoO_2$ after template removal. By using this method, mesoporous $LiCoO_2$ was obtained, maintaining the nanostructured morphology of Co_3O_4. Preliminary electrochemical data indicated that the nanostructurd $LiCoO_2$ exhibited remarkably less fade in discharge capacity on cycling as compared to normal low-temperature $LiCoO_2$. Herein, it should be noted that it is impracticable to mass produce nanostructured cathode materials with hard temperature in commercial use. Recently, Luo et al. reported a solf-chemical route for the synthesis of nanostrcutured spinel $LiMn_2O_4$ [124～126]. In their report, several spinel $LiMn_2O_4$ with different nanostructures have been successfully prepared by annealing the lithiated MnO_2 with various morphologies, in which the lithiated MnO_2 was obtained by the chemical lithiation of LiI with MnO_2. For instance, they successfully synthesized $LiMn_2O_4$ nanorods, nanothorn microshperes, and hollow nanospheres as enhanced cathode materials of lithium ion battery. In their method, MnO_2 nanorods, nanothorn microshperes and hollow nanospheres were first prepared by template free self-assembly process (Figure 5.22). Then, after the chemical lithiation of LiI with prepared MnO_2, the lithiated MnO_2 nanorods,

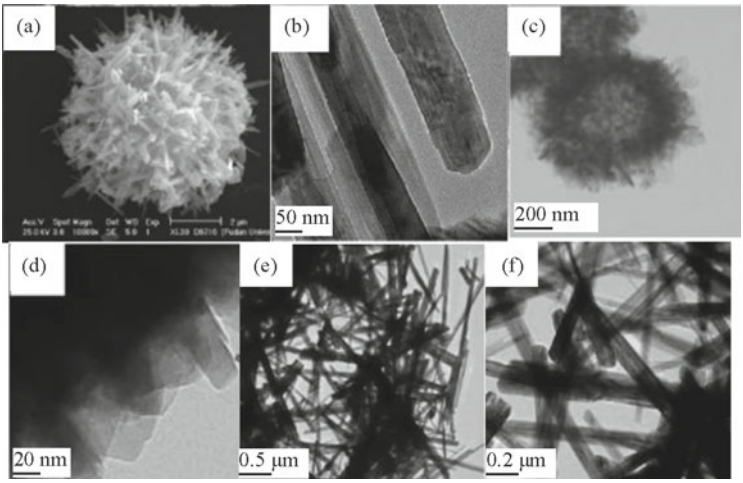

Figure 5.22 (a)、(b) SEM and TEM images of $LiMn_2O_4$ nanothorn microspheres. (c)、(d) SEM and TEM images of $LiMn_2O_4$ hollow nanospheres. (e)、(f) TEM images of $LiMn_2O_4$ nanorods[126] (Copyright 2008, American Chemical Society)

nanothorn microshperes and hollow nanospheres were transformed into $LiMn_2O_4$ nanorods, nanothorn microshperes and hollow nanospheres by annealing treatment [126]. Furthermore, they also investigated the electrochemical performance of these prepared $LiMn_2O_4$ as the cathode materials of lithium ion battery, and demonstrated that the performance of the nanostructured $LiMn_2O_4$ was superior to that of bulk $LiMn_2O_4$. This is because the nanosturcture properties provide a large reaction area, short lithium-ion diffusion distance, as well as stable structures. Very recently, Hosono et al[127] and Kim et al. [128] reported the synthesis of $LiMn_2O_4$ single crystalline nanowires and their high electrochemical performance. Besides these nanostructures mentioned above, nanoparticles of $LiMn_2O_4$ directly synthesized by one-step hydrothermal reaction also can exhibit the especially excellent high rate capability [129].

On the other hand, the use of the nanoparticulate forms of lithium transition metal oxides such as $LiCoO_2$, $LiNiO_2$, or their solid solutions can lead to greater reaction with electrolyte, and ultimately more safety problems, especially at high temperatures, than the use of such materials in the micrometer range. In the case of $LiMn_2O_4$, the use of small particles increases undesirable dissolution of Mn [92]. For these problems, it should be an effective solution to coat the electrode materials with a nanosized stabilizing surface layer. For example, Cho et al. successively fabricated a high-performance $LiCoO_2$ cathode by

a sol-gel coating of Al_2O_3 on $LiCoO_2$ particle surfaces and subsequent heat treatment at 600 °C [130]. Unlike bare $LiCoO_2$, the Al_2O_3-coated $LiCoO_2$ cathode

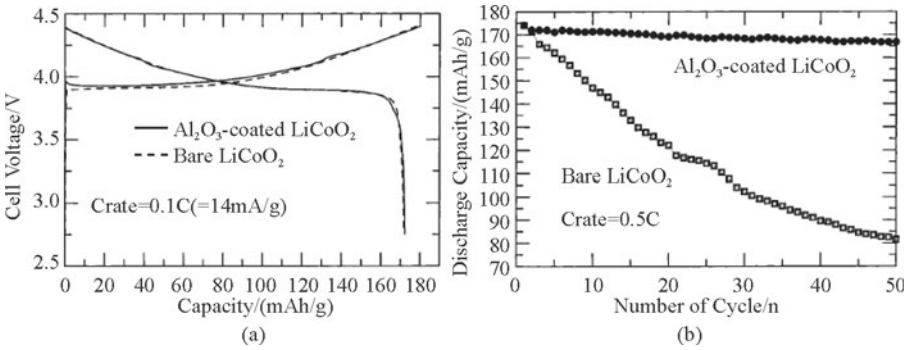

Figure 5.23 (a) Initial capacity and (b) cycle-life performances of bare and Al_2O_3 coated $LiCoO_2$ cathodes measured at the rate of 0.5 C between 4.4 and 2.75 V [130]
(Copyright 200, American Chemical Society)

exhibits no decrease in its original specific capacity of 174 mAh/g and excellent capacity retention (97% of its initial capacity) between 4.4 and 2.75 V (vs. Li/Li+) after 50 cycles (Figure 5.23). Even though the metal-oxide coatings are able to enhance the electrochemical properties, they failed to improve the thermal stability during overcharging. Cho et al.'s further investigation suggested that the uniformly coating of $AlPO_4$ nanoparticles can improve the thermal stability of $LiCoO_2$, especially at overcharging state [131]. Wang et al. recently prepared the high capacity layered $Li[Li_{0.2}Mn_{0.54}Co_{0.13}Ni_{0.13}]O_2$ solution which has been surface modified with single-layer and double layer coating with MPO_4 (M= Al and Co) and Al_2O_3 [132]. (Figure 5.24) The double-layer coated samples exhibit lower irreversible capacity, higher discharge capacity and better rate capability compared to both the pristine material and the single-layer coated samples. The double-layer coated composite cathodes exhibit an attractive discharge capacity of 300 mAh/g with a low irreversible capacity of 26 mAh/g. They believe that the higher discharge capacity values with a lower irreversible capacity of the double-layer coated samples are attributed to a retention of a higher number of oxide ion vacancies in the layered lattice after the first charge compared to that in the pristine and single-layer coated samples, the better rate capability is due to a fast charge transfer kinetics arising from the suppression of undesired SEI layers. Very recently, Myung et al. investigated the effect of AlF_3 coating on thermal behavior of chemically delithiated $Li_{0.35}[Ni_{1/3}Co_{1/3}Mn_{1/3}]O_2$, and concluded that the thermal properties of the $Li_{0.35}[Ni_{1/3}Co_{1/3}Mn_{1/3}]O_2$ were improved by the protection of the

active material from the oxygen loss by the AlF_3 coating and the sacrificing of the AlF_3 coating as a result of the formation of the Li-Al-O and Li-Al-F complexes on the surface, where the rhombohedral structure was actively transformed to the cubic spinel structure in the presence of the AlF_3 coating [133]. In addition to these reports mentioned above, nanoscalar metal oxides ($A_{l2}O_3$ or ZrO_2) as a coating layer on spinel $LiMn_2O_4$ powders have been tried as they can the suppress the undesirable dissolution of Mn [134]. For instance, Cho et al. reported the VO_x-coated $LiMn_2O_4$ nanorod clusters for lithium-ion battery cathode materials. In the coated spinel, the V atoms are distributed within ~ 30 nm of the particle surface without showing any coating layer, indicating the possible formation of a solid solution ($LiMn_2$-xV_xO_4) [135]. The coated nanorod clusters exhibit a comparable rate capability to an uncoated counterpart, showing high rate ability. Furthermore, in spite of the high BET surface area, a higher V concentration at the particle surface significantly decreases the dissolution of Mn under storage at 80 °C.

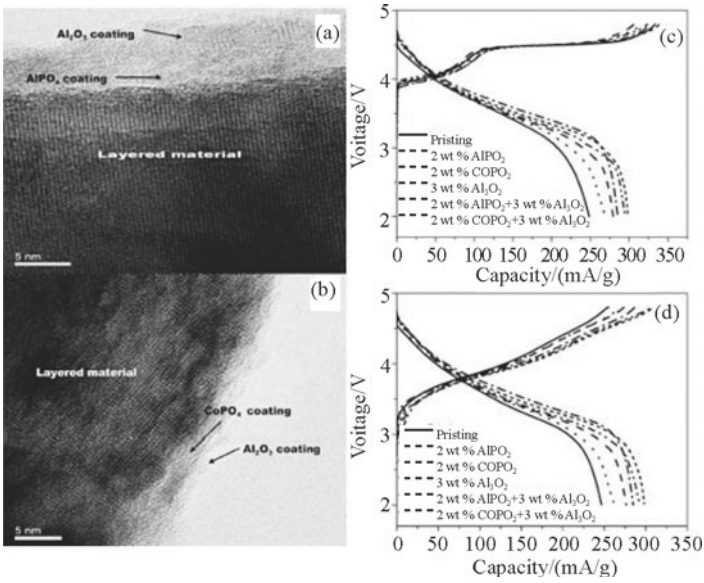

Figure 5.24 TEM images of the (a) 2 wt.% $AlPO_4$ + 3 wt.% Al_2O_3 and (b) 2 wt.% $CoPO_4$ + 3 wt.% Al_2O_3-coated samples; Comparison of the (c) first and (d) second charge–discharge profiles of $Li[Li_{0.2}Mn_{0.54}Ni_{0.13}Co_{0.13}]O_2$ before and after surface modification with 2 wt.% $AlPO_4$, 2 wt.% $CoPO_4$, 3 wt.% Al_2O_3 single-layer coatings and 2 wt.% $AlPO_4$ + 3 wt.% Al_2O_3 and 2 wt.% $CoPO_4$ + 3 wt.% Al_2O_3 double-layer coatings[132]

5.3.3 Olivine $LiFePO_4$

The electrochemical performance of $LiFePO_4$ was reported by Padhi et al. in 1997 [97]. Olivine $LiFePO_4$ has been considered as the most promising cathode candidate for next generation large scale lithium-ion battery used for HEVs or EVs because of its inherent merits including low toxicity, low cost, long cycle ability and high safety. However, its power performance is greatly limited by the slow diffusion of lithium ions across the two-phase boundary and/or the low conductivity. During the following years, many efforts have been made to improve the power performance of $LiFePO_4$ by carbon painting to improve the conductivity of the solid phase or using low-temperature routes to obtain tailored particles. Approaches based on the thermal decomposition of carbon-containing precursors have also been widely studied for the preparation of carbon-coated $LiFePO_4$ particles [136～143]. However, these methods generally involve a high-temperature treatment, during which an increase in crystallite size is inevitable, to ensure the conductivity of the resulting carbon materials. Accordingly, those approaches based on the thermal decomposition of carbon-containing precursors can only produce $LiFePO_4$ particles with a partial coating of carbon [137]. On the other hand, various low-temperature methods (synthesis temperature below 600 ℃), such as low temperature ceramic routes [144～147] or hydrothermal synthesis [148, 149], have been developed to lower the particle size of $LiFePO_4$, although none of them have been able to ensure the conductivity of the carbon coating. Furthermore, some low temperature routes are not able to produce the required highly crystalline olivine structure, thus reducing the electrochemical stability of $LiFePO_4$.

In 2008, Wang et al. reported an in situ polymerization restriction method for the synthesis of the $LiFePO_4$/carbon nano-composite [150]. In their report, the highly crystalline $LiFePO_4$ nanoparticles (20～40 nm in diameter) with the full coating of carbon layer (1～2 nm in thickness) were successfully prepared by high temperature treatment (Figure 5.25). Their strategy includes one in situ polymerization reaction and two typical restriction processes. First, aniline is polymerized in situ on the outer surface of the newly generated $FePO_4$ precipitate to form a green polyaniline (PANI) shell, which can effectively restrict the growth of the $FePO_4$ particles. Subsequent heat treatment at 700 ℃ under argon containing 5% H_2 in the presence of a lithium salt and some sugar led to the transformation of this $FePO_4$/PANI composite into a $LiFePO_4$/carbon composite.

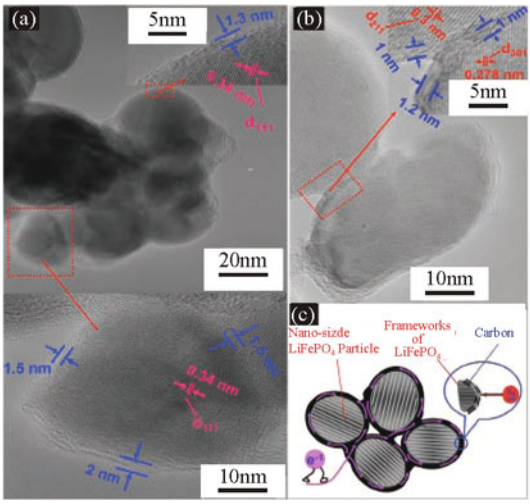

Figure 5.25 (a)、(b) TEM images of $LiFePO_4$ nanoparticles with full coating of carbon layer. (c) Schematic illustration summarizing the characters of $LiFePO_4$/carbon composite [150] (Copyright 2008, Wiley-VCH)

During this process the polymer shell is transformed into a carbon shell that restricts the in situ crystallite growth of $LiFePO_4$. As shown in Figure 5.25 (c), the full coating of carbon layer ensures electrons pass along the out surface of each $LiFePO_4$ particle, which effectively shortens the path length for electronic transport and reduces the interface resistance. Furthermore, the typical "nano-size" also reduces the path length over which lithium-ion has to move on intercalation/de-intercalation process. Thereby, the prepared $LiFePO_4$/carbon nanocomposite with a core-shell structure displayed a high power performance. It achieved a capacity of 90 mAh/g at the current density of 10A/g (rate of about 60 ℃), indicating a high power performance (Figure 5.26(a)). On the other hand, the carbon coating layer reduces the direct contact area between $LiFePO_4$ and electrolyte, preventing the undesired reaction of electrolyte. This improves the stability of the prepared $LiFePO_4$/carbon nanocomposite. As shown in Figure 5.26(b), the prepared composite also exhibits an excellent cycling performance, with less than 5% discharge capacity loss over 1100 cycles.

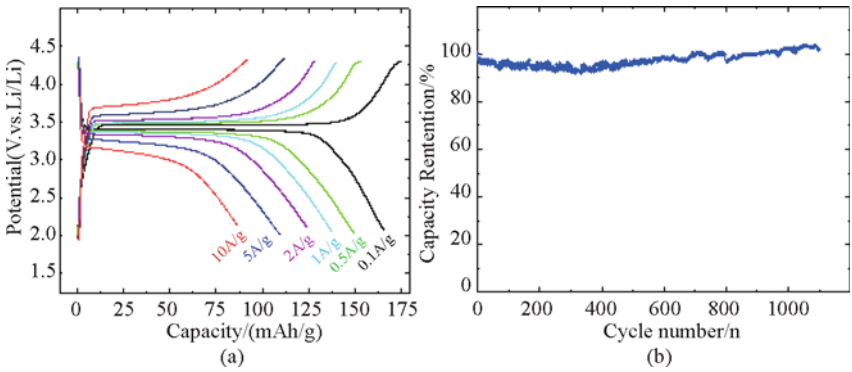

Figure 5.26 (a) Charge/discharge curves and (b) cycle performance of the prepared $LiFePO_4$/carbon composite [150]

(Copyright 2008, Wiley-VCH)

Very recently, Kang et al. prepared the stoichiometries of the type $LiFe_{1-2x}P_{1-x}O_{4-x}$ to improve the ionic conductivity of the surface [151]. The substoichiometry of iron was designed to produce an ionically conductive lithium phosphate glasses on the particle surface. Analysis of the surface coating revealed it is a phase similar to $Li_4P_2O_7$, although it could contain some FeP or Fe^{3+}. This prepared materials exhibited an exceptional capacity of 130 mAh/g even at a discharge rate of 50 ℃ . When the electrode materials is prepared with 65% mass of carbon additive, a capacity of more than 100 mAh/g is achieved at a very fast rate of 200 ℃. The achieved power performance is even higher than that of supercapacitor. Kang et al. alleged that the disordered nature of the coating material modifies the surface potential of lithium to facilitate the adsorption of Li-ions from the electrolyte by providing different lithium sites with a wide range of energies that can be matched to the energy of lithium in the electrolyte [151].

5.4 Conclusion

In this chapter, we simply review the advantages of nanostructured materials for application in lithium-ion batteries. The development of electrode materials of high-performance lithium-ion batteries can benefit from the distinct properties of nanomaterials, such as high surface areas, short diffusion paths, and large quantities of active sites, as well as freedom for volume change during charging–discharging cycles. It is undoubted that nano-materials will play a more and more important role in future research of lithium-ion batteries. To first analyze the inherent drawback of the electrode material, then design a special nano-size or nano-structure to alleviate this drawback, and finally prepare the designed materials should be one of the most promising ways to improve the

performance of lithium-ion batteries. However, it should be noted that nano active materials also have their disadvantages such as low density, high surface reaction and complicated synthesis route. Accordingly, when we design and prepare nanostructured materials for lithium-ion batteries, a balance between advantages and disadvantages for the practical application of nanostructured materials in lithium-ion batteries should be carefully considered.

Acknowledgements

The work was supported by the Scientific Research Startup Funding for the introduction of talent, Fudan University.

References

[1] Tarascon J M,Armand M. Issues and challenges facing rechargeable lithium batteries. Nature, 2001, 414(6861): 359～367.

[2] Armand M,Tarascon J M. Building better batteries. Nature, 2008, 451(7179): 652～657.

[3] Poizot P, Laruelle S, Grugeon S, et al. Nano-sized transition-metaloxides as negative-electrode materials for lithium-ion batteries. Nature, 2000, 407(6803): 496～499.

[4] Ohzuku T, Ueda A,Yamamoto N. Zero-strain insertion material of Li[Li1/3Ti5/3]O-4 for rechargeable lithium cells. Journal of the Electrochemical Society, 1995, 142(5): 1431～1435.

[5] Pereira N, Klein L C,Amatucci G G. The electrochemistry of Zn_3N_2 and LiZnN - A lithium reaction mechanism for metal nitride electrodes. Journal of the Electrochemical Society, 2002, 149(3): A262～A271.

[6] Boukamp B A, Lesh G C,Huggins R A. All-solid lithium electrodes with mixed-conductor matrix. Journal of the Electrochemical Society, 1981, 128(4): 725～729.

[7] Park M H, Kim M G, Joo J, et al. Silicon nanotube battery anodes. Nano Letters, 2009, 9(11): 3844～3847.

[8] Arico A S, Bruce P, Scrosati B, et al. Nanostructured materials for advanced energy conversion and storage devices. Nature Materials, 2005, 4(5): 366～377.

[9] Graetz J, Ahn C C, Yazami R, et al. Highly reversible lithium storage in nanostructured silicon. Electrochemical and Solid State Letters, 2003, 6(9): A194～A197.

[10] Chan C K, Peng H L, Liu G, et al. High-performance lithium battery anodes using silicon nanowires. Nature Nanotechnology, 2008, 3(1): 31～35.

[11] Ohara S, Suzuki J, Sekine K, et al. Li insertion/extraction reaction at a Si film evaporated on a Ni foil. Journal of Power Sources, 2003, 119: 591～596.

[12] Li H, Huang X J, Chen L Q, et al. A high capacity nano-Si composite anode material for lithium rechargeable batteries. Electrochemical and Solid State Letters, 1999, 2(11): 547～549.

[13] Lee J K, Kung M C, Trahey L, et al. Nanocomposites derived from phenol-functionalized Si nanoparticles for high performance lithium ion battery anodes. Chemistry of Materials, 2009, 21(1): 6～8.

[14] Kim H,Cho J. Superior lithium electroactive mesoporous Si@carbon core-shell nanowires for lithium battery anode material. Nano Letters, 2008, 8(11): 3688～3691.

[15] Dimov N, Kugino S,Yoshio M. Carbon-coated silicon as anode material for lithium ion batteries: Advantages and limitations. Electrochimica Acta, 2003, 48(11): 1579～1587.

[16] Magasinski A, Dixon P, Hertzberg B, et al. High-performance lithium-ion anodes using a hierarchical bottom-up approach. Nature Materials, 2010, 9(4): 353～358.

[17] Wang W,Kumta P N. Nanostructured hybrid Silicon/Carbon nanotube heterostructures: Reversible high-capacity lithium-ion anodes. Acs Nano, 2010, 4(4): 2233～2241.

[18] Cui L F, Yang Y, Hsu C M, et al. Carbon-silicon core-shell nanowires as high capacity electrode for lithium ion batteries. Nano Letters, 2009, 9(9): 3370～3374.

[19] Zhou S, Liu X H,Wang D W. Si/$TiSi_2$ heteronanostructures as high-capacity anode material for Li ion batteries. Nano Letters, 2010, 10(3): 860～863.

[20] Gomez-Camer J L, Martin F, Morales J, et al. Precipitation of CoS vs ceramic synthesis for improved performance in lithium cells. Journal of the Electrochemical Society, 2008, 155(3): A189～A195.

[21] Morales J, Sanchez L, Martin F, et al. Synthesis and characterization of nanometric iron and iron-titanium oxides by mechanical milling: Electrochemical properties as anodic materials in lithium cells. Journal of the Electrochemical Society, 2005, 152(9): A1748～A1754.

[22] Morales J, Sanchez L, Martin F, et al. Nanostructured CuO thin film electrodes prepared by spray pyrolysis: a simple method for enhancing the electrochemical performance of CuO in lithium cells. Electrochimica Acta,

2004, 49(26): 4589～4597.

[23] Liu Y, Mi C H, Su L H, et al. Hydrothermal synthesis of CO_3O_4 microspheres as anode material for lithium-ion batteries. Electrochimica Acta, 2008, 53(5): 2507～2513.

[24] Lou X W, Deng D, Lee J Y, et al. Thermal formation of mesoporous single-crystal CO_3O_4 nano-needles and their lithium storage properties. Journal of Materials Chemistry, 2008, 18(37): 4397～4401.

[25] Lou X W, Deng D, Lee J Y, et al. Self-supported formatnion of needlelike CO_3O_4 nanotubes and their application as lithium-ion battery electrodes. Advanced Materials, 2008, 20(2): 258-262.

[26] Li Y G, Tan B,Wu Y Y. Mesoporous CO_3O_4 nanowire arrays for lithium ion batteries with high capacity and rate capability. Nano Letters, 2008, 8(1): 265～270.

[27] Chou S L, Wang J Z, Liu H K, et al. Electrochemical deposition of porous CO_3O_4 nanostructured thin film for lithium-ion battery. Journal of Power Sources, 2008, 182(1): 359～364.

[28] Zhan F M, Geng B Y,Guo Y J. Porous CO_3O_4 nanosheets with extraordinarily high discharge capacity for lithium batteries. Chemistry-a European Journal, 2009, 15(25): 6169～6174.

[29] Wang Y, Fu Z W,Qin Q Z. A nanocrystalline CO_3O_4 thin film electrode for Li-ion batteries. Thin Solid Films, 2003, 441(1～2): 19～24.

[30] Li W Y, Xu L N,Chen J. CO_3O_4 nanomaterials in lithium-ion batteries and gas sensors. Advanced Functional Materials, 2005, 15(5): 851～857.

[31] Chen J, Xu L N, Li W Y, et al. Alpha-Fe_2O_3 nanotubes in gas sensor and lithium-ion battery applications. Advanced Materials, 2005, 17(5): 582-586.

[32] Liu H J, Bo S H, Cui W J, et al. Nano-sized cobalt oxide/mesoporous carbon sphere composites as negative electrode material for lithium-ion batteries. Electrochimica Acta, 2008, 53(22): 6497～6503.

[33] Yu Y, Chen C H, Shui J L, et al. Nickel-foam-supported reticular CoO-Li_2O composite anode materials for lithium ion batteries. Angewandte Chemie-International Edition, 2005, 44(43): 7085～7089.

[34] Reddy M V, Yu T, Sow C H, et al. Alpha-Fe_2O_3 nanoflakes as an anode material for Li-ion batteries. Advanced Functional Materials, 2007, 17(15): 2792～2799.

[35] Komaba S, Mikumo T, Yabuuchi N, et al. Electrochemical insertion of Li and Na ions into nanocrystalline Fe_3O_4 and alpha-Fe_2O_3 for rechargeable batteries. Journal of the Electrochemical Society, 2010, 157(1): A60～A65.

[36] Ortiz G F, Hanzu I, Lavela P, et al. A novel architectured negative electrode

based on titania nanotube and iron oxide nanowire composites for Li-ion microbatteries. Journal of Materials Chemistry, 2010, 20(20): 4041～4046.

[37] Chou S L, Wang J Z, Wexler D, et al. High-surface-area alpha-Fe_2O_3/carbon nanocomposite: One-step synthesis and its highly reversible and enhanced high-rate lithium storage properties. Journal of Materials Chemistry, 2010, 20(11): 2092～2098.

[38] Hassan M F, Rahman M M, Guo Z P, et al. Solvent-assisted molten salt process: A new route to synthesise alpha-Fe_2O_3/C nanocomposite and its electrochemical performance in lithium-ion batteries. Electrochimica Acta, 2010, 55(17): 5006～5013.

[39] Morales J, Sanchez L, Martin F, et al. Use of low-temperature nanostructured CuO thin films deposited by spray-pyrolysis in lithium cells. Thin Solid Films, 2005, 474(1～2): 133～140.

[40] Wang S Q, Zhang J Y,Chen C H. Dandelion-like hollow microspheres of CuO as anode material for lithium-ion batteries. Scripta Materialia, 2007, 57(4): 337～340.

[41] Xiang J Y, Tu J P, Zhang L, et al. Simple synthesis of surface-modified hierarchical copper oxide spheres with needle-like morphology as anode for lithium ion batteries. Electrochimica Acta, 2010, 55(5): 1820～1824.

[42] Zheng S F, Hu J S, Zhong L S, et al. Introducing dual functional CNT networks into CuO nanomicrospheres toward superior electrode materials for lithium-ion batteries. Chemistry of Materials, 2008, 20(11): 3617～3622.

[43] Venkatachalam S, Zhu H W, Masarapu C, et al. In-Situ formation of sandwiched structures of nanotube/Cu_xO_y/Cu composites for lithium battery applications. Acs Nano, 2009, 3(8): 2177～2184.

[44] Li C, Wei W, Fang S M, et al. A novel CuO-nanotube/SnO_2 composite as the anode material for lithium ion batteries. Journal of Power Sources, 2010, 195(9): 2939～2944.

[45] Ke F S, Huang L, Wei G Z, et al. One-step fabrication of CuO nanoribbons array electrode and its excellent lithium storage performance. Electrochimica Acta, 2009, 54(24): 5825～5829.

[46] Chen L B, Lu N, Xu C M, et al. Electrochemical performance of polycrystalline CuO nanowires as anode material for Li ion batteries. Electrochimica Acta, 2009, 54(17): 4198～4201.

[47] Kim I S, Blomgren G E,Kumta P N. Sn/C composite anodes for Li-ion batteries. Electrochemical and Solid State Letters, 2004, 7(3): A44～A48.

[48] Derrien G, Hassoun J, Panero S, et al. Nanostructured Sn-C composite

as an advanced anode material in high-performance lithium-ion batteries. Advanced Materials, 2007, 19(17): 2336～2340.

[49] Kepler K D, Vaughey J T,Thackeray M M. $Li_xCu_6Sn_5$ ($0 < x < 13$): An intermetallic insertion electrode for rechargeable lithium batteries. Electrochemical and Solid State Letters, 1999, 2(7): 307～309.

[50] Shi L H, Li H, Wang Z X, et al. Nano-SnSb alloy deposited on MCMB as an anode material for lithium ion batteries. Journal of Materials Chemistry, 2001, 11(5): 1502～1505.

[51] Zhang J J,Xia Y Y. Co-Sn alloys as negative electrode materials for rechargeable lithium batteries. Journal of the Electrochemical Society, 2006, 153(8): A1466～A1471.

[52] Lee C P, Lin C Y,Yen Y W. The 260 degrees C phase equilibria of the Sn-Sb-Cu ternary system and interfacial reactions at the Sn-Sb/Cu joints. Intermetallics, 2007, 15(8): 1027～1037.

[53] Dahn J R, Courtney I A,Mao O. Short-range Sn ordering and crystal structure of Li4.4Sn prepared by ambient temperature electrochemical methods. Solid State Ionics, 1998, 111(3～4): 289～294.

[54] Ehrlich G M, Durand C, Chen X, et al. Metallic negative electrode materials for rechargeable nonaqueous batteries. Journal of the Electrochemical Society, 2000, 147(3): 886～891.

[55] Hassoun J, Panero S, Simon P, et al. High-rate, long-life Ni-Sn nanostructured electrodes for lithium-ion batteries. Advanced Materials, 2007, 19(12): 1632～1635.

[56] Cui W J, Li F, Liu H J, et al. Core-shell carbon-coated Cu_6Sn_5 prepared by in situ polymerization as a high-performance anode material for lithium-ion batteries. Journal of Materials Chemistry, 2009, 19(39): 7202～7207.

[57] Kwon Y, Kim H, Doo S G, et al. $Sn_{0.9}Si_{0.1}$/carbon core-shell nanoparticles for high-density lithium storage materials. Chemistry of Materials, 2007, 19(5): 982～986.

[58] Zhu J J, Lu Z H, Aruna S T, et al. Sonochemical synthesis of SnO_2 nanoparticles and their preliminary study as Li insertion electrodes. Chemistry of Materials, 2000, 12(9): 2557～2566.

[59] Park M S, Wang G X, Kang Y M, et al. Preparation and electrochemical properties of SnO_2 nanowires for application in lithium-ion batteries. Angewandte Chemie-International Edition, 2007, 46(5): 750～753.

[60] Yuan L, Guo Z P, Konstantinov K, et al. Nano-structured spherical porous SnO_2 anodes for lithium-ion batteries. Journal of Power Sources, 2006, 159(1): 345～348.

[61] Lou X W, Wang Y, Yuan C L, et al. Template-free synthesis of SnO_2 hollow nanostructures with high lithium storage capacity. Advanced Materials, 2006, 18(17): 2325～2329.

[62] Yin X M, Li C C, Zhang M, et al. One-step synthesis of hierarchical SnO_2 hollow nanostructures via self-assembly for high power lithium ion batteries. Journal of Physical Chemistry C, 2010, 114(17): 8084～8088.

[63] Noh M, Kwon Y, Lee H, et al. Amorphous carbon-coated tin anode material for lithium secondary battery. Chemistry of Materials, 2005, 17(8): 1926～1929.

[64] Wang Y, Zeng H C,Lee J Y. Highly reversible lithium storage in porous SnO_2 nanotubes with coaxially grown carbon nanotube overlayers. Advanced Materials, 2006, 18(5): 645～649.

[65] Hu Y S, Demir-Cakan R, Titirici M M, et al. Superior storage performance of a Si@SiO_x/C nanocomposite as anode material for lithium-ion batteries. Angewandte Chemie-International Edition, 2008, 47(9): 1645～1649.

[66] Lou X W, Chen J S, Chen P, et al. One-pot synthesis of carbon-coated SnO_2 nanocolloids with improved reversible lithium storage properties. Chemistry of Materials, 2009, 21(13): 2868～2874.

[67] Takami N, Inagaki H, Kishi T, et al. Electrochemical kinetics and safety of 2-Volt class Li-Ion battery system using lithium titanium oxide anode. Journal of the Electrochemical Society, 2009, 156(2): A128～A132.

[68] Wu H M, Belharouak I, Deng H, et al. Development of $LiNi_{0.5}Mn_{1.5}O_4$/$Li_4Ti_5O_{12}$ System with long cycle life. Journal of the Electrochemical Society, 2009, 156(12): A1047～A1050.

[69] Belharouak I, Sun Y K, Lu W, et al. On the safety of the $Li_4Ti_5O_{12}$/$LiMn_2O_4$ lithium-ion battery system. Journal of the Electrochemical Society, 2007, 154(12): A1083～A1087.

[70] Prakash A S, Manikandan P, Ramesha K, et al. Solution-combustion synthesized nanocrystalline $Li_4Ti_5O_{12}$ as high-rate performance Li-Ion battery anode. Chemistry of Materials, 2010, 22(9): 2857～2863.

[71] Li J R, Tang Z L,Zhang Z T. Controllable formation and electrochemical properties of one-dimensional nanostructured spinel $Li_4Ti_5O_{12}$. Electrochemistry Communications, 2005, 7(9): 894～899.

[72] Tang Y F, Yang L, Qiu Z, et al. Preparation and electrochemical lithium storage of flower-like spinel $Li_4Ti_5O_{12}$ consisting of nanosheets. Electrochemistry Communications, 2008, 10(10): 1513～1516.

[73] Sorensen E M, Barry S J, Jung H K, et al. Three-dimensionally ordered macroporous $Li_4Ti_5O_{12}$: Effect of wall structure on electrochemical

properties. Chemistry of Materials, 2006, 18(2): 482～489.

[74] Jiang C H, Zhou Y, Honma I, et al. Preparation and rate capability of $Li_4Ti_5O_{12}$ hollow-sphere anode material. Journal of Power Sources, 2007, 166(2): 514～518.

[75] Wang Y G, Liu H M, Wang K X, et al. Synthesis and electrochemical performance of nano-sized $Li_4Ti_5O_{12}$ with double surface modification of Ti(III) and carbon. Journal of Materials Chemistry, 2009, 19(37): 6789～6795.

[76] Cheng L, Li X L, Liu H J, et al. Carbon-coated $Li_4Ti_5O_{12}$ as a high rate electrode material for Li-ion intercalation. Journal of the Electrochemical Society, 2007, 154(7): A692～A697.

[77] Cheng L, Yan J, Zhu G N, et al. General synthesis of carbon-coated nanostructure $Li_4Ti_5O_{12}$ as a high rate electrode material for Li-ion intercalation. Journal of Materials Chemistry, 2010, 20(3): 595～602.

[78] Park K S, Benayad A, Kang D J, et al. Nitridation-driven conductive $Li_4Ti_5O_{12}$ for lithium Ion Batteries. Journal of the American Chemical Society, 2008, 130(45): 14930～14931.

[79] Koudriachova M V, Harrison N M,de Leeuw S W. Effect of diffusion on lithium intercalation in titanium dioxide. Physical Review Letters, 2001, 86(7): 1275～1278.

[80] Hu Y S, Kienle L, Guo Y G, et al. High lithium electroactivity of nanometer-sized rutile TiO_2. Advanced Materials, 2006, 18(11): 1421～1426.

[81] Armstrong A R, Armstrong G, Canales J, et al. Lithium-ion intercalation into TiO_2-b nanowires. Advanced Materials, 2005, 17(7): 862～865.

[82] Armstrong G, Armstrong A R, Bruce P G, et al. TiO_2(B) nanowires as an improved anode material for lithium-ion batteries containing $LiFePO_4$ or $LiNi_{0.5}Mn_{1.5}O_4$ cathodes and a polymer electrolyte. Advanced Materials, 2006, 18(19): 2597～2600.

[83] Wilkening M, Lyness C, Armstrong A R, et al. Diffusion in confined dimensions: Li+ transport in mixed conducting TiO_2-B nanowires. Journal of Physical Chemistry C, 2009, 113(12): 4741～4744.

[84] Yue W B, Xu X X, Irvine J T S, et al. Mesoporous monocrystalline TiO_2 and its solid-state electrochemical properties. Chemistry of Materials, 2009, 21(12): 2540～2546.

[85] Ren Y, Hardwick L J,Bruce P G. Lithium intercalation into mesoporous anatase with an ordered 3D pore structure. Angewandte Chemie-International Edition, 2010, 49(14): 2570～2574.

[86] Armstrong G, Armstrong A R, Canales J, et al. TiO_2(B) nanotubes as

negative electrodes for rechargeable lithium batteries. Electrochemical and Solid State Letters, 2006, 9(3): A139～A143.

[87] Brezesinski T, Wang J, Polleux J, et al. Templated nanocrystal-based porous TiO_2 films for next-generation electrochemical capacitors. Journal of the American Chemical Society, 2009, 131(5): 1802～1809.

[88] Kim S W, Han T H, Kim J, et al. Fabrication and electrochemical characterization of TiO_2 three-dimensional nanonetwork based on peptide assembly. Acs Nano, 2009, 3(5): 1085～1090.

[89] Amine K, Belharouak L, Chen Z H, et al. Nanostructured anode material for high-power battery system in electric vehicles. Advanced Materials, 2010,

[90] Dambournet D, Belharouak I,Amine K. Tailored preparation methods of TiO_2 anatase, rutile, brookite: Mechanism of formation and electrochemical properties. Chemistry of Materials, 2010, 22(3): 1173～1179.

[91] Pol V G, Kang S H, Calderon-Moreno J M, et al. Autogenic reactions for preparing carbon-encapsulated, nanoparticulate TiO_2 electrodes for lithium-ion batteries. Journal of Power Sources, 2010, 195(15): 5039～5043.

[92] Wang Y,Cao G Z. Developments in nanostructured cathode materials for high-performance lithium-ion batteries. Advanced Materials, 2008, 20(12): 2251～2269.

[93] Ellis B L, Lee K T,Nazar L F. Positive electrode materials for Li-Ion and Li-batteries. Chemistry of Materials, 2010, 22(3): 691～714.

[94] Whittingham M S. Lithium batteries and cathode materials. Chemical Reviews, 2004, 104(10): 4271～4301.

[95] Mizushima K, Jones P C, Wiseman P J, et al. Lixcoo2 "(Oless-Thanxless-Than-or-Equal-to1) - a New Cathode Material for Batteries of High-Energy Density. Materials Research Bulletin, 1980, 15(6): 783～789.

[96] Thackeray M M, David W I F, Bruce P G, et al. Lithium insertion into manganese spinels. Materials Research Bulletin, 1983, 18(4): 461～472.

[97] Padhi A K, Nanjundaswamy K S,Goodenough J B. Phospho-olivines as positive-electrode materials for rechargeable lithium batteries. Journal of the Electrochemical Society, 1997, 144(4): 1188～1194.

[98] Whittingham M S. Journal of the Electrochemical Society, 1976, (123): 315.

[99] Sudant G, Baudrin E, Dunn B, et al. Synthesis and electrochemical properties of vanadium oxide aerogels prepared by a freeze-drying process. Journal of the Electrochemical Society, 2004, 151(5): A666～A671.

[100] Baudrin E, Sudant G, Larcher D, et al. Preparation of nanotextured VO_2[B] from vanadium oxide aerogels. Chemistry of Materials, 2006, 18(18): 4369～4374.

[101] Wei M D, Sugihara H, Honma I, et al. A new metastable phase of crystallized V_2O_4 center dot 0.25H(2)O nanowires: Synthesis and electrochemical measurements. Advanced Materials, 2005, 17(24): 2964-2969.

[102] Gao S K, Chen Z J, Wei M D, et al. Single crystal nanobelts of V_3O_7 center dot H_2O: A lithium intercalation host with a large capacity. Electrochimica Acta, 2009, 54(3): 1115～1118.

[103] Liu H M, Wang Y G, Wang K X, et al. Synthesis and electrochemical properties of single-crystalline LiV_3O_8 nanorods as cathode materials for rechargeable lithium batteries. Journal of Power Sources, 2009, 192(2): 668～673.

[104] Liu H M, Wang Y G, Li L, et al. Facile synthesis of NaV_6O_{15} nanorods and its electrochemical behavior as cathode material in rechargeable lithium batteries. Journal of Materials Chemistry, 2009, 19(42): 7885～7891.

[105] Shi S F, Cao M H, Fle X Y, et al. Surfactant-assisted hydrothermal growth of single-crystalline ultrahigh-aspect-ratio vanadium oxide nanobelts. Crystal Growth and Design, 2007, 7(9): 1893～1897.

[106] Lee K, Wang Y,Cao G H. Dependence of electrochemical properties of vanadium oxide films on their nano- and microstructures. Journal of Physical Chemistry B, 2005, 109(35): 16700～16704.

[107] Liu H M, Wang Y G, Wang K X, et al. Design and synthesis of a novel nanothorn VO_2(B) hollow microsphere and their application in lithium-ion batteries. Journal of Materials Chemistry, 2009, 19(18): 2835～2840.

[108] Cao A M, Hu J S, Liang H P, et al. Self-assembled vanadium pentoxide (V_2O_5) hollow microspheres from nanorods and their application in lithium-ion batteries. Angewandte Chemie-International Edition, 2005, 44(28): 4391～4395.

[109] Chabre Y,Pannetier J. Structural and electrochemical properties of the proton gamma-MnO_2 System. Progress in Solid State Chemistry, 1995, 23(1): 1～130.

[110] Machefaux E, Verbaere A,Guyomard D. Electrochemical synthesis of new substituted manganese oxides for lithium battery applications. Journal of Power Sources, 2006, 157(1): 443～447.

[111] Chen J,Cheng F Y. Combination of lightweight elements and nanostructured materials for Batteries. Accounts of Chemical Research, 2009, 42(6): 713～723.

[112] Thackeray M M. Manganese oxides for lithium batteries. Progress in Solid State Chemistry, 1997, 25(1～2): 1～71.

[113] Chou S L, Cheng F Y,Chen J. Electrodeposition synthesis and electrochemical properties of nanostructured gamma-MnO_2 films. Journal of Power Sources, 2006, 162(1): 727～734.

[114] Cheng F Y, Zhao J Z, Song W, et al. Facile controlled synthesis of MnO_2 nanostructures of novel shapes and their application in batteries. Inorganic Chemistry, 2006, 45(5): 2038～2044.

[115] West W C, Myung N V, Whitacre J F, et al. Electrodeposited amorphous manganese oxide nanowire arrays for high energy and power density electrodes. Journal of Power Sources, 2004, 126(1～2): 203～206.

[116] Wu M S, Chiang P C J, Lee J T, et al. Synthesis of manganese oxide electrodes with interconnected nanowire structure as an anode material for rechargeable lithium ion batteries. Journal of Physical Chemistry B, 2005, 109(49): 23279～23284.

[117] Luo J Y, Zhang J J,Xia Y Y. Highly electrochemical reaction of lithium in the ordered mesoporosus beta-MnO_2. Chemistry of Materials, 2006, 18(23): 5618～5623.

[118] Jiao F,Bruce P G. Mesoporous crystalline beta-MnO_{2-} a reversible positive electrode for rechargeable lithium batteries. Advanced Materials, 2007, 19(5): 657～660.

[119] Wang Y G, Wu W, Cheng L, et al. A polyaniline-intercalated layered manganese oxide nanocomposite prepared by an inorganic/organic interface reaction and its high electrochemical performance for Li storage. Advanced Materials, 2008, 20(11): 2166～2170.

[120] Larcher D,Reddy T B. Handbook of Batteries. New York: McGraw- Hill ,2002.

[121] Ronci F, Scrosati B, Albertini V R, et al. In situ energy dispersive X-ray diffraction study of $LiNi_{0.8}Co_{0.2}O_2$ cathode material for lithium batteries. Journal of Physical Chemistry B, 2001, 105(4): 754～759.

[122] Li X X, Cheng F Y, Guo B, et al. Template-synthesized $LiCoO_2$, $LiMn_2O_4$, and $LiNi_{0.8}Co_{0.2}O_2$ nanotubes as the cathode materials of lithium ion batteries. Journal of Physical Chemistry B, 2005, 109(29): 14017～14024.

[123] Jiao F, Shaju K M,Bruce P G. Synthesis of nanowire and mesoporous low-temperature $LiCoO_2$ by a post-templating reaction. Angewandte Chemie-International Edition, 2005, 44(40): 6550～6553.

[124] Luo J Y, Cheng L,Xia Y Y. $LiMn_2O_4$ hollow nanosphere electrode material with excellent cycling reversibility and rate capability. Electrochemistry Communications, 2007, 9(6): 1404～1409.

[125] Luo J Y, Wang Y G, Xiong H M, et al. Ordered mesoporous spinel $LiMn_{(2)}O_{(4)}$by a soft-chemical process as a cathode material for lithium-ion

batteries. Chemistry of Materials, 2007, 19(19): 4791～4795.

[126] Luo J Y, Xiong H M,Xia Y Y. $LiMn_2O_4$ nanorods, nanothorn microspheres, and hollow nanospheres as enhanced cathode materials of lithium ion battery. Journal of Physical Chemistry C, 2008, 112(31): 12051～12057.

[127] Hosono E, Kudo T, Honma I, et al. Synthesis of single crystalline spinel $LiMn_2O_4$ nanowires for a lithium ion battery with high power density. Nano Letters, 2009, 9(3): 1045～1051.

[128] Kim D K, Muralidharan P, Lee H W, et al. Spinel $LiMn_2O_4$ nanorods as lithium ion battery cathodes. Nano Letters, 2008, 8(11): 3948～3952.

[129] Jiang C H, Dou S X, Liu H K, et al. Synthesis of spinel $LiMn_2O_4$ nanoparticles through one-step hydrothermal reaction. Journal of Power Sources, 2007, 172(1): 410～415.

[130] Cho J, Kim Y J,Park B. Novel $LiCoO_2$ cathode material with Al_2O_3 coating for a Li ion cell. Chemistry of Materials, 2000, 12(12): 3788～3791.

[131] Cho J, Kim Y W, Kim B, et al. A breakthrough in the safety of lithium secondary batteries by coating the cathode material with $AIPO_{(4)}$ nanoparticles. Angewandte Chemie-International Edition, 2003, 42(14): 1618～1621.

[132] Wang Q Y, Liu J, Murugan A V, et al. High capacity double-layer surface modified $Li[Li_{0.2}Mn_{0.54}Ni_{0.13}Co_{0.13}]O$-2 cathode with improved rate capability. Journal of Materials Chemistry, 2009, 19(28): 4965～4972.

[133] Myung S T, Lee K S, Yoon C S, et al. Effect of AlF_3 coating on rhermal behavior of chemically delithiated Li-$0.35[Ni_{1/3}Co_{1/3}Mn_{1/3}]O$-2. Journal of Physical Chemistry C, 2010, 114(10): 4710～4718.

[134] Sun Y K, Hong K J, Prakash J, et al. Electrochemical performance of nano-sized ZnO-coated $LiNi_{0.5}Mn_{1.5}O_4$ spinel as 5 V materials at elevated temperatures. Electrochemistry Communications, 2002, 4(4): 344～348.

[135] Cho J. VO_x-coated $LiMn_2O_4$ nanorod clusters for lithium battery cathode materials. Journal of Materials Chemistry, 2008, 18(19): 2257～2261.

[136] Chen Z H,Dahn J R. Reducing carbon in $LiFePO_4$/C composite electrodes to maximize specific energy, volumetric energy, and tap density. Journal of the Electrochemical Society, 2002, 149(9): A1184～A1189.

[137] Salah A A, Mauger A, Zaghib K, et al. Reduction Fe_{3+} of impurities in $LiFePO_4$ from pyrolysis of organic precursor used for carbon deposition. Journal of the Electrochemical Society, 2006, 153(9): A1692～A1701.

[138] Shin H C, Cho W I,Jang H. Electrochemical properties of the carbon-coated $LiFePO_4$ as a cathode material for lithium-ion secondary batteries. Journal of Power Sources, 2006, 159(2): 1383～1388.

[139] Yun N J, Ha H W, Jeong K H, et al. Synthesis and electrochemical properties of olivine-type $LiFePO_4$/C composite cathode material prepared from a poly(vinyl alcohol)-containing precursor. Journal of Power Sources, 2006, 160(2): 1361～1368.

[140] Dominko R, Bele M, Goupil J M, et al. Wired porous cathode materials: A novel concept for synthesis of $LiFePO_4$. Chemistry of Materials, 2007, 19(12): 2960～2969.

[141] Zaghib K, Mauger A, Gendron F, et al. Surface effects on the physical and electrochemical properties of thin $LiFePO_4$ particles. Chemistry of Materials, 2008, 20(2): 462～469.

[142] Roberts M R, Spong A D, Vitins G, et al. High throughput screening of the effect of carbon coating in $LiFePO_4$ electrodes. Journal of the Electrochemical Society, 2007, 154(10): A921～A928.

[143] Amine K, Liu J,Belharouak I. High-temperature storage and cycling of C-$LiFePO_4$/graphite Li-ion cells. Electrochemistry Communications, 2005, 7(7): 669～673.

[144] Gabrisch H, Wilcox J D,Doeff M M. Carbon surface layers on a high-rate $LiFePO_4$. Electrochemical and Solid State Letters, 2006, 9(7): A360～A363.

[145] Meethong N, Huang H Y S, Carter W C, et al. Size-dependent lithium miscibility gap in nanoscale $Li_{1-x}FePO_4$. Electrochemical and Solid State Letters, 2007, 10(5): A134～A138.

[146] Delacourt C, Poizot P, Levasseur S, et al. Size effects on carbon-free $LiFePO_4$ powders. Electrochemical and Solid State Letters, 2006, 9(7): A352～A355.

[147] Choi D,Kumta P N. Surfactant based sol-gel approach to nanostructured $LiFePO_4$ for high rate Li-ion batteries. Journal of Power Sources, 2007, 163(2): 1064～1069.

[148] Ellis B, Kan W H, Makahnouk W R M, et al. Synthesis of nanocrystals and morphology control of hydrothermally prepared $LiFePO_4$. Journal of Materials Chemistry, 2007, 17(30): 3248～3254.

[149] Chen J J,Whittingham M S. Hydrothermal synthesis of lithium iron phosphate. Electrochemistry Communications, 2006, 8(5): 855～858.

[150] Wang Y G, Wang Y R, Hosono E J, et al. The design of a $LiFePO_4$/carbon nanocomposite with a core-shell structure and its synthesis by an in situ polymerization restriction method. Angewandte Chemie-International Edition, 2008, 47(39): 7461～7465.

[151] Kang B,Ceder G. Battery materials for ultrafast charging and discharging. Nature, 2009, 458(7235): 190～193.

Chapter 6
Fiber Solar Cells

Dechun Zou,Zhibin Lv,Dan Wang and Zengze Chu

Beijing National Laboratory for Molecular Sciences, Key Laboratory of Polymer, Chemistry and Physics of Ministry of Education, College of Chemistry and Molecular, Engineering, Peking University, Beijing 100871, China

Abstract

Flexible solar cells with the advantages of lightweight, foldability, and low cost, and extensive applications have attracted much academic interest and industrial attention during the last decades. The superiority of fiber cell is the most significant advantage of all non-fl at-structured solar cells: 1. The non-flat structured solar cell gets rid of the dependence on transparent conductive oxide. 2.The fiber cell, which has a three-dimensional (3-D) structure, can catch photons from all directions to increase the power output of cells for improved optical structure capability. Meanwhile, the fiber cell has very low dependence on incident light angle and can gather diffused reflected light to maintain weatherproof and stable power output. 3. The fiber cell is a macro 1-D structure and has a smaller package area ratio than the 2-D structure. Making a larger cell requires only increasing the length of the cell. 4. The flexible fiber cell can directly adopt traditional preparation technology, whereas special technologies must be adopted to make all kinds of traditional flexible flat cells (like OPV and DSSC) to ensure that the flexible substrate will not be damaged during the preparation process, such as by low temperature. 5. Existing textile techniques can be directly used in weaving for mass production of fiber cells, another further improvement of the traditional roll-to-roll technology for producing flexible electrical devices. This chapter reviews the various types of fiber-shaped flexible solar cells and their characteristics.

6. 1 Introduction

Fossil energy, represented by coal, petroleum, and natural gas, made a

significant contribution to the development and progress of human society over the past century. From polymer chemistry typified by the invention of plastic and solid electronics started with the birth of the transistor, to the progress of microelectronics, popularization of computers, development of the planet, and use of atomic energy, all these are directly or indirectly based on the use of chemical energy. In a manner of speaking, the four essential requirements of mankind—food, clothing, housing, and transportation—cannot be possible today without chemical energy. However, the use of fossil energy conceals a potential danger to the sustainable development of society. Many types of waste discharge arising from the usage of chemical energy cause serious damage to the environment. In particular, greenhouse gas emissions, acid rain, damage to the ozone layer, and other problems have emerged. Moreover, as the basic substance for energy and power of human society, the distribution of fossil energy in the world is extremely uneven. Therefore, long-distance transportation entails more expensive transportation cost. In addition, like petroleum, nuclear energy, and so on, recovering from the destruction to the environment due to leakages is difficult after several decades or even after a century. Most typical examples are the US–Mexico Gulf oil spill in 2010, the oil tanker leakage in Dalian, China. Moreover, fossil energy is limited. Fossil energy has been repeatedly reported to be exhausted by the end of the century. Therefore, the urgent concern is determining how to realize a balanced development of energy, environment, and economy, or the so-called 3E Problem[1–4].

The development of clean energy technology is an important way to solve the 3E Problem and realize the virtuous circle of their sustainable development. Governments around the world have realized the importance and urgency of developing clean energy technology. They have worked out medium- to long-term energy development strategies one after another and provided strong supports and investments including the development and promotion of solar, wind, tidal, geothermal, biological, nuclear and other energy technology sources[1, 5]. Among these, solar energy receives wide attention because of its advantage in quality and quantity. The total amount of energy from the sun's radiation to the Earth for one hour is equivalent to the current annual total energy consumption of human beings. Main solar energy processes include photovoltaic and photo-thermal conversions[6]. Photo-thermal conversion consists of two entirely different methods. One is the conversion of solar energy into thermal energy to drive turbines that generate electric power in large factories and the other is the solar heater mainly for household use. These types of photo-thermal conversion methods, particularly the method that converts light into thermal energy first and is then used to generate

electric power, do not only have lower energy conversion efficiency but also need large light concentration, thermal-concentrating devices, and sun-tracking systems. These characteristics limit the popularity and application of these methods[7~9]. Another major method of solar energy utilization is the use of photovoltaic devices (i.e., solar cells) to convert solar directly to electrical energy. As a kind of clean energy technology, this has incomparable specific advantages over other forms of power plants[10~13]: ① no moving parts, no risk of radiation, no risk of explosion, and clean energy can be produced quietly; ② simple maintenance, easily accessible, and automatic; ③ higher photoelectric conversion efficiency, allowing it to be used directly by houses or combined to the grid; ④ it comes in the most direct energy form required by most electrical energy-consuming equipment and can be transmitted over long distances at low cost.

Since Bell Laboratory in the US developed the first single crystalline solar cell with 6% photoelectric conversion efficiency in 1954[14], people have developed solar cells based on a succession of various materials, including the following:

(1)Silicon solar cell: silicon-based solar cell consisting of monocrystalline silicon solar cell, polycrystalline silicon solar cell, amorphous silicon solar cell, and others[14~20].

(2)Inorganic compound semiconductor solar cell: includes cadmium sulfide solar cell based on monocrystalline or polycrystalline cadmium sulfide, such as cuprous sulfide–cadmium sulfide solar cell(CIGS), cadmium telluride–cadmium sulfide solar cell(CdTe), and so on; gallium arsenide solar cell based on gallium arsenide(GaAs), such as homojunction and heterojunction gallium arsenide solar cells[21, 22].

(3)Sensitized nanocrystalline solar cell: made from dye-sensitized wide bandgap nano-oxide semiconductor (TiO_2, SnO_2, ZnO, etc.). The sensitized dyes include the widely used Ru-based dye, inorganic narrow bandgap semiconductor, organic dye/inorganic semiconductor composite, or depositing precious metals, and so on[23~27].

(4)Organic compound solar cell: includes organic p–n junction solar cell, organic Schottky-type solar cell, organic mixed heterojunction solar cell, and others[28~32]. Phthalocyanine, porphyrin, perylene, chlorophyll, conjugated polymers/C60, or other organic compounds are used as the active layer material.

To date, the research on all types of solar cells has come a long way[33, 34]. Photoelectric conversion efficiency has continuously improved. Figure 6.1 shows the photoelectric conversion efficiencies of all types of solar cells.

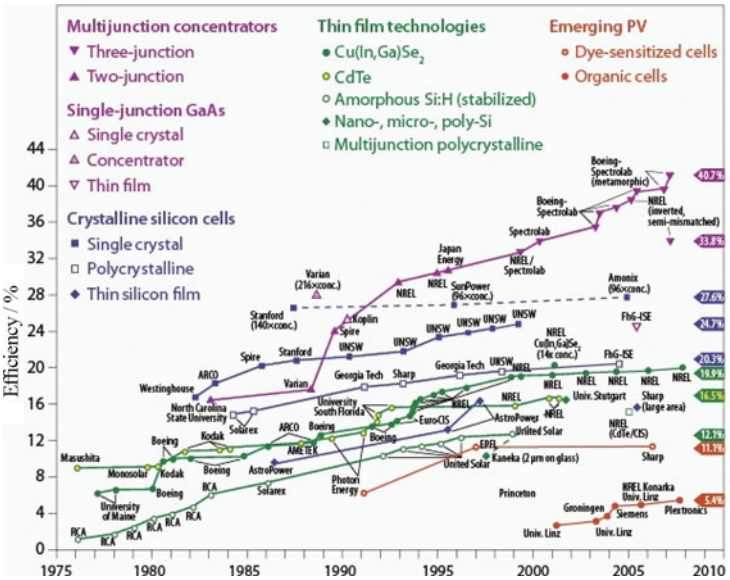

Figure 6.1 Progress in solar cell efficiencies for various research or laboratory devices. All these cell efficiencies have been confirmed and were measured under standard reporting conditions (Source:http://renewableenergyindex.com/solar/solar-cell-materials)

6.2 A summary of flexible flat plate cells

Traditional solar cells have rigid flat-shaped cells that mainly use silicon wafer, metal plate, glass, and so on as substrates. These cells are especially unfavorable for installation on curved surfaces or in environments that are subject to strong vibration and deformation due to their heavy weight and extreme brittleness. Therefore, the development of new types of solar cells on flexible substrate (flexible solar cells) has received wide attention[35~37]. Flexible solar cells are not only low cost but they also have the following special advantages. ① Soft and flexible: as the materials used are soft and flexible, they can be installed in all types of surfaces to meet various new application requirements. ② Free size: roll-to-roll technology can be used to produce flexible solar cells of any size. Based on the specific requirement of customers, the length and width of the cell can be customized. ③ Light and thin: the substrate is made of plastic or metal foil; therefore, flexible solar cell is light and can be fitted for all kinds of situations that have special weight requirements; it can also be applied to beautiful portable products. ④ Safe: flexible solar cells are different from the traditional crystal silicon or other types of film cells because they use flexible plastic or metal foil as substrate instead of friable glass. Therefore, they are stronger and safer to use;

⑤ Environment friendly: with rich raw materials, lower cost, and less power consumption during production process, the energy return cycle is one-fifth to one-third of that of traditional solar cells. With respect to preparation technology, the flexible solar cell adopts mature high-speed roll-to-roll technology to print the semiconductor material continuously onto conductive plastic rolled on the surface of the roll or stainless steel foil substrate[35]. The printing technology can save expensive raw materials and perform the process under atmospheric environment. The traditional film solar cell needs large and expensive vacuum deposition equipment. In comparison, the preparation technology of the flexible cell under ordinary air pressure can sharply reduce production cost, including workshops and equipment, power-consumption, and raw material costs.

The concept of flexible silicon cell has been proposed as early as 1967[38]. The main idea is to use plastic substrate instead of traditional non-flexible solid substrate to produce the flexible silicon cell array in order to decrease the thickness of the silicon cell. In 1976, the birth of the amorphous silicon solar cell showed the distinct advantage of the film solar cell and laid a solid foundation for the preparation of the flexible silicon cell. Silicon-based flexible solar cell consists of polycrystalline silicon and amorphous silicon solar cells[39]. In 1990, Matsuyama et al. prepared the first amorphous silicon solar cell based on flexible transparent plastic substrate[40]. Its thickness was only 0.12 mm and its bend radius was 5 mm. It had the highest energy mass ratio of all solar cells in the world at that time (275 mW/g). Amorphous silicon material has very high absorbance index. An amorphous silicon film less than 1 μm can completely absorb sunlight. However, the bandgap of amorphous silicon materials is wide, and many dangling bonds exist on the surface, which seriously affect the transmission of current carriers. In addition, due to the Staebler–Wronski effect, the long-term light stability of the amorphous silicon solar cell is poor; in particular, its performance reduces quickly under strong light[39]. To reduce the Staebler–Wronski effect, the stability of the amorphous silicon solar cell was improved by adopting a multi-junction structure. As it used absorption materials with different bandgaps, the spectral response of the cell was significantly developed and the photoelectric conversion efficiency of the cell was largely improved[41, 42].

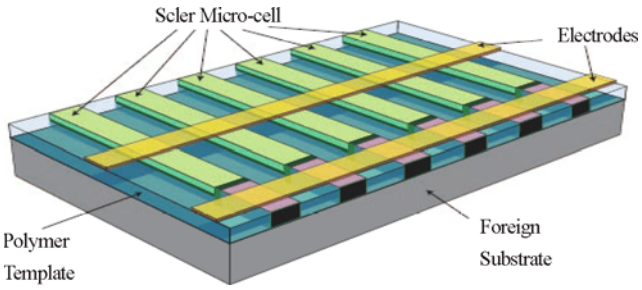

Figure 6.2 Schematic diagram of a flexible photovoltaic device based on crystalline silicon microcells. The solar microcells are first fabricated on a bulk silicon wafer and then transferred to a plastic substrate by printing process[44]

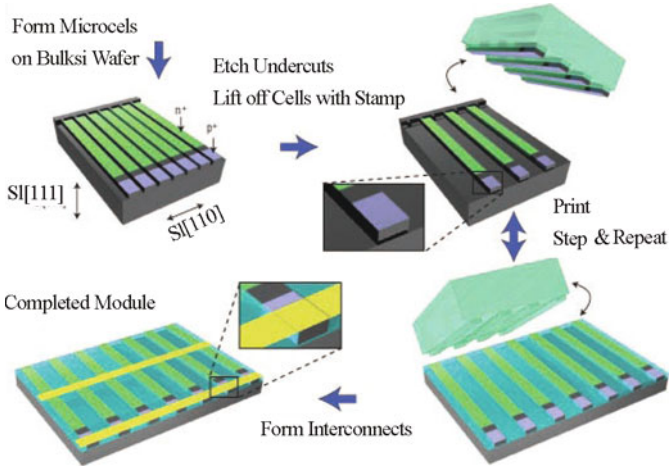

Figure 6.3 Schematic illustration of steps for fabricating ultrathin microcells from a bulk wafer, printing them onto a target substrate, and forming electrical interconnections to complete the module[45]

The monocrystalline silicon flexible solar cell was not reported until 2008. In 2008, Rogers et al. adopted the transfer printing technology to prepare successfully flexible monocrystalline silicon nanobelt array[43]. In the same year, Fan and Javey adopted this technology to prepare semitransparent and flexible monocrystalline silicon solar cells successfully designed by using a concentrated module[44, 45]. The manufacture process are shown in Figure 6.2 and Figure 6.3. These are the first reports of the flexible monocrystalline silicon solar cells prepared by adopting traditional photolithography and doping technology. The thickness of the flexible microcell array prepared was less than 100 nm, and the width was up to several

micrometers. By adopting etch technology, the microcell was taken from the silicon substrate, transferred, and printed onto the flexible and elastic substrate. The authors declared that the photoelectric conversion efficiency of a single microcell could reach 4%～13% if a reflection layer with proper thickness was prepared on the silicon substrate. They mainly employed traditional preparation technology on the monocrystalline silicon cell, including high-temperature doping, etching, and transfer-printing technology, which was used as the last process in order to transfer the cell onto the flexible substrate. The manufacture process are shown in Figure 6.2 and Figure 6.3.The handling of substrate mainly refers to the preparation of electrodes on the substrate. Therefore, this method is not limited by the substrate, and this technology can make use of established mature preparation technology of monocrystalline silicon cell for maximum production of large monocrystalline silicon flexible solar cells at a lower cost.

Since its introduction in the mid 1970s, CIGS solar cell in the laboratory has always maintained very high photoelectric conversion efficiency and its structure is shown in Figure 6.4(a)[21, 22]. CIGS film belongs to chalcopyrite crystal group with adjustable bandgap. The bandgap required by solar cells is within 1～1.7eV. The bandgap of CIGS can be adjusted by changing the contents of III-positive ions, including indium, gallium, and aluminum, and the contents of VI-negative ions, including selenium and sulfur. Compared with monocrystalline silicon solar cell, CIGS is characterized by less internal defects and more stable performance, with a solar module lifetime of up to 25 years. During the operation process of the module, the movement of the Cu ion can overcome the defects and the performance of the module will be continuously improved, completely in contrast to the light-induced degradation or Staebler–Wronski effect of the amorphous silicon solar cell[46]. As shown in Figure 6.4, the basic structure of the CIGS flexible solar cell consists of a substrate, a back contact electrode, a semiconductor absorption layer, and a conductive window layer. For the preparation of CIGS absorption layer with higher thermal stability, generally, the required temperature is up to 500～600 °C. If the temperature is lower than 350°C, the performance of the CIGS absorption layer will decrease. So the substrate generally require the following A minimum heat-resistant temperature of more than 350°C to ensure the CIGS performance and also there are many other requirements of the CIGS f;lexible substrate[46～54]: ① An appropriate expansion coefficient. The expansion coefficient of the substrate must be consistent with that of the CIGS layer. ② Chemical inertness. The substrate must not corrode during the technological process and usage, particularly during chemical reaction with the ingredient in CIGS. ③ Sufficient humidity and insulation performance. The substrate materials should prevent the active layer from environmental corrosion

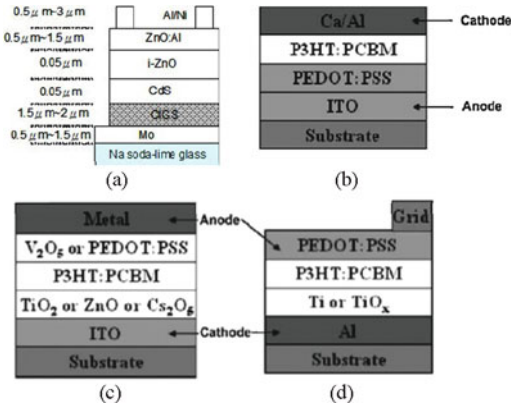

Figure 6.4 (a) Architecture of CIGS solar cell. (b)~(d) Architecture of polymer solar cells: (b) standard, (c) inverted (in terms of the roles of the electrodes), and (d) inverted (in terms of the alternative processing structure)

and destruction, especially humidity. ④ Smooth substrate surface. A rough surface may cause a short circuit in the front and rear contact electrodes, and also facilitate impurity deposits that can block the insulation layer. ⑤ Compatibility with vacuum technology. When the substrate is heated to deposit CIGS active layer, the gas-separation technology is unnecessary. Low cost, energy saving capacity, and material availability, as well as compatible specific gravity. Currently, CIGS flexible solar cell substrates mainly include flexible metal plate (e.g., stainless steel, molybdenum, and others) and polymer (e.g., polyester, polyimide, and so on)[48, 50, 52, 54]. The key in the preparation of CIGS on the flexible metal plate is to have better insulating layer. Higher deposition temperature is favorable for the deposition of active layer, but it aggravates the diffusion of unwanted impurity of the substrate to the active layer. Electrical insulating layer is also needed on the substrate to prepare a single integrated module. Maintaining insulation in each processing step is mandatory, and there should be no cracks at any single time, which is higher than the requirement of impurity diffusion and blocking layer[47, 53]. When polymer materials like polyester and polyimide are used, a heat-resistant problem exists. Developing proper preparation technology is necessary to obtain efficient cells with lower substrate temperature[52, 54].

The cost of inorganic flexible solar cell is lower than that of crystalline silicon. However, the cost of organic flexible solar cell is even lower[35, 55~59]. The organic flexible solar cell has the following advantages: ① The cost of equipment is lower because the organic semiconductor layer can be automatically synthesized with nanochemical technology, unlike inorganic film solar cell which needs more expensive film-coating apparatus. ② consumption of raw materials is less because

organic flexible solar cells can absorb the solar spectrum completely by simply using a semiconductor absorbing layer with a thickness of only 100 nm. For crystalline silicon, a thickness of 200～300 μm is needed, and a semiconductor absorption layer with a thickness of 1～2 μm is also needed for the inorganic flexible and inorganic film cells. ③ electrical performance is adjustable because the organic materials are synthesized as required to adjust the absorption spectrum and the transport property of carriers. The organic flexible cell also has the following disadvantages[56, 60～62]: ① The organic semiconductor has a smaller dielectric constant compared with the inorganic semiconductor, that is, the Coulombic force between excitons is very strong and is difficult to separate; ②organic semiconductor has an amorphous structure, and transporting the carriers is more difficult; ③ the power of the organic semiconductor rapidly decays, and its lifetime is lower than that of inorganic semiconductor; ④ encapsulating the organic semiconductor device is difficult because broken encapsulation will cause moistening of organic semiconductor materials and device failure.

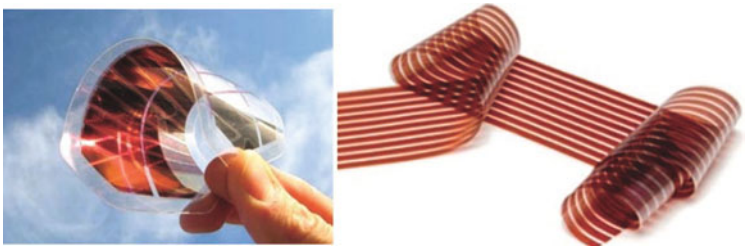

Figure 6.5 Final module manufactured by roll-to-roll printing
(Source:http://www.google.com.hk/search?q=flexible+solar+cell+and+image*&hl=zh-CN&newwindow=18&safe=strict&prmd=imvnsz&tbm=isch&tbo=u&source=univ&sa=X&ei=PXEbUKqfk8POrOfa-YCYDw&ved=0FC4QsAQ&biw=1420&bih=797)

Currently, the developed organic solar cell with flexible plate structure is mainly based on small molecular organic materials[63～65], polymer materials, and organic/inorganic compound materials. Polymer-based organic solar cell is the most widely researched. Polymer material is the most promising material for making flexible solar cell because it has better flexibility, a simple film-forming process, and its mechanical strength can be at par with other materials. The polymer solar cell generally has two kinds of basic structures[57, 66]: one is called the standard structure, and the other is the inverted structure. The standard structure refers to the ITO/PEDOT:PSS/active layer/cathode. The inverted structure includes two types, as shown in Figure 6.4. One type serves as substitute

for ITO in the standard cell structure with metal electrode. The structure can be prepared using screen printing and is favorable to roll-to-roll technology. The other type of inverted structure still uses the metal electrode as the cathode, but the preparation process is reversed; the metal electrode and the active layer are coated on the flexible substrate one after the other. The two types of structures have lower cost and higher photoelectric conversion efficiency. Figure 6.5 shows final module of flexible organic solar cell manufactured by roll-to-roll printing. The study of the flexible organic solar cell mainly focuses on suitable substrates because the active layer is flexible. In this type of flexible cell, the polymer substrate is the key material instead of the traditional glass substrate[55 – 57, 67]. These polymers must have better optical property and better mechanical and chemical characteristics, such as high transparency, large size, low thermal expansion coefficient, smooth surface, and better insulation property from water and air. The most typical and most widely used substrate material is ITO-coated or conductive polymer, such as PEDOT:PSS-coated polyester materials, including PET and PEN. Polyether, polycarbonate, and other materials are also used as flexible substrates[68].

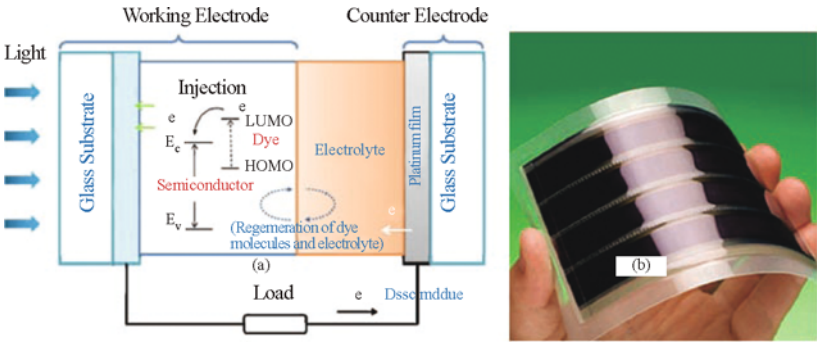

Figure 6.6 (a) Outline of a dye-sensitized solar cell (DSSC) constructed with a working electrode consisting of dye-sensitized semiconducting oxide film, a counter electrode made of platinum-coated glass substrate, and electrolyte filled between the working and counter electrodes. (b) Flexible DSSC module[69]

As early as the 1970s, people were already desirous of developing new types of solar cells by simulating photosynthesis. At that time, a layer of chlorophyll dye was absorbed on the surface of semiconductor TiO_2 and the concept of dye-sensitized solar cell (DSSC) has been proposed, but the transportation of electrons in chlorophyll was very difficult and the photoelectric conversion efficiency was very low. In 1991, the Swedish scientist Gratzel achieved substantial development in DSSCs by adopting nanotechnology[69, 70]. As shown in Figure 6.6, Gratzel

replaced the nano particle TiO_2 crystal with diameter of 20 nm to form an optical transparent film with a thickness of 10 μm, which can absorb dye molecules at its outer layer. The conversion efficiency of the first DSSC was up to 7.1%, and the current density was up to 12 mA/cm^2. Today, the world-record efficiency of DSSC is 11%. The DSSC is also a kind of film cell. Preparation of flexible DSSC on ITO-coated plastic substrate is very difficult. The highest heat-resistant temperature of commonly used flexible substrate made of polyimide is 330 °C, but the light transmittance ability is poor[71, 72]. Although the PET substrate has very high light transmittance, its maximum heat-resistant temperature is only 150 °C. In addition, generally, the temperature required by the follow-up sintering process of TiO_2 film is 450～500 °C; therefore, preparation of flexible DSSC needs special technology other than completely copying the common preparation technology of DSSC. Researchers have developed various TiO_2 film-forming methods under lower temperature[72～77], such as mechanical pressing, hydrothermal process, ultraviolet irradiation, microwave sintering, and so on. However, the performance of the device prepared with these methods is not higher than that of the device prepared by traditional high-temperature sintering. Researchers attempted to prepare flexible DSSC on the flexible metal substrate (such as stainless steel and so on) so that the DSSC can adapt to high-temperature sintering technology, maintain better mechanical performance, and provide a wider range for choosing the substrate. Flexible DSSC using titanium foil as the substrate was reported to have the highest efficiency, and the efficiency of this device was up to 7.2%. However, this method also has some disadvantages, such as it adopts a back-light illumination mode (serious photon loss) and still depends on transparent conductive electrode.

6.3 Flexible fiber cells

The flat flexible solar cell has made great progress, but it has some insurmountable shortcomings: ① Many flat flexible cells still depend on transparent conductive electrode; ② the demand for light transmittance, heat-resistant, humidity blocking, and purity of the substrates is high. Generally, the traditional non-flexible cell technology cannot be directly applied to the preparation of flexible cell; ③ the flat structure makes flat flexible solar cell inaccessible to fully use diffused and other stray lights.

In contrast, solar cells with non-flat structure, such as fiber solar cell[78], tubular solar cell[79], spherical solar cell[80], and so on, have distinctive advantages in the usage of photons and in device manufacturing and other aspects. The superiority of fiber cell is the most significant advantage of all non-flat-structured solar cells. ① The non-flat structured solar cell gets rid of the dependence on transparent

conductive oxide (TCO). The traditional solar cells and the reported tubular solar cell still use TCOs. Usually, TCO accounts for 30%～50% of the total cell costs. ②The fiber cell, which has a three-dimensional (3-D) structure, can catch photons from all directions to increase the power output of cells for improved optical structure capability. Meanwhile, the fiber cell has very low dependence on incident light angle and can gather diffused reflected light to maintain weatherproof and stable power output. ③ The fiber cell is a macro 1-D structure and has a smaller package area ratio than the 2-D structure. Making a larger cell requires only increasing the length of the cell. When the cell is increased to a certain size, the package area of the cell remains basically unchanged. This characteristic has direct significance in maintaining the stability of the cell, especially in applications to OPV(organic photovoltaic) and DSSC with larger size. ④ The flexible fiber cell can directly adopt traditional preparation technology, whereas special technologies must be adopted to make all kinds of traditional flexible flat cells (like OPV and DSSC) to ensure that the flexible substrate will not be damaged during the preparation process, such as by low temperature. ⑤ Existing textile techniques can be directly used in weaving for mass production of fiber cells, another further improvement of the traditional roll-to-roll technology for producing flexible electrical devices[56, 81, 82]. Therefore, the study of fiber cells has great significance in solving problems confronting traditional flat cells. Fiber cells also have a significant effect on large-scale application of solar energy to power generation, thus offering a solution to energy crisis and achieving sustainable development.

The studies of the fiber cells mainly focus on the organic and DSSCs. The keys in preparing fiber cells are solving the problems of photon harvesting and cell assembly. The methods adopted currently are the following[78]. ① Direct radiation: the incident light directly irradiates the active layer. ② Waveguide light harvesting: the light is introduced to the active layer by means of optical fiber or optical fiber analogs. ③ The cell assembly can combine the working electrode with the counter electrode of the same fiber, separate the working electrode from the counter electrode of different fibers, and then assembling these electrodes into the fiber cell. Based on the above strategies, researchers have successfully made prototypes of fiber cells using various kinds of structures. The descriptions of these prototypes are detailed in the following sections.

6.3.1 Organic fiber cells

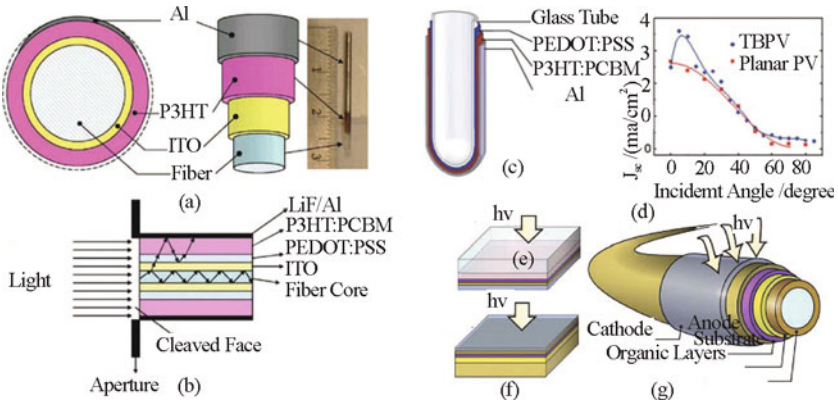

Figure 6.7 (a) Schematic of the fiber photovoltaic cell architecture. (b) Light illumination, ray diagram of light propagation, confinement of light inside the active medium through reflection from Al, and refractive index difference between the layers. (c) Schematic of the tube-based photovoltaic (TBPV) architecture and light illumination longitudinal section. (d) Comparison of the Jsc for TBPV and planar PV as a function of the incident angle. (e) ~ (g) Top illustration of the three types of PV cells fabricated and analyzed in this work. (e) An archetypal organic solar cell deposited onto ITO-coated glass. (f) A top-illuminated planar device on glass or flexible polyimide substrate. (g) Flexible polyimide-coated silica fiber substrate device with the layers deposited concentrically around the fiber and illuminated outside[83,84]

In 2007, Liu et al.[83, 84] reported an organic solar cell with a fiber structure. They prepared various functional layers on the outer layer of the optical fiber to form the structure shown in Figure 6.7(a) (Optical Fiber/ITO/PEDOT:PSS/P_3HT:PCBM/Al contact). The fiber cell with this type of structure also bends on curved surfaces, similar to the common flat structure. As shown in Figure 6.7 (b), the utilization of photon adopts the waveguide method, that is, to create a certain incident angle from one end of the optical fiber to the other end. Thus, cells can generate optical current resulting in the output performance of device dependent on the angle of the incident light. The authors found that when the incident light angle was 15° relative to the optical fiber cross section, the photoelectric conversion efficiency reached the maximum. In addition, the organic layer was very thin (around 100 nm), and the requirement for smoothness of the optical fiber substrate was very high. Therefore, forming an even film on the curved surface was difficult. Uneven film thickness of each functional layer caused many defects that seriously affected the device performance. For a fiber device with a diameter of 1.5 mm, the efficiency was less than 0.1%, and for a device with a diameter of 0.6 mm, the

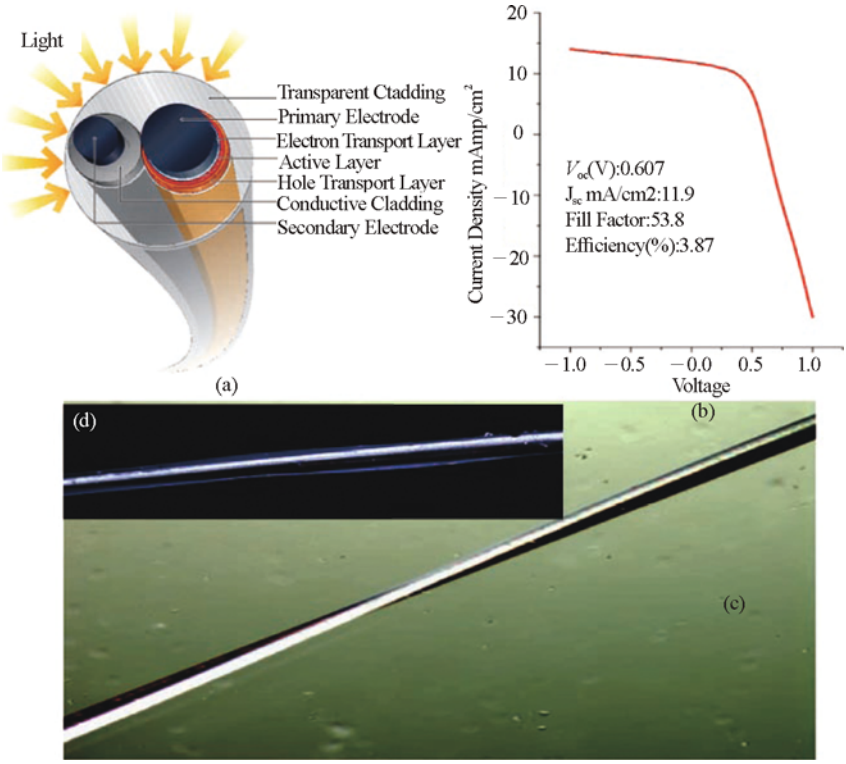

Figure 6.8 (a) Schematic of a complete fiber showing the potential for shadowing by the secondary electrode. (b) I–V curve for a PV wire with the best performance observed thus far. Jsc indicates short-circuit current. (c) Optical microscope picture of the (white) silver-coated secondary electrode wire wrapped around the coated primary electrode wire before cladding. (d) Digital microscope picture of a polymer-clad double wire[89]

efficiency was 0.6%. The length of the device was very short with a maximum of no more than 2 cm, and it was not flexible.

Li et al.[85] attempted to coat functional layer on the glass tube, adopted the waveguide method to capture light, and prepared tubular organic photovoltaic cell. The detailed structure is shown in Figure 6.7(c). Although this kind of cell had higher performance in perpendicular incidence than the flat cell, both showed no difference at higher angles. In other words, the tubular fiber cell was not different from the flat cell in relation to incident-angle dependence. The actual performance of the fiber device was similar to that of the flat cell, which is only around 0.5%. The preparation of high-efficiency fiber cell using the waveguide light harvesting method was more difficult.

O'Connor et al.[86] developed a fiber cell with another kind of structure (Figure 6.7(d)). Vacuum thermal evaporation method was adopted to prepare various functional films Mg/Mg:Au/Au/CuPc/C60/Alq3/Mg:Ag/Ag from inside to outside of a silicon-based fiber coated with polyimide film. The device used the incidence from the outermost layer to capture light. In comparison with the organic fiber cell reported by Liu et al., the device obtained through this method had lower incident-angle dependence. In the light incident-angle range from 0° to 180°, the device performance remained unchanged. Moreover, the performance of the flat cell at higher angles decreased sharply, showing the major feature of the fiber cell. It was found that the performance of the fiber cell had less dependence on its length. On the whole, the light-collecting method using outer layer transmission largely weakened the use of photons by fiber cell because of poor light transmittance in the outer layer. The photoelectric conversion efficiency of the fiber cell with a length of 3.5 cm prepared by this process was less than 0.4%.

The conclusion can be made that the preparation of efficient organic fiber cell will face many difficulties. For example, to prepare ultra-thin film of high-quality organic functional layer on the surface of the fiber electrode substrate, the requirement for device preparation technology is very high. In addition, the light-collecting area is too small using the waveguide method, and the performance of the device greatly depends on the incident angle. By adopting the external illumination method, light harvesting of organic fiber cell will be a serious problem if high-conductivity transparent counter electrode is not used. These issues significantly limit the development of the organic fiber cell. Inspired by the structural design of the fiber DSSC based on two twisted fiber electrodes[87, 88], Lee et al. adopted a double twisted structure to prepare the organic fiber photovoltaic cell[89], which largely improved the cell performance. Figure 6.8 shows the structure diagram of the cell prepared by Lee et al. and the picture of the object. Lee. et al. solved several problems faced by the previous organic fiber cells in the preparation. ① The functional layer of the organic fiber cell is very thin. The rough surface of the electrode will cause protuberance on the electrode surface more than the thickness of the functional layer; therefore, the electrodes will make contact, leading to short circuit. To solve this, they polished the surface of the metal electrode. ② As the transmission distance of excitons in organic materials is very short, n-type counter electrode materials with high conductivity and optical transparency have not been reported. Using two electrode twisted structures in fiber DSSC can successfully solve the second problem. The photoanode and counter electrode were prepared and wound for assembly, and the transparent protective layer was coated. Finally the whole fiber cell was obtained. The average

efficiency of the fiber cell prepared was 2.99%. After optimization of the electrode winding pitch, the photoelectric conversion efficiency reached 3.87%. For the organic fiber cell that they obtained with this structure, under an incident angle range of 0°~180°, the power output of the cell was largely maintained. With outer layer coating, due to the refractive effect of the coating, the performance of the cell was doubled, and its dependence on incident angle greatly decreased. Moreover, when the refractive index of the transparent coating on the outer of cell is different, its effect on the cell performance is also different. For example, when the diameter of the fiber is 100 μm and the thickness of the coating is 200 μm, the ratio is 0.5, the refractive index of the coating is 1.6, and the enhancement factor of photon utilization is 1.42, which mean that the cell can increase by 40% the utilization rate of photons through the refractive effect of the coating. Therefore, the coating can be used to further reduce optical loss and increase the output current of the cells. Thus, the cell produced in this study is definitely an organic fiber photovoltaic cell.

6.3.2 Dye-sensitized fiber solar cells

6.3.2.1 Dye-Sensitized diber solar cells based on TiO_2 nanoparticle photocathode

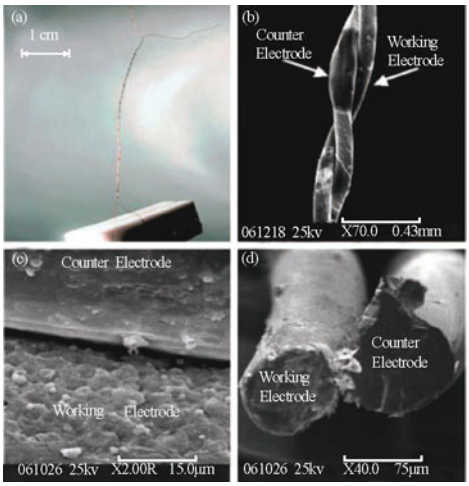

Figure 6.9 (a) Optical photograph of a twisted WSF-DSSC (Uncut; radius: 0.2 mm). (b) and (c) scanning electron microscopy (SEM) photographs of a WSF-DSSC (top view). (d) SEM photograph of a WSF-DSSC (sectional view)[87]

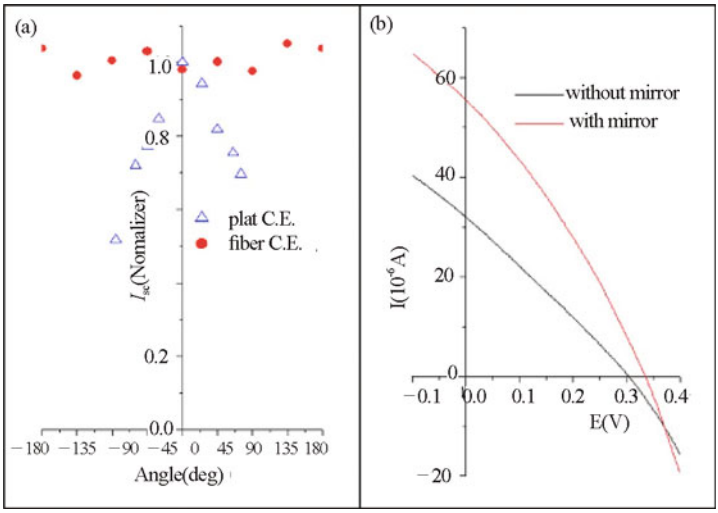

Figure 6.10 Color online Isc versus incident-light angle of cells (a) using fiber-type CE closed circle and (b) using foil-type CE open triangle. *I–V* performance of an ASFF-DSSC with or without a reflecting mirror behind[88]

DSSCs have received wide attention for more than 20 years due to their lower cost and higher efficiency[69, 77]. Fan et al.[87, 88] adopted the basic principle of DSSC to propose the fiber DSSC, and separately prepared the working and counter electrodes. The electrodes were then wound and packed into the fiber solar cell. Thereafter, the fiber cell was produced.Figure 6.9 shows the TiO_2 film on the stainless steel wire with diameter of less than 100 μm for the preparation of the optical anode of the fiber cell, which was wound together with the counter electrode (titanium wire, gold wire, Pt wire, and so on), to obtain the whole fiber cell. The photon can permeate from the gap between the counter electrode and the optical anode. In addition, the counter electrode and optical anode have a scattering effect on the incident light themselves. For this kind of fiber cell, the photon can be directly caught by the optical anode by means of scattering between electrodes. Light collection is no longer restricted. The TCO required by traditional flat cell has also been eliminated. The cell is flexible because it uses flexible metal wire. The other advantages in adopting stainless steel is that that it can be adopted directly to traditional high-temperature sintering technology used to prepare TiO_2 film in flat DSSCs. The performance of liquid fiber cell based on stainless steel substrate reported by Zou et al. was V_{oc}=610 mV, J_{sc}=1.2 mA/cm^2, FF=0.38, and PCE=0.28%. Meanwhile, Zou et al. prepared flexible solid-state

fiber cell on stainless steel substrate. This cell showed excellent stability. They compared the performance of the cells made of fiber electrode with that of the flat electrode with respect to the angle of incident light. Under the same angle of light incidence, the fiber cell had higher optical current. In addition, irrespective of the incident angle of the photon, almost no change in optical current was observed. If a reflective mirror was placed under the fiber cell, the short-circuit current and maximum output power increased exponentially, as shown in Figure 6.10. This unique 3-D light-collecting feature of the fiber cell is fully shown here in this work for the first time.

The photoelectric conversion efficiency of the liquid and solid state fiber cells prepared by Zou et al. was around 0.5%. The reason for the lower performance comes from many aspects. For example, stainless steel substrate was used in the beginning, and the energy level of the interface between TiO_2 and the stainless steel substrate was unmatched, which is disadvantageous in obtaining high open-circuit voltage. The cohesiveness of the TiO_2 colloid and stainless steel was poor; therefore, the film easily peeled off, resulting in unstable device performance. In addition, the availability of hole materials with high carrier transmission were scarce; the hole materials and bad contact of dye-sensitized optical anode placed restrictions on the improvement of the device performance. Thus, Zou et al. made many follow-up research improvements.

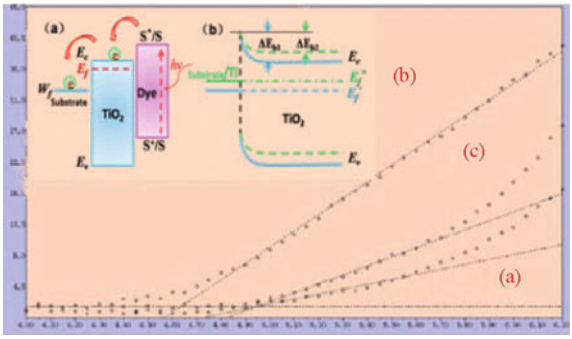

Figure 6. 11 Work function curves of (a) Ti wires cleaned with acetone and methanol and then rinsed with deionized water before drying in a nitrogen stream, (b) Ti wires sintered at 400 °C for 20 min, and (c) stainless steel wires with TiO_2 dense layer. Inset: Schematic diagram of energy level changes[92]

In DSSC, electrons are made to transfer from basic state to excited state after the dye is photo excited. Later, photons fill the conduction band (E_c) of semiconductor TiO_2. Electrons are transmitted into the TiO_2 film and cross the interface between the substrate and the TiO_2 and are then collected by the

conductive substrate. The open-circuit voltage of the device (V_{oc}) is the difference between the Fermi level (E_f) of the TiO_2 semiconductor and the oxidation–reduction potential (φI3-/I-) of the I3-/I- electron pair in the electrolyte, that is, V_{oc} = | E_f -φI^3-/I- |[70, 90]. As the electrolyte in the system is presumed to be unchanged, V_{oc} depends on the Fermi level of the TiO_2 semiconductor. In actual optical anode, when the substrate directly makes contact with TiO_2, the energy band of the TiO_2 semiconductor will combine. As shown in inset (b) of Figure 6.11, from the semiconductor TiO_2 to the substrate, the electron needs to cross an interface barrier ΔE_{b1}. Generally speaking, the surface work function of the substrate is deeper compared with the energy level of the TiO_2 conduction band; therefore, the contact between the substrate and TiO_2 will cause a negative offset of the Fermi level of the TiO_2 semiconductor, that is, if $|E_{f'}| > |E_f|$, then V_{oc} decreases[91]. If the interface barrier of the substrate and the TiO_2 is effectively decreased, the open-circuit voltage will also effectively increase. Therefore, the performance of the device will be improved. Figure 6.11 shows the titanium wire, sintered titanium wire, and the surface function curve of the stainless steel wire prepared for TiO_2. In the figure, the energy threshold value corresponding to the first knee point of each curve line expresses the surface function value. Curve lines a and c show that the surface functions of the titanium and treated stainless steel wires are 4.95 eV. After high-temperature sintering, the surface of the titanium will form into TiO_2 tectum, the surface work function reduces from 4.95 to 4.64 eV, the Fermi level increases accordingly ($|E_{f'}| > |E_{f'}|$), and the interface barrier also decreases ($\Delta E_{b2} < \Delta E_{b1}$), resulting in the reduction of the transmission resistance of the TiO_2/substrate. As the transmission and collection efficiency of the carriers increase, the comprehensive performance of the device is predicted to also increase. Table 6.1 shows the performance parameters of solid fiber cell using stainless steel and titanium wires as substrate. The titanium wire-based devices are better than the devices using stainless steel as substrate in open-circuit voltage, short-circuit current, packing factor, photoelectric conversion efficiency, and other aspects[92].

On the other hand, the pore-forming agent is used to enlarge the porosity in TiO_2 film, which can increase the contact area of the solid electrolyte CuI and the dye-sensitized TiO_2 nanoparticle to improve the transmission of carrier in the cell[92]. The detailed method is to use P25 TiO_2 colloid mixed with PS to prepare the TiO_2 film. The sintering method is used to remove PS small ball and to improve the porosity of the film, resulting in the increase of the hole-filling rate of solid electrolyte in the TiO_2 film. This presents a favorable condition for the formation of valid interface contact by decreasing the transfer resistance of the interface between the electrolyte and the TiO_2 and improving the device performance.

Figure 6.12 shows the surface appearance of the optical anode after sintering and being mixed with PS small ball. Doping result shows that the pore space between particles significantly increases, and the device performance clearly improves (Table 6.1). The optimized photoelectric conversion efficiency of the device can be further increased to 1.58%[92].

Table 6.1 All solid-state fiber-shaped solar cell based on stainless steel wire (S-based), Ti wire (Ti-based) and polystyrene (PS)

Sample	V_e/V	$J_{sc}/(mA/cm^2)$		$\eta/\%$
S-based	0.27	1.85	0.42	0.21
Ti-based	0.34	3.83	0.54	0.71
Ti-based-PS-2	0.36	6.49	0.58	1.38

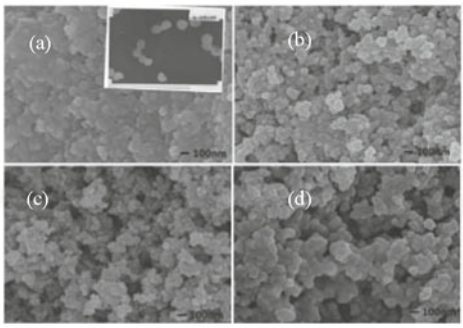

Figure 6.12 SEM images of the surface morphology of mesoporous films (top view) with varied PS emulsion volume ratios. (a)～(d) Samples in order of PS emulsion/P25 colloid 0, 0.15:1, 0.3:1, 0.6:1 (ml). Inset: Transmission electron microscopy (TEM) of PS emulsion; the size of the sphere is 100 nm[92]

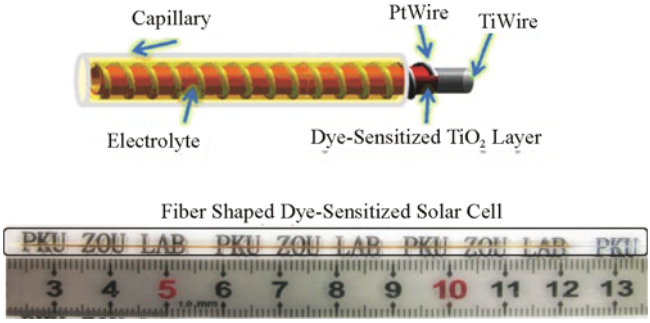

Figure 6.13 Structure schematic diagram and optical photograph of large-size fiber solar cell[94]

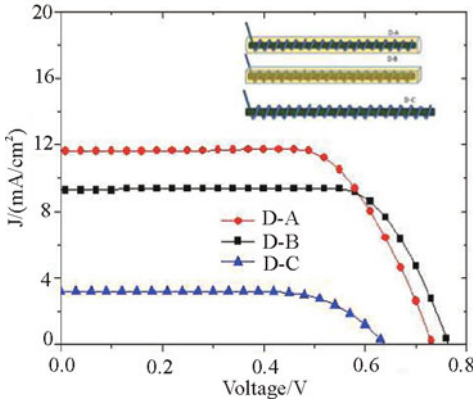

Figure 6.14 *J–V* curves of D-A, D-B, and D-C cells under standard illumination. The inset of Figure 6. 14 shows the different sealing of D-A, D-B, and D-C. D-A is sealed in a circular capillary tube, D-B is sealed in a rectangular glass slot, and D-C is not sealed. All cell lengths are 2.00 cm[94]

The solid fiber cell has low performance due to the limited hole transport materials. Liquid-state cell has more advantages. However, the traditional flat liquid-state electrolyte evaporates easily, and the encapsulation materials can be eroded and cause leakage of electrolyte, which can affect its stability. For the cell in the flat structure, the long encapsulation around the flat plate side may cause the following disadvantages: complicated time-consuming encapsulation process that is also costly in terms of material usage; longer encapsulation sideline; and greater leakage probability. Actually, the encapsulation part is a non-working section of the cell. The longer the encapsulation sideline, the lower the average area efficiency of the cell. Moreover, the sealing layer easily cracks because of the action of thermal expansion and stress after the two flat plates are encapsulated together, which also affects the stability of the flat cell[25, 93]. These issues limit the mass production and application of DSSCs with large flat plate area. For the liquid-state fiber cell, the required encapsulation area is very small. The larger the cell size, the smaller the encapsulation area ratio. The effective light-collecting area ratio also becomes large. Liquid-state fiber cell shows greater advantages than traditional flat cell, particularly in large-size cells. In most cases, due to limitations of sheet conductivity of FTO, the efficiency of the traditional flat cell will rapidly drop down with the increase of cell size. This is one of the most important factors hindering the practical application of DSSCs.

Lv et al[94]. used titanium wire instead of stainless steel wire and changed the previous double helix wound structure to a single wound structure (Figure 6.13) to prepare a 10 cm-long fiber solar cell. The photoelectric conversion efficiency

of the cell increased to 5.41%. Another feature was the use of capillary to make cell encapsulation. However, the light-concentrating action of the capillary on device performance had to be considered. Lv et al[94]. compared the effect of different encapsulation forms on the fiber cell. Figure 6.14 shows the comparison of D-A (round capillary encapsulation), D-B (square capillary encapsulation), and D-C (without any encapsulation). Testing was done immediately after using the capillary phenomenon of fiber cell to absorb the electrolyte. The device is characterized by the following: For the device adopting round casing encapsulation (D-A), the V_{oc}, J_{sc}, FF, and PCE are 0.733 V, 11.64 mA/cm^2, 0.684, and 5.84%, respectively. In contrast, the corresponding values of the device adopting square clamping casing encapsulation (D-B) are 0.765 V, 9.27 mA/cm^2, 0.750, and 5.32%, respectively. The former has −4%, 25%, −9%, and 9% difference than the latter in V_{oc}, J_{sc}, FF, and PCE. For the D-C cell without any encapsulation, the corresponding values are 0.643 V, 3.27 mA/cm^2, 0.675, and 1.42%, respectively. Except for open-circuit voltage, the other data are far smaller than those of D-A and D-B cells. The open-circuit voltage of DSSC mainly depends on the Fermi energy level of TiO_2 and energy level difference of the electrolyte redox couple. Therefore, the geometric shapes of the encapsulating casing have less influence. Generally, the parallel glass clamping casing has no light-concentrating function. Irrespective of the absorption of electrolyte liquid, the maximum illuminated area of the D-B cell is equal to the product of the projected area of the fiber cell and irradiation density. For the D-A device, if the light that enters into the capillary is completely concentrated onto the fiber cell, the illuminated area of the D-A cell can increase 1.6 times based on the ratio of diameter of the capillary (0.8 mm) to the diameter of the fiber cell (0.3 mm), irrespective of the surface reflection of the capillary. Under an assumption of unchanged absorption capacity of the dye, the short-circuit photocurrent should increase by a maximum of 160%; based on the light-concentrating effect reported in literature, the illuminated area of the D-A cell will increase by at least 60%, and the corresponding short-circuit current can increase by 60%. However, the short-circuit current of D-A increases only by 25%, and the device efficiency increases only by 9%. In comparison with D-B, D-A proves that, at least, the light-concentrating effect is not the most important factor for this type of cell in relation to high efficiency. The light-concentrating effect of round capillary has limited effect on the increase of device performance. The above results also indicate that using the projected area of fiber cell as the illuminated area to calculate the device efficiency is basically reasonable.

From the comparison of the D-A and D-B devices, the impact of the encapsulation tube's light-concentrating effect can be eliminated. The D-A and D-C

devices have the same kind of optical anode; thus, they have the same photon-absorption capacity. However, the D-A device has very high efficiency, whereas the D-C device has very low efficiency. In comparison with traditional flat structure, the structure of the D-A cell has the following characteristics: First, for the flat cell, the coverage rate of electrode to optical anode is 100%. In this kind of cell structure, the projected area ratio of the counter electrode to the working electrode meets Eq. (6.1). The counter electrode is not a flat but a round wire, thus

$$P_s = \frac{d\sqrt{(L_p^2 + \pi^2 D^2)}}{\pi D L_p} \quad ; \quad P_T = 1 - P_s \tag{6.1}$$

The direct contact area of the counter and working electrodes is far smaller than the value worked out based on Eq.(6.1). For example, under the condition that the diameter of the optical anode is 0.3 mm, the diameter of the counter electrode is 0.03 mm and the thread pitch is 0.3 mm; the maximum coverage rate of the counter electrode on the surface of the optical anode is 14%. Considering that the counter electrode wire is round-shaped, the actual coverage rate is far smaller than 14%. In other words, less than 14% of the surface of the optical anode of the fiber cell makes contact with the counter electrode. From the design principle of the flat cell, the above result is very disadvantageous for collecting electric charge. Second, for the flat devices, a separating space layer is present, and there is at least one electrolyte layer to separate the optical anode from the counter electrode. This corresponding separating layer or space, also present in the other structures of the fiber cell, is generally aimed at preventing short circuit and return pass of electric charge. In addition, in this kind of cells, the counter electrode contacts and winds with the working electrode. Third, in this kind of structure, the light can reach the sensitized layer and be absorbed by the dye molecules after it passes through the electrolyte solution (partial photon is absorbed by the electrolyte solution); therefore, part of the light is lost in the absorption of electrolyte solution, causing it to have no substantive contribution to the photoelectric conversion[95]. The D-A and D-C devices have the same characteristics. The only difference is that the D-A device uses capillary encapsulation, whereas the D-C device is bare. The structure of the D-A device is mainly designed to restrain the volatilization of the electrolyte solution to maintain the transport and supply of electrolyte and thus ensure high efficiency of the device. Theoretical and experimental evidence shows that the diffusion of I_3- in TiO_2 in porous film and in electrolyte solution is one of the most important factors that restrain device performance. Furthermore, for some systems, sufficient quantity of I_3-/I- redox electric couple can ensure efficient completion of the transport process of the internal carriers.

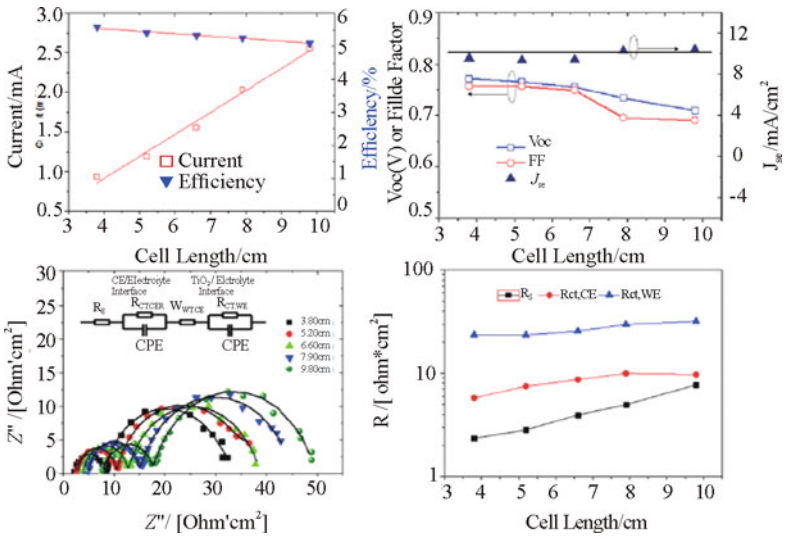

Figure 6.15 (a) Short-circuit current and efficiency of fiber-shaped solar cell D-A with varying device length from 3.80 to 9.80 cm. (b) V_{oc}, J_{sc}, and FF of the fiber-shaped solar cell D-A with various device lengths. (c) Nyquist plots of fiber-shaped DSSCs with different lengths under 100 mW/cm^2 and bias V_{oc}. Dots represent experimental data and lines represent fitting curves. Inset shows the equivalent circuit of EIS for fitting. (d) Parameters extracted from (b) versus cell length[94]

To realize practical application of the fiber cells, the cell size must be increased. The performance of the traditional flat cell may drop down sharply after the size is increased. However, the same is not true for the fiber cell. Zou et al. prepared a series of fiber cells with different lengths, and they compared the relationship between the *I*–*V* performance of the device and the length. Figure 6.15 shows that with device lengths from 3.8 to 9.8 cm, the short-circuit current increases linearly with increase in length; the short-circuit current density maintains the same level, but the device efficiency slightly drops. In Figure 6.15, the AC impedance test result shows that the interface transfer resistance of the cell, including Rct,WE, Rct,CE, and R_s, changes a little with the change of the cell size. These results indicate that size has little impact on the performance of the fiber cell. Therefore, the length of the cell must be increased to enlarge the size of the fiber cell.

6.3.2.2 Fiber solar cell based on TiO_2 nanotube array photocathode

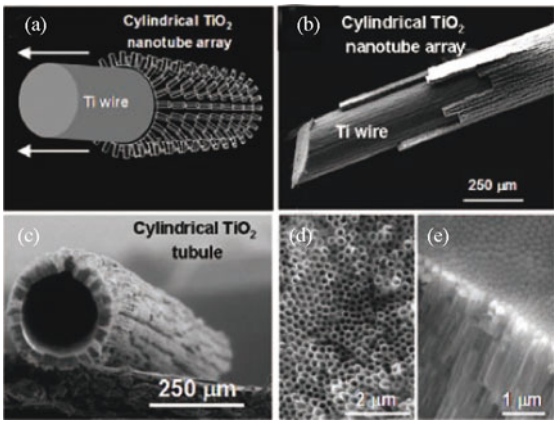

Figure 6.16 Structure characterization of the TNT arrays. (a) Schematic diagram of an anodized Ti wire with the TNT array outer layer wrapping the inner Ti core. (b) FESEM image of an anodized Ti wire whose outer TNT array was partially peeled off. (c) FESEM image of a free-standing cylindrical TiO_2 tubule with its Ti core completely removed by chemical etching. (d) Top and (e) bottom view of the TNT array by FESEM[100]

In an earlier report, the TiO_2 nanoparticle was coated on the stainless steel wire to prepare the fiber cell, which used two electrodes in the cross-wound structure. The connectivity of TiO_2 nanoparticle to the cell was poor. The TiO_2 nanoparticle film blocked electric transmission and aggravated electrical recombination because of the defects between particles, limiting the increase of the device performance. Adopting TiO_2 film in 1-D ordered nanostructure is one of the important methods for preparing more efficient fiber cells. TiO_2 nanotubes prepared by means of electrochemical oxidation have 1-D electric transmission path and high specific surface area. Traditional flat cells adopting TiO_2 nanotube array film on the surface can effectively improve the collection efficiency of electric charge, and the cell efficiency can reach more than 7%[96~99]. TiO_2 nanotube array can be applied in the preparation of middle- and high-efficiency fiber cells.

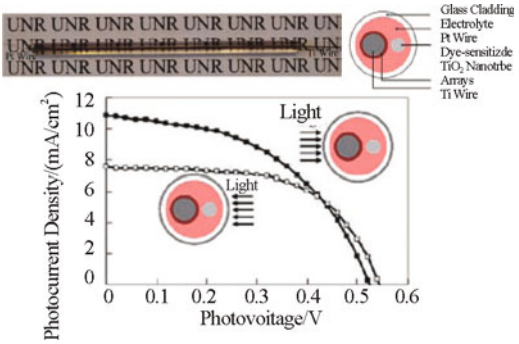

Figure 6.17 *J-V* curves of a prototype DSPVW using 55 m-long TiO_2 nanotube arrays under illumination from (solid symbols) the working electrode and from (hollow symbols) the platinum counter electrode. Insets show the incident direction of light irradiation[101]

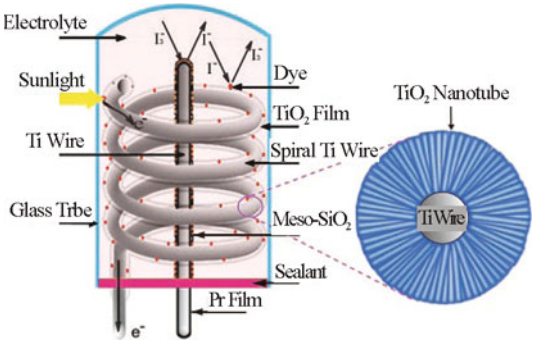

Figure 6. 18 Design and principle of a mini 3-D DSSC. TNA film, grown in situ on spiral-shaped titanium substrate, serves as the photoanode. A straight titanium wire substrate, coated with a layer of Pt, is used as the counter electrode. A porous SiO_2 film is coated on the counter electrode as an electronic insulator spacer. Electrodes and electrolyte are all enveloped in the capillary glass tube[102]

Yu and Wang et al.[100] adopted anodic oxidation method to prepare the optical anode of the fiber solar cell (Figure 6.16 shows the structure of optical anode) and attempted to prepare quasi solid-state and all-solid-state fiber solar cells based on this. The quasi-solid state efficiency was 1.5%, and the all solid-state efficiency was 0.21%. Even though the efficiency of their prepared device was not high, the anodic oxidation method made the preparation of the optical anode of the fiber solar cell very simple. The morphology, hole diameter, length, and other features of the TiO_2 nanotube can be controlled by electrolyte composition and adjustment of electrochemical parameters (e.g., voltage, electrolysis time,

and so on). Therefore, many works related to fiber cells adopted anodic oxidation method to prepare the fiber solar cells compared with other structures previously reported, such as fiber cells with structures where the working electrode is parallel to the counter electrode, helix optical anode structure, and quantum dot-sensitized flexible flat encapsulation structure.

Liu et al.[101] prepared TiO_2 nanoarray optical anode by means of anodic oxidation. The sensitized optical anode is placed parallel to the Pt wire as the counter electrode and packed in glass capillary to obtain the new fiber cell using a structure where the optical anode is parallel to the counter electrode. This kind of cell was 2 cm long (Figure 6.17), and the photoelectric conversion efficiency of the device was more than 2%. In comparison with the cells prepared without encapsulation, the efficiency improved to a certain extent. However, this cell had strong dependence on the angle of the incident light. When the light illuminates from the optical anode, the device performance is J_{sc} =10.9 mA/cm^2 and PCE=2.46%. When the light illuminates from the counter electrode, the performance of the device is J_{sc} =7.56 mA/cm^2 and PCE= 2.16 %,, which indicated a very strong dependence on the incident light angle. Obviously, the comprehensive performance of this fiber cell having such structure is worse than that of previous double-wound structure.

Wang et al.[102] prepared a fiber cell with a different kind of structure in terms of the optical anode. As shown in Figure 6.18, they made a spring-shaped titanium wire and used anodic oxidation method to grow TiO_2 nanotube array. Afterward, they inserted the Pt counter electrode into the center of the sensitized helix optical anode, and packed them in a capillary filled with electrolyte to prepare a kind of front-irradiated fiber solar cell. The photoelectric conversion efficiency was 4.05%. In addition, Wang et al. compared the difference between the performance of flat and fiber cells. They found that the fiber cell had higher performance and better spectral response. However, for this method, making the electrode helix was difficult. Control was also difficult because of the large distance between the two electrodes.

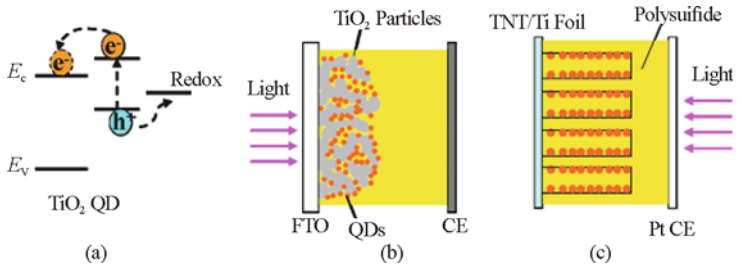

Figure 6. 19 (a) Energy diagram of QD-SSC. (b) Configurations of the front-side-illuminated QD-SSC-based TiO_2 nanoparticles. (c) Backside-illuminated QD-SSC based on TNT[103]

The quantum dot sensitized solar cell has received more attention recently. In comparison with traditional DSSC, it has the following characteristics: ① The bandgap of the quantum dot semiconductor can be regulated and controlled by means of the size of quantum dots to make the quantum absorption bandgap match the sun spectrum; ② The quantum dots have very high extinction coefficient, and the avalanche ion will generate many electron–hole pairs, thus obtaining very high photoelectric conversion efficiency; ③ It is anti-corrosive, has lower costs, and is easily synthesized. The basic working principle of quantum dots sensitized fiber cell is similar to that of traditional DSSC (Figure 6.19). The quantum dot sensitized solar cell consists of four parts: optical anode, quantum dot sensitizer, electrolyte, and counter electrode. During illumination, the excited state electrons fill quantum dots into the wide bandgap semiconductors (such as TiO_2 and ZnO), and the hole is eliminated by means of redox electric couple in electrolyte (generally S_2^{-}/Sn^{2-}). Meng et al[103]. conducted a process that led the quantum dots to the fiber cell. They used quantum dots to replace traditional metal coordination Ru dye, replaced the I^{3-}/I^{-} electrolyte with Na_2S electrolyte, and replaced the Pt counter electrode with sulfurated copper wire. They used the device structure proposed by Zou et al. to prepare the first low-cost quantum dot sensitized solar cell. When the film thickness in the TiO_2 nanotube array was 28 μm, the photoelectric efficiency of the device was 3.18%. However, the flexible flat cell encapsulation is not entirely a fiber cell, making it unfit for the modular method of weaving technology adopted in fiber cells.

6.3.2.3 Fiber solar cell based on ZnO nanoline optical anode

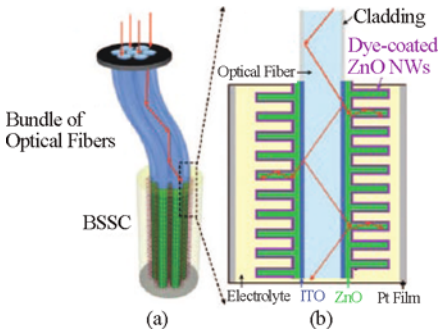

Figure 6. 20 Design and principle of a 3-D DSSC. The cross-section of the fiber can be cylindrical or rectangular. (a) The 3-D DSSC is composed of optical fibers, and ZnO NWs are grown vertically on the fiber surface. The top segment of the bundled optical fibers utilizes conventional optical fibers and allows for remote transmission of light. The bottom segment consists of 3-D DSSC for solar power generation at a remote/concealed location. (b) Detailed structure of the 3-D DSSC[104]

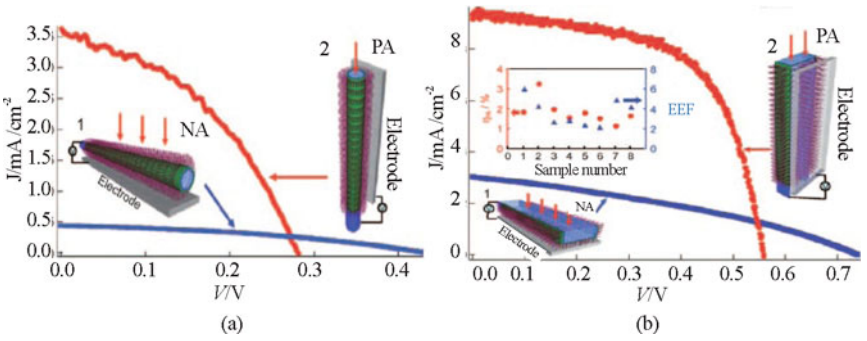

Figure 6. 21 (a) Cylindrical optical fiber-based 3-D DSSC and its performance. (b) Rectangular optical-fiber-based 3-D DSSC and its performance. Current density J and voltage V curves of a DSSC under one full sun illumination orientation (1) normal to the fiber axis (NA; 2-D case) and (2) parallel to the fiber axis (PA; 3-D case)[104]

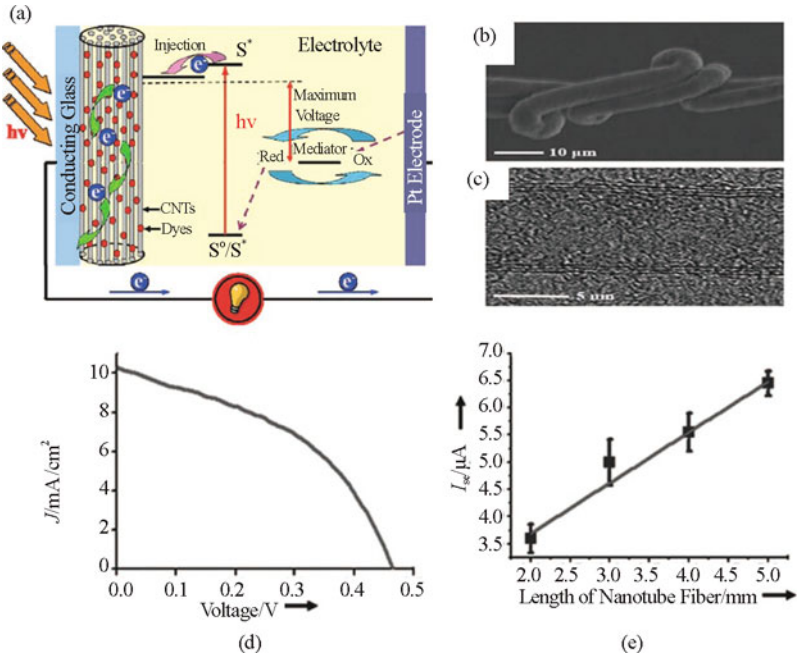

Figure 6. 22 (a) Schematic diagram of the production and transportation of photoelectron in a nanotube fiber solar cell. CNTs represent carbon nanotubes. (b) carbon nanotube fibers characterized by SEM and (c) TEM. (d) J-V curve of a solar cell under simulated 100 mW/cm^2 illumination. (e) Dependence of the short-circuit current on the length of nanotube fibers in solar cells[105]

Fiber cell technology fits all kinds of solar cell fiber substrates using several principles. Weintraub et al.[104] adopted ZnO nanowire grown on optical fiber to prepare a new type of fiber DSSC based on the optical fiber substrate (Figure 6.20). They coated a layer of ITO on the optical fiber. Thus, a layer of ordered ZnO nanowire array on the outside of round optical fiber was made to prepare the fiber cell after being dye-sensitized. This kind of cell includes two kinds of light-gathering methods (Figure 6.36). One is the waveguide method where the sunlight illuminates the solar cell from the optical fiber and is then absorbed by the active layer to generate photocurrent. The device performance is shown in Figure 6.21; J_{sc} =3.73 mA/cm^2, V_{oc} =0.283 V, FF=0.414, and PCEPA = 0.44%. Another method is the direct illumination (PA) where the device performance is shown in Figure 6.21; J_{sc} =0.44 mA/cm^2, V_{oc} =0.433 V, FF=0.375, and PCENA = 0.071%. In the NA method, the photoelectric conversion efficiency of the device is 6.1 times that in PA.

The fiber cell that adopts round optical fiber structure has very low photoelectric conversion efficiency (Figure 6.21). The photocurrent in PA is also far more than that in NA, but the photovoltage is smaller. Wang et al. believed that the reason to be the larger than usual average diffusion distance of the carrier on the round structural electrode. Therefore, they changed the round electrode fiber electrode with a square interface to prepare the corresponding electric device (Figure 6.21). Under NA condition, the device performance was J_{sc} = 3.02 mA/cm^2, V_{oc} = 0.739 V, FF=0.342, and PCE_{NA} =0.76%. Under PA condition, the performance was J_{sc} = 9.5 mA/cm^2, V_{oc} =0.559 V, FF=0.623, and PCE_{PA} =3.3%. Wang et al. believed that in the cells they prepared, the NA illumination method was for a 2-D cell light-collecting structure, whereas the PA illumination method was for a 3-D light-collecting structure. NA had a higher performance than PA. This result was in contrast to that of the fiber cell reported earlier. In particular, the fiber solar cell based on the principle of DSSC has higher performance in direct illumination (NA). The difference is that the fiber cell prepared by Wang et al. was equivalent to the sandwich flat device structure of traditional flat cell, and the fiber cell prepared by Zou et al. was a 3-D wound structure. This structural difference caused the difference in the performance, further proving the superiority of the 3-D structure of the fiber cell.

6.3.2.4 Fiber dye-sensitized solar cell based on carbon nanotube fiber

Carbon nanotube, which has very high specific surface area and better conductivity, is widely applied as electrode materials of DSSC. Carbon nanotube fiber is a new type of carbon material that has been recently developed. The

internal part is a high-order carbon nanotube array with excellent mechanical strength, high specific surface area, and better conductivity. Carbon nanotube has great potential application. Figure 6.22 shows a SEM picture of this new type of carbon material. Based on excellent characteristics of carbon nanotube, Chen et al.[105] used dye-sensitized carbon nanotube fiber to directly prepare flexible fiber solar cell. As shown in Figure 6.22, the working principle of this cell is not different from the traditional dye-sensitized cell. The only difference is that the TiO_2 anode is replaced by carbon nanotube fiber with high specific surface area. The basic performance of the fiber cell obtained under light intensity of 100 mW/cm^2 was J_{sc} = 10.3 mA/cm^2, V_{oc} = 0.47 V, FF = 0.45, and PCE = 2.2%, and the short-circuit current of the cell has a linear relationship with the length of the cell (Figure 6.22), conforming with the relationship between the performance of the fiber cell and the cell length reported by Lv et al[94]. However, as shown in Figure 6.22, even if the optical anode is fiber-shaped, the whole cell is flat. With little improvement, for example, after the optical anode of carbon nanotube fiber is wrapped around and combined with the counter electrode of the carbon fiber, the real definition of a fiber solar cell can be attained. In addition, this type of solar cell is cheaper with the complete elimination of ITO.

6.4 Module of the fiber cell

Fiber-based solar cell comes in single-wire or in modular form. The modular form of the fiber cell adopts direct current-weaving technology. The weaving technology is applied in the manufacture of the fiber sensor and detector. However, due to the limitation of current research, making a fiber-based cell module using direct weaving technology is difficult. Many key technologies remain to be explored, and the foregoing is one of the key problems to be addressed. People have attempted to use screen substrate as an alternative to make fiber solar cell.

6.4.1 Module of screen electrodes

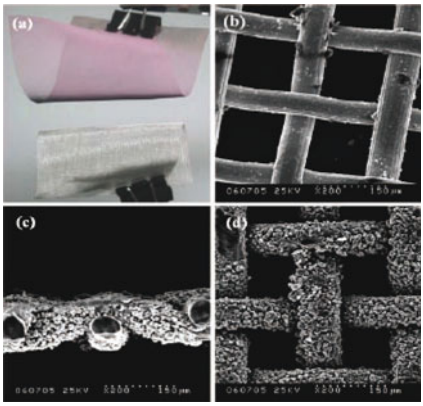

Figure 6.23 (a) Optical photograph of the as-prepared upper electrode of 45.7 cm^2 and the lower net substrate of 45.5 cm^2. (b) SEM photographs of the mesh substrate. (c) and (d) Top and sectional views of the as-prepared electrode, respectively[106]

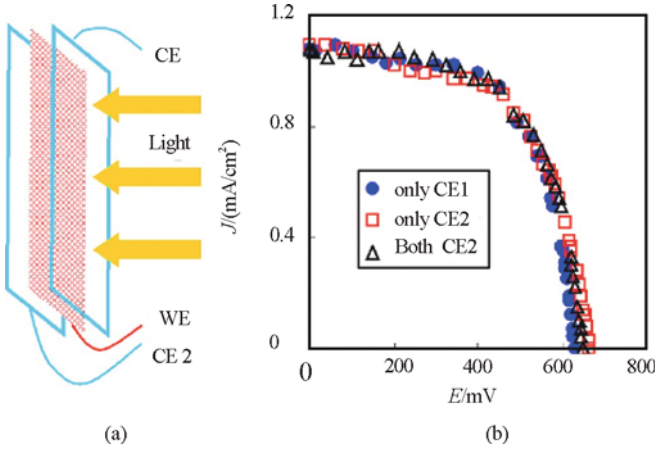

Figure 6.24 (a) Structure of the double counter electrode cell. (b) I–V performance of DCEC with CE1 only, CE2 only, and both CE1 and CE2[106]

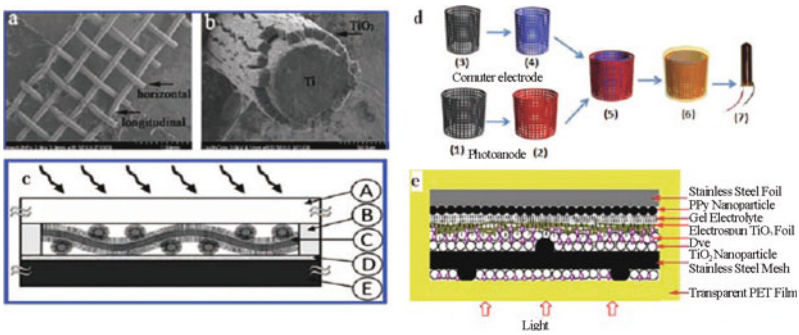

Figure 6. 25 FESEM images of TiO_2 nanotube arrays on Ti mesh (50 mesh) fabricated by anodization at 60 V for 3 h. (a) Low-magnification overall image of the anodized mesh. (b) Low-magnification cross-section of TiO_2 nanotube arrays on a single Ti wire. (c) Cross-sectional schematic of DSSC with a Ti mesh-TiO_2 nanotube architecture. Components are (A) cover glass, (B) 200 μm PTFE spacer, (C) anodized Ti wire mesh, (D) 30 μm porous PTFE membrane, and (E) cathode. The figure does not show the ring of unanodized mesh that surrounds the central anodized portion and the tab of mesh that extends past one edge of the glass/spacer for external connection. (d) Schematic flow diagram for the fabrication of the 3-D DSSC: (1) Ti mesh cylinder used as substrate of the photoanode. (2) Sensitized photoanode. (3) Ti mesh cylinder used as substrate of the counter electrode. (4) Counter electrode based on platinized Ti mesh cylinder. (5) Double-deck mesh-like electrodes. (6) Sealed 3-D DSSC. (7) Fabricated 3-D DSSC with lead wires. (e) Structure of the flexible quasi-solid DSSC based on stainless steel foil and mesh[107]

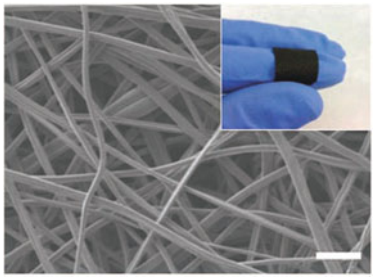

Figure 6.26 SEM image of the carbonized carbon fiber fabric with an average diameter of 1.16 μm. Scale mark corresponds to 10μm[107]

In 2007, Chen et al.[105] were the first to report the efficiency of DSSC based on stainless steel screen. They used a spray gun to coat TiO_2 film on stainless screen to prepare the optical anode. Figure 6.23 shows the electrode morphology. In the early stage, the performance of the cell was not good, with efficiency of

only 1.46% (Figure 6.24). However, using a double counter electrode cell, such as that shown in Figure 6.24, proved that the application of screen electrode does not affect the transportation of carriers in the cell. Thus, the transportation of carriers in the screen cell was not different from that of the traditional flat cell, serving as the basis of the later preparation of efficient screen cell. Shortly thereafter, Liu et al.[107] used titanium screen to replace stainless wire and adopted anodic oxide growth of TiO_2 nanotube to prepare a net-based solar cell. Figure 6.25(a) and (b) show that the photoelectric efficiency of the cell is equal to 1.47% of that of the stainless wire cell. Meanwhile, studies found that the hole diameter of the screen has an effect on the performance of the cell. DSSC prepared by a 50-mesh screen cell was better than DSSC prepared by a 30-mesh screen. In other words, although the weaving density of the screen was increased, the performance of the device did not worsen as a result of bad transmission of light to the screen. Thus, weaving technology can be used to prepare highly efficient fiber cell module. Unfortunately, the above-mentioned works did encapsulate the cells but directly filled in the electrolyte in their tests. From previous discussions, proper encapsulation is the key to preparing highly efficient fiber cell. Based on this idea, Rustomji et al.[108] encapsulated the cell pairs(Figure 6.25 (c))to prepare a fiber cell based on weaved titanium screen. Its efficiency largely improved to more than 5%. In addition, the screen is flexible; thus, the screen cell can be bent at will. Rustomji et al.[108] took advantage of this characteristic to bend the screen optical anode and counter electrode and then nested each in a glass tube to prepare a 3-D screen solar cell (Figure 6.25 (d)). At present, the photoelectric conversion efficiency of this structural device is up to 5.05%, and it still retains the 3-D light-collecting features of a fiber cell. For example, the performance does not change with the angle of incident light. However, the works of Lu et al. were based on the principle of liquid DSSC. In most cases, acetonitrile is used as I3-/I- electrolyte solvent. The electrolyte easily evaporates and is unfavorable for the stability of the cell. The encapsulation requirement is also high. Tan et al. started from the electrolyte to prepare quasi-solid flexible dye-sensitized screen cell based on stainless screen (Figure 6.25 (e)) for the structure of the cell. The efficiency of this device was J_{sc}=5.14 mA/cm^2, V_{oc}=0.746V, FF=0.730, and PCE= 2.80%. In addition, carbon fiber was also used to prepare the screen cell (Figure 6.26). The photoelectric conversion efficiency of the cell was less than 0.5% because the interface energy level was unmatched. Unfortunately, although the screen electrodes in these screen cells were flexible, the reported works adopted mostly a non-flexible encapsulating case, particularly glass, to make the encapsulation, which is disadvantageous to transportation and installation in the cell. Therefore, the flexible screen-based

DSSC reported previously was not entirely flexible. The device is flexible only when it uses flexible encapsulation. Currently, there is no report concerning works in this field, hence the absence of solid screen flexible cell. Therefore, study in this field still has much room for development.

6.4.2 Module of single-wire solar cell array arrangement

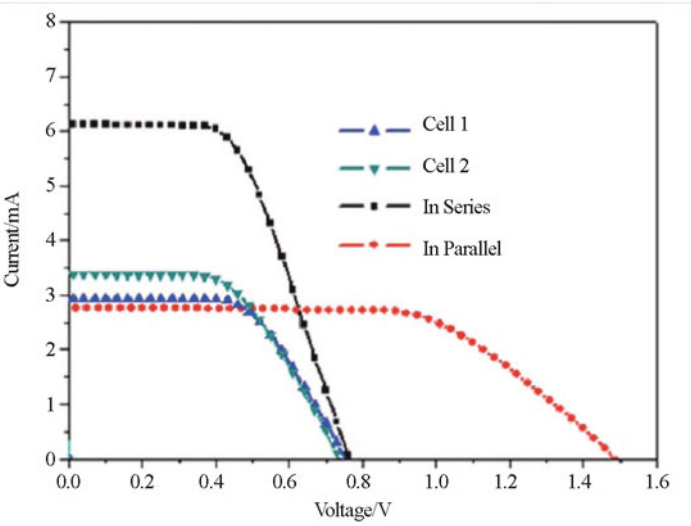

Figure 6.27 *I-V* curves of two different fiber cell units and their serial and parallel connections[94]

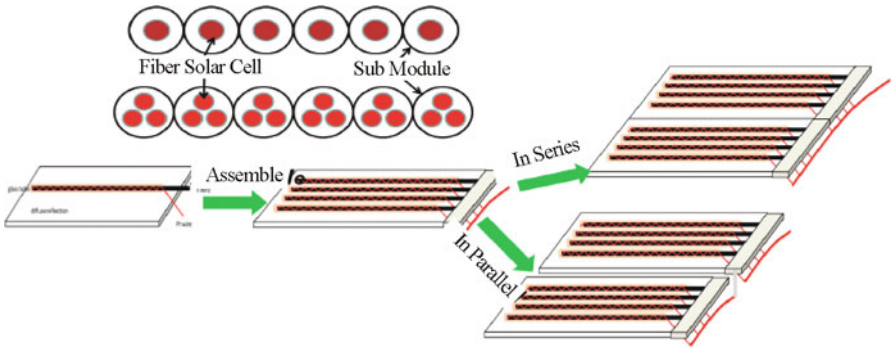

Figure 6.28 Scheme of the fabrication of solar cell module using fiber solar cells. Each fiber solar cell is placed on a diffusion board and is combined in series or parallel using a metal wire connection. Inset shows the crossing of the module and FDSC units [one cell in one capillary or multi-cell (e.g., three fiber solar cell units in one capillary)]

For the modular fiber cell preparation, another method is to use single cells connected in series and parallel to form the solar module. Actually, for an independent fiber cell unit (equivalent to an ordinary dry cell), only the combination of series and parallel connection can make the cell module attain the required current or voltage output[94]. In comparison with the complicated circuit of the flat cell, the previous process is simpler and more reliable. Figure 6.27 shows two independent fiber cells and their I-V performances after being connected in series and parallel: cell 1, V_{oc}=0.753 V; I_{sc}=2.96 mA and cell 2, V_{oc}=0.735 V and I_{sc}=3.39 mA. With parallel connection: V_{oc}=0.763 V and Itotal= 6.11 mA or equal to the sum of the short-circuit currents of two independent cells (6.35 mA). With series connection: V_{oc}=1.490 V or equal to the sum of the open-circuit voltages of two cells (1.488V). This result indicates that simple line-to-line connection can enable assembly of the device module with specific output current, voltage, and power, definitely very favorable for preparation of large-scale modules. Other advantages of the fiber cell module include the following. The electrolyte solution in the module or between modules can be recycled or replaced, such as connecting one end of the capillary with another electrolyte supply source, and a single module can be repaired when it fails. Figure 6.28 shows how to use a single fiber cell to prepare the fiber cell module. In fact, single fiber cell can be further designed to obtain submodules, including single- or multi-optical anode (e.g., three wires) for encapsulation to form a submodule, and this submodule is assembled to form a module by means of series and parallel connections. Finally, the series and parallel connections between modules are made to form a practical component. The performance of a submodular cell composed of three photoanodes is better than that of a submodular cell composed of a single cell. Therefore, the versatility of this modular design can meet design requirements for different voltages and currents for practical application.

6.4.3 Module of roll-to-roll, mass production, and weaving technology

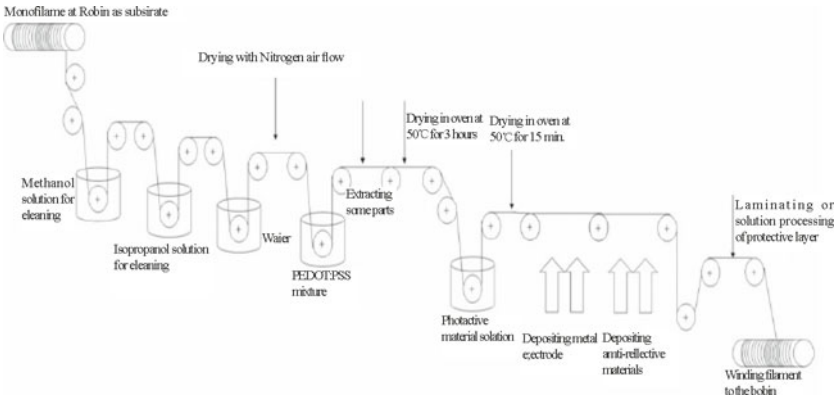

Figure 6.29 Possible manufacturing processes for photovoltaic fiber[110]

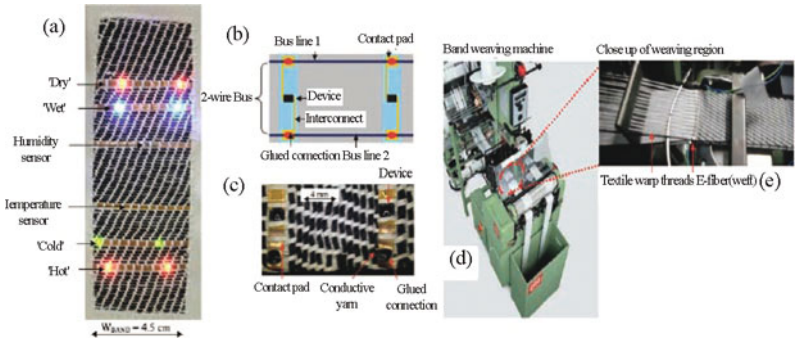

Figure 6. 30 (a) Close-up of smart textile band inside a tablecloth. (b) Schematic of a two-wire bus structure implemented in textile using conductive yarn to connect the contact pads of adjacent fibers. (c) Section of an actual textile containing woven e-fibers with digital temperature sensor integrated circuits that communicate using a two-wire bus protocol connected using conductive yarns. (d) Picture of the band weaving machine used and a close-up of the weaving region. (e) showing an inserted e-fiber being woven into the textile band[82]

The most attractive feature of the fiber cell is the adoption of the traditional preparation for original fiber and textile technology. Figure 6.29 shows a feasible industrial preparation technology for a single-electrode fiber cell based on organic photovoltaic principle[110]. Similarly, the industrial production technology for single-electrode fiber cell based on the DSSC principle can be adopted. After

completion of the single-electrode preparation, textile technology can be used to prepare the fiber cell. Currently, this technology is not used in the production of fiber cell fabrics; however, this has been applied to the manufacture of fabrics for other fiber electric devices[82]. Figure 6.30 shows the fiber sensor and OLED fabric. Therefore, we believe that the preparation of fiber cell fabric by means of the weaving technology will someday materialize based on the continuous innovation of materials and improvement of the preparation level of the device.

6.5 Three-dimensional light-collecting feature of fiber cell

One of the advantages of FPV(fiber photovoltaic) in photon collection is its 3-D light-collecting capability, i.e., its ability to capture photons from all directions. Therefore, the output power has very low dependence on the angle of incident light. In other words, it gives stable output power regardless of the incident angle of the photons. Therefore, many optical designs can be used to increase its output current and power, among which the most direct one is to use optical condensers to collect diffused light[111].

6.5.1 Diffused reflection and utilization of stray light

FPV is located at the center of a diffusion plate, as shown in Figure 6.31 and Figure 6.32. r is the distance of the cell's center away from the diffusion plated. To simplify the calculation, the following assumptions are made:

(1) The parallel incident light perpendicularly falls on the diffusion plate.

(2) The diffused light reflected from the diffusion plate is an ideal diffused light; no mirror reflection of light from the plate and no absorption and transmission in the plate exist.

(3) The diffused light intensity Id follows Lambert's law of diffused reflection. It is directly proportional to the cosine of the angle between the incident light direction and the normal direction at the surface of the reflection point, that is,

$$I_d = I_0 \times K_d \times \cos\phi \tag{6.2}$$

where I_0 is the incident light intensity, K_d ($0 < K_d \leqslant 1$) is the surface diffused reflection factor, and ϕ is the angle defined earlier. In ideal diffused reflection condition, $K_d = 1$; thus, the diffused reflection intensity at a distance x from the cell is simplified as

$$I_d(x) = I_0 \times \cos\phi. \tag{6.3}$$

(4) The short-circuit current is directly proportional to the diffused light intensity.

Based on the above assumptions, only a portion of the diffused reflected light for the angle θ at the diffused reflection point (x, 0) on the plate can be collected

by the fiber cell. Therefore, the ratio of the collected light to the total incident light intensity is defined as

$$\psi=\frac{\int_{\theta_1}^{\theta_2} I_0 \cos\phi \mathrm{d}\phi}{I_0}, \quad \theta_2-\theta_1=\theta \tag{6.4}$$

$$\theta_1=\frac{\pi}{2}-2\arcsin\frac{r}{\sqrt{x^2+r^2}}-\arctan\frac{d-r}{r} \tag{6.5}$$

$$\theta_2=\frac{\pi}{2}-\arctan\frac{d-r}{r} \tag{6.6}$$

$$\psi=\sin\theta_2-\sin\theta_1 \tag{6.7}$$

Subsequently, the ratio of the diffused reflection light in the range from ($-x$, 0) to (x, 0) on the diffusion plate collected by the fiber cell to total incident light should be

$$\psi(x)=2\int_{-x}^{x}(\sin\theta_2-\sin\theta_1)\,\mathrm{d}x \tag{6.8}$$

According to Assumption (4), the short-circuit current and power (directly proportional to the photoelectrical conversion efficiency) output of the cell due to the diffused reflection light is as follows:

$$J=J_0\times[1+\psi(x)], \tag{6.9}$$

$$P=P_0\times[1+\psi(x)], \tag{6.10}$$

where J_o and P_o are the short-circuit current and power output of the cell, respectively, without the diffusion plate; and J and P are the short-circuit current and power output of the cell, respectively, when the width of the diffusion plate is $2x$.

Furthermore, the diffusion enhancement factor is defined as

$$\beta=K\frac{J}{J_0}=\frac{P}{P_0}=K[1+\psi(x)] \tag{6.11}$$

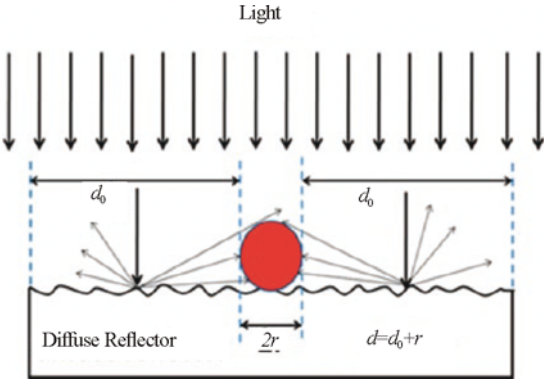

Figure 6.31 (a) Schematic of the diffused illumination mode DRM; DRM for diffused light illumination $d = d_0 + r$, where d is the half-width of the diffusion reflector and r is the radius of the sealing capillary[111]

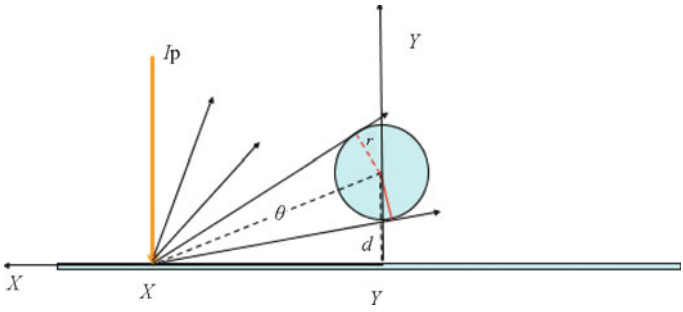

Figure 6.32 Schematic of the diffused reflection light model[111]

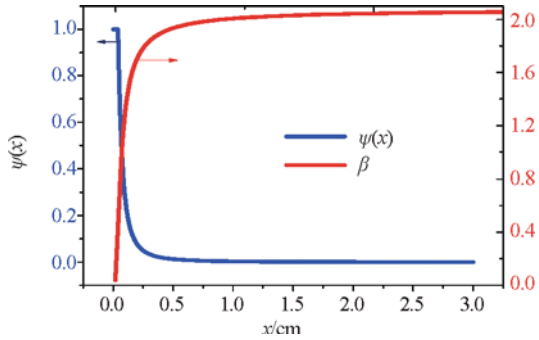

Figure 6.33 Relationships of the ratio of the diffused reflection light $\psi(x)$. Diffused reflection enhancement factor β to the half-width of the diffusion plate calculated when the cell's radius $r = 0.4$ cm and the diffusion plate is close to the cell ($d = 0$ mm)[111]

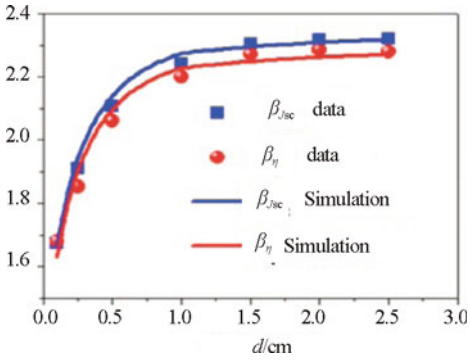

Figure 6.34 The ratio β (J_{sc} or η) of the short-circuit current and efficiency in the SM mode to those in the DRM as a function of d (SM for Standard Condition: AM 1.5; DRM for diffused light illumination, $d = d_0 + r$, where d is the half-width of the diffusion reflector and r is the radius of the sealing capillary)[111]

The diffusion enhancement factor shows the cell's ability to utilize the diffusion plate, where K is a correction factor. The reasons for introducing K are because the real diffused reflection is not ideal and the reflectivity of the cell's sealing tube to incident light at different incident angles is different. For ideal condition, K=1.00 and its caculation results are shown in Figure 6.33 For real conditions, we can adjust the K value to correct the simulation results to fit well with the experimental data. For example, in Figure 6.34, when K is equal to 1.10, the simulation results agree well with the experimental results.

Figure 6.34 shows the comparison between theoretical and experimental results of the short-circuit current enhancement and power-output enhancement as a function of d0. In Figure 6.34 , the line curves show the simulation results, which agree well with the experimental results using correction factor K=1.10 (supporting information found in Part 1). In other words, with a gradually increasing d_0, first, or rapidly increases and then remains nearly constant. The limiting value of or is about 2.32, indicating that the cell module has high utilization efficiency of diffused light, which endows FPVs with obvious advantages over planar cells both in outdoor and indoor environments because no diffused light is being taken up.

6.5.2 Dependence on angle

The 3-D structures of FPVFPV result in less dependence on incident angle compared with the planar cells. Figure 6.35(a) and (b) show the schematics of the light-collecting modes of the FPV (Cell A) and the traditional planar cell (Cell C). During the test, the cells were respectively spun around x-, y-, and z-axes to mimic the changes of the incident angles of daily sunlight.

For fiber solar cell A, the short-circuit current when FPV rotates along the corresponding axes satisfies

$$J_{F,x} = J_{F,z} = J_0,\ J_{F,y} = K \times J_0 \times \cos\theta \tag{6.12}$$

Fiber solar cell A with the diffusion plate underneath the devices satisfies

$$J_{F,x} = K \times J_0 \times (1 + \cos\theta), J_{F,y} = K \times J_0 \times \cos\theta, J_{F,z} = J_0 \tag{6.13}$$

while the planar cell C satisfies

$$J_{P,x} = J_0, J_{P,z} = J_{P,y} = K \times J_0 \times \cos\theta \tag{6.14}$$

where J_F,T is the short-circuit current in the corresponding coordinate, and the subscripts F and P denote the fibrous cell A and the planar cell B, respectively. T stands for x, y, and z. θ is the incident angle of light, and J_0 is the short-circuit current when $\theta = 0$.

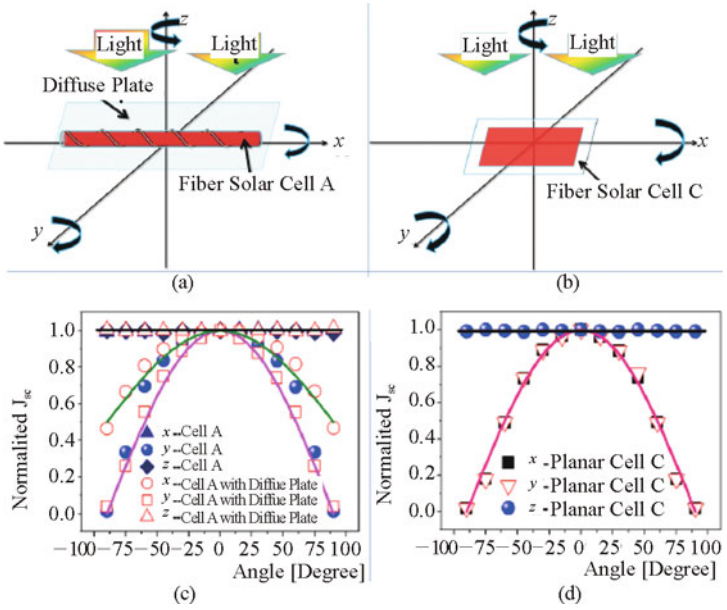

Figure 6.35 The 3-D light-collecting schematics of (a) the fiber-shaped solar cell (Cell A) and (b) the traditional plate solar cell (Cell C); and angle dependences of the normalized short-circuit current of (c) Cell A and that of composite Cell A, and (d) of plate Cell C[111]

Figure 6.35 (c) shows the dependences of the normalized short-circuit currents of Cell A alone and of the composite Cell A with the diffusion plate along the x, y, and z directions on the incident angle. Figure 6.35 (d) shows the dependence of the normalized short-circuit currents of the planar Cell C along the x, y, and z directions on the incident angle. In the above figures, the smooth curves are drawn

according to the above equations, whereas the points denote the experimentally measured data. The short-circuit current of Cell A does not vary with the incident angle along the *x* and *z* directions (Figure 6.35 (c)), whereas the planar Cell C is not dependent on the angle in the *z* direction [Figure 6.35 (d)]. In addition, the composite Cell A with the diffusion plate also has 1-D (*z* direction in (Figure6. 35 (c)) angular independence, whereas the *x* direction angle dependence is not as much as that in the planar cell, especially at larger incident angles (larger than 60°). For example, at an incidence angle of 60°, the maximum efficiency of the fiber cell with a diffusion plate beneath (dark green triangle in Figure 6.35 (c)) is >80% of the efficiency at normal incidence. However, for the planar geometry (black square in Figure 6.35 (d)), the efficiency drops to ~50% after tilting by 60°. The low angle dependence of FPV is helpful for the stereo layout of solar cell panels and for building integrated photovoltaic design.

6.5.3 Design of light-concentrating structure

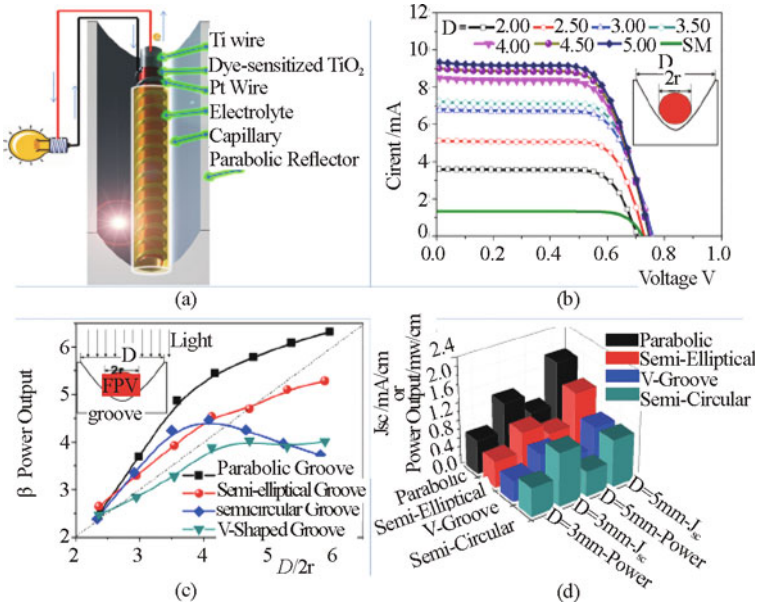

Figure 6.36 (a) Schematic of fiber-based DSSC housed in a parabolic condenser. (b) *I-V* curves of fiber solar cell housed in a parabolic condenser with different width *D* (unit: millimeter) at the open end of the parabola under SM and dark conditions. (c) β power output of the different condenser output power to the output power in SM as a function of ratio *D*/(2r) using different groove shapes, including parabolic, semi-eclipse, semicircular, and *V*-shaped condensers (45° of the *V* angle). *D* is the width of the upper condenser groove mentioned above, and r is the radius of the capillary. (d). Comparative histogram of the short-circuit currents and efficiencies for different condenser sizes *D* = 3 and 5 mm[111]

The 3-D light-collecting characteristic of FPVs also facilitates the manufacture of a novel high-efficiency light concentrator, as shown by the schematic in Figure 6.36 (a). A 5 cm-long FPV is placed at the focus line of a parabolic condenser coated with aluminum foil. The incident light is reflected by the aluminum foil and converges to the FPV located at the focus line of the parabolic condenser. Figure 6.36(b) shows the *I-V* curves of the fiber cell with parabolic grooves having a 0.4 mm focal length and different widths. As the width of the parabolic groove increases from 2.00 to 5.00 mm, the corresponding short-circuit current (I_{sc}) increases from 3.60 to 9.40 mA, and the corresponding maximum power output (P_{max}) dramatically increases from 1.92 to 4.78 mW. On the other hand, the I_{sc} and P_{max} of the same FPV under SM are 1.33 mA and 0.772 mW. The measurements confirm that the new designs are suitable for light harvesting to enhance the power output of FPVs. Here, we introduce the enhancement factor β power output, which is defined as the amount of output power acquired using collectors divided by the output power acquired in the SM mode. For instance, as shown in Figure 6.36(b), the power output of FPV gained under SM mode is 0.772 mW, whereas that of the FPV housed in a parabolic groove with a width of 2.00 mm is 1.92 mW. In such case, the β power output is equal to 1.92 mW/0.772mW = 2.48. Figure 6.36(c) shows the correlation between the enhancement factor β power output of the output power and the ratio of D to $2r$ ($D/2r$) combined with different concentrators, where D is the width of the concentrator and 2r is the diameter of the FPV's sealing glass capillary tube. As shown in Figure 6. 36(c), when $D/2r$ is 3.5, the β power output of the FPV combined with parabolic condenser is 4.8, confirming that using the light condenser significantly increases the output power of FPVs by a factor of ~5 compared with that of the FPV alone.

Aside from parabolic design, concentrators can also be designed in various shapes such as V-groove, semi-ellipse, semicircle, and so on; however, the parabolic condenser gives the best performance (Figure 6.36(c)). Due to the limited precision of our prepared light condensers, the η power output value using different concentrators other than a parabolic condenser is less than the maximum expected value. According to geometrical optics, the converged light should theoretically fall perpendicular to the arc surface of the FPV capillary tube after being reflected by the parabolic groove. Therefore, the relative amount of light reflected by the arc surface of the cell tube is less than that in the case of SM irradiation, where not all light fall perpendicular to the arc surface of the FPV capillary tube.

Figure 6.36(d) shows the comparison of the short-circuit current and power output of FPV combined with different concentrators when D (the width of the grooves) is equal to 3 and 5 mm. When D = 3 mm, the power output of the

parabolic, semi-ellipse, semicircle, and V-shaped (V angle = 45°) condensers reach 0.752, 0.604, 0.644, and 0.482 mW/cm, respectively. In this paper, mW/cm is used as the power output unit for convenience of calculation and comparison with that acquired under SM. In combination with the parabolic condenser with D = 5 mm, the short-circuit current is as high as 1.912 mA/cm and the power output reaches 0.9747 mW/cm. Under intense light, the FPV combined with the condenser still has relatively high output power and filling factor, possibly because of the following reasons: ① FPV is working under backside illumination, i.e., the incident light enters into the photoanode from the pitch space of the counter electrode. Most of its excitons are mainly separated at the anode surface. Therefore, the average distance that the regenerated I_3 will diffuse toward the counter electrode and pass through the porous TiO_2 obstacle 29 is smaller than that in the planar cell case which works under the front-lighting mode where the holes arrive through the counter electrode. ② The substrate is a metal wire whose thermal and electrical conductivities are several orders of magnitude higher than those of FTO, which reduces the resistances and thus the local temperature28. ③ The I_3- concentration (e.g., 0.1 M) in the electrolyte is high enough to ensure rapid transmission of the holes in the cell. This shows another advantage of the novel concentrator combined with DSSCs. In addition, because the size of the novel cells can be very small, such as d being equal to 1～2 mm, even with high magnification design, such as D/2r being equal to 5, the size of the condenser grooves would still remain very small. Thus, the thickness of the condenser cell module can still be very thin (<10 mm), far thinner than the conventional concentrator used for flat-type solar cells (with sizes varying from centimeters to even meters).

6.5.4 Colorful weaving cell

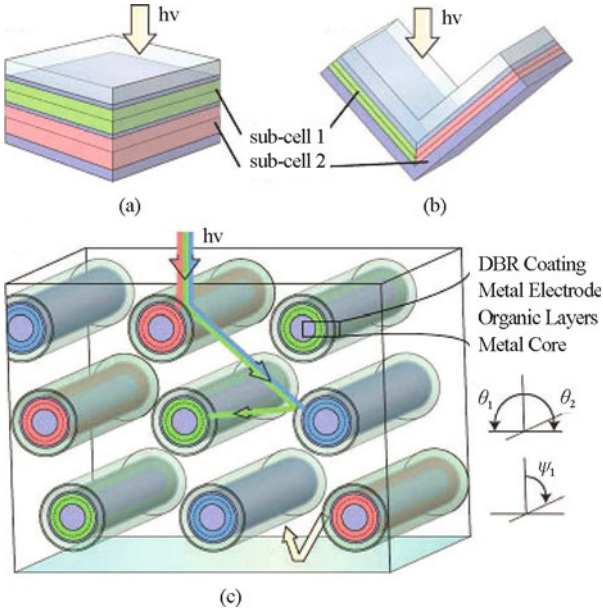

Figure 6.37 Tandem solar cell designs including (a) a traditional transmission solar cell design and (b) a reflective tandem solar cell in a V-shaped configuration. (c) Example of a reflective fiber-based tandem cell design consisting of three rows of three spectrally tuned photovoltaic sub-cells. The fiber OPV cells consist of a distributed Bragg reflector, a thick spacer layer, a transparent top electrode, active organic layers, and an optically thick center electrode. The fibers are not drawn to scale and are expected to be not less than 50 m in diameter[112]

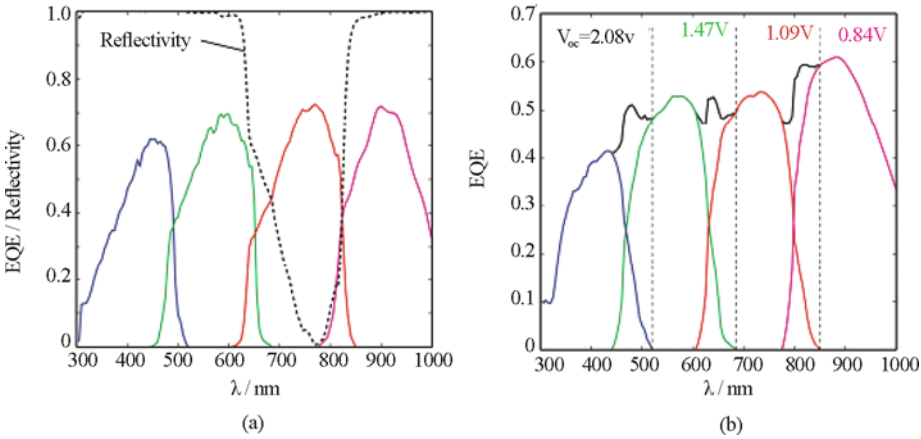

Figure 6.38 Performance parameters of the 10-row, 4-color-tuned OPV fiber bundle. (a) External quantum efficiencies (EQEs) of the planar counterparts of the four microcavity-tuned fiber OPV cells under normal illuminations. The reflectivity of one of the cells is also given to illustrate the high reflectivity of the off-resonant wavelengths. (b) Total EQEs along with the contributions of the separate color-tuned fibers in the 10-row, 4-color-tuned bundle. The predicted open-circuit voltage is also given for each sub-cell[112]

For common laminated solar cell, the absorption layer with different absorption bandgaps and complementary absorption spectrum is usually adopted to attain low thermal loss and improve the open-circuit voltage. The common organic photovoltaic laminated cell includes two kinds of structures, namely, transflective (Figure 6.37(a)) and reflective types (Figrue 6.37(b)). In the usual transflective type cell (Figure 6.37(a)), several single cells are stacked onto each other in series; thus, sunlight is absorbed by the front cell when it passes through the cell. The part not absorbed by the front cell is absorbed by the rear cell. The other type arranges two single cells in a V-shape (Figure 6.37(b)). In this way, the photon that cannot be absorbed by one cell is reflected to the other cell and absorbed. Theoretically, provided that the two cells form a sharp and big V-shaped angle, all incident lights will be captured and high photoelectric conversion efficiency can be reached. However, these two types of cells have insurmountable shortcomings. The former must make the front and rear cell match, which is difficult to do. If a solar follower is not used, this flat cell cannot absorb indirect light. The latter is limited by the condition that if the spectrum of the two cell units is complementary, the light intensity is mainly distributed at the pointed end of the V-shaped angle. The latter type has difficulty in attaining optimal energy output because the open-circuit voltage of the organic photovoltaic cell and filling factors are very sensitive to

light intensity.

Connor et al.[112] proposed a laminated solar cell with a new structure, as shown in Figure 6.37(c). It is a new type of solar cell that combines a series of fiber cell units with narrow-band spectrum absorption and adopts proper arrangement in space to realize full-spectrum absorption of the sun spectra, resulting in high efficiency (Figure 6.38). In the calculation results from a single cell combined with different absorption spectra, the open-circuit voltage of the cell reaches up to 5.24 V. If 10 rows of 4 single color cells are combined, the short-circuit current can reach more than 18 mA/cm^2. For combination of 20 rows of 4 single color cells, the short-circuit current can reach more than 20 mA/cm^2. Connor et al. predicted that, based on the optimization of the materials, including organic absorption layer, transmission layer, metal electrode, and DBR coating layer, they can finally realize 17% photoelectric conversion efficiency.

6.6 Conclusion and prospect

Experimental and theoretical calculations show that the fiber cell has more useful optical performance compared to the flat structural cell. In addition, the fiber cell is flexible; thus, it has great potential for application in flexible electric devices. Unlike traditional flexible flat cell technology, mass production of the fiber cell can be performed in many different styles, such as screen, arrangement, and weaving modular styles. These technologies can be simply realized when the materials are properly selected based on current technologies, providing possibilities to the creation of the next flexible electronic device that can be valuable and has promising potential for academic and industry research. The fiber solar cell products are expected to be introduced in the future into thousands of homes for the betterment of human lives.

References

[1] Ma L W, Liu P,Fu F,et al. Integrated energy strategy for the sustainable development of China.Energy, 2011, 36(2): 1143~1154.

[2] Yan X Y, Crookes R J. Energy demand and emissions from road transportation vehicles in China. Progress in Energy and Combustion Science, 2010, 36(6): 651~676.

[3] Mozafari A, Ahmadi A, Ehyaei M A. Optimisation of micro gas turbine by

exergy, economic and environmental (3E) analysis. International Journal of Exergy, 2010, 7(1): 1~19.

[4] Li Z, Gao D,Chang L,et al. Coal-derived methanol for hydrogen vehicles in China: Energy, environment, and economic analysis for distributed reforming. Chemical Engineering Research and Design, 2010, 88(1A): 73~80.

[5] Solangi K H, Islam M R,Saidur R,et al. A review on global solar energy policy. Renewable and Sustainable Energy Reviews, 2011, 15(4): 2149~2163.

[6] Mekhilef S, Saidur R, Safari A. A review on solar energy use in industries. Renewable and Sustainable Energy Reviews, 2011, 15(4): 1777~1790.

[7] Ibrahim A,Othman M Y,Ruslan M H,et al. Recent advances in flat plate photovoltaic/thermal (PV/T) solar collectors. Renewable and Sustainable Energy Reviews, 2011, 15(1): 352~365.

[8] Gastli A , Charabi Y. Solar water heating initiative in Oman energy saving and carbon credits. Renewable and Sustainable Energy Reviews, 2011, 15(4): 1851~1856.

[9] Alkilani M M, Sopian K,Alghoul M A, et al. Review of solar air collectors with thermal storage units. Renewable and Sustainable Energy Reviews, 2011, 15(3): 1476~1490.

[10] Wolden C A, Kurtin J,Baxter J B,et al. Photovoltaic manufacturing: Present status, future prospects, and research needs. Journal of Vacuum Science and Technology A, 2011, 29(3):030801.

[11] Tiwari G N, Mishra R K, Solanki SC. Photovoltaic modules and their applications: A review on thermal modelling. Applied Energy, 2011, 88(7): 2287~2304.

[12] Parida B, Iniyan S, Goic R. A review of solar photovoltaic technologies. Renewable and Sustainable Energy Reviews, 2011, 15(3): 1625~1636.

[13] El Chaar L,Lamont L A,El Zein N. Review of photovoltaic technologies. Renewable and Sustainable Energy Reviews, 2011, 15(5): 2165~2175.

[14] Goetzberger A, Hebling C, Schock H W. Photovoltaic materials, history, status and outlook. Materials Science and Engineering R-Reports, 2003, 40(1): 1~46.

[15] Konagai M. Present status and future prospects of silicon thin-film solar cells. Japanese Journal of Applied Physics, 2011, 50(3): 030001.

[16] Kazmerski L L. Solar photovoltaics RandD at the tipping point: A 2005 technology overview. Journal of Electron Spectroscopy and Related Phenomena, 2006, 150(2~3): 105~135.

[17] Chopra K L, Paulson P D, Dutta V. Thin-film solar cells: An overview. Progress in Photovoltaics, 2004, 12(2~3): 69~92.

[18] McCann M J, Catchpole K R,Weber K J, et al. A review of thin-film crystalline silicon for solar cell applications. Part 1: Native substrates. Solar Energy Materials and Solar Cells, 2001, 68(2): 135~171.

[19] Catchpole K R, McCann M J,Weber K J,et al. A review of thin-film crystalline silicon for solar cell applications. Part 2: Foreign substrates. Solar Energy Materials and Solar Cells, 2001, 68(2): 173~215.

[20] Aberle A G. Surface passivation of crystalline silicon solar cells: A review. Progress in Photovoltaics, 2000, 8(5): 473~487.

[21] Breeze A J, Ieee E D S. Reliability G, Next generation thin-film solar cells. 2008 Ieee International Reliability Physics Symposium Proceedings - 46th Annual. 2008(1): 168~171.

[22] Miles R W, Zoppi G, Forbes I. Inorganic photovoltaic cells. Materials Today, 2007,10(11): 20~27.

[23] Zhang Q F, Cao G Z. Nanostructured photoelectrodes for dye-sensitized solar cells. Nano Today, 2011, 6(1): 91~109.

[24] Zhang Q F, Dandeneau C S,Zhou X Y, et al. ZnO nanostructures for dye-sensitized solar cells. Advanced Materials, 2009, 21(41): 4087~4108.

[25] Yum J H, Chen P,Gratzel M,et al. Recent developments in solid-state dye-sensitized solar cells. Chemsuschem, 2008, 1(8~9): 699~707.

[26] Guenes S, Sariciftci N S. Hybrid solar cells. Inorganica Chimica Acta, 2008, 361(3): 581~588.

[27] Goncalves L M, Bermudez V D,Ribeiro H A,et al. Dye-sensitized solar cells: A safe bet for the future. Energy and Environmental Science, 2008, 1(6): 655~667.

[28] Crabtree R H. An organometallic future in green and energy chemistry? Organometallics, 2011, 30(1): 17~19.

[29] Wong W Y,Ho C L. Organometallic photovoltaics: A new and versatile approach for harvesting solar energy using conjugated polymetallaynes. Accounts of Chemical Research, 2010, 43(9): 1246~1256.

[30] Bredas J L, Norton J E,Cornil J,et al. Molecular understanding of organic solar cells: The challenges. Accounts of Chemical Research, 2009, 42(11): 1691~1699.

[31] Rand B P, Genoe J, Heremans P,et al. Solar cells utilizing small molecular weight organic semiconductors. Progress in Photovoltaics, 2007, 15(8): 659~676.

[32] Spanggaard H, Krebs F C. A brief history of the development of organic

and polymeric photovoltaics. Solar Energy Materials and Solar Cells, 2004, 83(2~3): 125~146.

[33] Green M A , Emery K,Hishikawa Y, et al. Solar cell efficiency tables (version 37). Progress in Photovoltaics, 2011, 19(1): 84~92.

[34] Saga T. Advances in crystalline silicon solar cell technology for industrial mass production NPG Asia. Mater, 2010,(3): 7~10.

[35] Yin Z P, Huang Y A,Bu N B, et al. Inkjet printing for flexible electronics: Materials, processes and equipments. Chinese Science Bulletin, 2010,55(30): 3383~3407.

[36] MouleA J. Power from plastic. Current Opinion in Solid State and Materials Science, 2010,4(6): 123~130.

[37] Cromeo A, Terheggen A,Abou-Ras D,et al. Development of thin-film Cu(In,Ga)Se-2 and CdTe solar cells. Progress in Photovoltaics, 2004,12(2~3): 93~111.

[38] Crabb R L,Treble F C. Thin silicon solar cells for large flexible arrays. Nature, 1967, 213(5082): 1223~1226.

[39] Staebler D L,Wronski C R. Reversible conductivity changes in discharge-produced amorphous Si. Applied Physics Letters, 1977, 31(4): 292~294.

[40] Matsuyama T, Wakisaka K, Kameda M, et al. Preparation of high-quality n-type poly-Si films by the solid-phase crystallization (SPC) method. Japanese Journal of Applied Physics Part 1-Regular Papers Short Notes and Review Papers, 1990, 29(11): 2327~2331.

[41] Li H, van der Werf C H M,Borreman A, et al. Flexible a-Si : H/nc-Si : H tandem thin film silicon solar cells on plastic substrates with i-layers made by hot-wire CVD. Physica Status Solidi-Rapid Research Letters, 2008, 2(4): 157~159.

[42] Soderstrom T, Haug F J,Terrazzoni-Daudrix V, et al. Optimization of amorphous silicon thin film solar cells for flexible photovoltaics. Journal of Applied Physics, 2008, 103(11): 114509.

[43] Kim D H, AhnJ H,Choi W M, et al. Stretchable and foldable silicon integrated circuits. Science, 2008, 320(5875): 507~511.

[44] Fan Z Y, Javey A. Photovoltaics Solar cells on curtains. Nature Materials, 2008, 7(11): 835~836.

[45] Yoon J, Baca Alfred J, Pak S, et al. Ultrathin silicon solar microcells for semitransparent, mechanically flexible and microconcentrator module designs. Nat Mater, 2008, 7(11): 907~915.

[46] Kessler F, Rudmann D. Technological aspects of flexible CIGS solar cells and modules. Solar Energy, 2004, 77(6):685~695.

[47] Herz K, Kessler E,Wachter R, et al, Dielectric barriers for flexible CIGS solar modules. Thin Solid Films, 2002, 403: 384~389.

[48] Bremaud D, Rudmann D,Kaelin M, et al. Flexible Cu(In,Ga)Se-2 on Al foils and the effects of Al during chemical bath deposition. Thin Solid Films, 2007, 515(15): 5857~5861.

[49] Repins I, Mueller T,Tress W,et al. 19.9%-efficient ZnO/CdS/CuInGaSe-2 solar cell with 81.2% fill factor. Progress in Photovoltaics, 2008, 16(3): 235~239.

[50] Rudmann D, Bremaud D,Zogg H,et al. Na incorporation into Cu(In,Ga)Se-2 for high-efficiency flexible solar cells on polymer foils. Journal of Applied Physics, 2005, 97(8): 084903.

[51] Singh U P, Patra S P. Progress in Polycrystalline Thin-Film Cu(In,Ga)Se-2 Solar Cells. International Journal of Photoenergy, 2010,3: 468147.

[52] Bremaud D, Rudmann D,Bilger G,et al. Towards the development of flexible CIGS solar cells on polymer films with efficiency exceeding 15%. Conference Record of the Thirty-First IEEE Photovoltaic Specialists Conference - 2005. New York:IEEE press,2005: 223~226.

[53] Zhang L, He Q, Jiang W L,et al. Mo back contact for flexible polyimide substrate Cu(In, ga)Se-2 thin-film solar cells. Chinese Physics Letters, 2008 ,25(9): 3452~3454.

[54] Ishizuka S, Hommoto H,Kido N,et al. Efficiency enhancement of Cu(In,Ga) Se-2 solar cells fabricated on flexible polyimide substrates using alkali-silicate glass thin layers. Applied Physics Express, 2008, 1(9): 092303.

[55] Krebs F C, Jorgensen M,Norrman K, et al. A complete process for production of flexible large area polymer solar cells entirely using screen printing-First public demonstration. Solar Energy Materials and Solar Cells, 2009, 93(4): 422~441.

[56] Krebs F C, Gevorgyan S A, Alstrup J. A roll-to-roll process to flexible polymer solar cells: Model studies, manufacture and operational stability studies. Journal of Materials Chemistry, 2009, 19(30): 5442~5451.

[57] Krebs F C. All solution roll-to-roll processed polymer solar cells free from indium-tin-oxide and vacuum coating steps. Organic Electronics, 2009, 10(5): 761~768.

[58] Kippelen B, Bredas J L. Organic photovoltaics. Energy and Environmental Science, 2009, 2(3): 251~261.

[59] Dennler G, Sariciftci N S. Flexible conjugated polymer-based plastic solar cells: From basics to applications. Proceedings of the IEEE, 2005, 93(8): 1429~1439.

[60] Jorgensen M, Norrman K, Krebs F C. Stability/degradation of polymer solar cells. Solar Energy Materials and Solar Cells, 2008, 92(7): 686~714.

[61] Hauch J A, Schilinsky P, Choulis S A,et al. Flexible organic P3HT : PCBM bulk-heterojunction modules with more than 1 year outdoor lifetime. Solar Energy Materials and Solar Cells, 2008, 92(7): 727~731.

[62] Zhu X Y, Yang Q, Muntwiler M. Charge-Transfer Excitons at Organic Semiconductor Surfaces and Interfaces. Accounts of Chemical Research, 2009, 42(11): 1779~1787.

[63] Bernede J C. Organic photovoltaic cells: History, principle and techniques. Journal of the Chilean Chemical Society, 2008, 53(3): 1549~1564.

[64] Nunzi J M. Organic photovoltaic materials and devices. Comptes Rendus Physique, 2002,3(4): 523~542.

[65] Hoppe H, Sariciftci N S. Organic solar cells: An overview. Journal of Materials Research, 2004, 19(7): 1924~1945.

[66] Hsiao Y S, Chen C P,Chao C H, et al. All-solution-processed inverted polymer solar cells on granular surface-nickelized polyimide. Organic Electronics, 2009, 10(4): 551~561.

[67] Krebs F C, Gevorgyan S A,Gholamkhass B, et al. A round robin study of flexible large-area roll-to-roll processed polymer solar cell modules. Solar Energy Materials and Solar Cells, 2009, 93(11): 1968~1977.

[68] Krebs F C, Biancardo M,Winther-Jensen B,et al.Strategies for incorporation of polymer photovoltaics into garments and textiles. Solar Energy Materials and Solar Cells, 2006,90(7~8): 1058~1067.

[69] Oregan B,Gratzel M. A low-cost, high-efficiency solar-cell based on dye-sensitized colloidal TiO_2 films. Nature, 1991, 353(6346): 737~740.

[70] Nazeeruddin M K, Kay A,Rodicio I, et al. Conversion of Light to Electricity by Cis-X2bis(2,2'-Bipyridyl-4,4'-Dicarboxylate)Ruthenium(Ii) Charge-Transfer Sensitizers (X = Cl-, Br-, I-, Cn-, and Scn-) on Nanocrystalline TiO_2 Electrodes. Journal of the American Chemical Society, 1993, 115(14): 6382~6390.

[71] Longo C, Freitas J,De Paoli M A. Performance and stability of TiO_2/dye solar cells assembled with flexible electrodes and a polymer electrolyte. Journal of Photochemistry and Photobiology a-Chemistry, 2003, 159(1): 33~39.

[72] Miyasaka T, Kijitori Y, Ikegami M. Plastic dye-sensitized photovoltaic cells and modules based on low-temperature preparation of mesoscopic titania electrodes. Electrochemistry, 2007, 75(1): 2~12.

[73] Pichot F, Pitts J R, Gregg B A. Low-temperature sintering of TiO_2 colloids:

Application to flexible dye-sensitized solar cells. Langmuir, 2000, 16(13): 5626~5630.

[74] Lindstrom H, Holmberg A,Magnusson E,et al. A new method to make dye-sensitized nanocrystalline solar cells at room temperature. Journal of Photochemistry and Photobiology a-Chemistry, 2001, 145(1~2): 107~112.

[75] Jiang C Y, Sun X W,Tan K W,et al. High-bendability flexible dye-sensitized solar cell with a nanoparticle-modified ZnO-nanowire electrode. Applied Physics Letters, 2008, 92(14): 143101.

[76] Kim K, Lee G W,Yoo K, et al. Improvement of electron transport by low-temperature chemically assisted sintering in dye-sensitized solar cell. Journal of Photochemistry and Photobiology a-Chemistry, 2009, 204(2~3): 144~147.

[77] Ning Z J, Fu Y, Tian H. Improvement of dye-sensitized solar cells: What we know and what we need to know. Energy and Environmental Science, 2010, 3(9): 1170~1181.

[78] Zou D C,Wang D, Chu Z Z, et al. Fiber-shaped flexible solar cells. Coordination Chemistry Reviews, 2010, 254(9~10): 1169~1178.

[79] Tachan Z, Ruhle S, Zaban A. Dye-sensitized solar tubes: A new solar cell design for efficient current collection and improved cell sealing. Solar Energy Materials and Solar Cells, 2010, 94(2): 317~322.

[80] Taira K, Nakata J. Catching rays. Nature Photonics, 2010, 4(9): 602~603.

[81] Bonderover E, Wagner S. A woven inverter circuit for e-textile applications. IEEE Electron Device Letters, 2004, 25(5): 295~297.

[82] Cherenack K, Zysset C,Kinkeldei T,et al. Woven electronic fibers with sensing and display functions for smart textiles. Advanced Materials, 2010, 22(45): 5178~5184.

[83] Liu J W, Namboothiry M A G, Carroll D L. Fiber-based architectures for organic photovoltaics. Applied Physics Letters, 2007, 90(6).

[84] Liu J W, Namboothiry M A G,Carroll D L.Optical geometries for fiber-based organic photovoltaics. Applied Physics Letters, 2007, 90(13): 133515.

[85] Li Y A, Peterson E D,Huang H H,et al. Tube-based geometries for organic photovoltaics. Applied Physics Letters, 2010, 96(24): 243505.

[86] O'Connor B, Pipe K P, Shtein M. Fiber based organic photovoltaic devices. Applied Physics Letters, 2008, 92(19).

[87] Fan X, et al.Wire-shaped flexible dye-sensitized solar cells. Advanced Materials, 2008, 20(3): 592~596.

[88] Fan X, et al. Fibrous flexible solid-type dye-sensitized solar cells without transparent conducting oxide. Applied Physics Letters, 2008, 92(11).

193306.

[89] Lee M R, Eckert R D,Forberich K, et al. Solar power wires based on organic photovoltaic materials. Science, 2009, 324(5924): 232~235.

[90] Rosenbluth M L, Lewis N S. Ideal behavior of the open circuit voltage of semiconductor liquid junctions. Journal of Physical Chemistry, 1989, 93(9): 3735~3740.

[91] Kamat P V, Tvrdy K,Baker D R, et al. Beyond Photovoltaics: Semiconductor Nanoarchitectures for Liquid-Junction Solar Cells. Chemical Reviews, 2010, 110(11): 6664~6688.

[92] Wang D, Hou S C,Wu H W,et al. Fiber-shaped all-solid state dye sensitized solar cell with remarkably enhanced performance via substrate surface engineering and TiO_2 film modification. Journal of Materials Chemistry, 2011, 21(17): 6383~6388.

[93] Sharma G D, Suresh P, Mikroyannidis J A. Quasi solid state dye-sensitized solar cells with modified TiO_2 photoelectrodes and triphenylamine-based dye. Electrochimica Acta, 2010, 55(7): 2368~372.

[94] Lv Z,Fu Y, Hou S C,et al. Large size, high efficiency fiber-shaped dye-sensitized solar cells. Physical Chemistry Chemical Physics, 2011, 13(21): 10076~10083.

[95] Yanagida S, Yu Y H, Manseki K. Iodine/Iodide-Free Dye-Sensitized Solar Cells. Accounts of Chemical Research, 2009, 42(11): 1827~1838.

[96] Law M,Greene L E,Johnson J C,et al. Nanowire dye-sensitized solar cells. Nature Materials, 2005, 4(6): 455~459.

[97] Mor G K, Shankar K,Paulose M, et al. Use of highly-ordered TiO_2 nanotube arrays in dye-sensitized solar cells. Nano Letters, 2006, 6(2): 215~218.

[98] Kim D, Lee N E, Park J S,et al. Dye-sensitized solar cells using anodic TiO_2 mesosponge: Improved efficiency by $TiCl_4$ treatment. Electrochemistry Communications, 2010, 12(4): 574~578.

[99] Wang J, Lin Z Q. Dye-sensitized TiO_2 nanotube solar cells with markedly enhanced performance via rational surface engineering. Chemistry of Materials, 2010, 22(2): 579~584.

[100] Yu J F, Wang D,Huang Y N, et al. A cylindrical core-shell-like TiO_2 nanotube array anode for flexible fiber-type dye-sensitized solar cells. Nanoscale Research Letters, 2010, 6(1).

[101] Liu Z Y, Misra M. Dye-sensitized photovoltaic wires using highly ordered TiO_2 nanotube arrays. Acs Nano, 2010, 4(4): 196~2200.

[102] Wang H, LiuY,Li M,et al. Hydrothermal growth of large-scale macroporous TiO_2 nanowires and its application in 3D dye-sensitized solar cells. Applied

Physics a-Materials Science and Processing, 2009, 97(1): 25~29.
[103] Huang S Q, Zhang Q X,Huang X M,et al. Fibrous CdS/CdSe quantum dot co-sensitized solar cells based on ordered TiO_2 nanotube arrays. Nanotechnology, 2010, 21(37): 375201.
[104] Weintraub B, Wei Y G, Wang Z L. Optical fiber/nanowire hybrid structures for efficient three-dimensional dye-sensitized solar cells. Angewandte Chemie-International Edition, 2009, 48(47): 8981~8985.
[105] Chen T, Wang S T,Yang Z B,et al. Flexible, light-weight, ultrastrong, and semiconductive carbon nanotube fibers for a highly efficient solar cell. Angewandte Chemie-International Edition, 2011, 50(8): 1815~1819.
[106] Fan X, Wang F Z,Chu Z Z,et al. Conductive mesh based flexible dye-sensitized solar cells. Applied Physics Letters, 2007, 90(7): 073501.
[107] Liu, Z Y,Subramania V, Misra M. Vertically oriented TiO_2 nanotube arrays grown on Ti meshes for flexible dye-sensitized solar cells. Journal of Physical Chemistry C, 2009, 113(31): 14028~14033.
[108] Rustomji C S, et al. Dye-sensitized solar cell constructed with titanium mesh and 3-D array of TiO_2 nanotubes. Journal of Physical Chemistry B, 2010, 114(45): 14537~14543.
[109] Wang Y H , Yang H X , Lu L. Three-dimensional double deck meshlike dye-sensitized solar cells. Journal of Applied Physics, 2010, 108(6): 064510.
[110] Liao K S , Yambem S D,Haldar A,et al. Designs and Architectures for the next generation of organic solar cells. Energies, 2010, 3(6): 1212~1250.
[111] Fu Y,Lv Z B, Hou S C, et al. Conjunction of fiber solar cells with groovy micro-reflectors as highly efficient energy harvester. Energy and Environmental Science, 2011, 4 (9): 3379~ 3383.
[112] O'Connor B,Nothern D. Pipe K P, et al. High efficiency, broadband solar cell architectures based on arrays of volumetrically distributed narrowband photovoltaic fibers. Optics Express, 2010, 18(19): A432~A443.

Chapter 7
Semiconductors for Photoelectrochemical Hydrogen Generation

Zhaosheng Li,[1,2] Zaisan Yang[1],Wenjun Luo [1] and Zhigang Zou[1,2]

1Ecomaterials and Renewable Energy Research Center, National Laboratory of Solid Microstructures, Nanjing University, Nanjing, 210093, PR China

2Department of Materials Science and Engineering, School of Engineering and Applied Science,Nanjing University, Nanjing, 210093, PR China

Abstract

Photoelectrochemical cells have abilities to capture the solar energy and convert it into electric power or chemical fuels. The direct conversion of solar energy into hydrogen represents an attractive but challenging alternative for PEC cells. Photoelectrode materials play a vital role in PEC cells. Photoelectrode materials play the most important role in PEC cells. This chapter briefly introduced history and basic concepts of the PEC cells for hydrogen generation. We also give an overview of photoelectrode materials, such as TiO2, WO3, hematite, BiVO4, and some (oxy)nitrides, for solar hydrogen production. Future development of photoelectrode research will be indicated finally.

7.1 Introduction

The rapid increase in the level of anthropogenic carbon dioxide is a matter of great concern because combustion of fossil fuels has brought a series of global environmental problems, for example global warming. Many countries are seeking to become low-carbon economies by developing clean energy. Solar energy will play an important role in the development of new clean energy sources, since approximately 120 000 TW of solar energy continuously reaches the Earth. With

* Mailing address: Prof. Zhaosheng Li / Ecomaterials and Renewable Energy Research Center, National Laboratory of Solid Microstructures, Nanjing University, Nanjing, 210093, P. R. China; Fax: +86-25-83686632; Email:zsli@nju.edu.cn

the background of energy crisis and environmental concerns, more and more attention has been paid to sustainable hydrogen production through direct use of solar energy.

Photoelectrochemical (abbreviated as PEC) cells can capture the solar energy and convert it into electric power or chemical fuels, for example hydrogen. Photoelectrochemical cells for producing electric power are called regenerative cells (for example Grätzel cells), while PEC cells for hydrogen generation are also named as photosynthetic cells [1~3]. The photon energy may be converted to chemical energy only when a largely positive barrier in the Gibbs free energy through water splitting should be overcome. Compared with photocatalytic hydrogen production using particle catalysts, the use of PEC cells for hydrogen production offers several vital advantages: ① the external bias voltage across a photoelectrode can be used; ② the ability to produce hydrogen and oxygen in separate compartments; ③ the higher photoconversion efficiencies because the external bias favors the transfer and separation of photoinduced electrons and holes, as well as decreasing their recombination; ④ the ease of removing the photoactive materials from water.

Study on semiconductor photochemistry can be traced back to a discovery of the French scientist named Edmond Becquerel in 1839 [4]. In his experiments, a photovoltage and a photocurrent were observed when a silver chloride electrode, immersed in an electrolyte solution and connected to a counter electrode, was irradiated with sunlight. In 1955, the origin of this phenomenon, called the Becquerel effect, was elucidated by Brattain and Garret and the modern era of photoelectrochemistry was born [5]. Later, the PEC properties of Si, CdS, ZnS, CdSe, ZnSe, ZnTe, GaAs, GaP, ZnO, $KaTaO_3$, and Ta_2O_5 have been studied [6~12]. In 1972, the first PEC for overall water splitting, i.e. $2H_2O \rightarrow 2H_2+O_2$, was reported by Fujishima and Honda using a rutile TiO_2 photoanode and Pt counter electrode [13]. Such PEC cells based on semiconductor-liquid junctions have attracted intensive and growing interest , due to their potential applications as solar energy converters and increasing public awareness that the Earth's oil reserves may run out during this century.

Early PEC studies have been focused on single-crystal photoelectrodes, because they exhibit few defects and it is easy to study their intrinsic properties, for example the flat band potential. Owing to the complexity of single-crystal sample preparation, especially for complex oxide semiconductors, it is difficult to explore new photoelectrode materials of single crystal. Bard et al. found that the PEC properties of polycrystalline TiO_2 and Fe_2O_3, which were prepared by chemical vapor deposition, were close to those of single-crystal samples [14]. It

suggested that photoelectrochemical properties of a photoelectrode material can be gained on a polycrystalline sample, thus affording a nice approach to develop novel photoelectrodes.

It is well known that one of the most important objectives to develop PEC cells is producing high efficient photoelectrodes that are stable in aqueous solution and can absorb a significant portion of the solar spectrum effectively. However, the reported photoconversion (solar to hydrogen) efficiencies are much lower than the benchmark one of 10%, which is generally considered to be required for commercial implementation [15].

Titanium dioxide has been the favored semiconductor photoelectrode for PEC cells. Unfortunately, the band gap of TiO_2 (3.0～3.2 eV) is too large to absorb visible light in the sunlight, thus leading to low photoconversion efficiencies. Many efforts have been devoted to shifting the spectral response of TiO_2 into the visible region, or to developing alternative semiconductors affording water cleavage by visible light. Some oxides with narrower band gaps, WO_3 and Fe_2O_3, have been studied intensively as photoelectrode materials due to their visible light response and fairly good stability [16]. Also, much effort has gone into finding new electrode structures (for example heterojunction) to produce efficient photoelectrodes [17~19].

7.2 Basic mechanisms and types of PECs for H_2 production

In most cases, a PEC cell for hydrogen generation is composed of an n-type semiconductor photoanode associated with a conventional metal cathode, as shown in Figure 7.1.

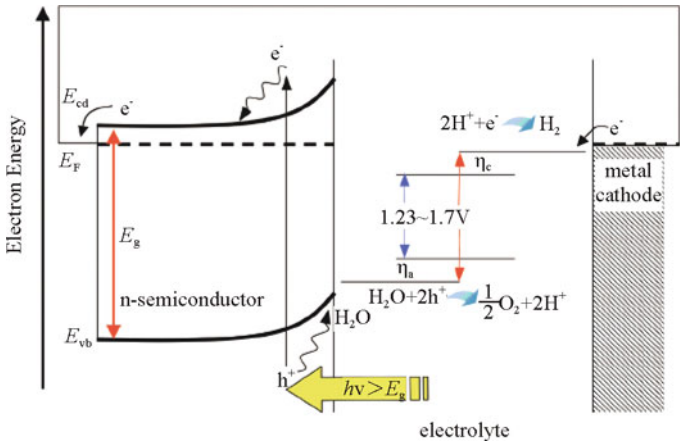

Figure 7.1 A schematic diagram of photo-generated carriers transfer in a n-type photoelectrode without bias. Ef is Femi level of the semiconductor.

For an n-type semiconductor, the highest occupied band (the valence band, Ey) and the lowest unoccupied energy band (the conduction band, Ec) are separated by a band gap (*E*g), a region devoid of energy levels in a perfect crystal. When illuminated with photons that have an energy that is equal to or larger than the band gap of the semiconductor material, photoelectrons are excited from the valence band into the conduction band. The photoinduced electrons travel to the back contact and then are transported to the counter metal electrode where they reduce water to produce hydrogen gas. The photoinduced holes remained in the valence band can migrate to the surface of the semiconductor anode, where they oxidize water to evolve oxygen gas. When a pH value of the electrolyte is equal to 0, the water splitting to H_2 and O_2 involves the redox half-cell reaction shown as following equations.

$$2H_2O(l) \rightarrow O_2(g)+4H+(aq)+4e^-,\ E_{red}{}^o=1.23\ V\ (vs.\ NHE) \quad (7.1)$$

$$4H+(aq)+4e^- \rightarrow 2H_2(g),\ E_{red}{}^o=0\ V\ (vs.\ NHE) \quad (7.2)$$

If water splitting is carried out without bias, the potential of the conduction band of an ideal semiconductor should be more negative than the $H+/H_2$ redox potential. Similarly, the potential of the valence band edge should be more positive than that corresponding to the O_2 evolution potential.

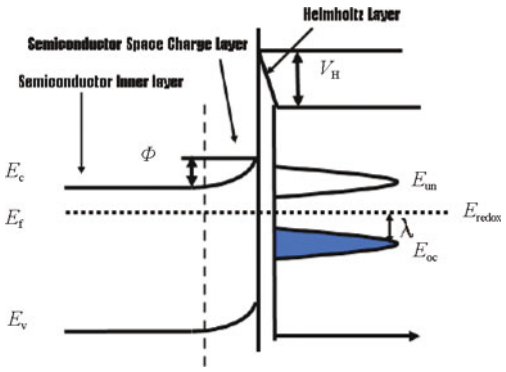

Figure 7.2 A potential profile of the semiconductor-electrolyte junction under dark condition. (Φ is band bending; V_H is voltage decrease in Helmholtz double layer; E_{redox} is standard reduction-oxidation level; E_{un} and E_{oc} are energy level of unoccupied and occupied state; λ is reorganization energy)

The semiconductor-electrolyte junction plays a very important role in PEC cells. For a single crystal or multi crystal photoelectrode, a potential profile of semiconductor-electrolyte junction under dark condition is shown in Figure 7.2. Without light irradiation, the semiconductor-electrolyte junction can be divided into four layers [20~26]:

(1) *Inner layer of semiconductor*. The properties of this region are as the same as those of the bulk semiconductor.

(2) *Space charge layer*. When a semiconductor photoelectrode is contacted with an electrolyte solution, the excess charge does not lie on the surface, but rather extends into the electrode for approximately 5～200 nm, depending upon the conductivity and the band bending [27]. This region is called the space charge layer. It is different from metal electrodes, where the space charge layer is infinitesimally small and charges induced in the electrode essentially reside at the surface.

(3) *Helmholtz layer*. Charge transfer from the semiconductor to electrolyte leads to the formation of surface charge, which is then compensated by a charge of opposite sign induced in the electrolyte within a localized layer known as the Helmholtz layer. The Helmholtz layer is formed by oriented water molecule dipoles and adsorbed electrolyte ions at the electrode surface. The width of the Helmholtz layer is generally of the order of a few angstroms. The potential drop across the Helmholtz layer depends upon the specific ionic equilibrium at the surface [28].

(4) *Diffusion layer of electrolyte*(also named Gouy-Chapman layer). Based on Helmholtz layer model, Gouy and Chapmen developed a diffuse ionic double layer model, in which the potential at the surface decreases exponentially due to chemisorbed counter ions from the electrolyte solution. Thus the movement of the ionic counter charges of an electrolyte, near the surface of a metal electrode, makes them lose part of their solvation shell. When the electrolyte concentration is very high, the diffusion layer of electrolyte can be omitted [29].

Equilibrium between the two phases of solid and liquid at the semiconductor-electrolyte interface can only be achieved if they have the same electrochemical potentials. When their electrochemical potentials are not equal, movement of charge across the semiconductor - solution interface continues until the two phases equilibrate with a corresponding energy band bending (Φ). When a reversed voltage is applied on the circuit to make the energy band bending disappear (Φ=0), this reversed voltage is defined as the flat band potential of the semiconductor (V_{fb}).

When the diffusion layer of electrolyte is omitted, equivalent circuit diagram of the semiconductor-electrolyte junction consists of three capacitors (Figure 7.3): the capacitor of the space charge layer (C_{sc}), the capacitor of the surface state (C_{ss}), and the capacitor of the Helmholtz layer (C_H) [30]. In general, for a single-crystal photoelectrode, C_H is much larger than C_{sc}, and C_{sc} is much larger than C_{ss}. Therefore the effect of C_{ss} and C_H on the circuit can be omitted. The space-charge capacitance C varies with the potential drop V over the space charge layer

according to the Mott-Schottky equation [31,32].

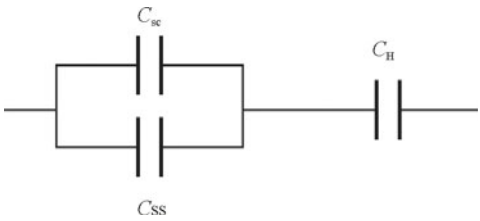

Figure 7.3 An equivalent-circuit diagram of the semiconductor-electrolyte junction under dark condition

$$\frac{1}{C_{sc}^{2}} = \frac{2(V - V_{fb} - kT/e_0)}{e_0 \varepsilon_r \varepsilon_0 N_d} \tag{7.3}$$

where C_{sc} is the capacitance of the space charge layer, V and V_{fb} is the electrode potential and the flat potential of the semiconductor electrode, respectively; k is Boltzman constant, T is the temperature, e_0 is the electron charge, ε_r is the dielectric constant, ε_0 is the permittivity of vacuum, N_d is the carrier concentration.

When illuminated, the relation between the photocurrent of n-type semiconductor and applied potential can be expressed as follows [33~35]:

$$J_p = \Phi \alpha \sqrt{\frac{2e\varepsilon\varepsilon_0}{N_d}(V - V_{fb})} \tag{7.4}$$

Where J_p is the photocurrent; Φ is the photon flux; α is the absorption coefficient; V is the electrode potential.

Besides common PEC cells constructed from a photoanode in conjunction with a metal cathode (as shown in Figure 7.1), there are some general types of photoelectrochemical devices using semiconductor electrodes for the conversion of water into hydrogen.

(1) p-n type PEC cells

In 1976, Nozik reported a p-n type PEC cell consisted of a photoanode (n-TiO_2) and a photocathode (p-GaP) [36]. The efficiency of photoelectrolysis under solar radiation can be greatly enhanced by using simultaneously illuminated n- and p-type photoelectrodes. H_2 and O_2 are produced in the n-TiO_2/ p-GaP cell without an external anodic bias. The efficiency of n-TiO_2|H_2SO_4|p-GaP is only 0.25% though this PEC cell can split water without any external bias, due to not only high internal resistance but also the low efficiency of single photoelectrode. Later,

n-TiO_2/p-CdTe, n-$SrTiO_3$/p-CdTe, n-$SrTiO_3$/p-GaP, n-Fe_2O_3/p-Fe_2O_3 and n-TiO_2/p-$LuRhO_3$ were also studied, but their efficiencies were very low[37].

(2) Tandem cells

The concept of a tandem cell was used in photovoltaic cell very early. In the field of photovoltaic cell, a tandem cell is multi-junction one that subdivides the broad solar spectrum into different energy ranges and to convert each range with a solar cell of a well matched band gap. The concept of the tandem cell was introduced into PEC cell later. In 1998, Turner reported that a tandem cell consisted of GaAs p-n heterojunction photoelectrode and p-$GaInP_2$ photovoltaic cell. The solar energy conversion efficiency of this PEC with tandem structure reached 12.4%. But this cell has two defects: one is high price, and the other is severe photocorrosion [38]. In order to decrease the price, Mill et al. designed a-Si(PV)/TiO_2,WO_3, or Fe_2O_3 structure in 2003. The efficiency of a-Si(PV)/WO_3 can reach 2.2%. [39] In 1999, Grätzel reported a new kind of tandem cell. Unlike p-n PEC cell, a photoanode of this tandem cell is dye-sensitized TiO_2, while WO_3 or Fe_2O_3 act as a photocathode. This PEC cell is similar to photosynthesis. Therefore, it can be called artificial leaf. The solar-to-hydrogen efficiency of this cell is up to 4.5%. [40]

Reliable measurement of the photoconversion efficiency for semiconductor electrodes is essential to the assessment of electrode PEC performances. Murphy et al. discussed detailedly efficiency of solar water splitting using semiconductor electrodes. In addition to the spectrum of the incident radiation, the photoconversion efficiency depends on many factors, such as the band gap of the semiconductor, reflection of radiation before reaching the semiconductor, the level of absorption of the radiation in the semiconductor, and the transport of charge carriers through the semiconductor [41]. The photoconversion efficiency can be calculated as following:

$$\eta = \frac{e(V_0 - V_{app})\int_0^{1240/E_g} N(\lambda)\,IPCE(\lambda)\,d\lambda}{I_0} \tag{7.5}$$

where E_g is band gap of a semiconductor, $N(\lambda)$ is the incident photon flux passed by the monochromator when set to wavelength λ, IPCE(λ) is photo-to-electron conversion efficiency (IPCE) at wavelength λ, V_0= 1.229V is the potential corresponding to the Gibbs free energy change per photon required to split water, and V_{app} is the bias voltage applied between the working and counter electrodes.

However, the photoconversion efficiency of a photoelectrode material depends on the measurement system (a two-electrode or three-electrode method), the light source, the counter electrode, the distance between the electrodes, the contact

resistance and so on. Measurements of efficiency performed under xenon lamp and solar illumination are compared with efficiencies calculated by integrating the IPCE over the lamp and solar spectra by Plumb's group [41]. It is shown that use of a xenon lamp as the light source can lead to a large overestimate of the solar-to-hydrogen efficiency, relative to that obtained under standard AM1.5 solar illumination[41]. The IPCE of photoelectrode using the three-electrode method under standard AM1.5 solar illumination are often used as an important factor to evaluate the photochemical activity.

7.3 Photoelectrode materials for PEC H_2 generation

Photoelectrode materials play a vital role in PECs. The choice of a suitable system is severely restricted by the fact that the only semiconductors that are photochemically stable in water are metal oxides. Metal oxides represent ideal photoelectrodes for solar-driven hydrogen production because of their low cost and high stability in aqueous solution. Here some important photoelectrode materials are introduced as following.

7. 3. 1 TiO_2

Titanium dioxide (TiO_2) occurs in nature as well-known minerals rutile (3.0 eV), anatase (3.2 eV) and brookite(3.4eV). As a photoanode, rutile exhibits the highest IPCE among these phases. The IPCE of rutile photoanode is close to 100% under ultraviolet irradiation. Owing to the large band gap (3.0~3.4 eV), only the ultraviolet part of the solar irradiation (amounting to ~4% of the incoming solar energy on the earth's surface) can be absorbed by TiO_2, and the theoretic calculation has shown that the highest ssolar-to-hydrogen efficiency cannot be over 2.2% under the irradiation of sunlight.

The morphology of TiO_2 can influence its photoelectrochemical properties[42~44]. For example, TiO_2 nanoparticle film exhibits different photoelectrochemical properties from bulk TiO_2. When the nanoparticle is smaller in size than the width of the space charge layer, photoinduced electrons and holes can separate efficiently. Therefore, the separation of photoinduced carriers is mainly drove by diffusion, instead of drift by internal electric field. Nanotube and nanoribbon will change the transfer route of photoinduced carriers, and improve their separation and enhance the absorption of light, thus increasing the solar-to-hydrogen efficiency. In 2005, Mor et al. reported the enhanced photoelectrochemical properties of TiO_2 nanoarray photoelectrode. Its IPCE is up to 90% at 337 nm (bias 1V) and its photoconversion efficiency is 6.8% (at 320 ~ 400 nm). In the next year, they

reported photoconversion efficiency of ordered TiO_2 nanoarray photoelectrode reached 16.25%. Note that the light resource is special ultraviolet light, instead of simulated sunlight. Therefore, the photoconversion efficiency is not solar energy conversion efficiency.

In 2008, Allam et al. also synthesized TiO_2 nanotube array films by anodization of Ti foil in HCl electrolytes containing different H_2O_2 concentrations. The nanotube arrays obtained from the ethylene glycol electrolytes show relatively higher photocurrents (0.8 mA/cm^2 under AM 1.5). Rodriguez et al. reported that PEC cells with photonic crystal show much better photoelectrical performances when the titania electrode is structured to localize photons [45] .

For designing highly efficient and low cost PEC cells systems, doping with various metal cations, such as Ta, Mo, W, Nb, Re, Cr, V, Fe, Mn, Ni, Co, Al, has been introduced to extend the optical absorption of TiO_2-based systems to visible region[46]. Among these samples, the absorption edge of Cr doping TiO_2 photoanode can reach 600 nm, while that of *V* doping TiO_2 photoanode is up to 750 nm[47,48]. However, the photoconversion efficiencies of these photoanodes have not been obviously improved in solar spectrum due in part to increase of carrier recombination centers.

On the other hand, anionic nonmetal dopants, such as N, C, B and S atoms, have also been investigated widely, aiming at extending the response of TiO_2-based photoanode materials into the visible region[49~53]. Asahi et al. reported that N-doped TiO_2 showed dramatic improvement over undoped TiO_2 in its optical absorption and photocatalytic activity for visible light. Based on their analysis of the density of states, they concluded that the substitution doping of N for O in the anatase TiO_2 crystal can yield a band-gap narrowing driven by mixture of N 2p states and O 2p states.

Although visible light absorption of TiO_2-based photoelectrodes can be enhanced by doping metal cations or nonmetal anions, this approach often results in little or no increase in overall photoconversion efficiency, because there are some disadvantages as following [49~53] :

(1) The absorption coefficients of the samples is very low in visible region, therefore they cannot absorb the visible light efficiently.

(2) Doping cannot change the peak in IPCE spectrum of the photoanodes, and the IPCE reaches the maximum at 350 nm, corresponding to the transition of O 2p to Ti 3d; therefore, the photoconversion efficiency in solar spectrum has not been improved obviously.

(3) Doping can increase the probability of photoinduced electron and hole recombination, and may decrease the IPCE in ultraviolet region.

(4) Doping with nonmetal element often decreases the stability of photoanode.

In order to improve the photoconversion efficiency in solar spectrum, it is necessary to develop photoanode materials with narrow band gap.

7. 3. 2 WO_3

Tungsten trioxide has a band gap of 2.7 eV and its absorption edge can be extended to 460 nm. It also exhibits good stability in acid solution. Therefore, it has attracted much attention in PEC cells. However, its conduction band is lower than the H^+/H_2 level, therefore it can split water only under external bias voltage.

In 2000, Lindquist et al. studied the photoelectrochemical properties of nanostructured WO_3 thin films in a 0.5 M $NaClO_4$ solution with the pH value of 4.68. The photocurrent onset was at 0.1 V, and the saturation photocurrent was at potentials >0.8 V [54]. The IPCE was high, but depending on the incidence of the light (front or back side). At 380 nm, the IPCE of WO_3 is 70% illuminated from the back side, while it is only 50% illuminated from the front side. The IPCE of WO_3 is much lower than that of TiO_2, because the absorption coefficient of WO_3 is much smaller than that of TiO_2. Porous structure can improve the absorption of WO_3, thus enhancing the efficiency.

In 2001, Santato et al. prepared highly transparent nanoporous WO_3 films and found that its IPCE can reach 75% for the photogeneration of oxygen from 1 M aq $HClO_4$ and reach 190% in the presence of methanol in the solution when used simulated solar AM 1.5 illumination, denoting in the latter case the occurrence of a perfect photocurrent doubling [55~57].

Berger et al. prepared porous WO_3 by anodic oxidation method, in order to improve photocurrent by increasing contact surface between the photoanode and electrolyte [58]. But the IPCE is only 25% at 350 nm, which is far lower than the values in the literatures of Lindquist and Augustynski. Yang et al. synthesized nanostructured crystalline WO_3 films using a peroxopolytungstic acid precursor with addition of mineral acids, HCl, $HClO_4$ and H_2SO_4, aiming at adjusting the morphology of the crystalline WO_3 films [59]. Marsen et al. reported dense and crystalline WO_3 electrode at 270 ^oC by sputtering. Under AM 1.5 illumination, the photocurrent reaches 2.7 mA/cm^2 at 1.6 V vs. SCE(saturated calomel electrode) [60]. Now, the latest record is ca. 3 mA/cm^2 reported by Augustynski's group [16].

Nanoporous WO_3 films with preferential orientation of the (002) planes and pore diameter of 70～90 nm were prepared by anodization in neutral F−-containing strong electrolytes. Under visible light irradiation, the photocurrent density (at 1.6 V vs. Ag/AgCl) by the annealed nanoporous film were 3.45 mA/cm^2 and 0.91%, respectively. In their experiments, a 500W Xe lamp served as

the visible light source with an intensity of 100 mW/cm^2, which is different in spectrum from AM 1.5. Therefore, the photocurrent cannot be compared with other literatures. The annealed nanoporous WO_3 films show maximum IPCE of 92% at 340 nm at 1.2 V vs. Ag/AgCl, which are higher than that of annealed compact WO_3 film due to the large interfacial heterojunction area[61].

Doping with elements, such as C and N, has been used to improve the PEC properties of WO_3 photoelectrode [62,63]. Doping with nonmetal often decreases its photochemical stability. C-doped WO_3 films were produced using a spray-pyrolysis methodology, with glucose used as the carbon dopant source. The C-doped WO_3 electrodes exhibited photocurrent densities up to 1.6 mA/cm^2 in 1 M HCl electrolyte and as high as 2.6 mA/cm^2 with the addition of methanol as a sacrificial agent. The photocurrent density of C-doped WO_3 was approximately 50% higher than that of the undoped WO_3 electrode synthesized using the same procedures. Cole et al. studied the effects of N doping on the properties of WO_3 film photoelectrode. Thin films of WO_3 were fabricated by reactive RF magnetron sputtering at partial pressures in the range of 0～6 mTorr N_2. The photocurrent density under AM 1.5 illumination showed a degradation from 2.68 mA/cm^2 for pure WO_3 to 0.67 mA/cm^2 for the nitrogen doped sample (6 mTorr), which is attributed to a degradation of the electron transport properties as a result of a highly defective lattice.

In theory, the maximum solar energy conversion efficiency of WO_3 is about 4.8%, and the utmost theoretical photocurrent is 3.9 mA/cm^2 under AM 1.5 illumination [41]. The best experiment record of ca. 3 mA/cm^2 is very near to the utmost theoretical value. In order to improve the photoconversion efficiency in solar spectrum, more attention should be paid to develop photoanode materials with narrower band gap, for example α-Fe_2O_3.

7. 3. 3 Fe_2O_3

Hematite (α-Fe_2O_3) is common on the earth, stable, and also probably the cheapest semiconductor with a band gap of 2.0 eV, thereby allowing visible light absorption up to 600 nm. Hematite is stable in most electrolytes at pH > 3 and it is nontoxic. Therefore, α-Fe_2O_3 is expected to be an ideal candidate photoanode for photoelectrochemical cell systems [64,65]. Unfortunately, pure-phase hematite is a charge transfer-type Mott insulator with intrinsically poor conductivity which limits the photoconversion efficiency for solar hydrogen production [66~71]. Electron conduction in hematite generally takes place along the same layers where all the iron atoms have unidirectional magnetic moment, thus exhibiting bad electron conductivity [66~71]. Despite the favorable band gap of around 2 eV,

α-Fe_2O_3 has poor photoelectrochemical performance because of the short charge carrier diffusion length, low electron mobility, and high resistance. To improve upon intrinsic electronic properties of hematite, substituitional doping with Si, Ti, Pt, Mo, Cr, Zn, Ge, Sn, and Nb among other atoms has been reported [72~84]. Yan et al. have studied the band structures for α-Fe_2O_3 doped with transition metals and reported that the electron effective mass of α-Fe_2O_3 is reduced significantly after doping with Ti, Pt, Cr, which would significantly improve the conductivity and therefore enhance the PEC performances as observed experimentally [66~71]. However, doping with Mn would create more localized defects bands leading to possible increased carrier recombination, but decrease the performances [66~71].

Element doping, such as doping Si or Ti in the place of Fe^{3+}, has been used to enhance the photoconversion efficiency of α-Fe_2O_3 photoanode, owing to the improvement in conductivity introduced by the increased donor concentrations[72~84]. However, the doping concentration is limited by the mismatch between ion radius of Si^{4+} (or Ti^{4+}) and Fe^{3+}, thus obtaining low donor concentration. Since the ions radius of Si^{4+}< Fe^{3+}< Ti^{4+}, codoping with Si and Ti can balance the ion radius difference between Fe^{3+} and Si^{4+} (or Ti^{4+}) and enhance the donor concentration further, which is helpful to improvement in the photoconversion efficiency [72~84]. The Si and Ti codoped α-Fe_2O_3 film showed much higher photocurrent and IPCE than those of Si-doped or Ti-doped film. The results suggest that codoping is a preferred choice to enhance α-Fe_2O_3 photoelectrochemical properties. Yan et al. have also proposed that codoping with Ti and N may lead to even improved PEC performance, because of the following effects: ① enhancing the doping solubility for both Ti and N; ② increasing optical absorption in the energy region near the band gap of α-Fe_2O_3; and ③ improving electron conductivity [66~71].

In 1999, Khan et al. have prepared nanocrystal Fe_2O_3 film using ultrasonic spray pyrolysis (USP), the photocurrent density of which can reach 3.7 mA/cm^2 at 0.7 V vs. SCE [85]. Because the light source is not simulated sun (AM 1.5) in the experiments of Khan, it is not reasonable to compare this data with other literatures. For improving the electron transfer, Beermann et al. have synthesized arranged nanorod Fe_2O_3 in 2000 [86]. In 2004, Khan et al. have reported Zn-doped Fe_2O_3 photoanode with p-type semiconductor using ultrasonic spray pyrolysis. The IPCE of 4% Zn-doped Fe_2O_3 is the highest and reaches 21.1%, which is the record for p-type Fe_2O_3 semiconductor photoanode and much larger than 3% of Mg doped Fe_2O_3 (p-type) [87]. This data has not been repeated by others.

PEC cells prepared from highly ordered and vertically grown a-Fe_2O_3 nanorod arrays on a Au nanorod substrate showed about 8 mA/cm^2 photocurrent density under 1 sun condition without any hole scavenger. Since the IPCE value was

not shown in this report, the photocurrent data cannot be compared with other literatures. The photoelectrochemical properties of the a-Fe_2O_3 nanorod arrays as a photoanode were studied by evaluating their photocurrent-potential behavior in 1M NaOH electrolyte under AM1.5 100 mW/cm^2 illumination. Also, the dependence of the PEC of the a-Fe_2O_3 nanorod arrays on their length was studied and the optimum rod length was determined [88].

Mesoporous hematite photoelectodes was prepared by a solution-based colloidal method, yielding photocurrents of 0.56 mA/cm^2 under irradiation of AM 1.5G (100 mW/cm2) and 1.23 V vs. RHE (reversible hydrogen electrode,) and over 1.0 mA/cm^2 before the dark current onset (1.55 V vs. RHE) [89]. IrO_2 nanoparticles (ca. 2 nm diameter) were deposited by electrophoresis onto the hematite photoanode, and one observed a dramatic shift in the onset potential from +1.0 to +0.8 V vs. RHE and an increase in the plateau photocurrent from 3.45 to 3.75 mA/cm^2, which is the best record of hematite. Compared with WO_3, the bias required for Fe_2O_3 is much higher. This deposition method was found to be superior to methods for example soaking [90].

A promising route to improve the performance of α-Fe_2O_3 photoelectrodes for solar hydrogen production is to use an extremely thin layer of this visible light absorber on a nanostructured scaffold. However, the typically poor performance of ultrathin (ca. 20 nm) films of α-Fe_2O_3 has been the limiting factor in implementing this approach. A substrate pretreatment using tetraethoxysilicate (TEOS) results in drastic improvements in the PEC performances of 12.5nm-thick hematite films [91]. A monolayer of SiO_x on the substrate changes the hematite nucleation and growth mechanism, increases its crystallinity, and reduces the concentration of carrier trapping states of the ultrathin films [91].

Cobalt phosphate (Co-Pi) was discovered to exhibit electrochemical oxygen evolution at relatively low overpotentials under mild ambient conditions (pH = 7~9.2, 1 atm, and room temperature). Recently, composite Co-Pi/a-Fe_2O_3 photoanodes were explored for PEC water splitting [92~94]. The Co-Pi modified semiconductor photoanodes allow photon absorption, carrier separation, and redox surface catalysis to be effectively decoupled, yielding improved performance.

Though α-Fe_2O_3 has band gap of 2.0 eV, the maximum IPCE appear in ultraviolet light region, which is the reason that it exhibits low photoconversion efficiency. Besides, the maximum IPCE of α-Fe_2O_3 is much lower than that of TiO_2 and WO_3. However, because of its favorable band gap, photochemical stability and matchless abundance, utilization of α-Fe_2O_3 to produce hydrogen on a global scale is realistic. Optimization of hematite to meet the requirement for practical use is still on the growing.

7.3.4 $BiVO_4$

The band gap of monoclinic scheelite $BiVO_4$ is 2.4 eV, which is 0.3 eV narrower than that of WO_3. In theory, the maximum solar-to-hydrogen efficiency of WO_3 is about 4.8%, while it is about 9.1% for $BiVO_4$ because the photon flux between 480~520 nm are very high in AM1.5 global solar spectrum. Moreover, it is reported that the visible light absorption of $BiVO_4$ originates in the direct transition from the hybridization of Bi 6s and O 2p to V 3d [95,96].

The nanocrystalline $BiVO_4$ film electrode were prepared by a modified method of metal-organic decomposition and its IPCEs at the bias voltage of 1.9 vs. RHE were ca. 33% at 400 nm and 29% at 420 nm for the decomposition of water under the irradiation of visible light, respectively [97,98].

In experiments, the maximum IPCE in a $BiVO_4$ photoelectrode after Ag^+ treatment is 44 % at 420 nm even at a very high potential (1.58V vs. RHE)[99]. Moreover, the photochemical stability of $BiVO_4$ electrode under illumination is not quite good even after Ag^+ treatment [99]. More recently, Sayama et al. have reported that carbonate ions in the aqueous electrolyte solution improved both the photocurrent and the stability of a porous $BiVO_4$ semiconductor electrode used for water splitting under the irradiation of visible light up to 520 nm. The photocurrents in $AHCO_3$ (A = Na and K) solutions at 1.23V were approximately six times higher than that in Na_2SO_4 aqueous solution. The maximum incident photon-to-current efficiency (IPCE) was 45% at 420 nm without any surface modifications [100].

Monoclinic scheelite $BiVO_4$ thin films have been successfully prepared by a chemical solution approach of polymer-assisted deposition [101]. The films are transparent yellow with granular morphology and show a strong absorption in the visible light region. The photoresponse of the films on conducting oxide electrode substrates is observed. $BiVO_4$ films were deposited on fluorine-doped tin oxide substrates by chemical bath deposition. The compact films with a smaller microcrystal exhibited better performance, which was helpful to understand the relationship between the morphologies of other microcrystal electrodes and their photoelectrochemical properties [102]. $BiVO_4$ electrodes were prepared by pasting the obtained fine $BiVO_4$ particles on FTO plates and subsequently calcining at 673 K. The $BiVO_4$ electrode gave an excellent anodic photocurrent with 12% of an IPCE at 440 nm at 1.5 V vs. Ag/AgCl(0.1 M K2SO4) [103]. Remarkable 10-fold enhancement in PEC photoelectrochemical water splitting reaction is observed on composite photoelectrode of $BiVO_4$ and graphene oxide, compared with pure $BiVO_4$ under visible illumination. This improvement is attributed to the longer electron lifetime of excited $BiVO_4$ as the electrons are injected to graphene oxide

instantly at the site of generation, leading to a minimized charge recombination. Another reason is improvement in contact between $BiVO_4$ particles with transparent conducting electrode using graphene oxide scaffold [104].

Thin films of $BiVO_4$ with monoclinic structure were deposited onto indium-doped tin oxide (ITO) glass by ultrasonic spray pyrolysis. The effects of tungsten doping and hydrogen reducing were investigated. When treated with hydrogen reducing, the carrier density of the photoelectrode increased due to more oxygen vacancies, resulting higher IPCE than the non-doping samples. Substituting 1% vanadium with equal mole tungsten can increase IPCE remarkably, which achieved about 10% at 0.3 V vs. SCE potential under 400~450 nm wavelength photo irradiation [105]. The shortcomings of $BiVO_4$ are that its IPCE value is very low at low bias potentials, and that its photochemical stability is bad.

The doping effects of several transition metal impurities for monoclinic $BiVO_4$ are studied and the IPCE of $BiVO_4$ can be increased from 9% to 41% (at 420 nm and 1.0 V vs. RHE) by doping Mo (3%) in the sites of V [106].

7.3.5 Other semiconductor photoelectrode materials

Except TiO_2, WO_3, Fe_2O_3, and $BiVO_4$, there are some oxide semiconductors that can act as photoelectrodes. $SrTiO_3$ has been the first photoelectrode material so far for unassisted photo-cleavage of water in PEC cell [107,108]. Other materials require the application of a bias to assist with the reduction of water. Doping with some elements, for example Nb, has been used to enhance the photoelectrochemical properties of $SrTiO_3$.

Some other oxide materials, such as $BiFeO_3$ and $CaFe_2O_4$, have been used as photoelectrode materials [109,110]. An (hk0)-oriented $CaFe_2O_4$ photocathode with the band gap of 1.9 eV was prepared, and hydrogen and oxygen gases were produced from a photocell short-circuited by connecting the $CaFe_2O_4$ and n-type TiO_2 electrodes under illumination without applying an external voltage. The open-circuited voltage was 0.97 V and the short-circuit current was about 200 mA/cm^2, and the amount of evaluated hydrogen and oxygen after 2 days of reaction were about 70 and 4 μmol, respectively.

Non-oxide semiconductor photoelectrode materials, such as Si, Ge, GaAs, CdX (X= S, Se, Te), WS_2, FeS_2, $CuInSe_2$ and $CuInS_2$, have been studied for many years [111~115]. Though their band gaps are narrow and can absorb visible light, most of them exhibit serious photocorrosion, thus hindering their applications in PEC cells for H_2 generation. Some p-type semiconductors, such as GaP, InP and $GaInP_2$, exhibit good photostability, and can act as photocathode for H_2 generation [116,117]. In 1981, Heller reported the cell of p-InP(Ru)|1M HCl+1M

KCl|Pt, and the cell can work stably for a week without oxygen. Bogdanoff et al. reported that the stability of InP photocathode was bad when using H_2SO_4 as an electrolyte, and that its stability and IPCE can be improved by loading Pt onto the surface. In 1998, Turner et al. reported p-$GaInP_2$ exhibited better photochemical stability in acid electrolyte than in base or neutral electrolyte [38].

(Oxy)nitride materials, for example TaON, are expected to perform as not only photocatalysts but also visible-light-driven photoelectrodes[118~121]. Abe et al. studied PEC properties of a porous TaON photoelectrode under visible light irradiation. The photocurrent was significantly improved by $TiCl_4$ treatment on the TaON electrode. The TiO_2 necking formed between the TaON particles may favor the electron transport within the porous electrode [122]. Banerjee et al. reports the synthesis of TaON nanotube arrays as efficient visible light driven photocatalysts for photoelectrochemical generation of hydrogen from water [123].

The porous oxynitride TaON film electrode prepared on FTO substrates showed significantly high IPCE ca. 76% at 400 nm at 0.6 V vs (Ag/AgCl) in an aqueous Na_2SO_4 solution (0.1 M, pH=6), after loading of $IrO_2 \cdot nH_2O$ nanoparticles as a cocatalyst for water oxidation. Overall water splitting into H_2 and O_2 under visible light was demonstrated using an $IrO_2 \cdot nH_2O$-loaded TaON photoanode combined with a Pt electrode under an externally applied bias (0.6~1 V) [124].

Tantalum nitride (Ta_3N_5) thin film is investigated as a visible light-driven photoelectrode material. The photoelectrochemical properties of the material are investigated on the basis of cyclic voltammograms and current-time curves, and the conduction and valence band edges of Ta_3N_5 are determined from the photocurrent voltage response. The potentials of the conduction and valence bands are found to be satisfactory for the reduction of H^+ to H_2 and the oxidation of H_2O to O_2. Anodic photocurrent associated with the oxidation of water is obtained under visible-light irradiation, although the Ta_3N_5 itself undergoes simultaneous oxidation. Through sustained photoinduced redox cycling on the Ta_3N_5 electrode in aqueous $Fe(CN)_6^{3-}/Fe(CN)_6^{4-}$ solution,Ta_3N_5 thin film is demonstrated to function as a stable electrode for generating electric current under visible light [125].

A lanthanum titanium oxynitride ($LaTiO_2N$) was studied as a visible-light driven photoelectrode for water splitting by Nishimura and his coworkers [126]. The as-prepared electrode exhibited an anodic photocurrent based on water oxidation under visible-light irradiation ($\lambda > 420$ nm) in an electrolyte (Na_2SO_4) solution. This current was increased by post-treatment with titanium (IV) chloride ($TiCl_4$) solution, due to the improvement of inter-particle electron transfer in the $LaTiO_2N$ thin film.

Photochemical stability of nonoxide photoelectrodes is worse than that of

oxide photoelectrodes. Sacrificial regent can be used to improve the stability of these photoelectrodes. III-Nitride semiconductors, for example InxGa1-xN, are expected to have suitable band gaps to utilize solar energy [127~132]. Theuwis et al. have studied the photoeletrochemical PEC properties and defects of III-Nitride semiconductors. Fujii et al. have investigated the photoelectrochemical water splitting for hydrogen production in $In_xGa_{1-x}N$. In their reports, the indium content (x) of $In_xGa_{1-x}N$ was less than 0.09 and the band gap was larger than 3 eV. It meant that almost no visible light can be used to split water, and the photocorrosion problem has not been resolved. $InxGa_{1-x}N$ with a higher concentration indium has a narrower band gap, but will suffer more serious photocorrosion. For instance, GaN is stable in HCl solution under illumination, while $In_xGa_{1-x}N$ ($0<x<0.1$) is photocorroded in the same solution. Luo et al. used some proper electrolytes (for example HBr) to prevent the photo-etching of $In_xGa_{1-x}N$ electrode. It was found that $In_{0.20}Ga_{0.80}N$ responded to 480 nm and showed high stability in HBr solution.

7. 3.6 Heterojunction photoelectrode materials

Semiconductor photoelectrodes with wide band gap exhibit good photostability, though they cannot absorb visible light. Heterojunction structure, consisted of narrow-band-gap semiconductor covered by wide-band-gap one, was reported to improve the photochemical stability of PEC cells. In 1977, Tomkiewicz and Woodall reported such heterojunction PEC cells consisted of some narrow-band-gap semiconductors (such as GaAs and GaAlAs) covered by wide-band-gap semiconductor, such as TiO_2, SnO_2, Nb_2O_5, Al_2O_3, or Si_3N_4 [133]. However, their photocurrent is very low and even smaller than that of the single component electrode. In addition, photoinduced holes cannot transfer into the electrolyte over TiO_2 layer, which cannot avoid photocorrosion of the narrow-band-gap semiconductors. Bard et al. prepared the photoelectrodes composited of narrow band gap n-Si, P-Si, n-CdS, n-GaP, n-InP covered by dense TiO_2 film [134]. Though the photochemical stability was improved, the photocurrent of heterojunction PEC cells is low than that of TiO_2. Because the conduction band of Si is more negative than that of TiO_2, photoinduced electrons in TiO_2 can transfer into the conduction band of Si over interface barrier. The valence band of TiO_2 is much more positive than that of Si, therefore the photoinduced holes in the valence band of Si cannot transfer into that of TiO_2 if there is no very large band bending. All the photo-electrodes mentioned above were composed of a single crystal and a thin film; the interface barrier was formed due to the band bend on the surface and, therefore, thus decreasing the efficiency. In 1982, a TiO_2/Fe_2O_3 heterojunction PEC cells was found to exhibit good stability against photocorrosion [135]. The photocurrent of the

heterojunction is larger than that of Fe_2O_3, but still lower than that of TiO_2. It is interesting that the photogenerated holes in the valence band of Fe_2O_3 can transfer into the electrolyte over the TiO_2 layer. Later, TiO_2/SnO_2, CdS/TiO_2, $CdSe/TiO_2$, Fe_2O_3/TiO_2 and TiO_2/In_2O_3 heterojunctions were studied. The photocurrents of the heterojunctions are a little larger than that of TiO_2 [136~140]. Though band match and stability against photocorrosion is considered in these researches, the photocurrent is still low because the interface diffusion takes place.

Nanostructures were also explored to remove the interface barrier of the heterojunction photoelectrodes, because photoinduced electrons and holes can be separated efficiently when the nanoparticle is smaller than the width of the space charge layer. Moreover, the photo-generated holes in the bottom can react with the electrolyte, but not through the upper layer, which reduces the diffusion length of the holes and improves the conversion efficiency. Shiyanovskaya and coworkers reported a TiO_2/WO_3 nanostructure that improved the photocurrent in comparison with the single component electrode [141].

Wang et al. reported the WO_3/Fe_2O_3 heterojunction electrode exhibited enhanced photocurrent compared with Fe_2O_3 photoelectrode because the photogenerated electrons could transfer more easily in WO_3/Fe_2O_3 heterojunction[142] .Photoelectrochemical performances of the $SrTiO_3/\alpha\text{-}Fe_2O_3$ heterojunction electrode were reported to enhance the photocurrent densities and external quantum efficiencies by improving the transfer of the photogenerated holes [143].

Lin et al. have exploited the idea of forming nanoscale heterojunction for efficient charge collection [144~146]. A key factor enabling this design is the discovery of the $TiSi_2$ nanonet, which exhibits high conductivity and suitably high surface area[147,148]. The introduction of $TiSi_2$ nanonets has been applied to improve the performance of TiO_2, WO_3, and $\alpha\text{-}Fe_2O_3$, respectively[144~146]. The highest external quantum efficiency measured on $\alpha\text{-}Fe_2O_3$ without intentional doping is 46% at 400 nm of wavelength. The combined advantages of $TiO_2/TiSi_2$ core/shell heteronanostructure led to the high PEC performance, and a peak efficiency of 16.7% was achieved under monochromic UV illuminations of 330 nm. The versatility of the approach was further demonstrated by incorporating W into the TiO_2 shell to boost its visible light performance, and a peak efficiency of 0.83% was achieved [144~146].

Turner et al. studied the photoelectrochemical properties of $GaInP_2$ photocathodes paired with nanostructured hematite and tungsten trioxide photoanodes. For the p-$GaInP_2$/hematite system, under illumination at open-circuit conditions, the potential of hematite shifts cathodically and that of the $GaInP_2$ shifts anodically. Under short-circuit condition and visible light illumination of 1 W/cm^2,

the $GaInP_2$/hematite combination can split water, though with a very low rate of a few μA/cm^2. Similar potential shifts were observed with the nanostructured WO_3/$GaInP_2$ combination. The WO_3/$GaInP_2$ combination can split water under visible light with light intensities of above 0.2 W/cm^2 [149].

A heterojunction CdS/TiO_2 photoelectrode is prepared by filling CdS nanoparticles into one-dimensional TiO_2 nanotube array films. The self-assembled TiO_2 nanotubes are fabricated by an anodization method and sensitized with CdS nanoparticles by the close space sublimation technique. Under AM1.5 illumination, a 5.6 mA/cm^2 short-circuit current density is achieved using the CdS modified photoelectrode, which represents an enhancement by a factor of 36 in photoactivity compared with that of the plain TiO_2 nanotube array film [150].

Gaillard et al. reported that Mo incorporation in the bulk of the film (WO_3:Mo) results in poor PEC performance when compared with pure WO_3, most likely due to defects that trap photo-generated charge carriers. When a WO_3:Mo/WO_3 bilayer electrode is used, a 20% increase of the photocurrent density at 1.6 V vs. SCE is observed compared with pure WO_3. Coherent growth of the WO_3:Mo top layer on the WO_3 bottom layer allows an optimization of the electronic surface structure of the electrode while maintaining good crystallographic properties in the bulk [151].

7.4 Conclusions and future developments

In summary, we have briefly reviewed basic concepts of PEC cells and semiconductor materials which appear to be the most promising photoelectrode candidates for solar hydrogen production. Many attempts have been made over the past several decades to extend the photo-response of wide-band gap semiconductors (for example TiO_2) to the visible region by doping. However, such doping does not lead to improvement in the conversion efficiency, owing to a concomitant increase in recombination. Recent developments indicate that smaller band gap metal oxide semiconductors, especially hematite and $BiVO_4$, offer a more promising direction of research. Future developments may involve expansion of the range of materials to include mixed oxide materials. [16] This requires accurate control over the composition and the defect chemistry, which is especially important in the case of ternary oxides. New photoelectrode materials with band gap of ca. 2.0 eV, good stability, long diffusion distances of electrons and holes are required in the future.

Parkinson et al. presented a new simple and high-throughput combinatorial method to search for photoelectrode materials capable of the PEC water splitting [152]. This method of combinatorial chemistry will play important role for finding effectively new photoelectrode materials. DFT theoretical study will

favor searching new photoelectrodes, because it can understand the effects of the electronic structure on PEC properties [153].

Porous structures are used to improve the incident photon-to-electron conversion efficiency of photoelectrodes due to following reasons: (1) improvement in light absorption, (2) decrease in the distance of hole diffuses, (3) favoring the electrolyte diffusion, and (4) high specific surface area to increase the density of active sites at which the redox reactions can take place.

The structure of photonic crystal has also been introduced to the photoelectrodes. A photonic crystal is a periodic dielectric structure which forbids propagation of light in a certain frequency range [154]. Photonic-crystal-based optical coupling offers a unique way of light-matter interaction to increase the light harvesting, especially around the absorption edge of a semiconductor [155]. The light in a photonic crystal undergoes strong coherent multiple scattering and travels with very low group velocity near the stop band edges, referred to as slow light. Such a slow-light effect can considerably increase the effective optical path length, therefore leading to a delay and storage of light in photonic materials [156,157].

Surface modification with electrical catalysts is an important way to improve the output characteristics of photoelectrodes. Electrical catalysts for O_2 production, such as Co-Pi, IrO_2, and Rh_2O_3, are required in photoanode materials (n-type semiconductors), while electrical catalysts for H_2 production, for example Pt, are needed in photocathode materials (p-type semiconductors). The tandem cell is also one way to overcome unfavorable band energetics associated with many photoanodic materials [8]. PV/PEC cells attract more and more interest of researchers. Photoelectrochemical cells may also be constructed from a photoanode in conjunction with a photocathode, thus enhancing solar to hydrogen efficiency of PEC cells. However, their development has been substantially retarded by a lack of p-type semiconductor materials with narrow band-gap and photochemical stability.

Although many impressive results have been achieved, there is still a long way for PEC cells to go into practical use. Innovation and developments in new photoelectrode materials, structure and conceptions are still demanding. Development of high efficient and stable photocathodes will push this field forward.

Acknowledgements

Financial support from the National Basic Research Program of China (Grant No. 2007CB613305), the National Natural Science Foundation of China (Grant Nos. 21073090 and 50902068) and the Fundamental Research Funds for

the Central Universities (Nos. 1095021338, 1114021304, and 1116021308) is gratefully acknowledged.

References

[1] Grätzel M. Photoelectrochemical cells. Nature, 2001, 414(6861): 338~344.
[2] Grimes C A, Varghese O K, Ranjan S. Light, Water, Hydrogen: The Solar Generation of Hydrogen by Water Photoelectrolysis. New York Springer, 2008.
[3] Miller E L, Gaillard N, Kaneshiro J, et al. Progress in new semiconductor materials classes for solar photoelectrolysis. International Journal of Energy Research, 2010, 34(14): 1215~1222.
[4] Becquerel A E. On electric effects under the influence of solar radiation. Comptes Rendus, 1839, 9: 561.
[5] Brattain W H, Garret C G B. Experiments on the interface between germanium and an electrolyte. Bell. Syst. Tech. J., 1955, 34: 129~176.
[6] Turner D R. the anode behavior of germanium in aqueous solutions. Journal of the Electrochemical Society, 1956, 103(4): 252~256.
[7] Boddy P J. Oxygen evolution on semiconducting TiO2. Journal of the Electrochemical Society, 1968, 115(2): 199~203.
[8] Dewald J F. the charge distribution at the zinc oxide-electrolyte interface. Journal of Physics and Chemistry of Solids, 1961, 14: 155~161.
[9] Williams R. Becquerel photovoltaic effect in binary compounds. Journal of Chemical Physics, 1960, 32(5): 1505~1514.
[10] Morrison S R, Freund T. Chemical role of holes and electrons in ZnO photocatalysis. Journal of Chemical Physics, 1967, 47(4): 1543~1551.
[11] Gomes W P, Freund T, Morrison S R. Chemical reactions involving holes at the zinc oxide single crystal anode. Journal of the Electrochemical Society, 1968, 115(8): 818~823.
[12] Memming R, Schwandt G. Electrochemical properties of gallium phosphide in aqueous solutions. Electrochimica ACTA, 1968, 13(6): 1299~1310.
[13] Fujishima A, Honda K. Electrochemical photolysis of water at a semiconductor electrode. Nature, 1972, 238(5358): 37.
[14] Hardee K L, Bard A J. X. PEC behavior of several polycrystalline metal oxide electrodes in aqueous solutions. Journal of the Electrochemical Society, 1977, 124(2): 215~224.
[15] Bard A J, Fox M A. Artificial photosynthesis: Solar splitting of water to

hydrogen and oxygen. Accoumts of Chemical Researoh, 1995, 28(3): 141~145.

[16] Alexander B D, Kulesza P J, Rutkowska I, et al. Metal oxide photoanodes for solar hydrogen production. Journal of Materials Chemistry, 2008, 18(20): 2298~2303.

[17] Hou Y, Li X Y, Zhao Q D, et al. Fabrication of Cu_2O/TiO_2 nanotube heterojunction arrays and investigation of its photoelectrochemical behavior. Applied Physics Letters, 2009, 95(9): 093108.

[18] Lin Y, Zhou S, Liu X, et al. $TiO_2/TiSi_2$ heterostructures for high-efficiency photoelectrochemical H_2O splitting. Journal of the American Chemical Society, 2009, 131(8): 2772~2773.

[19] Sun J, Zhong D K, Gamelin D R. Composite photoanodes for photoelectrochemical solar water splitting. Energy and Environmental Science, 2010, 3(9): 1252~1261.

[20] Elliot D, Zellmer D L, Laitinen H A. Electrochemical properties of polycrystalline tin oxide. Journal of the Electrochemical Society, 1970, 117(11): 1343~1348.

[21] Boddy P J. Oxygen evolution on semiconducting TiO_2. Journal of the Electrochemical Society, 1968, 115(2): 199~203.

[22] Gerischer H. Physical Chemistry. New York:Academic Press, 1970.

[23] DeGryse R, Gomes W P, Cardon F, et al. On the interpretation of Mott-Schottky plots determined at semiconductor/electrolyte systems. Journal of the Electrochemical Society, 1975, 122(5): 711~712.

[24] Morrison S R. Electrochemistry at Semiconductors and Oxidized Metal Electrodes. New York: Plenum Press, 1980.

[25] Gomes W P, Cardon F. Electron energy levels in semiconductor electrochemistry. Progress in Surface Science, 1982, 12(2): 155~215.

[26] Jaegermann W, Tributsch H. Interfacial properties of semiconducting transition metal chalcogenides. Progress in Surface Science, 1988, 29(1,2): 1~167.

[27] Bard A J, Faulkner L R. Electrochemical Methods Fundamentals and Applications. New York, John Wiley and Sons, 2001.

[28] Nozik A J. Photoelectrochemistry: Applications to solar energy conversion. Annual Review of Physical Chemistry, 1978, 29: 189~222.

[29] McBroom R B, McQuarrie D A. Interaction of planar double layers in the modified Gouy-Chapman approximation. Cell Biophys, 1987, 11: 65~75.

[30] Bard A J, Bocarsly A B, Fan F F, et al. the concept of Fermi level pinning at semiconductor/liquid junctions. Consequences for energy conversion

efficiency and selection of useful solution redox couples in solar devices. Journal of The American Chemical Society, 1980, 102: 3671~3677.

[31] Bulter M A, Ginley D S, Eibschutz M. Photoelectrolysis with $YFeO_3$ electrodes. Journal of Applied Physics, 1977, 48(7): 3070~3072.

[32] Gelderman K, Lee L, Donne S W. Flat-band potential of a semiconductor: Using the Mott–Schottky equation. J. Chem. Educ., 2007, 84(4): 685~688.

[33] Ginley D S, Butler M A. The photoelectrolysis of water using iron titanate anodes. Journal of Chemical Education, 1977, 48(5): 2019~2021.

[34] Butler M A. Photoelectrolysis and physical properties of the semiconducting electrode WO_2. Journal of Applied Physics, 1977, 48(5): 1914~1920.

[35] Ghosh A K, Morel D L, Feng T, et al. Photovoltaic and rectification properties of Al/Mg phthalocyanine/Ag Schottky-barrier cells. Journal of Applied Physics, 1974, 45(1): 230~236.

[36] Nozik A J. p-n photoelectrolysis cells. Applied Physics Letters, 1976, 29(3): 150~153.

[37] Kainthla R C, Zelenay B, Bockris J O M. Significant efficiency increase in self-driven photoelectrochemical cell for water photoelectrolysis. Journal of the Electrochemical Society, 1987, 134(4): 841~845.

[38] Khaselev O, Turner J. A. A Monolithic photovoltaic-photoelectrochemical device for hydrogen production via water splitting. Science, 1998, 280(5362): 425~427.

[39] Miller E L, Rocheleau R E, Deng X M. Design considerations for a hybrid amorphous silicon/photoelectrochemical multijunction cell for hydrogen production. International Journal of Hydrogen Energy, 2003, 28(6): 615~623.

[40] Grätzel M. the artificial leaf, bio-mimetic photocatalysis. Cattech, 1999, 3: 4~17.

[41] Murphy A B, Barnes P R F, Randeniya L K, et al. Efficiency of solar water splitting using semiconductor electrodes. International Journal of Hydrogen Energy, 2006, 31(14): 1999~2017.

[42] Mor G K, Shankar K, Paulose M, et al. Enhanced photocleavage of water using titania nanotube arrays. Nano Letters, 2005, 5(1): 191~195.

[43] Paulose M, Shankar K, Yoriya S, et al. Anodic growth of highly ordered TiO_2 nanotube arrays to 134 μm in length. Journal of Physical Chemistry B, 2006, 110(33): 16179~16184.

[44] Allam N K, Shankarb K, Grimes C A. Photoelectrochemical and water photoelectrolysis properties of ordered TiO_2 nanotubes fabricated by Tianodization in fluoride-free HCl electrolytes. Journal of Materials

Chemistry, 2008, 18: 2341~2348.

[45] Rodriguez I, Ramiro-Manzano F, Atienzar P, et al. Solar energy harvesting in photoelectrochemical solar cells. Journal of Materials Chemistry, 2007, 17: 3205~3209.

[46] Aroutiounian V M, Arakelyan V M, Shahnazaryan G E. Metal oxide photoelectrodes for hydrogen generation using solar radiation-driven water splitting. Solar Energy, 2005, 78: 581~592.

[47] Bicelli L P. A review of photoelectrochemical methods for the utilization of solar energy. Surface Techonology, 1983, 20(4): 357~381.

[48] Pleskov Y V, Gurevich Y Y. Semiconductor Photoelectrochemistry. New York: Consultants Bureau,1986.

[49] Sato S. Photocatalytic activity of NOx-doped TiO_2 in the visible light region. Chemical Physics Letters, 1986, 123(1,2): 126~128.

[50] Asahi R, Morikawa T, Ohwaki T, et al. Visible-light photocatalysis in nitrogen-doped titanium oxides. Science, 2001, 293(5528): 269~271.

[51] Khan S U M, Al-Shahry M, Ingler W B Jr. Efficient photochemical water splitting by a chemically modified n-TiO_2. Science, 2002, 297(5590): 2243~2245.

[52] Lu N, Quan X, Li J Y, et al. Fabrication of boron-doped TiO_2 nanotube array electrode and investigation of its photoelectrochemical capability. Journal of Physical Chemistry C, 2007, 111(32): 11836~11842.

[53] Randeniya L K, Murphy A B, Plumb I C. A study of S-doped TiO_2 for photoelectrochemical hydrogen generation from water. J. Mater. Sci., 2008, 43(4): 1389~1399.

[54] Wang H L, Lindgren T, He J J, et al. Photolelectrochemistry of nanostructured WO3 thin film electrodes for water oxidation: mechanism of electron transport. Journal of Physical Chemistry B, 2000, 104(24): 5686~5696.

[55] Santato C, Odziemkowski M, Ulmann M, et al. Crystallographically oriented mesoporous WO_3 films: Synthesis, characterization and applications. Journal of the American Chemical Society, 2001, 123(43): 10639~10649.

[56] Santato C, Ulmann M, Augustynski J. Photoelectrochemical properties of nanostructured tungsten trioxide films. Journal of Physical Chemistry B, 2001, 105(5):936~940.

[57] Santato C, Ulmann M, Augustynski J. Enhanced visible light conversion efficiency using nanocrystalline WO_3 films. Advanced Matericals, 2001, 13(7): 511~514.

[58] Berger S, Tsuchiya H, Ghicov A, et al. High photocurrent conversion efficiency in self-organized porous WO_3. Applied Physics Letters, 2006, 88(20): 203119.

[59] Yang B, Barnes P R F, Bertram W, et al. Strong photoresponse of nanostructured tungsten trioxide films prepared via a sol-gel route. Journal of Materials Chemistry, 2007, 17(26): 2722~2729.

[60] Marsen B, Miller E L, Paluselli D, et al. Progress in sputtered tungsten trioxide for photoelectrode applications. International Journal of Hydrogen Energy, 2007, 32(15): 3110~3115.

[61] Li W, Li J, Wang X, et al. Visible light photoelectrochemical responsiveness of self-organized nanoporous WO_3 films. Electrochimica ACTA, 2010, 56(1): 620~625.

[62] Sun Y, Murphy C J, Reyes-Gil K R, et al. Photoelectrochemical and structural characterization of carbon-doped WO_3 films prepared via spray pyrolysis. International Journal of Hydrogen Energy, 2009, 34(20): 8476~8484.

[63] Cole B, Marsen B, Miller E, et al. Evaluation of nitrogen doping of tungsten oxide for photoelectrochemical water splitting. Journal of Physical Chemistry C, 2008, 112(13): 5213~5220.

[64] Eggleston C M. Toward new uses for hematite. Science, 2008, 320(5873): 184~185.

[65] Kleiman-Shwarsctein A, Huda M N, Walsh A, et al. Electrodeposited Aluminum-doped α-Fe_2O_3 photoelectrodes: Experiment and theory. Chemistry of Materials, 2010, 22(2): 510~517.

[66] Duret A, Grätzel M. Visible light-induced water oxidation on mesoscopic α-Fe_2O_3 films made by ultrasonic spray pyrolysis. Journal of Physical Chemistry B, 2005, 109(36): 17184~17191.

[67] Cesar I, Kay A, Martinez J A G, et al. Translucent thin film Fe_2O_3 photoanodes for efficient water splitting by sunlight: Nanostructure-directing effect of Si-doping. Journal of the American Chemical Society, 2006, 128(14): 4582~4583.

[68] Glasscock J A, Barnes P R F, Plumb I C, et al. Enhancement of photoelectrochemical hydrogen production from hematite thin films by the introduction of Ti and Si. Journal of Physical Chemistry C, 2007, 111(44): 16477~16488.

[69] Kleiman-Shwarsctein A, Hu Y S, Forman A J, et al. Electrodeposition of α-Fe_2O_3 doped with Mo or Cr as photoanodes for photocatalytic water splitting. Journal of Physical Chemistry C, 2008, 112(40): 15900~15907.

[70] Kay A, Cesar I, Grätzel M. New benchmark for water photooxidation by nanostructured α-Fe_2O_3 films. Journal of the American Chemical Society, 2006, 128(49): 15714~15721.

[71] Yan Y DOE. Hydrogen Program: FY 2009 Annual Progress Report, 2010, 208.

[72] Kay A, Cesar I, Grätzel M. New benchmark for water photooxidation by nanostructured α-Fe_2O_3 films. Journal of the American Chemical Society, 2006, 128(49): 15714~15721.

[73] Kennedy J H, Anderman M, Shinar R. Photoactivity of polycrystalline α-Fe_2O_3 electrodes doped with group IVA elements. Journal of the Electrochemical Society, 1981, 128(11): 2371~2373.

[74] Leygraf C, Hendewerk M, Somorjal G A. Heterogeneous catalysis on the molecular scale. Journal of Physical Chemistry B, 1982, 86(16): 3070~3078.

[75] Glasscock J A, Barnes P R F, Plumb I C, et al. Enhancement of photoelectrochemical hydrogen production from hematite thin films by the introduction of Ti and Si. Journal of Physical Chemistry C, 2007, 111(44): 16477~16488.

[76] Hu Y S, Kleiman-Shwarsctein A, Stucky G D, et al. Improved photoelectrochemical performance of Ti-doped α-Fe2O3 thin films by surface modification with fluoride. Chemical Communications, 2009,45(19): 2652~2654.

[77] Hu Y S, Kleiman-Shwarsctein A, Forman A J, et al. Pt-doped α-Fe_2O_3 thin films active for photoelectrochemical water splitting. Journal of Materials, 2008, 20(12): 3803~3805.

[78] Kumari S, Tripathi C, Singh A P, et al. Characterization of Zn-doped hematite thin films for photoelectrochemical splitting of water. Current Science, 2006, 91: 1062~1064.

[79] Sanchez C, Hendewerk M, Sieber K D, et al. Synthesis, bulk, and surface characterization of niobium-doped Fe_2O_3 single crystals. Journal of Solid State Chemistry, 1986, 61(1): 47~55.

[80] Sanchez C, Sieber K D, Somorjai G A. The photoelectrochemistry of niobium doped α-Fe_2O_3. Journal of Electroanalytical Chemistry, 1988, 252(2): 269~290.

[81] Aroutiounian V M, Arakelyan V M, Shahnazaryan G E, et al. Photoelectrochemistry of tin-doped iron oxide electrodes. Solar Energy, 2007: 81(11), 1369~1376.

[82] Hu Y S, Kleiman-Shwarsctein A, Forman A J, et al. Pt-doped α-Fe_2O_3

thin films active for photoelectrochemical water splitting. Chemistry of Materials , 2008, 20(12): 3803~3805.

[83] Kleiman-Shwarsctein A, Hu Y S, Forman A J, et al. Electrodeposition of α-Fe_2O_3 doped with Mo or Cr as photoanodes for photocatalytic water splitting. Journal of Physical Chemistry C, 2008, 112(40): 15900~15907.

[84] Zhang M L, Luo W J, Li Z S, et al. Improved photoelectrochemical responses of Si and Ti codoped α-Fe_2O_3 photoanode films. Applied Physics Letters, 2010,97(4): 042105.

[85] Khan S U M, Akikusa J. Photoelectrochemical splitting of water at Nanocrystalline n-Fe_2O_3 thin-film electrodes. Journal of Physical Chemistry B, 1999, 103(34): 7184~7189.

[86] Beermann N, Vayssieres L, Lindquist S E, et al. Photoelectrochemical studies of oriented nanorod thin films of hematite. Journal of the Electrochemical Society, 2000, 147(7): 2456~2461.

[87] Ingler W B, Baltrus J P, Khan S U M. Photoresponse of p-type zinc-doped Iron(III) oxide thin films. Journal of the American Chemical Society, 2004, 126(33): 10238~10239.

[88] Mao A, Han G Y, Park J H. Synthesis and photoelectrochemical cell properties of vertically grown α-Fe_2O_3 nanorod arrays on a gold nanorod substrate. Journal of Materials Chemistry, 2010, 20(11): 2247~2250.

[89] Sivula K, Zboril R, Formal F L, et al. Photoelectrochemical water splitting with mesoporous hematite prepared by a solution-based colloidal approach. Journal of the American Chemical Society, 2010, 132(21): 7436~7444.

[90] Tilley S D, Cornuz M, Sivula K, et al. Light-induced water splitting with hematite: Improved nanostructure and iridium oxide catalysis. Angewandte Chemie-International Edition, 2010, 49(36): 6405~6408.

[91] Le Formal F, Grätzel M, Sivula K. Controlling photoactivity in ultrathin hematite films for solar water-splitting. Advanced Functional Materials, 2010, 20(17): 1099~1107.

[92] Kanan M W, Nocera D G. In situ formation of an oxygen-evolving catalyst in neutral water containing phosphate and Co^{2+}. Science, 2008, 321(5892): 1072~1075.

[93] Zhong D K, Sun J, Inumaru H, et al. Solar water oxidation by composite catalyst/α-Fe_2O_3 photoanodes. Journal of the American Chemical Society, 2009, 131(17): 6086~6087.

[94] Zhong D K, Gamelin D R. Photoelectrochemical water oxidation by cobalt catalyst ("Co−Pi")/α-Fe_2O_3 composite photoanodes: Oxygen evolution and resolution of a kinetic bottleneck. Journal of the American Chemical

Society, 2010, 132(12): 4202~4207.

[95] Murphy A B, Barnes P R F, Randeniya L K, et al. Efficiency of solar water splitting using semiconductor electrodes. International Journal of Hydrogen Energy, 2006, 31(14): 1999~2017.

[96] Walsh A, Yan Y, Huda M N, et al. Band edge electronic structure of $BiVO_4$: Elucidating the role of the Bi s and V d Orbitals. Chemistry of Materials , 2009, 21(3): 547~553.

[97] Galembeck A, Alves O. $BiVO_4$ thin film preparation by metalorganic decomposition. Thin Solid Films, 2000, 365(1): 90~93.

[98] Sayama K, Nomura A, Zou Z, et al. Photoelectrochemical decomposition of water on nanocrystalline $BiVO_4$ film electrodes under visible light. Chemical Communications, 2003, 39(23): 2008~2009.

[99] Sayama K, Nomura A, Arai T, et al. Photoelectrochemical decomposition of water into H_2 and O_2 on porous $BiVO_4$ thin-film electrodes under visible light and significant effect of Ag ion treatment. Journal of Physical Chemistry B, 2006, 110(23): 11352~11360.

[100] Sayama K, Wang N, Miseki Y, et al. Effect of carbonate ions on the photooxidation of water over porous $BiVO_4$ film photoelectrode under visible light. Chemistry Letters, 2010, 39(1): 17~19.

[101] Luo H, Mueller A H, McCleskey T M, et al. Structural and photoelectrochemical properties of $BiVO_4$ thin films. Journal of Physical Chemistry C, 2008, 112(15): 6099~6102.

[102] Luo W J, Wang Z Q, Li Z S, et al. Synthesis, growth mechanism and photoelectrochemical properties of $BiVO_4$ microcrystal electrodes. Journal of Physics D:Applied Physics, 2010, 43(40): 405402.

[103] Iwase A, Kudo A. Photoelectrochemical water splitting using visible-light-responsive $BiVO_4$ fine particles prepared in an aqueous acetic acid solution. Journal of Materials Chemistry, 2010, 20(35): 7536~7542.

[104] Ng Y H, Iwase A, Kudo A, et al. Reducing graphene oxide on a visible-light $BiVO_4$ photocatalyst for an enhanced photoelectrochemical water splitting. Chemistry Physical Letters, 2010, 1(17): 2607~2612.

[105] Li M, Zhao L, Guo L. Preparation and photoelectrochemical study of $BiVO_4$ thin films deposited by ultrasonic spray pyrolysis. International Journal of Hydrogen Energy, 2010, 35(13): 7127~7133.

[106] Luo W J, Yang Z S, Li Z S, et al. Solar hydrogen generation from seawater with a modified $BiVO_4$ photoanode . Energy Environmental Science, 2011, 4(10): 4046~4051.

[107] Mavroides J G, Kafalas J A, Kolesar D F. Photoelectrolysis of water in cells

with $SrTiO_3$ anodes. Applied Physics Letters, 1976, 28(5): 241~243.

[108] Yin J, Ye J, Zou Z. Enhanced photoelectrolysis of water with photoanode Nb:$SrTiO_3$. Applied Physics Letters, 2004, 85(4): 689~691.

[109] Chen X Y, Yu T, Gao F, et al. Application of weak ferromagnetic $BiFeO_3$ films as the photoelectrode material under visible-light irradiation. Applied Physics Letters, 2007, 91(2): 022114.

[110] Ida S, Yama K, Matsunag T, et al. Preparation of p-type $CaFe_2O_4$ photocathodes for producing hydrogen from water. Journal of the American Chemical Society, 2010, 132(49): 17343~17345.

[111] Heller A, Vadimsky R G. Efficient solar to chemical conversion: 12% efficient photoassisted electrolysis in the [p-type InP(Ru)]/HCl-KCl/Pt(Rh) cell. Physical Review Letters, 1981, 46(17): 1153~1156.

[112] Quinlan K P. the mechanism of the photoelectrochemical etching of p-InP in nitric acid solutions. Journal of the Electrochemical Society, 1997, 144(10): 3469~3473.

[113] Khaselev O, Turner J A. Photoelectrolysis of HBr and HI using a monolithic combined photoelectrochemical/photovoltaic device. Electrochemical and Solid State Letters, 1999, 2(7): 310~312.

[114] Valderrama R C, Sebastian P J, Enriquez J P, et al. Photoelectrochemical characterization of CIGS thin films for hydrogen production. Solar Energy, 2005, 88(2): 145~155.

[115] Alanis A L, Garcia J R V, Rivera R, et al. Protective rhutenium thin films on $CuInSe_2$ for hydrogen evolution in acidic media. Int. J. Hydrogen Energy, 2002, 27(2): 143~147.

[116] Quinlan K P. A study of hydrogen evolution at irradiated p-InP electrodes in nitric acid solutions. Journal of the Electrochemical Society, 1999, 146(12): 4514~4516.

[117] Khaselev O, Turner J A. Electrochemical stability of p-$GaInP_2$ in aqueous electrolytes toward photoelectrochemical water splitting. Journal of the Electrochemical Society, 1998, 145(10): 3335~3339.

[118] Ishikawa A, Takata T, Kondo J N, et al. Oxysulfide $Sm_2Ti_2S_2O_5$ as a stable photocatalyst for water oxidation and reduction under visible light irradiation ($\lambda \leq 650$ nm). Journal of the American Chemical Society, 2002, 124(45): 13547~13553.

[119] Chun W J, Ishikawa A, Fujisawa H, et al. Conduction and valence band positions of Ta_2O_5, TaON, and Ta_3N_5 by UPS and electrochemical methods. Journal of Physical Chemistry B, 2003, 107(8): 1798~1803.

[120] Ishikawa A, Takata T, Kondo J N, et al. Oxysulfides $Ln_2Ti_2S_2O_5$ as stable

photocatalysts for water oxidation and reduction under visible-light irradiation. Journal of Physical Chemistry B, 2004, 108(8): 2637~2642.

[121] Ito S, Thampi K R, Comte P, et al. Highly active meso–microporous TaON photocatalyst driven by visible light. Chemical Communications, 2005, 41(2): 268~270.

[122] Abe R, Takata T, Sugihara H, et al. the use of $TiCl_4$ treatment to enhance the photocurrent in a TaON photoelectrode under visible light irradiation. Chemistry Letters, 2005, 34(8): 1162~1163.

[123] Banerjee S, Mohapatra S K, Misra M. Synthesis of TaON nanotube arrays by sonoelectrochemical anodization followed by nitridation: A novel catalyst for photoelectrochemical hydrogen generation from water. Chemical Communications, 2009, 45(46): 7137~7139.

[124] Abe R, Higashi M, Domen K. Facile fabrication of an efficient oxynitride TaON photoanode for overall water splitting into H_2 and O_2 under visible light irradiation. Journal of the American Chemical Society, 2010, 132(34): 11828~11829.

[125] Nakamura R, Tanaka T, Nakato Y. Oxygen photoevolution on a tantalum oxynitride photocatalyst under visible-light irradiation: How does water photooxidation proceed on a metal−oxynitride surface? Journal of Physical Chemistry B, 2005, 109(18): 8920~8927.

[126] Nishimura N, Raphael B, Maeda K, et al. Effect of $TiCl_4$ treatment on the photoelectrochemical properties of $LaTiO_2N$ electrodes for water splitting under visible light. Thin Solid Films, 2010, 518(20): 5855~5859.

[127] Wu J, Walukiewicz W, Yu K M, et al. Superior radiation resistance of In1−xGaxN alloys: Full-solar-spectrum photovoltaic material system. Journal of Applied Physics, 2003, 94: 6477~6482.

[128] Theuwis A, Strubbe K, Depestel L M, et al. A photoelectrochemical study of InxGa1–xN films. Journal of the Electrochemical Society, 2002, 149(5): E173~E178.

[129] Fujii K, Ohkawa K. Hydrogen gas generation by splitting aqueous water using n-Type GaN photoelectrode with anodic oxidation. Journal of Applied Physics, 2005, 44(16 ~ 19): L543~L545.

[130] Fujii K, Kusakabe K, Ohkawa K. Photoelectrochemical properties of InGaN for H_2 generation from aqueous water. Journal of Applied Physics, 2005, 44(10): 7433~7435.

[131] Huygens I M, Strubbe K, Gomes W P. Electrochemistry and Photoetching of n-GaN. Journal of the Electrochemical Society, 2000, 147(5): 1797~1802.

[132] Luo W, Liu B, Li Z, et al. Stable response to visible light of InGaN

photoelectrodes. Applied Physics Letters, 2008, 92(26): 262110.

[133] Tomkiewicz M, Woodall J M. Photoelectrolysis of water with semiconductor materials. Journal of the Electrochemical Society, 1977, 124(9): 1436~1440.

[134] Kohl P A, Frank S N, Bard A J. XI. Behavior of n-and p-Type single crystal semconductors covered with thin n-TiO_2 films. Journal of the Electrochemical Society, 1977, 124(2): 225~229.

[135] Liou F T, Yang C Y. Photoelectrolysis at Fe_2O_3/TiO_2 heterojunction electrode. Journal of the Electrochemical Society, 1982, 129: 342~345.

[136] Vinodgopal K, Bedja I, Kamat P V. Nanostructured semiconductor films for photocatalysis. Photoelectrochemical behavior of SnO_2/TiO_2 composite systems and its role in photocatalytic degradation of a textile azo dye. Chemistry of Materids,1996, 8: 2180~2187.

[137] Vinodgopal K, Kamat P V. Enhanced rates of photocatalytic degradation of an azo dye using SnO_2/TiO_2 coupled semiconductor thin films. Environmental Science and Technology, 1995, 29(3): 841~845.

[138] Liu D, Kamat P V. Photoelectrochemical behavior of thin cadmium selenide and coupled titania/cadmium selenide semiconductor films. Journal of Physical Chemistry B, 1993, 97(44): 10769~10773.

[139] Sheng J, Fukami T, Karasawa J. Anomalous current rise and electrochemical reduction in Fe_2O_3-TiO_2 ceramics. Journal of the Electrochemical Society, 1998, 145(5): 1592~1598.

[140] K S Chandra Babu, D Singh and O N Srivastava. Investigations on the mixed oxide material TiO_2-In_2O_3 in regard to photoelectrolytic hydrogen production. Semiconductor Science and Technology, 1990, 5(4): 364~368.

[141] Shiyanovskaya I, Hepel M. Bicomponent WO_3/TiO_2 films as photoelectrodes. Journal of the Electrochemical Society, 1999, 146(1): 243~249.

[142] Wang Y, Yu T, Chen X, et al. Enhancement of photoelectric conversion properties of SrTiO3/α-Fe2O3 heterojunction photoanode. Journal of Physics D:Applied Physics, 2007, 40(13): 3925~3930.

[143] Luo W, Yu T, Wang Y, et al. Enhanced photocurrent–voltage characteristics of WO_3/Fe_2O_3 nano-electrodes. Journal of Physics D:Applied Physics, 2007, 40(4): 1091~1096.

[144] Lin Y, Zhou S, Liu X, et al. TiO_2/$TiSi_2$ heterostructures for high-efficiency photoelectrochemical H_2O splitting. Journal of the American Chemical Society, 2009, 131(8): 2772~2773.

[145] Liu R, Lin Y J, Chou L Y, et al. Water splitting by tungsten oxide prepared by atomic layer deposition and decorated with an oxygen-evolving catalyst. Angewandte Chemie-International Edition, 2011, 50(2): 499~502.

[146] Lin Y, Zhou S, Sheehan S W, et al. Nanonet-based hematite heteronanostructures for efficient solar water splitting. Journal of the American Chemical Society, 2011, 133(8): 2398~2401.

[147] Zhou S, Liu X H, Lin Y J, et al. Spontaneous growth of highly conductive two-dimensional single-crystalline $TiSi_2$ nanonets. Angewandte Chemie-International Edition, 2008, 47(40): 7681~7684.

[148] Zhou S, Liu X, Lin Y, et al. Rational synthesis and structural characterizations of complex $TiSi_2$ nanostructures. Journal of Materials, 2009, 21(6): 1023~1027.

[149] Wang H, Deutsch T, Turner J A. Direct water splitting under visible light with nanostructured hematite and WO_3 photoanodes and a $GaInP_2$ photocathode. Journal of the Electrochemical Society, 2008, 155(5): F91~F96.

[150] Gao X F, Sun W T, Hu Z D, et al. An efficient method to form heterojunction CdS/TiO_2 photoelectrodes using highly ordered TiO_2 nanotube array films. Journal of Physical Chemistry C, 2009, 113(47): 20481~20485.

[151] Gaillard N, Cole B, Kaneshiro J, et al. Improved current collection in WO_3:Mo/WO_3 bilayer photoelectrodes. J. Mater. Res., 2010, 25(1): 45~51.

[152] Woodhouse M, Herman G S, Parkinson B A. Combinatorial Approach to Identification of Catalysts for the Photoelectrolysis of Water. Chemistry of Materials, 2005, 17 (17):4318~4324.

[153] Zhao Z, Luo W, Li Z, et al. Density functional theory study of doping effects in monoclinic clinobisvanite $BiVO_4$. Physics Letters A, 2010, 374(48): 4919~4927.

[154] Joannopoulos J D, Villeneuve P R, Fan S H. Photonic crystals: putting a new twist on light. Nature, 1997, 386(6621): 143~149.

[155] Arpin K A, Mihi A, Johnson H T, et al. Multidimensional architectures for functional optical devices. Advanced Materials, 2010, 22(10): 1084~1101.

[156] Sakoda K. Enhanced light amplification due to group-velocity anomaly peculiar to two- and three-dimensional photonic crystals. Optics Express, 1999, 4(5): 167~176.

[157] Baba T. Slow light in photonic crystals. Nature Photon, 2008, 2(8): 465~473.

Chapter 8
The Application of Metal-Organic Frameworks to CO_2 Capture

Jianfeng Yao, Dan Li and Huanting Wang

Department of Chemical Engineering, Monash University, Clayton, Victoria 3800, Australia

Abstract

Metal-organic frameworks (MOFs), composed of organic bridging ligands coordinated to metal-based nodes, are new materials that have similar topological structure with zeolites. MOFs have large surface areas, adjustable pore sizes and controllable surface properties. Such unique properties make them very promising materials for gas selectivity and separation. This paper is mainly focused the progress on CO_2 capture using MOFs in the last five years from the ranges of thin-layer membrane to powder adsorbents.

8.1 Introduction

Metal-organic frameworks (MOFs) are new microporous materials composed of organic bridging ligands or "struts" coordinated to metal-based nodes to form a three-dimensional networks with uniform pore diameters typically in the range of 3~20 Å[1~4]. The nodes generally consist of one or more metal ions (e.g., Zn^{2+}, Cu^{2+}, Cr^{3+}, or Fe^{3+}) to which the organic bridging ligands coordinate through a specific functional group. MOFs, also called porous coordination polymers (PCPs)[5], and porous coordination networks (PCNs)[6], have similar topological structure with zeolite, and their pore size and surface properties could be tuned to a great extent by choosing different metal centres and organic ligands.[7] MOFs are ideal adsorbents for gas storage and separation due to their large surface areas, adjustable pore sizes and controllable surface properties[8].

CO_2 is a very small gas molecule with a smaller kinetic diameter of 3.3 Å, which was smaller than lighter gases, such as O_2 (3.46 Å), N_2 (3.64 Å), and CH_4 (3.8

Å). In fact, among permanent gases, only He (2.59 Å) and H_2 (2.89 Å) are smaller than CO_2. On the other hand, CO_2 also has a relatively high molecular weight and a large quadruple moment, enabling it to naturally adsorb more strongly to or dissolve at much higher concentrations in these membrane materials compared to many other gas species[9]. The separation of carbon dioxide from methane is an important process in natural gas upgrading because CO_2 reduces the energy content of natural gas and induces pipeline corrosion. Adsorption and separation of CO_2 using MOFs have received much attention during the last decade. Several reviews dedicated on CO_2 capture using MOFs have been published[3,8,10~12]. such as selective gas adsorption and separation in metal-organic frameworks in Chem. Soc. Rev.[8], carbon dioxide capture: prospects for new materials in Angew. Chem. Int. Ed.[3], and can metal–organic framework materials play a useful role in large-scale carbon dioxide separations in ChemSusChem[10]. In this review, we mainly focused the progress on CO_2 capture using MOFs in the last five years (2006~2010).

8.2 MOF membrane for CO_2 separation

Membranes have been widely studied for zeolites, where thin-film of zeolite crystals are typically fabricated on a porous support[13]. As MOFs are new materials and only extensively studied in the last several years, there is limited study focused on the preparation of MOF membranes[7,14~22].

Liu et al[18]. prepared ZIF-69 membranes on α-alumina substrate for the first time and conducted single-gas permeation experiments by a vacuum method at room temperature using H_2, CH_4, CO, CO_2 and SF_6, respectively. The permeances were in the order of H_2 >CO_2 >CH_4 >CO>SF_6. The separation of CO_2/CO gas mixture was investigated by gas chromatograph and the permselectivity of CO_2/CO was 3.5±0.1 with CO_2 permeance of $3.6\pm0.3\times10^{-8}$ $mol/m^2 \cdot s \cdot Pa$ at room temperature. Li and co-workers prepared ZIF-7 membranes on alumina by the microwave-assisted seeded growth method[19,20].The permeances of H_2, CO_2, N_2, and CH_4 were 7.40, 1.10, 1.10, and 1.18×10^{-5} $mol/m^2 \cdot s \cdot Pa$ at 200 ℃. They also prepared crack-free and dense ZIF-8 membranes (Figure 8.1) on porous titania support by a microwave-assisted method. The membrane exhibited a CO_2 permeance of 1.33×10^{-5} $mol/m^2 \cdot s \cdot Pa$ at 25 ºC. [21] Reproducible thin ZIF-8 membranes with an about 5~9 μm thickness were synthesized by secondary seeded growth on tubular α-Al_2O_3 porous supports. The membranes displayed unprecedented CO_2 permeances as high as 2.4×10^{-5} $mol/m^2 \cdot s \cdot Pa$ with CO_2/CH_4 separation selectivities of about 4[22].

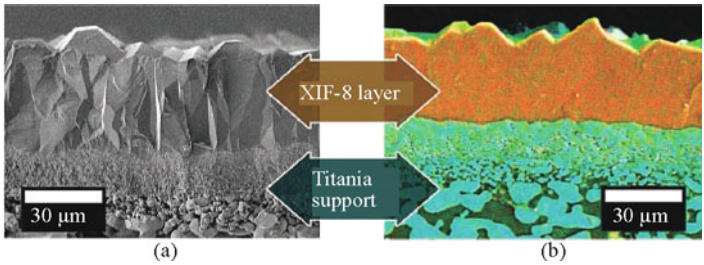

Figure 8.1 (a) SEM image of the cross section of a simply broken ZIF-8 membrane. (b) EDXS mapping of the sawn and polished ZIF-8 membrane (color code: orange, Zn; cyan, Ti)[21]

8.3 Selectivity adsorption

8.3.1 Carbon dioxide adsorption in rigid metal-organic frameworks

Millward and Yaghi[23] reported that MOF-177 with a BET surface area of 4508 m^2/g was the most effective structure for CO_2 capture amongst a series of nine isoreticular MOFs (IRMOF-1, IRMOF-3, IRMOF-6, IRMOF-11, MOF-2, MOF-74, MOF-177, MOF-505, and Cu_3-$(BTC)_2$). The CO_2 adosrption capacity of MOF-177 was 33.5 mmol CO_2/g at 42 bar. Figure 8.2 shows the CO_2 adsorption isotherms, and MOF-177 exhibits the highest CO_2 sorption capacity, and MOF-2 is the lowest[23].This is a significant improvement over commercially available zeolites sorbents (7.4 mmol/g for zeolite 13X at 32 bar)[24].

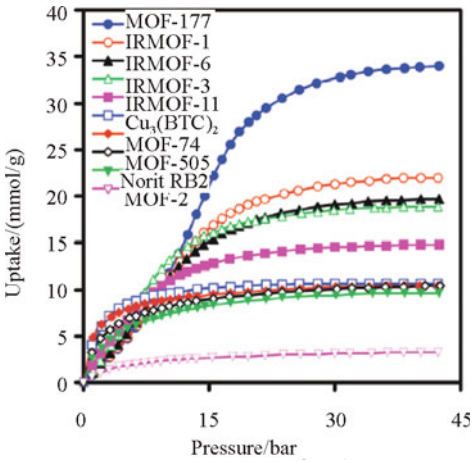

Figure 8.2 Comparison of gravimetric CO_2 capacities for several MOFs (and an activated carbon Norit RB_2 as a reference) determined at ambient temperature and pressures up to 42 bar[23]

$Cu_3(BTC)_2$ (Cu-BTC or HKUST-1) is an interesting candidate for the

separation of CO_2 by adsorption[25~27]. Hamon et al. found that Cu-BTC had a CO_2/CH_4 selectivity of 8 and a high delta loading (difference between adsorption capacity under conditions of adsorption and desorption) and therefore appeared to be a good compromise between zeolites, with high selectivity for CO_2, but low delta loadings, and activated carbons, with high delta loadings, but low selectivity, for pressure swing adsorption applications[25]. The CO_2 adsorption capacity for Cu-BTC (12.7 mol/kg) is much higher than for zeolite 13X (6.9 mol/kg) at 25 °C and 15 bar[26]. The potential application of Cu-BTC in a pressure swing adsorption (PSA) system to selectively capture CO_2 was evaluated by measuring a series of sorption isotherms, for CO_2, CH_4, and N_2 using an intelligent gravimetric analyser between 0 and 15 bar and at temperatures ranging from 25 to 105 °C. The results show that the working capacity of Cu-BTC (8.1 mol/kg) in a PSA system, at 25 °C, is almost four times that of the benchmark material zeolite 13X (2.2 mol/kg) [26]. Yazaydin et al[28]. reported an interesting discovery that the CO_2 uptake and its selectivity over N_2 and CH_4 on Cu-BTC were significantly increased by the presence of water molecules coordinated to open-metal sites in the framework. This was first predicted by molecular simulations and later validated by experiments[28].

Wu et al.[29] reported a detailed study of CO_2 adsorption in two important metal-organic framework (MOF) compounds (Mg-MOF-74 and HKUST-1). In both MOFs, the open metal ions were identified as the primary binding sites through neutron diffraction measurements. The relatively strong metal-CO_2 binding was attributed to an enhanced electrostatic interaction, and vibrational mode analysis shows that the adsorbed CO_2 molecule is strongly attached through one of its oxygen atoms while the rest of the molecule is relatively free. This high orientational disorder is the reason for the large apparent O-C-O bond bending angle derived from diffraction measurements. Mg-MOF-74, with open magnesium sites, represents a breakthrough for high-capacity storage of CO_2 with moderate regeneration conditions (Figure 8.3)[30]. It has a dynamic capacity of 8.9 wt.% CO_2, takes up more CO_2 than NaX, which has a dynamic capacity of 8.5 wt. %. Moreover, after regneration, NaX regains 71% of its capacity (6.4 wt.%), whereas Mg-MOF-74 regains 87% of its capacity (7.8 wt.%).30 The Co-MOF-5 materials prepared by Botas et al[31]. exhibited higher adsorption capacities for H_2, CO_2, and CH_4 at high pressure than their Co-free homologue. However, the amount of Zn that could be substituted seemed to be limited, being no more than 25% of total metal content. The selectivity of CO_2 from CH_4/CO_2 mixtures in Li-modified MOFs is greatly improved, due to the enhancement of electrostatic potential in the materials by the presence of the metals[32].

CO_2 adsorption equilibrium and diffusion on homemade metal-organic framework (MOF-5) crystals with sizes of about 40~60 μm were studied by the gravimetric method in the pressure range up to 1 atm [33]. MOF-5 has CO_2 adsorption capacity of 2.1 mmol/g (or 9.24%) at 295.7 K and 1 atm. CO_2 diffusion in MOF-5 crystals is an activated process with diffusivity in the range of 8.1~11.5 $\times 10^{-9}$ cm^2/s in 295~331 K and activation energy for diffusion of 7.6 kJ/mol. Saha et al.[34] compared CO_2 adsorption capacities on three adsorbents, MOF-5, MOF-177 and zeolite 5A. The adsorption of CO_2 on MOF-5, MOF-177 and Zeolite 5A at 298 K and 14 bar were 47.98, 39.69, and 22.27 wt%. The average diffusivity of CO_2 in MOF-5 and MOF-177 was in the order of 10^{-9} m^2/s, as compared to 10^{-11} m^2/s in zeolite 5A. MOF-5 prepared by microwave-assisted method exhibited up to 3.8 wt% CO_2 uptake at atmospheric pressure and up to 300 °C[35].

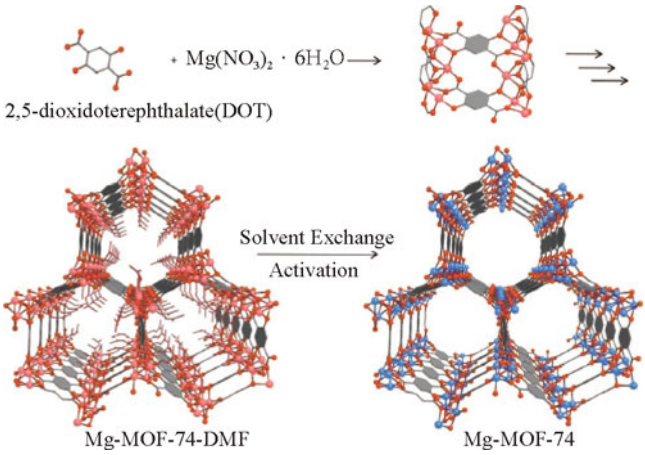

Figure 8.3 Single crystal structure of Mg-MOF-74, formed by reaction of the DOT linker with $Mg(NO_3)_2 \cdot 6H_2O$. The structure consists of 1D inorganic rods linked by DOT to form linear hexagonal channels[30]

Ferey et al.[36] designed and created a crystal structure for porous chromium terephthalate, MIL-101, (MIL=Material Institut Lavoisier) with very large pore sizes (~30~34 Å) and surface area (Langmuir surface area of ~5900 m^2/g). MIL-101 is stable over months under air atmosphere and was not altered when treated with various organic solvents at room temperature or under solvothermal conditions. These properties, together with high adsorption capacities, make MIL-101 an attractive candidate for the adsorption of gas or large molecules. Within the experimental pressure up to 10 bar, MIL-101 has better capacity for CO_2 and CH_4 as compared to Al-based MOF and MIL-53. The dual site Langmuir model proves to be particularly useful to model pure gas adsorption on this class of materials that

have two distinct adsorption sites[37]. MIL-101 chromium carboxylates adsorbed very large amounts of CH_4 and CO_2 at relatively high pressures (<5 MPa) at 300 K. MIL-101 activated by ethanol and NH_4F exhibits the highest loading of CO_2 reported so far with a capacity of 40 mmol/g at 5 MPa[38]. Till now, a variety of MOFs with very high surface areas, large pore diameters, and giant pore volumes have been synthesized including MOF-177, MIL-100 and MIL-101, and UMCM-1 (4100 m^2/g)[39]. The carbon dioxide capacities for various high performance MOFs and other adsorbents are summarized in Table 8.1[38].

CO_2 capture from flues gaes generated by coal-fired power plants has drawn considerable attention by using MOFs[40,41]. However, because the CO_2 partial pressures in flue gases are usually under 1 bar, it is of greater importance to understand CO_2 adsorption in MOF materials in the low pressure region than at high pressures for their applications as novel adsorbents to remove CO_2 from flue gases[42]. Liu et al.[43] applied HKUST-1 and Ni/DOBDC (CPO-27-Ni or Ni/MOF-74) pellets for flue gas application (25 ^oC, 0.1 atm CO_2 partial pressure), and high CO_2 capacities of 0.55 and 3.28 mol/kg were observed, respectively. Ni/DOBDC has a higher CO_2 capacity than benchmark zeolites. A small amount of H_2O in flue gases does not decrease and may actually increase the CO_2 capacity of HKUST-1, which was consisted with that reported by Yazaydin and coworkers[28]. Compared to 5A and NaX zeolites, HKUST-1 and Ni/DOBDC do not affect much by H_2O on CO_2 adsorption. Furthermore, H_2O would be more easily removed from the MOFs by regeneration. Ni/DOBDC retains substantial CO_2 capacity with moderate H_2O loadings, and it may have a promising future for capturing CO_2 from flue gases.[43] Two water tolerant three-dimensional pillared-layer metal organic frameworks (MOFs) $M_2(BDC)_2(Dabco)$ (M = Zn, Ni, BDC=1,4-benzenedicarboxylate, Dabco=1,4-diazabicyclo[2.2.2]octane) were synthesized to selectively adsorb and separate CO_2[44]. The isotherms indicate that CO_2 adsorption capacities are 13.7 and 12.5 mol/kg for $Zn_2(BDC)_2(Dabco)$ and $Ni_2(BDC)_2(Dabco)$ at 25 oC and 15 bar, respectively. These values are higher than those for most MOFs, though lower than those for the best MOFs for CO_2 adsorption such as MOF-17723 and MIL-101[36]. Both materials have higher CO_2/N_2 selectivity than CO_2/CH_4 selectivity and low heats of adsorption[44]. The selectivity of CO_2 over CH_4 in a highly hydrophobic metal-organic framework $Zn(BDC)(TED)_{0.5}$ (BDC: benzenedicarboxylate, TED: triethylenediamine) increased with increasing pressure as CO_2 is proximal to the metal oxides and TED linkers[45]. H_2O has a negligible effect on the separation of CO_2/CH_4 in $Zn(BDC)(TED)_{0.5}$ and a

prewater treatment is perhaps not required.

Table 8.1 Carbon dioxide adsorption capacities for various high performance adsorbents

Materials	CO_2 uptake (mmol/g)	conditions	Refevence
MOF-177	33.5	298 K/42 bar	[23]
IRMOF-1	21.7	298 K/42 bar	[23]
Cu-BTC	12.7	298 K/15 bar	[26]
MIL-101(Cr)	18.0	304 K/5.0 MPa	[38]
MIL-101c (Cr)[a]	40.0	304 K/5.0 MPa	[38]
$Zn_2(BDC)_2(Dabco)$[b]	13.7	298 K/15 bar	[44]
$Ni_2(BDC)_2(Dabco)$[b]	12.5	298 K/15 bar	[44]
SNU-6	25.8	195 K/1 atm	[46]
PCN-17	10.7	195 K/800 Torr	[47]
MIL-53(Cr)	8.5	304 K/11 bar	[48]
Hydrated MIL-53(Cr)	7.7	304 K/11 bar	[48]
13X	7.4	298 K/32 bar	[24]
Activated carbon Norit R1	11.0	298 K/4.0 MPa	[49]

a) Sample MIL-101 activated by EtOH + NH_4F treatments

b) BDC=1,4-benzenedicarboxylate, Dabco=1,4-diazabicyclo[2.2.2]octane

Yazaydin et al.[50] compared 14 MOFs for CO_2 capture from flue gas. MOFs possessing a high density of open metal sites are found to adsorb significant amounts of CO_2 even at low pressure. Figure 8.4 presents the experimental CO_2 uptake at 0.1 bar (the anticipated partial pressure of CO_2 in flue gas) and room temperature for the 14 MOFs. It confirms that MOFs with a large capacity for CO_2 at high pressures often do not perform well at low pressures. IRMOF-1 and MOF-177 are among the lowest performing materials here. Changing the metal from Zn in M/DOBDC to Mg, Co, or Ni provides big changes in CO_2 uptake. Sumida et al.[51] reported the synthesis and characterization of the iron-based sodalite-type metal–organic framework $Fe_3[(Fe_4Cl)_3(BTT)_8(MeOH)_4]_2$ (Fe-BTT). The exposed Fe^{2+} cation sites within Fe-BTT also lead to the selective adsorption of CO_2 over N_2, with isotherms collected at 298 K indicating uptake ratios of 30.7 and 10.8 by

weight at 0.1 and 1.0 bar, respectively.

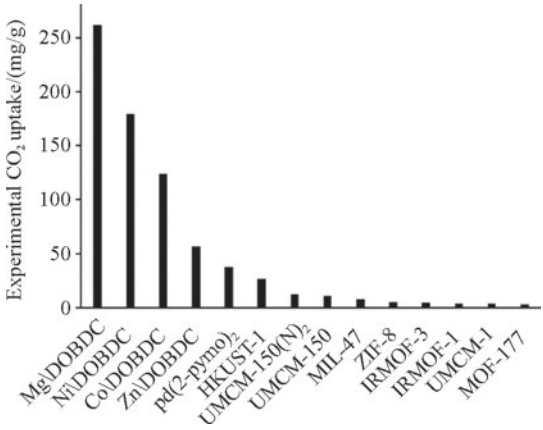

Figure 8.4 Experimental CO_2 uptake in screened MOFs at 0.1 bar. Data obtained at 293~298 K[50]

Demessence et al.[52] prepared triazolate-bridged frameworks $H_3[(Cu_4Cl)_3(BTTri)_8]$ (H_3BTTri = 1,3,5-tris (1H-1,2,3-triazol-5-yl) benzene) and ethylenediamine functionalized MOF. At low pressures (up to 0.06 bar), alkylamine functionalized MOF takes up a greater amount of CO_2: 0.366 mmol/g (1.6 wt %) versus 0.277 mmol/g (0.92 wt %) in the plain MOF. At pressures above 0.1 bar, however, the CO_2 uptake for alkylamine functionalized MOF is less than that for the plain MOF. This behaviour can be explained by the greater attraction of CO_2 to the more basic amine sites at low pressures, followed by a filling of the available pore volume at higher pressures.

The framework structure of desolvated solid, $[Cu_2(BPnDC)_2(bpy)]_n$ (SNU-6, SNU=Seoul National University) exhibits high permanent porosity (1.05 cm^3/g) with high Langmuir surface area (2910 m^2/g). It shows high CO_2 gas storage capacity of 113.8 wt% at 195 K and 1 atm.46 $[Zn_2(BPnDC)_2(bpy)]$ (BPnDC=benzophenone 4,4'-dicarboxylic acid, bpy=4,4'-bipyridine) (SNU-9) has Langmuir surface area of 1030 m^2/g , pore volume of 0.366 cm^3 /g, and high gas uptake capacities for O_2, CO_2, and H_2 gases. For CO_2 adsorption isotherm at 195 K and 1 atm, a two-step curve was observed. In the initial step, SNU-9 adsorbs 11.8 wt% CO_2 (2.69 mmol /g, 60.1 cm^3/g at STP), and in the second step it stores up to 43.0 wt% CO_2 (9.78 mmol/g, 219 cm^3/g at STP)[53]. The CO_2 gas uptake at 273 K and 1 atm reported is 38.5 wt% (8.75 mmol/g) for SNU-5[54]. CO_2 sorption capacities at 298 K were 9.3 wt% at 1 atm and 15 wt% at 10 bar for $[(Ni_2L_2)(bptc)]$ (SNU-M10, bptc: 1,1'-biphenyl-3,3',5,5'-tetracarboxylate), and 21 wt% at 30 bar for $[(Ni_2L_4)(bptc)]$ (SNU-M11). $[CoII_4\ (\mu\text{-}OH_2)_4(MTB)_2]n$ (SNU-15') exhibits selective gas sorption properties for H_2 and O_2 gases over N_2 at 77 K, as well as for CO_2 over CH_4 at 195 and 273 K. SNU-15' adsorbs CO_2 gas up to 15.3 wt%

(3.48 mmol/g) at 195 K and 1 atm, and 7.02 wt% (1.59 mmol/g) at 273 K and 1 atm[55]. Mg-based MOFs can provide a reduced framework density as the molar mass of Mg is much smaller than those of transition metals, such as Zn^{2+} and Cu^{2+}. Mg(TCPBDA) (SNU-25, $TCPBDA^{2-}$: N,N,N',N'-tetrakis (4-carboxyphenyl)-biphenyl- 4,4'-diamine) adsorbs CO_2 gas up to 26.3 wt% (134.05 cm^3/g at STP, 5.99 mmol/g) at 195 K and 1 atm, 9.1 wt% (46.38 cm^3/g at STP, 2.07 mmol/g) at 273 K and 1 atm, and 6.5 wt% (33.43 cm^3/g at STP, 1.49 mmol/g) at 298 K and 1 atm[56].

Ma et al.[47] prepared a ytterbium MOF with coordinatively linked, doubly interpenetrated, (8,3)-connected nets (PCN-17). PCN-17 can adsorb a large amount of CO_2 (240 cm^3/g) at 195 K and 800 Torr. Li et al.[57] reported a novel guest-free MOF material, [Zn (dtp)] constructed from a new developed di-topic tetrazolate ligand, 2,3-di-1H-tetrazol-5-ylpyrazine (H_2dtp). This MOF could adosorb a significant amount of O_2 (77 K) and CO_2 (195 K). The uptake amounts at 1.0 atm are 79.3 and 98.8 cm^3/g for O_2 and CO_2, respectively. Similarly, the metal–organic frameworks M_2(dhtp) (CPO-27-M, M=Ni, Mg) can be activated to give the empty framework compounds M_2(dhtp) with a honeycomb analogous structure containing large micropores of 1.1~1.2 nm diameter and a high concentration of open metal sites. The maximum excess adsorption of CO_2 observed at 298 K was 51 wt.% for Ni_2(dhtp) and 63 wt.% for Mg_2(dhtp). A surprisingly large amount of CO_2, in the range 25~30 wt.%, was still adsorbed at 473 K[58].

The microporous metal-organic framework Ni_2(dhtp) (H_4dhtp= 2,5-dihydroxyterephthalic acid) shows distinct end-on CO_2 coordination to coordinatively unsaturated nickel sites giving rise to high CO_2 adsorption capacity at sub-atmospheric pressures and ambient temperatures[59]. Very recently, a new two-dimensional (2D) metal-organic framework, Cu-TP-1, has been synthesized under solvothermal conditions (DMF) from the transition metal cation Cu(II) and 2-tetrazole pyrimidine ($C_5H_5N_6$, H-TP). Cu-TP-1 show interesting H_2 and CO_2 uptake. CO_2 uptake of Cu-TP-1 (at 298 K, 1 atm pressure) is seen to be comparable to the recently reported ZIF-95 which outperforms ZIF-100 and BPL carbon[60]. $CO_2(ad)_2(CO_2CH_3)_2 \cdot 2DMF \cdot 0.5H_2O$ (bio-MOF-11) was prepared via a solvothermal reaction between cobalt acetate tetrahydrate and adenine in N,N-dimethylformamide (DMF). The calculated CO_2/N_2 selectivity is 81:1 at 273 K with a CO_2 adsorption of 6 mmol/g and 75:1 with a CO_2 adsorption of 4.1 mmol/g at 298 K[61]. Co(II) carborane-based porous coordination polymers containing pyridines showed very large CO_2/CH_4 and CO_2/N_2 selectivities of about 47 and 95, respectively[62]. A robust, porous, catenated coordination polymer based on a neutral, flexible imidazole-derived tripodal ligand (a 'tripodal imidazole framework', TIF) could reversibly absorb H_2 and CO_2. CO_2 is adsorbed at 22 ^oC up

to 3.5 mmol/g at 20 bar, with little hysteresis observed upon desorption[63].

Post-synthesis modification of a MOF by replacing coordinated solvent molecules with highly polar ligands (Figure 8.5). The final product exhibited high CO_2/N_2 selectivity of about 42 at low pressure (about 0.4 bar)[64]. Grafting of amines onto surfaces of silica-based sorbents and zeolites has been developed to enhance adsorption of acidic CO_2[65,66]. To date, several types of MOFs containing amino groups have been prepared to capture CO_2. Arstad et al.[67] reported CO_2 adsorption on three new types of amine-functionalized MOFs. At 298 K the materials adsorb significant amount of carbon dioxide. The highest adsorption was around 14 wt% CO_2 at 1.0 atm CO_2 pressure. At 25 atm CO_2 pressure, up to 60 wt% CO_2 can be adsorbed.

In order to increase CO_2 capacity, most research is focused on either increasing the MOF pore volume and surface area, or modifying the pore chemistry by incorporating functional moieties having high affinities for CO_2. Little experimental effort has focused on determining the optimal pore size for effectively condensing and adsorbing CO_2[68]. Tetramethylammonium (TMA), tetraethylammonium (TEA), and tetrabutylammonium (TBA) were introduced into the pores of MOF via cation exchange to optimize its CO_2 adsorption properties. The pore volumes and BET surface areas were systematically decreased, and CO_2 adsorption capacities increased from 3.41 mmol/g for bio-MOF to 4.46 mmol/g for TMA@bio-MOF-1, 4.16 mmol/g for TEA@bio-MOF-1 and 3.44 mmol/g TBA@bio-MOF-1at 273 K and 1 bar[68]. Arstad et al.[67] prepared a selection of MOF adsorbents (USO-1-Al, USO-2-Ni and USO-3-In and their amine functionalised analogues) that maintain open porosity upon desolvation and the open structures have been tested as low temperature adsorbents for CO_2. The best adsorbents reach carbon dioxide capacity levels of 14 wt% (3.18 mmol/g) at atmospheric pressures of CO_2 and as high as 60 wt% (13.6 mmol/g) at 25 atm at CO_2 pressure and 298 K.

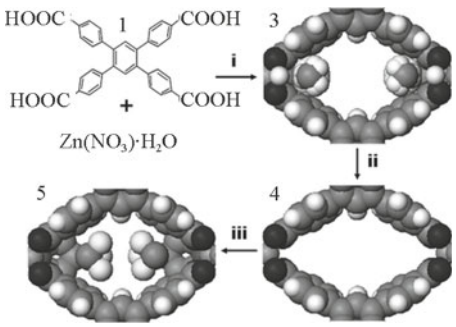

Figure 8.5 Post-synthesis modification of a MOF. Preparation methods of 3, 4, and 5. i) DMF/80 °C/24 h, followed by evacuation while heating at 100 °C. ii) evacuation while heating at 150 °C. iii) soak in a solution of $CHCl_3$/4-(trifluoromethyl)pyridine, followed by evacuation while heating at 100 °C[64]

Noro et al. designed and synthesized the one-dimensional CuII coordination polymer $[Cu(PF_6)_2(bpetha)_2]_n$, which shows the property of highly selective adsorption for CO_2 and C_2H_2 gases. The axial ligand-exchanged frameworks, $[Cu(PF_6)_{1.4}(BF_4)_{0.6}(bpetha)_2]_n$ and $([Cu(bpetha)_2(DMF)_2]\cdot 2PF_6)_n$ showed properties of controling the onset pressure and maximum adsorption amount for targeted CO_2 gases[69]. A metal organic framework with amine-lined pores exhibited a notable CO_2 adsorption at lower pressures. The uptake was 4.35 mmol/g (97.5 cm^3 (STP)/g) at partial pressures as low as 1.2 bar (P/P0=0.034) at 273 K. Adsorption and desorption cycles were repeated eight times with complete reversibility. Surprisingly, this MOF did not show any appreciable uptake of N_2, Ar or H_2 under comparable conditions[70].

$[Cu(Hoxonic)(bpy)_{0.5}]_n$ have been studied in detail, revealing an unusual behaviour[71]. Guest uptake is facilitated by increasing the thermal energy of both the guest and the framework. Thus, neither N_2 at 77 K nor CO_2 at 195 K is incorporated, and CH_4 is only minimally adsorbed at 273 K and high pressures (0.5 mmol/g at 2500 kPa). By contrast, CO_2 is readily incorporated at 273 K (up to 2.5 mmol/g at 2500 kPa). Separation of CO_2/CH_4 mixtures was studied in carborane-based MOF $[Zn_3(OH)(p\text{-}CDC)_{2.5}(DEF)_4]_n$ [p-CDC^2_: deprotonated form of 1,12-dihydroxydicarbonyl- 1,12-dicarba-closo-dodecaborane; DEF: diethylformamide], and high selectivities for CO_2 over CH_4 (~17) are obtained[72]. The adsorption of CO_2 and CH_4 in a mixed-ligand metal-organic framework (MOF) $Zn_2(NDC)_2(DPNI)$ (NDC: 2,6-naphthalenedicarboxylate, DPNI: N,N′-di-(4-pyridyl)-1,4,5,8-naphthalene tetracarboxydiimide) was investigated using volumetric adsorption measurements and grand canonical Monte Carlo (GCMC) simulations. The MOF was synthesized by two routes: conventional oven heating and microwave heating. The microwave sample shows a selectivity of 30 for CO_2 over CH_4, which is among the highest selectivities reported for this separation[73]. Mu et al.[74] prepared $[Cu_2(HBTB)_2(H_2O)(EtOH)]$ •H_2O•EtOH from the reaction of H_3BTB (H3BTB: 1,3,5-tris(4-carboxyphenyl) benzene) with $Cu(NO_3)_2$•$3H_2O$ in a mixture of ethanol and water. Upon activation, the copper atoms become coordinatively unsaturated. For CO_2 and CH_4 adsorption in the MOF, CO_2 is more strongly adsorbed than CH_4, which is expected because CO_2 has a significant quadrupole moment, whereas CH_4 is essentially nonpolar. A microporous MOF Zn(BDC)(4,4'-Bipy)0.5 (MOF-508b, BDC=1,4-benzenedicarboxylate, 4,4'-Bipy= 4,4'-bipyridine) was examined for the separation and removal of CO_2 from its binary CO_2/N_2 and CO_2/CH_4 and ternary $CO_2/CH_4/N_2$ mixtures by fixed-bed adsorption. MOF-508b exhibits highly selective adsorption to CO_2 with the adsorption capacity of 26.0 wt % at 303 K and 4.5 bar[75].

Zeolitic imidazolate frameworks (ZIFs) are a new class of metal–organic frameworks (MOFs), which have ordered porous structures with hybrid frameworks consisting of inorganic metal ions or metal clusters coordinated with organic imidazole/imidazolate ligands[76,77]. Because of the strong bonding between the imidazolate linker and the metal center, many ZIFs have high thermal (>673 K) and moisture stability compared with many other MOF structures[78].The chemical and thermal stability of ZIFs permit many applications, such as the capture of CO_2 and its selective separation from industrially relevant gas mixtures. Currently, ZIFs are the best porous materials for the selective capture of CO_2 and show exceptionally high capacity for CO_2 among adsorbents operating by physisorption.[11] Yaghi and coworkers[79] measured CO_2 uptake by the ZIFs and compared with that by BPL carbon, which is currently widely used in industry for gas separations. The CO_2 uptake values at 1 bar varied widely (Figure 8.6), in the sequence -NO_2 (ZIF-78) >-CN, -Br, -Cl (ZIF-82, -81, -69) > -C_6H_6, -Me (ZIF-68, -79) > -H (ZIF-70) > BPL carbon. This order is in agreement with the greater attraction expected between the polar functional groups in the ZIFs and CO_2, which has a significant quadrupole moment. ZIF-78 takes up 3 times as much CO_2 as BPL carbon and outperforms the other ZIFs as well. Thus, the adsorption capacity of CO_2 as well as the CO_2/CH_4 and CO_2/N_2 selectivity are tunable from respectably high values down to values close to those for an activated carbon material[79].

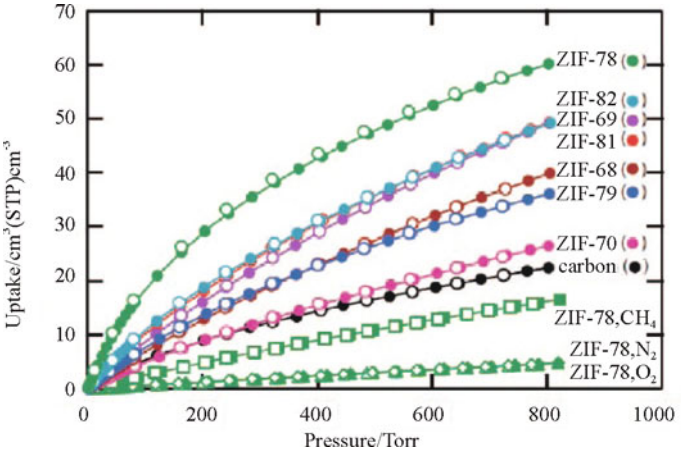

Figure 8.6 CO_2 isotherms of the GME ZIFs (excluding ZIF-80) and BPL carbon at 298 K. CH_4, N_2, and O_2 isotherms for ZIF-78 are also shown. Filled and open symbols represent adsorption and desorption branches, respectively[79]

Morris et al.[80] prepared a series of five zeolitic imidazolate frameworks (ZIFs), namely ZIF-25, -71, -93, -96, and -97 with different pendant functionalities (-CH_3, -OH, -Cl, -CN, -CHO, and -NH_2). Experimental results show CO_2 uptake at approximately 800 Torr and 298 K ranging from 0.65 mmol/g on ZIF-71 to 2.18 mmol/g in ZIF-96. Molecular modeling calculations reproduce the pronounced dependence of the equilibrium adsorption on functionalization and suggest that polarizability and symmetry of the functionalization on the imidazolate are key factors leading to high CO_2 uptake.

Complete retention of CO_2 and passage of CO through the pores of ZIF-68, 69, and 70 are found when they are exposed to streams containing a binary mixture of CO_2/CO (50:50 v/v) at room temperature. ZIF-68, -69, and -70 have higher CO_2/CO selectivities of 19.2, 20.9, and 37.8[81]. One liter of ZIF-69 can store 82.6 liters (162 g) of CO_2 at 273 K. ZIF-95 and ZIF-100 with colossal cages were fabricated[82]. One litre of ZIF-100 can hold up to 28.2 l (55.4 g, or 1.7 mmol per g of ZIF-100) of CO_2 at 273 K. ZIF-100 and ZIF-95 exhibited high gas separation selectivities of CO_2 over CH_4, CO, and N_2. Debatin et al.[83] successfully prepared zinc–organic frameworks with imidazolate-4-amide-5-imidate ligand as the linker and this MOF showed high CO_2 adsorption as high as about 48 cm^3/g, which was very similar to that of ZIF-78 and ZIF-82 synthesized by using imidazolates containing the functional groups NO_2 and CN reported by Banerjee et al[79].

8.3.2 Carbon dioxide adsorption in flexible metal-organic frameworks

In contrast to the rigid frameworks discussed above which retain their porosity upon adsorption and desorption, flexible and dynamic frameworks collapse upon removal of guest solvent molecules, but restore their porous structures by adsorption of gas molecules at high pressures[3,84]. The adsorption isotherms are typically characterized with a distinct step[12], where the material "opens up" as gas molecules enter the pores. In some cases, there is almost no adsorption below a pressure threshold.

The structure of MIL-53 is built up from infinite chains of corner-sharing $MO_4(OH)_2$ octahedra (M=Cr^{3+}, Al^{3+}, Fe^{3+}) interconnected by benzenedicarboxylate units[85]. In the presence of water, the MIL-53 (Cr^{3+}, Al^{3+}) solids exhibit an original breathing phenomenon upon hydration-dehydration (Figure 8.7). The highest CO_2 adsorption capacities are around 8.5 mmol/g for dehydrated MIL-53 and 7.7 mmol/g for hydrated MIL-53 at 11-18 bar[48].

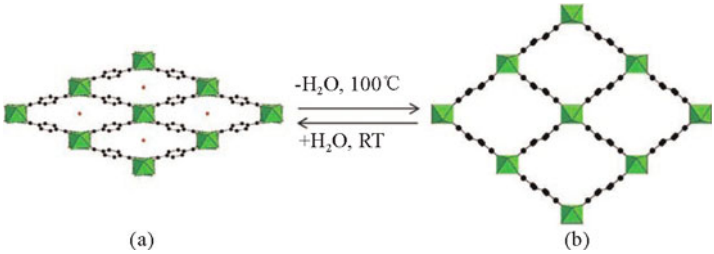

Figure 8.7 Hydration and dehydration process occurring in MIL-53(Cr, Al). (a) hydrated MIL-53; (b) dehydrated MIL-53[48]

Based on computational studies, MIL-53(Al^{3+}) (MIL: Material from Institut Lavoisier) metal-organic framework materials were functionalized by OH^-, $COOH^-$, NH^{2-}, and CH^{3-} (Figure 8.8) with the aim of improving the CO_2 adsorption capacity. The enormous impact of the functional groups in enhancing CO_2 capture in the pressure range 0.01~0.5 bar and at room temperature was illustrated. The material $(OH)_2$-MIL-53(Al^{3+}) was proposed as an optimal candidate for improved CO_2 capture at low pressures[86].

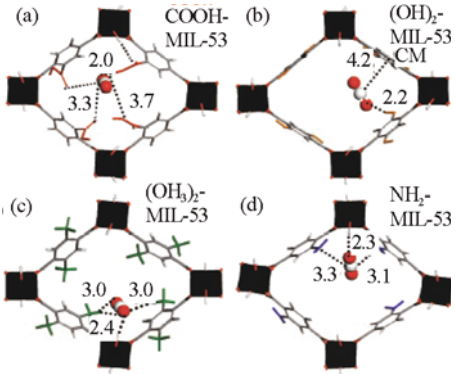

Figure 8.8 Most stable adsorption site for CO_2 in substituted lp forms of MIL-53(Al^{3+}), calculated by DFT at 0 K (a) COOH- (b) $(OH)_2$- (c) $(CH_3)_2$- (d)NH_2-. Distances are reported in angstroms[86]

The coadsorption of CO_2 and CH_4 in the flexible MIL-53(Cr) structure using a large variety of techniques was investigated[87]. CO_2-rich and equimolar CO_2-CH_4 mixtures lead to a breathing of the MIL-53(Cr) structure, i.e., a large-pore (LP) to narrow-pore (NP) transition and then back to LP form as the pressure increases. CH_4-rich mixtures (≥75% CH_4) always maintain the solid in the LP form as with pure CH_4. The closing and opening of the structure is entirely controlled by the

partial pressure of CO_2. Amine-functionalized MIL-53 had increased selectivity in CO_2/CH_4 separations by orders of magnitude while maintaining a very high capacity for CO_2 capture at about 2.3 mmol/g at 5 bar [88]. A comprehensive Density Functional Theory (DFT) study of the possible CO_2 adsorption geometries in the MIL-53 (Al, Cr) and MIL-47 hybrid organic-inorganic materials has been performed, as a preliminary step to gain a deeper understanding of the CO_2 adsorption mechanism in these systems and to help explain the "breathing" effect displayed by the MIL-53 materials[89,90]. Grand Canonical Monte Carlo simulations have explained the breathing of a metal–organic framework upon CO_2 adsorption[91,92].

Kishan et al.[93] reported three metal–organic supramolecular isomers synthesized using a flexible tetrahedral organic linker and Zn_2 clusters. At high pressure, the calculated weight percentage of CO_2 adsorption was 6~24 wt%. A breathing 2-fold interpenetrated microporous metal−organic framework was synthesized with a flexible tetrahedral organic linker and Zn_2 clusters that have a CO_2 sorption capacity of 7.1 mmol/g[94]. The two flexible compounds with an interdigitation motif of 2D layers, $[(Zn(5\text{-}NO_2\text{-}ip)(bpy))(0.5DMF{\cdot}0.5MeOH)]_n$ (CID-5; 5-NO_2-ip=5-nitroisophthalate, bpy=4,4'-bipyridyl, and CID=coordination polymer with an interdigitated structure), and $[(Zn(5\text{-}MeO\text{-}ip)(bpy))(0.5DMF{\cdot}0.5MeOH)]_n$ (CID-6; 5-MeO-ip=5-methoxyisophthalate), were prepared[95]. The selective adsorption uptake of CO_2 from a CO_2/CH_4 mixture (CO_2/CH_4=1:1 by volume) under the conditions of 101.3 kPa and 273 K was investigated. CID-5 has a closed-pore system, and so only CO_2 could be captured with negligible uptake (2.5 mL/g). On the other hand, CID-6, which has an open-pore system, can adsorb more CO_2 (40 mL/g), but it also simultaneously adsorbs some CH_4 (2 mL/g), thus resulting in an unsatisfactory separation for each compound.[95] A metal-organic honeycomb-like 2D pillared-bilayer open framework $[(Cu(pyrdc)(bpp))_2]_n$ (pyrdc=pyridine-2,3-dicarboxylate, bpp=1,3-bis(4-pyridyl)propane) has been constructed which shows sponge-like dynamic behavior with bond breaking and bond formation triggered by guest removal and inclusion. The CO_2 adsorption capacity of this MOF is about 100 ml/g (20 wt%) at 195 K and 1 bar[96]. Similarly, dynamic $[Cu(dhbc)_2(4,4'\text{-}bpy)]$ (dhbc=2,5-dihydroxybenzoate, bpy=bipyridine) [97] had a CO_2 capacity of 80 ml/g at 298 K and 50 atm.

Choi et al.[98] prepared highly flexible 3D pillared coordination networks $[(Ni_2L_2)(bptc)]$ (SNU-M10) by using NiII bismacrocyclic complexes. The networks can open and close their channels depending on the gas type, temperature, and pressure. The CO_2/N_2 selectivity of SNU-M10 at 298 K is 24:1 (v/v) at 0.61 atm

and 98:1 (v/v) at 1.0 atm[98]. A porous material constructed from zinc-adeninate macrocycles (Zn_6(adeninate)$_6$- (pyridine)$_6$(dimethylcarbamate)$_6$) can be tailored to discriminate between gases of different kinetic diameter (e.g., CO_2 and N_2), and can trap CO_2 within its cavities. Careful removal of the coordinated pyridine molecules that "gate" the cavity entrances allows for modulation of the cavity aperture dimensions and therefore discrimination of adsorbate molecules based on their kinetic diameter[99].

As well as pressure, temperature can be used to induce gating effects, particularly in frameworks which possess graphitic-type structures such as [M(bpy)$_2$(BF_4)$_2$] (M=Cu, Ni; bpy=4,4'-bipyridine; BF_4-=tetrafluoroborate) and [M(bpy)$_2$(CF_3SO_3)$_2$] (M=Co, Cu)[100,101]. Mesh-adjustable molecular sieves (MAMS) are another type of materials for gas separations and are based on temperature induced gating phenomena[102]. As the temperature increases the gates of [Ni_8(5-bbdc)$_6$(μ_3-OH)$_4$] (MAMS-1, bbdc: 5-tert-butyl-1,3-benzenedicarboxylate) open linearly, thus giving rise to an unprecedented molecular sieve with an adjustable mesh that can separate any two gases with kinetic diameters in the range of 2.9 to 5.0 Å, which corresponds to the size limits of most commercially relevant gases. In principle, by precise temperature control, any mesh size within this range can be achieved. In fact, all the pairs of gases listed above have been separated by using MAMS-1[102].

8.4 Future prospects

Although tens of thousands of metal-organic frameworks have been developed, the diffusion data for the single component gas and multicomponent gases are very limited. Most of the available adsorption data are based on the isothermal tests, which might mislead us that MOFs have a great and glorious future. In fact, such data might not be effective in practical applications. In order to solve these problems, fundamental research, including diffusion data, adsorption mechanisms, should be carried out. Compared to zeolites, MOFs have low thermal and water stabilites. This issue is one of the most concerns of MOFs that can decide the direction of MOFs.[10] Nevertheless, researchers will design and fabricate new types of MOFs, which will meet our requirements for practical application.

Acknowledgements

This work was supported by Australian Research Council. J.Y. thanks the Monash Fellowship by Monash University.

References

[1] Eddaoudi M, Moler D B, Li H L, et al. Modular chemistry: Secondary building units as a basis for the design of highly porous and robust metal-organic carboxylate frameworks. Aocounts of Chemical Research, 2001, 34 (4): 319~330.

[2] Yaghi O M, O'Keeffe M, Ockwig N W, et al. Reticular synthesis and the design of new materials. Nature, 2003, 423 (6941): 705~714.

[3] D'Alessandro D M, Smit B, Long J R. Carbon dioxide capture: prospects for new materials. Angewandte Chemie-International Edition, 2010, 49 (35): 6058~6082.

[4] O'Keeffe M, Peskov M A, Ramsden S J, et al. the reticular chemistry structure resource (RCSR) database of, and symbols for, crystal nets. Aocounts of Chemical Research, 2008, 41 (12): 1782~1789.

[5] Kitagawa S, Kitaura R, Noro S. Functional porous coordination polymers. Angewandte Chemie-International Edition, 2004, 43 (18): 2334~2375.

[6] Ma S Q, Zhou H C. A metal-organic framework with entatic metal centers exhibiting high gas adsorption affinity. Journal of the American Chemical Society, 2006, 128 (36): 11734~11735.

[7] Ranjan R, Tsapatsis M. Microporous metal organic framework membrane on porous support using the seeded growth method. Chemistry of Materials, 2009, 21 (20): 4920~4924.

[8] Li J R, Kuppler R J, Zhou H C. Selective gas adsorption and separation in metal-organic frameworks. Chemical Society Reviews, 2009, 38 (5): 1477~1504.

[9] Ebner A D, Ritter J A. State-of-the-art adsorption and membrane separation processes for carbon dioxide production from carbon dioxide emitting industries. Separation Science and Technology, 2009, 44 (6): 1273~1421.

[10] Keskin S, van Heest T M , Sholl D S. Can metal-organic framework materials play a useful role in large-scale carbon dioxide separations? ChemSusChem, 2010, 3 (8): 879~891.

[11] Phan A, Doonan C J, Uribe-Romo F J, et al. Synthesis, structure, and carbon dioxide capture properties of zeolitic imidazolate frameworks. Aocounts of Chemical Research, 2010, 43 (1): 58~67.

[12] Suh M P, Cheon Y E, Lee E Y. Syntheses and functions of porous metallosupramolecular networks. Coordination Chemistry Reviews, 2008, 252 (8~9): 1007~1026.

[13] Choi J, Jeong H K, Snyder M A, et al. Grain boundary defect elimination in a zeolite membrane by rapid thermal processing. Science, 2009, 325 (5940): 590~593.

[14] Guo H L, Zhu G S, Hewitt I J, et al. "Twin Copper Source" growth of metal-organic framework membrane: $Cu_3(BTC)_2$ with high permeability and selectivity for recycling H_2. Journal of the American Chemical Society, 2009, 131 (5): 1646~1647.

[15] Gascon J, Aguado S ,Kapteijn F. Manufacture of dense coatings of $Cu_3(BTC)_2$ (HKUST-1) on alpha-alumina. Microporous and Mesoporoas Materials, 2008, 113 (1~3): 132~138.

[16] Perez E V, Balkus K J, Ferraris J P, et al. Mixed-matrix membranes containing MOF-5 for gas separations, Journal of Membrane Science, 2009, 328 (1~2): 165~173.

[17] Huang A S, Bux H, Steinbach F, et al. Molecular-sieve membrane with hydrogen permselectivity: ZIF-22 in LTA topology prepared with 3-Aminopropyltriethoxysilane as covalent linker, Angewandte Chemie-International Edition, 2010, 49 (29): 4958~4961.

[18] Liu Y Y, Hu E P, Khan E A, et al. Synthesis and characterization of ZIF-69 membranes and separation for CO_2/CO mixture. Journal of Membrane Science, 2010, 353 (1~2): 36~40.

[19] Li Y S, Liang F Y, Bux H, et al. Molecular sieve membrane: Supported metal-organic framework with high hydrogen selectivity. Angewandte Chemie-International Edition, 2010, 49 (3): 548~551.

[20] Li Y S, Liang F Y, Bux H G, et al. Zeolitic imidazolate framework ZIF-7 based molecular sieve membrane for hydrogen separation. Journal of Membrane Science, 2010, 354 (1~2): 48~54.

[21] Bux H, Liang F Y, Li Y S, et al. Zeolitic imidazolate framework membrane with molecular sieving poperties by mcrowave-asisted slvothermal snthesis. Journal of the American Chemical Society, 2009, 131 (44): 16000~16001.

[22] Venna S R, Carreon M A. Highly permeable zeolite imidazolate framework-8 membranes for CO_2/CH_4 separation. Journal of the American Chemical Society, 2010, 132 (1): 76~78.

[23] Millward A R, Yaghi O M. Metal-organic frameworks with exceptionally high capacity for storage of carbon dioxide at room temperature. Journal of the American Chemical Society, 2005, 127 (51): 17998~17999.

[24] Cavenati S, Grande C A, Rodrigues A E. Adsorption equilibrium of methane, carbon dioxide, and nitrogen on zeolite 13X at high pressures. Journal of Chemical and Engineering Data, 2004, 49 (4): 1095~1101.

[25] Hamon L, Jolimaitre E ,Pirngruber G D. CO_2 and CH_4 Separation by adsorption using Cu-BTC metal-organic framework. Industrial and Engineering Chemistry Research, 2010, 49 (16): 7497~7503.

[26] Liang Z J, Marshall M, Chaffee A L. CO_2 adsorption-based separation by metal organic framework (Cu-BTC) versus zeolite (13X). Energy Fuels, 2009, 23: 2785~2789.

[27] Aprea P, Caputo D, Gargiulo N, et al. Modeling carbon dioxide adsorption on microporous substrates: Comparison between Cu-BTC metal-organic framework and 13X zeolitic molecular sieve. J. Chem. Eng. Data, 2010, 55 (9): 3655~3661.

[28] Yazaydin A O, Benin A I, Faheem S A, et al. Enhanced CO_2 adsorption in metal-organic frameworks via occupation of open-metal sites by coordinated water molecules. Chemistry of Materials, 2009, 21 (8): 1425~1430.

[29] Wu H, Simmons J M, Srinivas G, et al. Adsorption sites and binding nature of CO_2 in prototypical metal-organic frameworks: A combined neutron diffraction and first-principles study. Journal of Physical Chemistry Letters, 2010, 1 (13): 1946~1951.

[30] Britt D, Furukawa H, Wang B, et al. Highly efficient separation of carbon dioxide by a metal-organic framework replete with open metal sites. Proceedings of the National Academy of Sciences, 2009, 106 (49): 20637~20640.

[31] Botas J A, Calleja G, Sanchez-Sanchez M, et al. Cobalt Doping of the MOF-5 Framework and Its Effect on Gas-Adsorption Properties. Langmuir, 2010, 26 (8): 5300-5303.

[32] Xu Q, Liu D H, Yang Q Y, et al. Li-modified metal-organic frameworks for CO_2/CH_4 separation: A route to achieving high adsorption selectivity. Journal of Materials Chemistry, 2010, 20 (4): 706~714.

[33] Zhao Z X, Li Z, Lin Y S. Adsorption and diffusion of carbon dioxide on metal-organic framework (MOF-5). Industrial and Engineering Chemistry Research, 2009, 48 (22): 10015~10020.

[34] Saha D, Bao Z B, Jia F, et al. Adsorption of CO_2, CH_4, N_2O, and N_2 on MOF-5, MOF-177, and zeolite 5A. Environmental Science and Technology, 2010, 44 (5): 1820~1826.

[35] Lu C M, Liu J, Xiao K F, et al. Microwave enhanced synthesis of MOF-5 and its CO_2 capture ability at moderate temperatures across multiple capture and release cycles. Journal of Chemical Engineering, 2010, 156 (2): 465~470.

[36] Ferey G, Mellot-Draznieks C, Serre C, et al. A chromium terephthalate-based solid with unusually large pore volumes and surface area. Science, 2005, 309 (5743): 2040~2042.

[37] Chowdhury P, Bikkina C, Gumma S. Gas adsorption properties of the chromium-based metal organic framework MIL-101. Journal of Physical Chemistry C, 2009, 113 (16): 6616~6621.

[38] Llewellyn P L, Bourrelly S, Serre C, et al. High uptakes of CO_2 and CH_4 in mesoporous metal-organic frameworks MIL-100 and MIL-101. Langmuir, 2008, 24 (14): 7245~7250.

[39] Mu B, Schoenecker P M, Walton K S. Gas adsorption study on mesoporous metal-organic framework UMCM-1. Journal of Physical Chemistry C, 2010, 114 (14): 6464~6471.

[40] Mueller U, Schubert M, Teich F, et al. Metal-organic frameworks - prospective industrial applications. Journal of Materials Chemistry, 2006, 16 (7): 626~636.

[41] Walton K S, Millward A R, Dubbeldam D, et al. Understanding inflections and steps in carbon dioxide adsorption isotherms in metal-organic frameworks. Journal of the American Chemical Society, 2008, 130 (2): 406~407.

[42] Mofarahi M, Khojasteh Y, Khaledi H, et al. Design of CO_2 absorption plant for recovery of CO_2 from flue gases of gas turbine. Energy, 2008, 33 (8): 1311~1319.

[43] Liu J A, Wang Y, Benin A I, et al. CO_2/H_2O adsorption equilibrium and rates on metal-organic frameworks: HKUST-1 and Ni/DOBDC. Langmuir, 2010, 26 (17): 14301~14307.

[44] Liang Z J, Marshall M, Chaffee A L. CO_2 adsorption, selectivity and water tolerance of pillared-layer metal organic frameworks. Microporous and Mesoporoas Materials, 2010, 132 (3): 305~310.

[45] Chen Y F, Lee J Y, Babarao R, et al. A highly hydrophobic metal organic framework $Zn(BDC)(TED)_{0.5}$ for adsorption and separation of CH_3OH/H_2O and CO_2/CH_4: An integrated experimental and simulation study. Journal of Physical Chemistry C, 2010, 114 (14): 6602~6609.

[46] Park H J, Suh M P. Mixed-ligand metal-organic frameworks with large pores: Gas sorption properties and single-crystal-to-single-crystal transformation on guest exchange. Chemistry-A European Journal, 2008, 14 (29): 8812~8821.

[47] Ma S Q, Wang X S, Yuan D Q, et al. A coordinatively linked Yb metal-organic framework demonstrates high thermal stability and uncommon gas-

adsorption selectivity. Angewandte Chemie-International Edition, 2008, 47 (22): 4130~4133.

[48] Llewellyn P L, Bourrelly S, Serre C, et al. How hydration drastically improves adsorption selectivity for CO_2 over CH_4 in the flexible chromium terephthalate MIL-53. Angewandte Chemie-International Edition, 2006, 45 (46): 7751~7754.

[49] Dreisbach F, Staudt R, Keller J U. High pressure adsorption data of methane, nitrogen, carbon dioxide and their binary and ternary mixtures on activated carbon. Adsorpt, 1999, 5 (3): 215~227.

[50] Yazaydin A O, Snurr R Q, Park T H, et al. Screening of metal-organic frameworks for carbon dioxide capture from flue gas using a combined experimental and modeling approach. Journal of the American Chemical Society, 2009, 131 (51): 18198~18199.

[51] Sumida K, Horike S, Kaye S S, et al. Hydrogen storage and carbon dioxide capture in an iron-based sodalite-type metal-organic framework (Fe-BTT) discovered via high-throughput methods. Journal of Chemical Sciences, 2010, 1 (2): 184~191.

[52] Demessence A, D'Alessandro D M, Foo M L, et al. Strong CO_2 binding in a water-stable, triazolate-bridged metal-oganic famework fnctionalized with ehylenediamine. Journal of the American Chemical Society, 2009, 131 (25): 8784~8786.

[53] Park H J, Suh M P. Stepwise and hysteretic sorption of N_2, O_2, CO_2, and H_2 gases in a porous metal-organic framework $[Zn_{-2}(BPnDC)_2(bpy)]$. Chemical Communications, 2010, 46 (4): 610~612.

[54] Lee Y G, Moon H R, Cheon Y E, et al. A comparison of the H_{-2} sorption capacities of isostructural metal-organic frameworks with and without accessible metal sites: $\{Zn_{-2}(abtc)(dMf)_2\}_3$ and $\{Cu_{-2}(abtc)(dMf)_2\}_3$ versus $\{Cu_{-2}(abtc)\}_3$. Angewandte Chemie-International Edition, 2008, 47 (40): 7741~7745.

[55] Cheon Y E, Suh M P. Selective gas adsorption in a microporous metal-organic framework constructed of Co^{II}_4 clusters. Chemical Communications, 2009(17): 2296~2298.

[56] Cheon Y E, Park J, Suh M P. Selective gas adsorption in a magnesium-based metal-organic framework. Chemical Communications, 2009(36): 5436~5438.

[57] Li J R, Tao Y, Yu Q, et al. Selective gas adsorption and unique structural topology of a highly stable guest-free zeolite-type MOF material with N-rich chiral open channels. Chemistry-A European Journal, 2008, 14 (9):

2771~2776.

[58] Dietzel P D C, Besikiotis V, Blom R. Application of metal-organic frameworks with coordinatively unsaturated metal sites in storage and separation of methane and carbon dioxide. Journal of Materials Chemistry, 2009, 19 (39): 7362~7370.

[59] Dietzel P D C, Johnsen R E, Fjellvag H, et al. Adsorption properties and structure of CO_2 adsorbed on open coordination sites of metal-organic framework Ni_2(dhtp) from gas adsorption, IR spectroscopy and X-ray diffraction. Chemical Communications, 2008(41): 5125~5127.

[60] Pachfule P, Das R, Poddar P, et al. Structural, magnetic, and gas adsorption study of a two-dimensional tetrazole-pyrimidine based metal-organic framework. Crystal Growth and Design, 2010, 10 (6): 2475~2478.

[61] An J, Geib S J, Rosi N L. High and selective CO_2 uptake in a cobalt adeninate metal-organic framework exhibiting pyrimidine- and amino-decorated pores. Journal of the Amevican Chemical Society, 2010, 132 (1): 38~39.

[62] Bae Y S, Spokoyny A M, Farha O K, et al. Separation of gas mixtures using Co(II) carborane-based porous coordination polymers. Chemical Communications, 2010, 46 (20): 3478~3480.

[63] Willans C E, French S, Barbour L J, et al. A catenated imidazole-based coordination polymer exhibiting significant CO_2 sorption at low pressure. Dalton Transactions, 2009(33): 6480~6482.

[64] Bae Y S, Farha O K, Hupp J T, et al. Enhancement of CO_2/N_2 selectivity in a metal-organic framework by cavity modification. Journal of Materials Chemistry, 2009, 19 (15): 2131~2134.

[65] Chatti R, Bansiwal A K, Thote J A, et al. Amine loaded zeolites for carbon dioxide capture: Amine loading and adsorption studies. Microporous and Mesoporoas Materials, 2009, 121 (1~3): 84~89.

[66] Hiyoshi N, Yogo K, Yashima T. Adsorption characteristics of carbon dioxide on organically functionalized SBA-15. Microporous and Mesoporoas Materials, 2005, 84 (1~3): 357~365.

[67] Arstad B, Fjellvag H, Kongshaug K O, et al. Amine functionalised metal organic frameworks (MOFs) as adsorbents for carbon dioxide. Adsorpt, 2008, 14 (6): 755~762.

[68] An J, Rosi N L. Tuning MOF CO_2 adsorption properties via cation exchange. Journal of The American Chemical Society, 2010, 132 (16): 5578~5579.

[69] Noro S, Tanaka D, Sakamoto H, et al. Selective gas adsorption in one-

dimensional, flexible Cu-II coordination polymers with polar units. Chemistry of Materials, 2009, 21 (14): 3346~3355.

[70] Vaidhyanathan R, Iremonger S S, Dawson K W, et al. An amine-functionalized metal organic framework for preferential CO_2 adsorption at low pressures. Chemical Communications, 2009. (35): 5230~5232.

[71] Barea E, Tagliabue G, Wang W G, et al. A flexible pro-porous coordination polymer:Non-conventional synthesis and separation properties towards CO_2/CH_4 Mixtures. Chemistry-A European Journal, 2010, 16 (3): 931~937.

[72] Bae Y S, Farha O K, Spokoyny A M, et al. Carborane-based metal-organic frameworks as highly selective sorbents for CO_2 over methane. Chemical Communications, 2008. (35): 4135~4137.

[73] Bae Y S, Mulfort K L, Frost H, et al. Separation of CO_2 from CH_4 using mixed-ligand metal-organic frameworks. Langmuir, 2008, 24 (16): 8592~8598.

[74] Mu B, Li F, Walton K S. A novel metal-organic coordination polymer for selective adsorption of CO_2 over CH_4. Chemical Communications, 2009, (18): 2493~2495.

[75] Bastin L, Barcia P S, Hurtado E J, et al. A microporous metal-organic framework for separation of CO_2/N_2 and CO_2/CH_4 by fixed-bed adsorption. Journal of Physical Chemistry C, 2008, 112 (5): 1575~1581.

[76] Hayashi H, Cote A P, Furukawa H, et al. Zeolite a imidazolate frameworks. Nature Materials, 2007, 6 (7): 501~506.

[77] Huang X C, Lin Y Y, Zhang J P, et al. Ligand-directed strategy for zeolite-type metal-organic frameworks: Zinc(II) imidazolates with unusual zeolitic topologies. Angewandte Chemie-International Edition, 2006, 45 (10): 1557~1559.

[78] Park K S, Ni Z, Cote A P, et al. Exceptional chemical and thermal stability of zeolitic imidazolate frameworks. Proceedings of the National Academy of Sciences, 2006, 103 (27): 10186~10191.

[79] Banerjee R, Furukawa H, Britt D, et al. Control of pore size and functionality in isoreticular zeolitic imidazolate frameworks and their carbon dioxide selective capture properties. Journal of the American Chemical Society, 2009, 131 (11): 3875~3877.

[80] Morris W, Leung B, Furukawa H, et al. A combined experimental-computational investigation of carbon dioxide capture in a series of isoreticular zeolitic imidazolate frameworks. Journal of the American Chemical Society, 2010, 132 (32): 11006~11008.

[81] Banerjee R, Phan A, Wang B, et al. High-throughput synthesis of zeolitic

imidazolate frameworks and application to CO_2 capture. Science, 2008, 319 (5865): 939~943.

[82] Wang B, Cote A P, Furukawa H, et al. Colossal cages in zeolitic imidazolate frameworks as selective carbon dioxide reservoirs. Nature, 2008, 453 (7192): 207~206.

[83] Debatin F, Thomas A, Kelling A, et al. In situ synthesis of an imidazolate-4-amide-5-imidate ligand and formation of a microporous zinc-organic framework with H_2-and CO_2-storage ability. Angewandte Chemie-International Edition, 2010, 49 (7): 1258~1262.

[84] Horike S, Shimomura S, Kitagawa S. Soft porous crystals. Nature Materials, 2009, 1 (9): 695~704.

[85] Serre C, Millange F, Thouvenot C, et al. Very large breathing effect in the first nanoporous chromium(III)-based solids: MIL-53 or Cr^{III}(OH)center dot{O_2C-C_6H_4-CO_2}center dot{HO_2C-C_6H_4-CO_2H}$_x$. H_2Oy. Journal of the American Chemical Society, 2002, 124 (45): 13519~13526.

[86] Torrisi A, Bell R G, Mellot-Draznieks C. Functionalized MOFs for enhanced CO_2 capture. Crystal Growth and Design., 2010, 10 (7): 2839~2841.

[87] Hamon L, Llewellyn P L, Devic T, et al. Co-adsorption and separation of CO_2-CH_4 mixtures in the highly flexible MIL-53(Cr) MOF. Journal of the American Chemical Society, 2009, 131 (47): 17490~17499.

[88] Couck S, Denayer J F M, Baron G V, et al. An amine-functionalized MIL-53 metal-organic framework with large separation power for CO_2 and CH_4. Journal of the American Chemical Society, 2009, 131 (18): 6326~6327.

[89] Ramsahye N A, Maurin G, Bourrelly S, et al. Probing the adsorption sites for CO_2 in metal organic frameworks materials MIL-53 (Al, Cr) and MIL-47 (V) by density functional theory. Journal of Physical Chemistry C, 2008, 112 (2): 514~520.

[90] Ramsahye N A, Maurin G, Bourrelly S, et al. Charge distribution in metal organic framework materials: Transferability to a preliminary molecular simulation study of the CO_2 adsorption in the MIL-53 (Al) system. Physical Chemistry Chemical Physics, 2007, 9 (9): 1059~1063.

[91] Ramsahye N A, Maurin G, Bourrelly S, et al. Adsorption of CO_2 in metal organic frameworks of different metal centres: Grand Canonical Monte Carlo simulations compared to experiments. Adsorpt, 2007, 13 (5~6): 461~467.

[92] Ramsahye N A, Maurin G, Bourrelly S, et al. On the breathing effect of a metal-organic framework upon CO_2 adsorption: Monte Carlo compared to microcalorimetry experiments. Chemical Communications, 2007(31):

3261~3263.

[93] Kishan M R, Tian J, Thallapally P K, et al. Flexible metal-organic supramolecular isomers for gas separation. Chemical Communications, 2010, 46 (4): 538~540.

[94] Thallapally P K, Tian J, Kishan M R, et al. Flexible (Breathing) interpenetrated metal-organic frameworks for CO_2 separation applications. Journal of the American Chemical Society, 2008, 130 (50): 16842~16843.

[95] Fukushima T, Horike S, Inubushi Y, et al. Solid solutions of soft porous coordination polymers: Fine-tuning of gas adsorption properties. Angewandte Chemie-International Edition, 2010, 49 (28): 4820~4824.

[96] Maji T K, Mostafa G, Matsuda R, et al. Guest-induced asymmetry in a metal-organic porous solid with reversible single-crystal-to-single-crystal structural transformation. Journal of the American Chemical Society, 2005, 127 (49): 17152~17153.

[97] Kitaura R, Seki K, Akiyama G, et al. Porous coordination-polymer crystals with gated channels specific for supercritical gases. Angewandte Chemie-International Edition, 2003, 42 (4): 428~431.

[98] Choi H S, Suh M P. Highly selective CO_2 capture in flexible 3D coordination polymer networks. Angewandte Chemie-International Edition, 2009, 48 (37): 6865~6869.

[99] An J Y, Fiorella R P, Geib S J, et al. Synthesis, structure, assembly, and modulation of the CO_2 adsorption properties of a zinc-adeninate macrocycle. Journal of the American Chemical Society, 2009, 131 (24): 8401~8403.

[100] Kanoh H, Kondo A, Noguchi H, et al. Elastic layer-structured metal organic frameworks (ELMS). Journal of Colloid and Interface Science, 2009, 334 (1): 1~7.

[101] Kondo A, Chinen A, Kajiro H, et al. Metal-ion-dependent gas sorptivity of elastic layer-structured MOFs. Chemistry-A European Journal, 2009, 15 (31): 7549~7553.

[102] Ma S Q, Sun D F, Wang X S, et al. A mesh-adjustable molecular sieve for general use in gas separation. Angewandte Chemie-International Edition, 2007, 46 (14): 2458~2462.

Chapter 9
CO_2 Selective Separation Membranes

Dan Li,[1,2] Jianfeng Yao,[1] and Huanting Wang[1*]

[1]Department of Chemical Engineering, Monash University, Clayton, Victoria 3800, Australia

[2]Environmental Engineering, School of Environmental Science, Murdoch University, Murdoch, Western Australia 6150, Australia

Abstract

Over the past two decades, membrane technology has attracted tremendous attention at CO_2 separation from other gases, which has shown great potential to significantly improve energy efficiency and reduce cost associated with processes. The membrane structures and chemistry properties greatly affect their CO_2 separation performances, including selectivity and permeability. In recent years, there has been significant progress in the development of CO_2-selective membranes. This chapter reviewed the recent activities relating to the fabrication and separation performances of polymeric, inorganic and mixed-matrix membranes for CO_2 separation purposes.

9.1 Introduction

Carbon dioxide (CO_2) has been regarded as one of the main factors which are responsible for anthropogenic greenhouse effect and thus accelerate the rate of climate change[1]. CO_2 emission from human activities, which include the burning of fossil fuels in energy production and the use of petroleum or diesel in transportation, has increased dramatically in the past few decades[2]. If there are not significant control methods and techniques carried out, it is believed that the concentration of CO_2 in atmosphere will continuously increase in the future. Until now, there have been some strategies utilized to reduce or limit CO_2 emission. For instance, great effort has been conducted to increase efficiency in fuel combustion processes and to develop the feasibility of replacing conventional fossil fuels with

renewable energy resources [3]. Another possible option to reduce CO_2 emission is CO_2 separation and capture, which can be achieved by different techniques, including solvent/solid absorption, cryogenic distillation, membrane separation, and mineralization processes [4].

In particular, membrane gas separation has been considered as an attractive technique due to its advantages, such as low energy requirement and capital investment cost, as well as relatively simple and easy operation [5,6]. A good membrane candidate used for CO_2 separation should possess high CO_2 permeability/selectivity; thermal and chemical stability; and low cost [7]. The purpose of this review is to present an overview of recent development in the area of CO_2-selective separation membranes, including polymeric, inorganic, and mixed-matrix membranes. In last several years, there have been a large number of review papers published on gas separation membranes, some of which are relating to CO_2-selective separation membranes [5-15].

9.2 Fundamental Background

The gas permeability and selectivity of membranes are strongly affected by several factors, including the properties of membranes and gas species, and their interaction [3, 5, 7, 16]. Generally, the transport of gas molecules is governed by different mechanisms based on the properties of membranes, including solution-diffusion, Knudsen diffusion, surface diffusion, capillary condensation, and molecular sieving [16]. For instance, the gas transport through a polymeric membrane is mainly explained by a solution-diffusion mechanism. The relationship between permeability, diffusivity and solubility for gas A can be described by the following equation [16]:

$$P_A = S_A \times D_A$$

where P_A is the permeability coefficient [cm^3 (STP) cm^{-2} s^{-1} $cmHg^{-1}$], D_A is the diffusivity coefficient (cm^2 s^{-1}) and S_A is the solubility coefficient [cm^3 (STP) $cmHg^{-1}$]. Barrer [10^{-10} cm^3 (STP) cm^{-2} s^{-1} $cmHg^{-1}$] is commonly used as the unit of P_A.

The membrane selectivity to different gas molecules is governed by the abilities of specific molecules passing through the membrane matrix [7,16]. The permselectivity or ideal separation factor in the pure gas permeation, α, is determined by the permeabilities of different gases, A and B [3]:

$$\alpha_{A,B} = \frac{P_A}{P_B}$$

As seen, the permselectivity or ideal separation factor in pure gas permeation

can been also described by:

$$\alpha_{A,B} = \frac{S_A}{S_B} \times \frac{D_A}{D_B} \quad \text{or} \quad \alpha_{A,B} = \alpha_S \times \alpha_D$$

The real separation factor in the mixed gas permeation can be defined as [3]:

$$\alpha_{A,B} = \frac{y_A}{y_B} \times \frac{x_A}{x_B}$$

where y_A and y_B are the molar fractions of gases A and B in the feed; and x_A and x_B are the molar fractions of gases A and B in the permeate, respectively.

There is a trade-off tendency existing between the selectivities and permeabilities of gas separation membranes. The permeability-selectivity trade-off relationships for different gas pairs have been summarized by Robeson in 1991 and updated in 2008, suggesting the presence of upper bounds [17,18]. Figure 9.1 shows two examples of upper bounds in the separations of CO_2/N_2 and CO_2/CH_4. As seen, there are only a few of polymeric membranes exhibiting superior performances above the upper bounds [7, 17, 18]. Inorganic membranes and mixed-matrix membranes have been suggested with great potential to exceed the Robeson's upper bounds [7, 19].

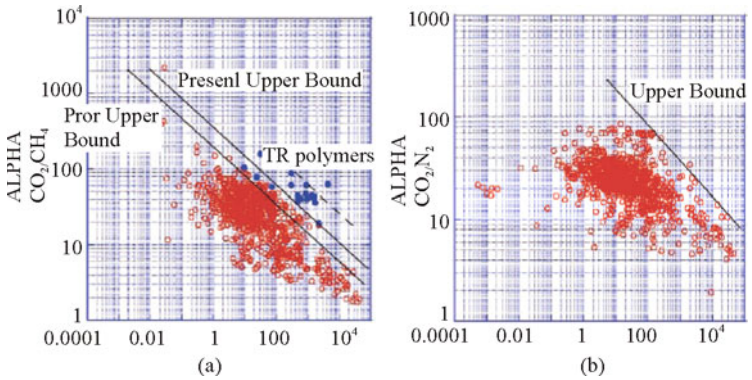

Figure 9.1 Upper bound correlations for the separation of CO_2/CH_4 (a) and CO_2/N_2 (b) [17,18]

9.3 Polymeric membranes

9.3.1 Structures, Fabrication and Materials

In general, polymeric membranes for gas separation can be fabricated

in the form of different configurations, including homogeneous symmetric, asymmetric and composite membrane structures as shown in Figure 9.2 [16]. Homogeneous symmetric polymeric membranes (Figure 9.2(a)) are easily fabricated and show intrinsic separation properties directly; hence they are commonly prepared and tested in the lab-scale gas separation [16]. However, the homogenous symmetric membranes exhibit low gas permeability. As a result, some other configurations, such as asymmetric or composite membranes have been developed for commercial purposes. An asymmetric membrane consists of a thin dense layer on the top of a porous support layer which is made of the same material (Figure 9.2(b)) [16]. The decrease of effective skin thickness can enhance the separation properties of resulting membranes, especially gas permeability [20]. Phase inversion technique is usually utilized to prepare asymmetric membranes, which can be further classified into dry phase inversion, wet phase inversion and thermal phase inversion [21]. For example, Jansen et al. used dry phase inversion to prepare asymmetric gas separation membranes with a thin dense skin made from a modified poly(ether ether ketone) material [20~22]. A composite membrane is made of a defect-free thin skin layer coating on the top of support (Figure 9.2c). In order to decrease the thickness of thin layer and improve the fluxes, a gutter layer with high permeability and low selectivity is commonly introduced [16]. In the composite membranes, the material of thin layer is different from that of substrate, thus they may exhibit better separation performances than the asymmetric membranes to some extent [23]. Most importantly, by utilizing composite structures, it is feasible to minimize the membrane cost, which meets the needs of industry. Interfacial polymerization has been used to fabricate composite membranes for gas separation [24~27]. In order to prepare high-performance composite membranes, especially thin film composite (TFC) membranes, the compatibility of coating material and the porosity of support layer are required to be controlled carefully [28]. The optimization of coating conditions and the use of post-treatment may assist the fabrication of non-defect selective skin layers in composite membranes [29~31]. Conventional liquid-liquid or vapor-liquid interfacial polymerization may easily cause surface microvoids, resulting in a decrease of membrane selectivities [33~35]. Therefore, Du and co-workers developed a solid-liquid interfacial polymerization method. The resulting poly(*N,N*-dimethylaminoethyl methacrylate) TFC membranes possessed a greater permeance (P_{CO2} = 85 GPU) with a similar selectivity [$\alpha(CO_2/N_2)$ = 50], as compared with those fabricated from the liquid-liquid interfacial polymerization [33, 35].

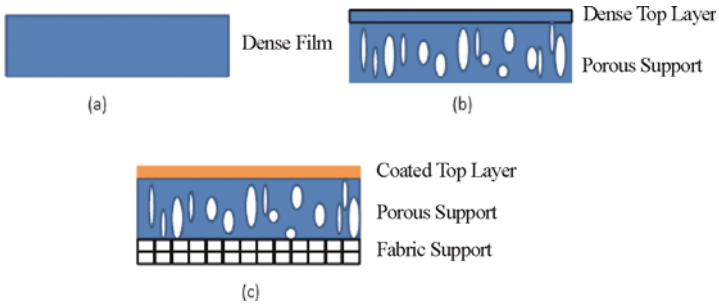

Figure 9.2 Schematic representations of three different types of membrane configurations: (a) homogeneous symmetric membrane, (b) asymmetric membrane and (c) composite membrane [16]

With the use of polymers as membrane materials, the CO_2-selective separation membranes can be easily fabricated into hollow fiber membrane modules [8]. The hollow fiber module, which is generally composed of thousands of fibers, provides a high surface area-to-volume ratio, low resistance to feed flow, and pressure stability [8]. Each of those advantages contributes to their high productivity and performance in gas separation [36~40]. Previous studies have proven that the asymmetric or composite hollow fibers show an impressive CO_2 separation performance, particularly as compared with dense films [41,42]. The fabrication of novel poly(amidoamine) (PAMAM) dendrimer composite hollow fiber membranes was reported by Kouketsu et al. (Figure 9.3) for the first time, in which an ultra-thin PAMAM active layer was coated on the chitosan-modified ultrafiltration membrane substrate. The resulting composite hollow fiber membranes exhibited an excellent CO_2/N_2 selectivity (400) and CO_2 permeance [1.6×10^{-7} m^3 (STP) m^{-2} s^{-1} kPa^{-1}] at 100 kPa and 40 °C [43].

The inherent properties of polymer materials are the most important factor in determining the performances of CO_2-selective separation membranes. Therefore, there have been a large number of polymeric materials investigated and developed for gas separation applications, including cellulose acetate, polyphenyleneoxide, polymethylpentene, polyimides, polysulfone, etc. [8, 15, 44]. However, the number of polymers which have been utilized in the fabrication of commercial gas separation membranes is still limited [15].

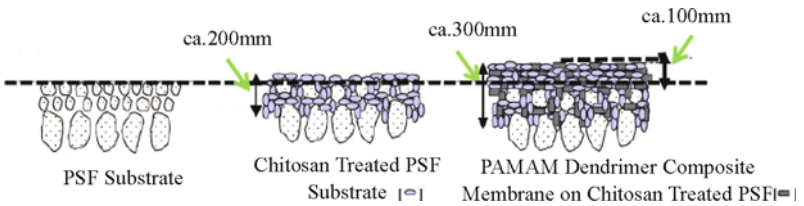

Figure 9.3 Schematic diagram of cross-section of PSF substrate, chitosan-treated substrate, and poly(amidoamine) (PAMAM) dendrimer composite membrane [43]

Polyimides (PIs) are a class of high-performance polymers, possessing many attractive properties, such as excellent thermal stability, solvent resistance, and mechanical strength. Commercially avalable PIs include Matrimid, P84, Kapton polyimide, etc. [45]. PIs are generally prepared after the polycondensation of polyamic acid, which is formed after the reaction between a diamine and a diahydride in an aprotic solvent [7]. To date, various diahydrides and diamines have been used in the synthesis of PI membranes for CO_2 gas separation. In particular, PIs prepared from 2,2-bis (3,4-dicarboxyphenyl)hexafluoropropane dianhydride (6FDA) and/or fluorine-containing diamines have attracted great attention due to their excellent gas permeabilities with high selectivities [7, 46~48]. However, fluorinated PIs are relatively expensive, which limits their use to manufacture asymmetric membranes. The development of PI composite membranes consisting of an expensive high-performance selective fluorinated PI layer and an inexpensive substrate (e.g. PSF) may reduce the cost in the production of fluorinated PIs for CO_2 separation [49]. The CO_2/CH_4 selectivity and CO_2 permeance of 6FDA-Durene/PSF composite membrane, which was treated further with silicon rubber, were 17 and 8.6 GPU, respectively [49].

Polysulfones (PSFs) have attracted great interest because of their reasonable gas separation performance and low cost. In general, PSFs are synthesized in a condensation reaction between a bisphenol and a dihalogenated diphenylsulfone [7]. PSFs, including Udel, Radel, and Ultrason, are well-known in the fabrication of membranes with attractive gas separation properties [50]. By using different monomers, the fabricated PSF membranes possess a wide range of CO_2 permeabilities and selectivities. For example, Camacho-Zuñiga and co-works reported the synthesis of new PSF copolymers from bis(4-fluorophenyl)sulfone and based on equimolar mixtures of the rigid naphthalene moiety with bulky connectors from bisphenols [51]. The resulting membranes showed attractive CO_2 separation properties, in which their CO_2/CH_4 selectivities were 29~38 and CO_2

permeabilities were 5~7 Barrer at 35 °C and 2 atm [51].

Aromatic polyamide (PA) membranes have been studied for their gas transport and separation properties [25, 27, 52~54]. Espeso et al. reported that the CO_2/CH_4 selectivities of aromatic PA membranes were in the range of 19.2 – 27.7 with the CO_2 permeabilities varying from 0.47 Barrer to 2.24 Barrer [54]. The membrane selectivity was further improved by forming a silicone-coating on the top of polyamide which repaired the inherent defects in the thin layer [25]. However, the use of aromatic PA in the fabrication of CO_2-selective membranes has not attracted significant attention, due to their poor solubility in highly polar organic solvents [7, 27, 54]. Moreover, their inherent structures, such as high chain rigidity, cohesive energy and molecular packing density, limit their performances in gas separation [27, 54].

9.3.2 Chemical Modification and Physical Blending

In order to improve the gas transport properties of polymeric membranes, physical blending and chemical modification have been studied widely; although it is important to further develop novel polymeric materials to fabricate ideal CO_2-selective separation membranes.

The introduction of crosslinkable monomers or polymers with different properties into the precursor polymers or monomers can be an effective way to modify the separation performances of resulting CO_2-selective separation membranes. As shown in Figure 9.4, the polymer structure of CO_2-selective membranes can be tailored by the combination of hard block and soft block [7]. The hard block which is synthesized from a more rigid polymer provides a structural support for membranes; whilst the soft block is synthesized from a more flexible polymer, which provides a better permeability for membranes than the hard block [7]. Clearly, polymers with various ratios and types of hard/soft blocks can possess different gas separation performances [7]. For example, the novel polyurethane/urea membranes, which are composed of two soft segments, poly(propylene oxide) (PU) and polydimethylsiloxane (PDMS), showed improved permeabilities of CO_2 and N_2 when the PDMS loading was high in the resulting membranes [55]. After the copolymerization of polybenzoxazole (PBO) and polyimides (PI) at 450 °C, the resulting copolymer membranes with 10 mol% PBO showed an increase of CO_2, N_2 and CH_4 permeabilities by 2 order of magnitudes; however the CO_2/CH_4 selectivity decreased by more than 73%, when compared to the separation performance of plain PI membranes [56].

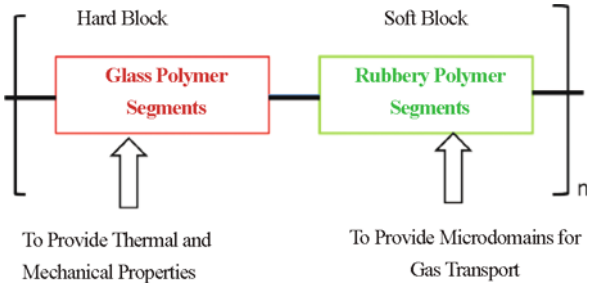

Figure 9.4 Polymer structures of CO_2-selective separation membranes: hard and soft blocks [7]

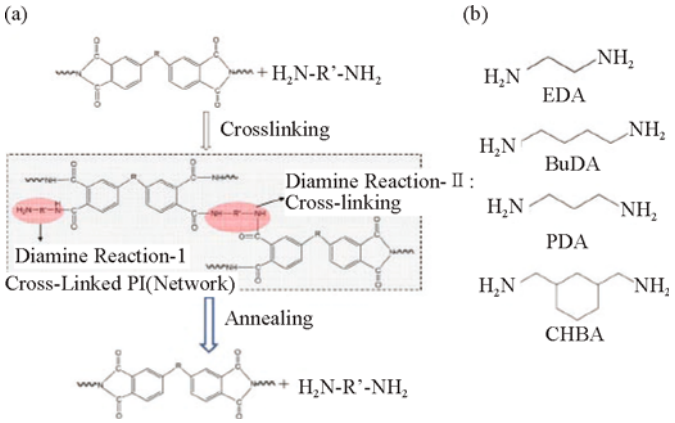

Figure 9.5 Possible reaction mechanisms of crosslinked polyimides by diamines [57~59]

Previous studies have reported that there is a favorable interaction between CO_2 and some functional groups, such as amine. Therefore, the use of amine-functionalized polymer can be a way to vary the CO_2 permeabilities and selectivities of resulting membranes. For example, the amine-substituted silicon rubber membranes showed improved CO_2 permeabilities and selectivities, which were 15% and 22%~34% greater than those of unmodified silicon rubber membranes, respectively [28]. The introduction of amine functionalities into poly(ethylene glycol)diacrylate membranes enhanced the membrane separation performances for CO_2/H_2, which were above the Robeson's trade-off bound [60]. The functionalization of poly(dimethylsiloxane) (PDMS) membranes with 2,6-diisopropyl phenyl amino-hydroxy groups resulted in an increase of CO_2/CH_4 permeselectivity without a significant change in permeabilities [61]. An

interesting study was reported by Chung and co-workers by making use of the reactive sites from amine groups in various diamines (i.e. ethylenediamine (EDA), 1,3-propane diamine (PDA), 1,4-butane diamine (BuDA), and 1,3-cyclohexanebis(methylamine) (CHBA)). Annealing and heating (e.g. >200 °C) under vacuum resulted in the reversed cross-linking reaction with liberating the diamine in the cross-linked polyimide sample (Figure 9.5) [57~59]. For 6FDA-durene membranes, the diamino cross-linking enhanced the selectivity for CO_2 over CH_4; whereas the modified Matrimid membranes encountered a decrease of CO_2/CH_4 selectivity [59]. Similar results were also reported in Qiao's work by introducing 1,3-diaminobenzene as a crosslinker [62].

Other moieties have also been studied to graft or crosslink polymers. For example, the membranes made of poly(vinyl chloride) (PVC) with poly(oxyethylene methacrylate) (POEM) side chains possessed better CO_2 permeabilities without lowering selectivities, when the portions of POEM were increased in the copolymers [63]. In particular, the membranes with 70 wt% of POEM showed 100 Barrer for CO_2 permeability at 25 °C, which was about 70 times higher than that of pure PVC membrane [63]. In Koros's work, PI polymer with a carboxylic acid pendent group was cross-linked by 1,3-propanediol [64]. The resulting cross-linked PI membranes were proven to be particularly effective to separate CO_2 from CH_4 in natural gas application, with a permeability and CO_2/CH_4 selectivity in excess of 75 Barrer and around 45 [64]. The introduction of 3-[tris-(trimethylsiloxy)silyl] propyl acrylate (TRIS-A) in poly(ethylene glycol) diacrylate increased the polymer fractional free volume and the strong broadening of glass-rubber relaxation. Gas permeabilities were improved significantly for the polymer membranes with greater TRIS-A contents. However, the strongly non-polar property of TRIS-A reduced the CO_2 affinity to the resulting membranes; hence, there was a decrease of CO_2/light gas selectivities accompanied [65].

Some chemical modifications, such as sulfonation, were adopted to modify the polymer membranes. Sulfonated polycarbonate exhibited strong potential to effectively separate CO_2, when compared with their parent membranes [66]. The enhancement in selectivities was reported with the use of sulfonated poly(phenylene oxide) (PPO) membranes in gas separation, which was ascribed to the availability of large number of polar sites in the membranes for CO_2 gas sorption [67]. However, lower permeabilities were recorded for the sulfonated polymeric membranes [66,67].

Chemical modification of polymers shows great potential to improve membrane separation properties; however, physical blending is considered as a useful, simple, and economical method in the preparation of CO_2-selective

separation membranes with enhanced mechanical and separation properties. A mixture of two polymers, which are not covalently bonded, is called as a polymer blend [6]. Many polymers have been used as the blend agents, including polyethylene glycol, poly(amidoamine), pentaerythrityl tetraethylenediamine, etc. With the introduction of blend agents, particularly polyethylene glycol (PEG), most of the resulting membranes possessed improved CO_2 selectivities, sometimes with higher permeabilities [68~71]. Due to the presence of polar moieties in its main chains and high segmental flexibilities, PEG possesses considerable CO_2 gas solubility, thus enhancing the selectivities of resulting blend membranes [72]. Sadeghi et al. revealed that the blend polyvinylchloride (PVC) membranes with PEG of high molecular weight showed better CO_2 permeabilities, as well as ideal selectivities of CO_2/CH_4 and CO_2/N_2, as compared with the blend membranes containing PEG of lower molecular weights. It was also found that the gas permeabilities of PVC/PEG blend membranes rapidly increased with higher PEG concentration [73]. The CO_2 permeability of PEG/Pebax® membrane with 50 wt% of PEG was increased by two fold regarding to that of pristine Pebax®. Despite the unchanged selectivities for CO_2/N_2 and CO_2/CH_4, the separation factors of CO_2/H_2 for PEG/Pebax® were improved from 9 to around 11[74].

9.4 Inorganic Membranes

The earliest application of porous inorganic membranes can date back to 1945, long ahead of the development of synthetic organic membranes [75]. Inorganic membranes are normally classified into two main groups based on their structures, porous and dense (non-porous) inorganic membranes. In addition, porous inorganic membranes show two different structures: asymmetric and symmetric. Generally, there is a limited utilization of dense membranes in industry, due to their low permeability, as compared to the porous inorganic membranes. Therefore, the porous inorganic membranes are currently dominating the commercial market of inorganic membranes [75]. Inorganic membranes are more expensive than organic polymeric membranes; however, they possess some attractive advantages, including thermal stability, wear resistance, stable structure, and chemical inertness [75]. To date, there has been increasing interest on the development of zeolites and carbon molecular sieves as CO_2-selective separation membranes [75, 76].

9.4.1 Zeolites

In the past decades, zeolite membranes have been intensively studied in terms of preparation techniques and separation properties, due to their superior thermal, mechanical, and chemical stability to polymeric membranes. Typically, zeolites

are crystalline inorganic materials with uniform pore and channel structures sizing from 0.3 to 1.0 nm [13]. Therefore, zeolites can work effectively as molecular sieving materials in different gas separation applications. The chemical affinity, electrical charge or polarity of zeolites may function to attract or sort specific gas molecules [3, 77]. In many cases, the chemical affinity and reaction between zeolite and permeating molecules is as important as the properties (e.g. shapes and sizes) of zeolite pores and gas molecules at affecting the separation performances [78~82]. For example, by exchanging MFI zeolite membranes with different cations, it is possible to modify the interaction between membranes and gas species, which results in different selectivities of zeolite membranes [83].

Zeolite membranes can be fabricated by synthesizing a continuous and intergrown polycrystalline zeolite film on a porous support. Similarly to polymeric membranes, in addition to commonly studied flat configuration, zeolite membranes can be fabricated as either tubes or hollow fibers, which show superior gas separation performances [84~87]. Furthermore, at high temperature, the mass transfer within the membranes prepared as tubes or hollow fibers is mainly controlled by zeolite pores, which can retain the good molecular sieving selectivities of zeolite inorganic membranes [87~88], instead of intercrystalline openings in flat configurations [84]. The porous supports (e.g. stainless steel, ceramic, α-alumina, or γ-alumina support tubes or disks or fibres) used in the fabrication of zeolite membranes provide the mechanical strength to zeolitic membranes and enable the growth of thin zeolite selective layers on top [89,90]. However, in the growth of zeolite membranes, the support materials, such as aluminum or silica, may leach out; thereby zeolite crystals nucleate and form inside the support pores. This blocks the inner pores of substrates, resulting in the formation of thicker films with low gas permeances [89,90]. In order to further improve gas permeance as well as selectivity, one of the effective strategies is to choose a suitable substrate. Macroporous stainless-steel nets with the 50 × 50 μm aperture were used as substrates [91,92]. The resulting SAPO-34 membrane possessed a good CO_2 permeance [2.5×10^{-6} mol/(m^2sPa)], with a CO_2/CH_4 selectivity ratio at around 9 [92]. To avoid the growth of zeolite crystals inside the support pores, another way is to mask the support before the synthesis of zeolite membranes. It can reduce the aluminum leaching from the support and promote the intergrowth of extremely thin polycrystalline zeolite layers [89, 93~94].

Among different established strategies in the preparation of zeolite membranes, the widely used methods can be classified into one-step or two-step (multi-step) methods [95]. In the one-step process, both nucleation and growth of zeolite take place on the support surface to yield a continuous and compact zeolite layer [95].

The limitations by using this method include the formation of heterogeneously intergrown films and the depletion of nutrients caused by the preferential growth of zeolite crystals in the bulk solution [94,95]. Therefore, synthesis is repeated for cycles to ensure the well growth of robust and defect-free zeolite layers [94]. However, the produced zeolite membranes usually show unsatisfactory separation permeances [96]. The two-step (multi-step) method is developed with seeding and then followed by crystal growth in hydrothermal treatment. The uniformly seeding of support surface prior to hydrothermal synthesis can enhance the reproducibility of membrane and well intergrowth of zeolite layer. Especially, it is effective for the growth of oriented zeolite membranes with good fluxes [98,99]. However, there is still challenge to completely prevent the formation of non-selective pores, thus the fabrication of high-performance zeolite membranes [77]. There have been several attempts to solve this problem. For instance, the number of intercrylstalline voids could be minimized by post-treatment, e.g. by dip-coating with polymeric silica solution or counter-diffusion chemical vapor deposition modification [100~102]. On the other side, in order to better control the synthesis process, multiple structure-directing agents (SDAs) could be added during both of seed and membrane preparation. Typically, a structure-directing agent (SDA) works as a pore-filling agent and assists the zeolite framework formation. By utilizing multiple SDAs, the prepared SAPO-34 membranes displayed high CO_2 permeance with competitive CO_2/N_2 or CO_2/CH_4 separation selectivities [103,104]. The high fluxes and good selectivities of resulting SAPO-34 membranes, even at elevated pressures or temperatures, could meet the requirements of commercial consideration in natural gas separation [103~105].

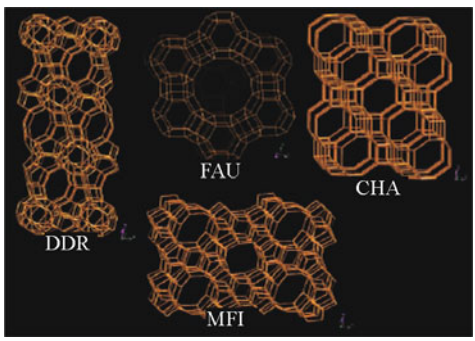

Figure 9.6 Frameworks of some commonly used zeolites [107]

Since Suzuki and co-workers patented the fabrication of zeolite membranes for the first time in 1987 [106], different types of zeolite membranes, including large

pores (e.g. FAU and MOR), medium pores (e.g. MFI, MEL, FER), and small pores (e.g. T, SAPO-34 and DDR), have been reported for their use in gas separation [108~137]. Some frameworks of the zeolites mentioned in this chapter are shown in Figure 9.6 [107]. Gas molecules, such as N_2 (0.36 nm), H_2 (0.29 nm), CO_2 (0.33 nm) and CH_4 (0.38 nm), are smaller than the pore sizes of large- and medium-pore zeolites. Therefore, the CO_2 separations from those gases within these membranes are mainly governed by the competitive adsorption, thus low membrane selectivities are usually observed. Small-pore zeolites possess pore sizes which are similar to the size of CH_4 molecule, but larger than that of CO_2 molecule. For this reason, they are expected to be highly suitable for CO_2/CH_4 separation purpose.

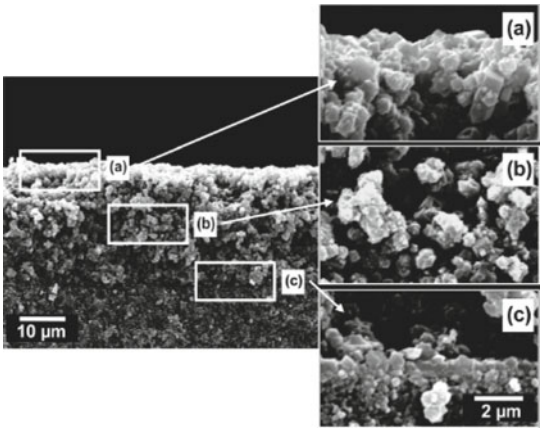

Figure 9.7 Cross-sectional SEM images of a zeolite Y membrane highlighted by three different regions: porous top and middle layer ((a) and (b)) with a thickness of 25 μm, and dense layer (c) present on the alumina support with a thickness 350~600 nm [108]

FAU-type zeolite has a three dimensional channel system with pores of 12 T-atoms and a pore opening of 0.73 nm. Zeolite Y, a typical FAU-type zeolite, shows non-steric hindrance for the transport of molecules, i.e. CO_2, CH_4, H_2 or N_2, into the pores, because of large window size [108]. However, it is found that CO_2 molecule preferentially interacts with the aluminosilicate framework and extraframework cations of zeolite Y [108]. Thus, by feeding the gas mixtures, e.g. CO_2 and N_2 or CH_4, CO_2 preferentially permeates through zeolite Y by surface diffusion; whereas N_2 or CH_4 is excluded from the FAU pores because of CO_2 adsorption and pore constriction [108~110]. Separation temperatures and extra-framework cations affect the CO_2 selectivities of zeolite Y membranes. The selectivities of CO_2/N_2 decreased at higher temperatures and increased when

the membranes were ion-exchanged with some alkali cations (e.g. Cs^+, Rb^+, K^+) [109,110, 113~118]. Gas permeation in zeolite membranes can be improved by reducing membrane thickness or support thickness. However, these may increase the concentration of membrane defects or decrease the mechanical strength of membranes. White et al. successfully synthesized zeolite Y membranes, in which an ultrathin dense membrane with 350~600 nm thickness was covered by a 25-μm thick porous zeolite layer (Figure 9.7) [108]. The thin layer determined the overall transport properties, which resulted in a dramatically higher permeance than that of 2-μm uniform zeolite membranes. The CO_2/N_2 separation selectivities of fabricated zeolite Y membranes were above 500 [108].

MFI zeolite possesses smaller zeolitic pore size (0.55nm) than that of FAU [119]. Similarly as FAU-type zeolite, molecular sieving effect does not play a significant role in controlling the separations of CO_2/N_2 and CO_2/CH_4 [119]. The CO_2 permeation through ZSM-5 (MFI) membranes is suggested to be mainly governed by both mechanisms of adsorption/surface diffusion and the activated micropore diffusion; whilst the transport of N_2 may be only governed by the activated micropore diffusion [100]. The gas permeances decreased at higher pressure, despite an increase of CO_2/CH_4 and CO_2/N_2 selectivities which was caused by the reduced competitive adsorption [100, 120]. Interestingly, Shin et al. reported that the separation factors of CO_2/N_2 for Na-ZSM-5 membranes were nearly independent on the moisture in the feed [100]. However, after ion-exchange, the CO_2/H_2 separation factors of Ba-ZSM-5 membranes increased when the moisture was added to the feed, which was ascribed to "sorption enhanced separation" [83]. The presence of counter ions in the pores of ZSM-5 membranes reduced the effective pore size, thus lower diffusivity, as compared with silicalite-1 (MFI) membranes [83]. When ZSM-5 lattice contained the ions with larger effective radius, these zeolite membranes exhibited lower gas permeabilities but higher CO_2 selectivities. For example, Ba-ZSM-5 exhibited lower gas (H_2, CO_2, N_2) permeabilities and higher separation factors of CO_2/H_2, as compared with other types of membranes (e.g. silicalite-1, Na-ZSM-5 and Li-ZSM-5). The pores of B-ZSM-5, which are smaller than the channels in Na-ZSM-5, were blocked by CO_2 in gas separation [119]. In addition, the effect of weaker acidity arising from B-ZSM-5 favored the CO_2 adsorption. As a result, the better separation performances were observed by utilizing B-ZSM-5 than the use of Na-ZSM-5 [119]. ZSM-5 membranes with lower Si/Al ratio were suggested to likely possess much higher separation factors; however more work is required [83].

The abbreviation DD3R is referred to all-silica DDR zeolite, which consists of cages connecting 8-ring window openings of 0.36 × 0.44 nm [101, 121]. The pore

diameter of DD3R is close to the molecular sizes of light hydrocarbons and CO_2 [122]. The permeation of light gases through the DDR-type zeolite membranes is governed by their molecular sizes; whilst the adsorption affinity of CO_2 to DDR zeolites strongly affects the membrane permeance and selectivity [122]. Tomita et al. reported for the first time that the CO_2/CH_4 selectivities of DDR-type zeolite membranes were 220 and 100 at 301 K and 373 K with a pressure drop of 0.5 MPa, respectively; and the corresponding CO_2 permeances were 7×10^{-8} and 4×10^{-8} mol/(m^2sPa) [123]. The CO_2/CH_4 separation selectivities and CO_2 permeabilities of DDR-type zeolite membranes decreased as the feed pressures increased [122,123]. Bergh and co-workers investigated the permeation of different gases through their prepared DD3R membranes over a temperature range of 220~773 K and a feed pressure of 101~500 kPa [124~126]. There were excellent performances of membranes, both in selectivity and permeability, exhibited, which were over 4000 and 1.0×10^{-7} mol/(m^2sPa) at 101 kPa and 225 K [126]. The separation performances of DDR membranes were maintained after several months of testing, including continuous testing for ~5 days at high temperature and numerous (>10) full temperature cycles [124]. By considering their long-term stability and high CO_2 selectivities/fluxes, the DD3R membranes were strongly suggested with potential for high-temperature CO_2 separation [124].

SAPO-34 structure is a silicoaluminophosphate zeolite with the composition of $Si_xAl_yP_zO_2$, where $x = 0.01 – 0.98$, $y = 0.01 – 0.60$, and $z = 0.01 – 0.52$ [127]. The pore size of SAPO-34 (0.38 nm) is similar to the molecular sizes of CH_4 or N_2 but larger than that of CO_2; hence the competitive adsorption and the difference in diffusivities govern CO_2 separation [128]. The Si/Al ratio of SAPO-34 zeolite significantly affected CO_2 and CH_4 adsorption properties [128], thus separation performances. In a SAPO-34 membrane, as the feed pressures were increased, both of CO_2 fluxes and CO_2/CH_4 separation selectivities increased. The separation selectivities decreased as temperature increased, partially due to the preferential adsorption of CO_2 [129,130]. Li et al. reported the CO_2/CH_4 selectivity of SAPO-34 with a Si/Al gel ratio of 0.15 was 170 at 295 K and a pressure drop of 140 kPa. The corresponding CO_2 permeance was 1.2×10^{-7} mol/(m^2sPa) [130]. The use of SAPO-34 membranes could achieve an effective separation between CO_2 and CH_4 at or near industrial conditions [130]. The ion exchange of H–SAPO-34 membranes with different cations, e.g. Li^+, Na^+, K^+, NH^{4+} and Cu^{2+}, increased the ideal separation factors of CO_2/CH_4 up to 60% [131]. However, the steric hindrance from large cations in lattice caused a decrease in CO_2 permeances of membranes [131].

In addition to those above-mentioned zeolites, there are other types of zeolite membranes reported in the literature. For example, zeolite T is an intergrowth-type

zeolite of erionite and offretite, with pore sizes 0.36 nm × 0.51 nm and 0.67 nm × 0.68 nm [122]. Cui et al. reported that the selectivities of T-type zeolite membranes decreased with increasing operation temperatures. For instance, their selectivities for CO_2/N_2 and CO_2/CH_4 pairs were 107 and 400 at 308 K, respectively. At 473 K, the CO_2/N_2 and CO_2/CH_4 selectivities dropped to 20 and 52, respectively [132]. Titanosilicate ETS-10 is characterized with three-dimensional 12-ring pore system (0.76 × 0.49 nm) [133,134]. ETS-10 membranes could separate CO_2 from binary mixtures of CO_2 and N_2 or H_2, due to the CO_2 preferential adsorption and diffusion. The maximum separation factors for CO_2/N_2 were between 7 and 10 in the pressure range of 6~22 bar at room temperature [135].

It is noted that zeolite membranes have been mostly tested at low feed pressures for CO_2 separation; however, the feed pressure might be as high as 7 MPa in industrial applications, such as natural gas processing [122]. Until now, several types of zeolite membranes have been studied at high feed pressures. For example, by using SAPO-34 membranes at a pressure drop of 3 MPa, Li et al. found that the separation selectivity of CO_2/CH_4 was ~60 at 295 K [129]. At 7 MPa, the CO_2/CH_4 separation selectivity of SAPO-34 membrane was 100 at 295 K [129]. Its permeances and selectivities were constant for a week by feeding 75% CO_2 at 5.7 MPa [128]. Himeno et al. reported that the DDR-type zeolite membranes retained high CO_2/CH_4 selectivity and CO_2 permeance, which were 80 and 1×10^{-7} mol/(m^{-2} s^{-1} Pa^{-1}), respectively, at the pressures up to 3.0 MPa [122].

On the other side, natural gas and biogases contain moinsture and impurities, such as H_2O, N_2, H_2S, and hydrocarbons, in addition to CO_2. Zeolite membranes have shown a great potential at the CO_2 separation from CH_4 or N_2; however most of studies only foucus on the pure gas mixtures so far. In a few studies, the effect of impurities on the CO_2 separation performances of zeolite membranes was investigaed. Gu et al. reported the NaY membrane exhibited a CO_2 separation factor of 31.2 at room temperature by feeding dry mixture of equimolar CO_2 and N_2 [115]. At the temperature above 110 °C, the addition of water vapor to gas mixture significantly increased the CO_2 selectivity, whereas it resulted in a decrease of CO_2 permeances [115]. The DDR-type zeolite membranes were only slightly affected by water vapor. Their CO_2 permeance and CO_2/CH_4 selectivity with saturated water vapor at 298 K remained at 1.1×10^{-7} mol m^{-2} s^{-1} Pa^{-1} and 100, respectively [122]. With the use of SAPO-34 membranes, the CO_2 permeance decreased with increasing humidity; whereas the CO_2/CH_4 selectivity was stable after 12-day exposure to 170 ppm water vapor [136]. The presence of hydrocarbons in feed caused a reduction in both of permeances and selectivities of SAPO-34 membranes, in particular n-C_4H_{10} hydrocarbon [137]. However, Li et al. reported that

their permeances and selectivities were not permanently reduced by impurities, which could be restored after removing the impurities from the feed or calcinating membranes [137].

9.4.2 Carbon

The concept of carbon membranes or films for gas separations was firstly reported in 1970s [138]. The significant development of carbon membranes started after the successful preparation of crack-free molecular sieving hollow fiber carbon membranes via carbonization of cellulose hollow fibers [139~141]. Based on the structures, carbon membranes can be categorized into two main types: supported and unsupported membranes [76]. When compared with the low mechanical strength and gas permeance of unsupported carbon membranes [13], the supported membranes are more suitable in large-scale industrial application [142]. In terms of commercial implementation, a new honeycomb configuration of carbon molecular sieve membranes was reported by Lagorsse et al. [143]. There was great potential to scale up the synthesis of those carbon membranes with uniform and reproducible properties, by using flat membranes as starting precursors [143].

In general, carbon membranes used for gas separation are fabricated by pyrolyzing thermosetting polymers, i.e. polyimides, poly(furfuryl alcohol), cellulose, poly(vinylidene chloride), phenol formaldehyde, or different biomasses [75, 144,145]. In the fabrication of carbon membranes, there are several factors which determine their separation performances, including the membrane preparation method; carbonization processes; and selection of precursor polymers [146]. For instance, previous research suggested that the intermediate stage, in which the polymer precursors start decomposition but the carbon structures have not been formed yet, be important for the pore formation of carbon membranes as well as the membrane separation properties [147]. The final pyrolysis temperatures also affected the membrane microstructures, thus the performances of carbon membranes [148]. When heating at the same temperature, the atmosphere, e.g. vacuum, nitrogen, argon, helium, influenced the porous structures of carbon membranes and subsequently membrane gas separation performances [149,150]. The pyrolysis under nitrogen atmosphere resulted in the formation of carbon films with good gas permeation; whereas the pyrolysis under argon led to the fabrication of carbon membranes with high selectivities [149,150].

In addition to preparation and carbonization processes, the use of different precursors affects the gas separation properties of resulting carbon membranes, due to the different thermal degradation mechanisms of polymeric precursors and the microstructures of derived carbon membranes [151]. As an ideal precursor candidate,

no defects or pinholes should be formed on the resulting carbon membrane surface after its pyrolysis [75]. Furthermore, the properties of selected precursor polymers affect the preparation simplicity of membranes, which is essential for scale-up. The cost of precursors should be carefully considered for commercial feasibility. Until now, there has been great effort continuously contributing to develop better precursors. Some precursor polymers have been successively developed, such as polypyrrolone, lignin, heteropolyacid, poly(phenylene oxide), resorcinol/formaldehyde, ion-exchanged sulfonated poly(aryl ether ketone), etc. [152~158]. Table 9.1 summarizes the recent development of carbon membranes for CO_2 separation, including the types of precursors and their CO_2 separation performances.

Polyimides (PIs) have been proven as good candidates to form carbon membranes with superior gas separation performances [159,160]. However, most of the PIs are expensive and some are only synthesized on a laboratory scale, such as 6FDA-durene [147, 161]. Therefore, the commercially available polyimides, such as Kapton, Matrimid, and P84, are preferred as the precursors in the fabrication of carbon membranes [146, 159, 161~163]. The pretreatment of PI precursors [162~165], such as thermal treatment, chemical crosslinking and solvent pretreatment, can vary the separation performances of resulting carbon membranes. In Xiao's work, the bromination of commercial polyimide could increase the polymer chain rigidity and maintain the membrane morphology during pyrolysis [146]. With the use of bromination pretreatment, the resulting carbon membranes showed higher gas permeabilities and selectivities as compared with untreated carbon membranes [146]. With the pretreatment of precursor by cesium carbonate, the cesium (Cs)-incorporated carbon membranes had superior CO_2 permeances and separation factors under humid condition, ascribed to the improved hydrophilicity and the presence of larger carbon pores [166]. However, the high cost and limited number of PI commercial species are still the main obstacles in the development of PI-derived carbon membranes.

Table 9.1 Summary of recent development in carbon membranes for CO_2 separation.

Precursor	Modification of Precursor	Separation Performances	Reference
Polymide (Matrimid)	Cross-linking pretreatment by p-xylenediamine in methanol	CO_2: 319 ~ 609 Barrer CO_2/ CH_4: 56 ~ 78 CO_2/N_2: 17 ~ 23	[163]
Polymide (Matrimid)		CO_2: 1808 ~ 499 Barrer CO_2/ CH_4: 22 ~ 89	[161]

Polymide (Matrimid; P84)	Nonsolvent pretreatment of precusor(methanol, ethanol, 1-propanol, and 1-butanol)	CO_2: 199 ~ 565 Barrer CO_2/ CH_4: 61~ 78 CO_2/ N_2: 23 ~ 31	[162]
Polymide (Matrimid)	Pretreatment of precursor by bromination	CO_2: 402 ~ 2900 Barrer CO_2/ CH_4: 25 ~ 63	[146]
Polyimide [bis(phenyl) fluorene-based cardo polyimide]	Addition of cesium carbonate	CO_2: 0.1 ~ 20 × 10^{-11} cm^3(STP) ·s^{-1}·m^{-2}·Pa^{-1} CO_2/ N_2: 1.5 ~ 47	[166]
Polyimide	Addition of nano-sized ZSM-5	CO_2: 680 ~ 11501 Barrer CO_2/ N_2: 32 ~ 116	[170]
Cellulose		CO_2: 11 ~ 480 Barrer	[168]
Cellulose	Addition of metal additives	CO_2: 14 ~ 310 Barrer	[167]
Polyetherimide	Addition of multi-wall carbon nanotubes (MWCNTs) or PVP	CO_2: 63.8 Barrer (PVP) or 1463.0 Barrer (MWCNTs) CO_2/N_2 13.7: (PVP) or 48.8 (MWCNTs)	[171]
Phenol–formaldehyde resin		CO_2: 3.03 ~ 5.28 ×10^{-7} cm^3 cm^{-2} s^{-1} $cmHg^{-1}$ CO_2/CH_4: 1.8 ~ 4.8	[142]
Phenol–formaldehyde resin	Addition of poly(ethylene glycol) (PEG)	CO_2: 1.1 ~ 3 ×10^{-10} mol m^{-2} s^{-1} Pa^{-1} CO_2/ CH_4: 18.4 ~ 11.6	[172]
Phenol–formaldehyde resin	Addition of carbon molecular sieve particles	CO_2: 0.84 ~ 68.22×10^{-10} mol m^{-2} s^{-1} Pa^{-1} CO_2/ CH_4: 0.55 ~ 17.86	[173]
Phenol–formaldehyde resin	Sulfonation	CO_2: 800 ~ 0.12 GPU CO_2/ CH_4: 22 ~ 44	[169]
Poly(phthalazinone ether sulfone ketone)	—	CO_2: 1.2 ~ 86.1 Barrer CO_2/ CH_4: 2.3 ~ 213.8	[174]
Poly(phthalazinone ether sulfone)	—	CO_2: 3.3 ~ 439.9 Barrer CO_2/ CH_4: 6.1~16.3	[151]
Poly(phthalazinone ether sulfone ketone)	Addition of polyvinylpyrrolidone (PVP) or zeolite (ZSM-5)	CO_2: 24.39 ~ 791.50 Barrer CO_2/ N_2: 12.0 ~171.1	[175]
Poly(2,6-dimethyl-1,4-phenylene oxide)	Addition of polyvinylpyrrolidone (PVP)	CO_2: 1~20 × 10^{-9} mol m^{-2} s^{-1} Pa^{-1} CO_2/ CH_4: 0 ~ 70	[176]
Phenolic resin	Addition of zeolite NaA (250 nm)	CO_2: 3.39 ~ 5.68 × 10^{-7} mol m^{-2} s^{-1} Pa^{-1} CO_2/ N_2: 6.04 CO_2/ CH_4: 7.78 ~ 28.4	[177,178]
Phenolic resin	Addition of nano-sized zeolite NaA	CO_2: 13 ~ 19 × 10^{-10} mol m^{-2} s^{-1} Pa^{-1} CO_2/ N_2: 27.9 ~159	[179]
Polyfurfuryl alcohol	Addition of nano-sized zeolite L	CO_2: 572 ~ 594 Barrer CO_2/ N_2: 3.32 ~ 20.43 CO_2/ CH_4: 4.21 ~ 35.75	[180]

Cellulosic materials are another type of precursor materials; their low cost and catalyst-free carbonization process make them more economically attractive in the fabrication of carbon membranes. Stable gas performance was lasting for about 7 days with the use of carbon membranes made from pure cellulosic materials [167]. The incorporation of metal oxides into the cellulosic materials increased the micropore volumes in carbon matrix and improved the electronic interactions between carbon membranes and CO_2, which subsequently enhanced the CO_2 transport [167,168]. The CO_2/CH_4 separation performances of carbon membranes derived from the cellulosic materials, which were modified with Fe, Cu, Ag, Ca nitrates or oxides, were above Robeson's upper bound [167,168].

Phenolic resins present suitable features as the precursors for making carbon membranes. Wei et al. utilized one coating – pyrolysis cycle, which can avoid complex and unpractical multicoating processes, to carbonize the porous resin support which is coated by novolac phenol–formaldehyde resin and hexamine [142]. The resulting carbon membranes exhibited the selectivities of CO_2/CH_4 in the range of 1.8 ~ 4.8 [142]. By pyrolyzing phenol formaldehyde resin (PF)/ sulfonated phenol formaldehyde resin (SPF), the fabricated carbon membranes exhibited attractive separation performances, which were 800 GPU and 27 for CO_2 permeance and CO_2/CH_4 ideal selectivity at 35 °C and 1 atm [169]. This was attributed to the presence of sulfonic acid groups which were linked to thermostable polymer chains acting as "bonded templates" to CO_2 molecules [169].

Poly(phthalazinone ether sulfone ketone) (PPESK) possesses bulky sulfone and ketone segments, as well as a rigid phthalazinone structure in their frameworks [174]. These feature units can prevent the intersegmental packing and segmental mobility during carbonization, which leads to the formation of more porous or less compact carbon membranes [181]. Most importantly, PPESK is available at a lower cost when compared to other polymer precursors, such as polyimide. Zhang et al. reported that the maximum CO_2/N_2 ideal separation factor of PPESK-derived carbon membranes was 213.8 and the CO_2 permeability was 34.2 Barrer [174]. The addition of thermally labile polymers into PPESK, such as polyvinylpyrrolidone (PVP), could form porous structures and in turn change the separation performances [175]. For instance, the carbon membranes fabricated from the blend of PVP and PPESK polymer precursors showed dramatically higher CO_2 permeability (792 Barrer) with a lower CO_2/N_2 selectivity (41) at 0.1 MPa and 30 °C, when compared with 85 Barrer and 125 for the permeability and separation factor of PPESK-derived carbon membranes [175]. Poly(phthalazinone ether sulfone) (PPES) is a special member of PPESK polymers, which possess large sulfone and rigid phthalazinone units [151]. For the carbon membranes prepared by pyrolyzing PPES at 650 °C,

the CO_2 and N_2 gas permeabilities were 439.90 and 26.95 Barrer, respectively, accompanied with the CO_2/N_2 selectivity of 16.3. In particular, PPES is the cheapest in the group of PPESK polymers [151]; thereby it is one of the promising low-cost precursors for the fabrication of carbon membranes.

As mentioned, the blend of polymer precursors with foreign additives has been suggested as an effective way to modify the gas permeation properties of resulting carbon membranes. These additives include organic materials, e.g. poly(vinyl butyral), poly(ethylene glycol) and polyvinylpyrrolidone; and inorganic particulates, i.e. metals, metal oxides and zeolite [158, 172, 175,176]. In particular, different zeolites, such as zeolite L, A and ZSM-5, have been utilized as fillers in carbon membranes, which can create a synergic effect and improve the membrane gas separation properties. For example, a dramatic increase in CO_2 permeabilities was observed with the incorporation of ZSM-5 into carbon membranes, despite a decrease in their CO_2/N_2 selectivies [170]. The increase in the CO_2 permeabilities was attributed to the preferential adsorption of CO_2 molecules onto the pore walls of zeolite [182,183]. Therefore, the mechanisms governing the gas transport inside ZSM-5/carbon composite membranes include both molecular sieving and selective adsorption [175]. A similar result was also reported with the use of zeolite A/carbon composite membranes [178,179]. Zeolite L/carbon composite materials exhibited the improved CO_2 separation performances for CO_2/CH_4 gas pairs, which could exceed the Robson's trade-off line (2008) [180]. However, the mechanism of CO_2 separation inside zeolite/carbon composite membranes is still not well understood. Hence, more studies are required in the future, especially at the effects of particle sizes, interfaces between zeolite/carbon, and separation conditions on the membrane separation, etc.

9.5 Mixed-Matrix Membranes

Mixed-matrix membranes (MMMs) have shown promising potential to enhance the inherent characteristics and separation properties of polymeric membranes [9]. Typically, MMMs consist of inorganic materials (e.g. zeolite, silica [184], clay [185], carbon, metal oxide, etc.) in the form of micro-sized or nano-sized particles dispersing inside the continuous polymeric matrix, as shown in Figure 9.8 [9]. By using two materials with different separation characteristics, including fluxes and selectivities, there is a feasibility to design a CO_2-selective separation membrane with superior separation performances. Moreover, the incorporation of inorganic particles into polymeric membranes can be a relatively easy modification strategy to fabricate large-surface separation membranes, especially when compared with inorganic membranes, which are normally brittle and difficult for

scale-up [15]. The incorporation of inorganic fillers can also improve the physical, thermal, and mechanical properties of polymer matrix [15]. However, there is still continuous research conducting to reduce the cost of MMMs and overcome the difficulties in the large-scale manufacturing [9]. To fabricate a high-performance CO_2-selective separation membrane, it is important to select suitable polymer matrixes and inorganic fillers; to determine sizes of inorganic fillers; to eliminate the sedimentation and agglomeration of particles in membrane fabrication; and to retain a good interfacial interaction between polymer and fillers, etc [9].

Figure 9.8 Schematic diagram of a mixed matrix membrane (MMM) [9].

9.5.1 Zeolite fillers

In 1970s, Paul and co-workers observed a delayed diffusion time lag effect for CO_2 and CH_4 with the use of 5A zeolite/polydimethyl siloxane MMMs for the first time [186]. The separation between CO_2 and H_2 has been successfully demonstrated by UOP LLC in the mid-1980s by utilizing silicalite/cellulose acetate MMMs [187]. Afterwards, a large number of studies focus on the fabrication and use of CO_2-selective MMMs by combining different types of zeolites and polymers [188,193].

In the fabrication of MMMs, the effect of particle sizes has been considered as an important factor affecting the separation performances of resulting membranes [194,195]. In the most of early studies relating to zeolite/polymer MMMs, commercially available large particles were used as inorganic fillers. Significantly improved gas permeability was observed; however, the selectivity decreased [194]. Especially, in the MMMs with higher zeolite loadings, the influence of particle sizes on permeabilities is more significant [194]. With the incorporation of smaller particles, a better interfacial contact between polymers and particles is expected to improve the separation performances of MMMs [9, 196]. In addition, polymeric membranes are usually shaped into asymmetric hollow fibers with a thin (e.g. 100 nm) selective layer for practical applications [197]. Clearly, smaller particles, such as nanoparticles, are more suitable for use in the fabrication of MMMs [197]. In recent years, several studies demonstrated that the MMMs containing well-dispersed "flakes" showed significantly enhanced separation performances [198~200]. As shown in Figure 9.9 [193], when the "flakes" were parallel to the membrane skin, especially

the pores facing to the direction of streams, the simulation work revealed that the separation performances of resulting MMMs could exceed Robeson's upper bound with the addition of a small amount of well-dispersed sieving "flakes" [15, 201]. The selective-flake /polymer MMMs with the addition of 10 wt% of layered AlPO showed improved CO_2 selectivities over other gases, e.g. N_2, O_2, and CH_4. Tsapatsis and co-workers attributed this to the molecular sieving property of AlPO layers with high aspect ratio [193].

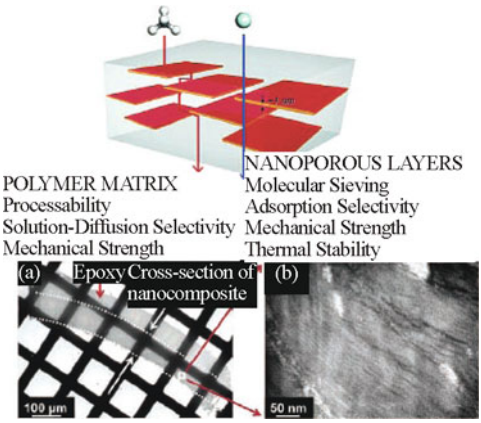

Figure 9.9 Schematic of gas transport through selective-flake/polymer membranes. TEM images of MMMs: (a) a cross-section of the composite membrane embedded in epoxy and (b) region marked in (a) revealing intercalated layers [193]

The selection of zeolite types is another important factor to determine the properties of zeolite-polymer MMMs. For example, due to the molecular sieving effect, the movement of large gas molecules, such as CH_4, is hindered by the pores of silicalite (MFI). Hence, with the incorporation of silicalites into polydimethyl siloxane, the methane permeability of resulting MMMs decreased [202]. The CO_2 permeability remained almost unchanged ascribed to the combined effect of sorption onto the crystal surface and the permeation through the host matrix [202]. However, the incorporation of NaX (FAU) zeolite into the polymeric matrix lowered the permeability of all gas species without the effect of molecular sieving, which was attributed to the polymer chains plugging in the pores of NaX. In the MMMs with NaA (LTA), polymers did not penetrate into zeolite channels, but simply enveloped around NaA crystals. Due to the high affinity of CO_2 to zeolite walls, there was a decay in the permeabilities of NaA-incorporated MMMs, as compared with the pure polymer [202].

It is known that the separation properties, including selectivities and permeabilities of MMMs, are strongly affected by the presence of interfacial voids or defects, which are formed from a poor interaction between organic and inorganic phases. There have been some studies illustrating those in detail, in which the interfacial interactions between inorganic and organic phases can be classified into “sieve-in-a-cage”, “leaky interface”, and “matrix rigidificaiton” morphologies [8,9, 203~205]. Post-treatment has been suggested as a way to repair interfacial defects, such as the use of silicon rubber coating on top of MMMs [206]. However, the post-treatment may cause a decrease in the CO_2 permeances of MMMs. Until now, there have been some other strategies developed to eliminate those unselective gaps or defects and fabricate high-performance MMMs [15, 192, 204,205, 207,208]. For instance, surface modification on zeolites can be a way to avoid the interfacial defects between zeolites and polymers. One of the examples is to improve the hydrophobicity of zeolite surfaces via the linking of surface hydroxyls with hydrophobic functional groups. Hollow fibers with the incorporation of Grignard-treated zeolites HSSZ-13 showed 17% and 25% enhancement in the separation factors of CO_2/CH_4 in a pure gas pair and a mixed gas, respectively [209]. Until now, more interest has been attracted at the use of coupling agent to modify the surface properties of zeolite fillers, especially silane coupling agents, such as (3-aminopropyl)-triethoxy silane, N-β-(aminoethyl)-γ-aminopropyltrimethyoxy silane, (γ-glycidyloxypropyl)-trimethoxy silane, (3-aminopropyl)-dimethylethoxy silane and so on [192, 210~212]. Ismail and co-workers used a novel Dynasylan Ameo silane agent to successfully improve the adhesion between polymer and zeolite surfaces [206]. The CO_2/CH_4 selectivity of resulting MMMs was improved by over 4 fold; however, the CO_2 gas permeation was lower [206]. Similar findings were also reported in other studies, which were ascribed to the rigidification of polymer chains and partial pore blockage of zeolites [212,213]. The addition of large pore-size zeolites in MMMs may offset the negative effect arising from the pore blockage of zeolites [212]. However, in some cases, the modification of zeolites with silane agents could not effectively and completely eliminate unselective voids or improve the compatibility between zeolites and polymers, thus no enhancement in the selectivities of MMMs [206, 209]. Other drawbacks for the use of coupling agents include their limited utilization to specific pairs of polymers and zeolites, fabrication complexity and extra cost for scale-up.

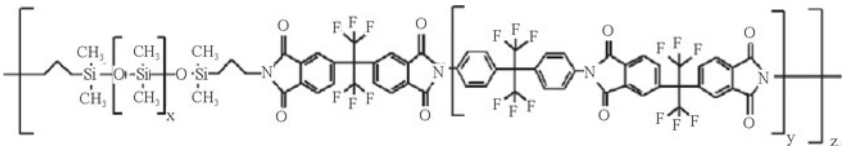

Figure 9.10 Structure of poly(imide siloxane) copolymer matrix [191]

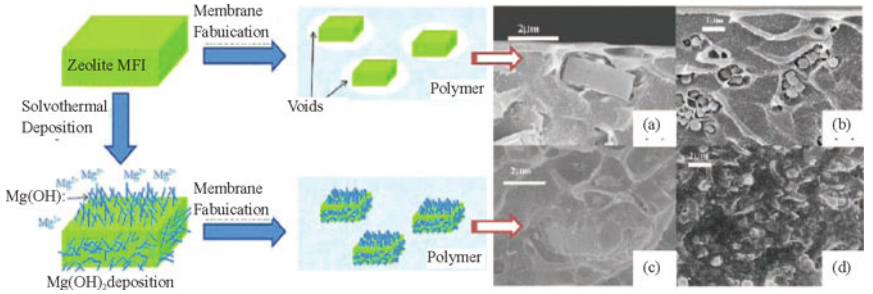

Figure 9.11 Facile high-yield solvothermal deposition of zeolite crystals for mixed matrix membrane fabrication. Cross-sectional SEM images of MFI-poly(etherimide) MMMs. (a) 5 μm untreated MFI, (b) 300 nm untreated MFI, (c) 5 μm solvothermally treated MFI, and (d) 300 nm solvothermally treated MFI [214]

In recent years, there has been some new progress reported in the literature to prevent the formation of voids between zeolites and polymers. For example, Pechar et al. incorporated zeolites L into a block copolymer poly(imide siloxane) (Figure 9.10), which contains both flexible polydimethyl siloxane (PDMS) and rigid polyimide (PI) portions, to form defect-free MMMs [191]. The flexible PDMS could retain a good interfacial contact with zeolite surface and the rigid PI provided better selectivity than PDMS [191]. However, a loss of separation performance was observed for the resulting MMMs, which was attributed to the blocking of zeolite pores by PDMS chains [191]. More recently, Bae and co-workers reported that the separation performances of MMMs by adding the $Mg(OH)_2$-deposited MFI, which was prepared via a facile and inexpensive solvothermal process (Figure 9.11) [214], transcended the Robeson's upper bound. In particular, the CO_2 permeability and CO_2/CH_4 selectivity of poly(etherimide) MMMs with 20 wt% modified-MFI were 57% and 13% greater than those of pure membrane [214]. Hudiono and co-workers fabricated a novel MMM composed of three components, including polymerizable room-temperature ionic liquids (poly(RTIL)), room-temperature ionic liquids (RTIL) and zeolite materials (SAPO-34). The existence

of RTIL component enhanced the interfacial adhesion between inorganic zeolite surface and organic polymer matrix. However, The CO_2/CH_4 selectivity of three-component SAPO-34-RTIL-poly(RTIL) MMM was slightly lower, as compared to that of two-component SAPO-34-poly(RTIL) MMM [215].

9.5.2 Carbon fillers

In addition to zeolites, carbon molecular sieves (CMS) have been used as inorganic fillers in MMMs. The attractive properties of CMS, such as large surface area and well-defined pore structure, show great potential to enhance the gas separation performances of resulting MMMs by introducing a molecular sieving effect [8]. As compared with zeolite molecular sieves, CMS particles seemingly provide a better affinity to polymers, thus a good polymer-filler relationship [216]. Most importantly, the permeation properties of CMS particles can be varied by modifying the pyrolysis protocol, suggesting the good adaptability for different gas separation purposes (Table 9.2) [216]. Activated carbon (AC) was also incorporated into polymer matrix as an inorganic filler in the fabrication of MMMs. For instance, Marchese et al. filled AC into acrylonitrile-butadiene-styrene (ABS) copolymer [217]. The resulting AC-ABS membrane exhibited high separation performance for CO_2/CH_4, indicating there was a good contact between AC and ABS matrix [217]. Similarly, AC was introduced into poly(ether-block-amide) (PEBAX-2533) by solvent evaporation. The CO_2 permeance of 50%-loaded AC-PEBX-2533 was 1.6-fold higher than that of plain polymer membrane, without any significant reduction in CO_2/CH_4 selectivity at the 10 kg/cm^2 feed pressure [218]. The blend of benzylamine-modified C_{60} fullerenes within polyimide (PI) retained the selectivities of resulting membranes, despite lower gas permeabilities which were caused by the polymer rigidification [219].

Very recently, the incorporation of carbon nanotubes (CNTs) in polymeric membranes for gas separation has gained intensive attention. Early MD atomic simulations revealed the fast gas transport rates in CNTs, which was attributed to the smoothness of inner surfaces of atomic-scale pores [213, 220~225]. In particular, the single-walled carbon nanotubes (SWCNT) with smaller pore opening (4 ~ 12 Å), may be size selective for gas mixtures. There are several strategies to make CNTs/polymer composite membranes, including solution mixing, melt blending, melt spinning and in situ polymerization [226]. Similarly to zeolite-filled MMMs, it is important to achieve the uniform dispersion of CNTs throughout polymer matrix as well as the good adhesion between CNTs and polymers. By finely dispersing multi-walled carbon nanotubes (MWCNTs) with the use of surfactants, Liu and co-workers prepared MMMs with a strong interfacial interaction between MWCNTs and polyetherimide throughout the matrix [226]. Organic-functionalized CNTs (i.e. COOH-CNTs) were found more

uniformly dispersed in brominated poly(2,6-diphenyl-1,4-phenylene oxide). In particular, the polymer chains could pack tightly on the surfaces of modified-CNTs so that the formation of unselective gaps could be minimized [196]. In the fabrication of high-performance CNTs-polymer MMMs, one of the crucial issues is to align the pores of CNTs vertically relative to the penetrant stream [15]. However, some synthetic methods, such as chemical vapor deposition, are expensive, time-consuming, and difficult for large-scale fabrication [227]. A combination of self-assembly and filtration methods was reported for the first time by Li et al, which was a simple, fast, and practical technique to vertically align CNTs on a porous support (Figure 9.12). Most importantly, this work provided the first experimental data to demonstrate the transport of CO_2/CH_4 gas mixtures through CNTs membranes [227].

Table 9.2 Permeation properties of carbon molecular sieve films pyrolyzed from flat Matrimid® 5218 films [216]

	Pyrolysis conditions (vacuum)	Permeability (Barrer)		Permselectivity
		CO_2	CH_4	CO_2 / CH_4
Carbon Molecular Sieve	550 °C (2h)	1250	20	63
	550 °C (8h)	375	4.2	89
	800 °C (2h)	43.5	0.21	200

Different combinations of CNTs and polymers have been studied for CO_2 separation. The addition of acid-treated open-ended single-walled carbon nanotubes (SWCNTs) in poly(imide siloxane) increased the gas permeabilities of CO_2 and CH4 [228]. The incorporation of CNTs in brominated poly(2,6-diphenyl-1,4-phenylene oxide) ($BPPO_{dp}$) increased the CO_2 permeability with a similar CO_2/N_2 selectivity, as compared to those of pure $BPPO_{dp}$ membranes [196, 229]. In Murali's work, the CO_2/N_2 selectivity of cross-linked Pebax MMMs filled with 2% MWCNTs was 83.2 at 1 MPa feed pressure, as compared to 54.9 for cross-linked Pebax membranes. The resulting MWCNTs/Pebax membranes show great potential in the practical separations, such as power plants, chemical production, welding and medical industries [230].

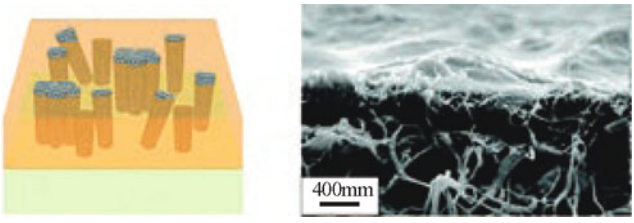

Figure 9.12 Scheme and side-view SEM image of aligned nanotube/PSF nanocomposite membrane after spin-coating [227]

9.5.3 Silica fillers

The addition of silica particles into polymer matrix can affect the inherent properties and separation performances, including selectivity and permeance, of resulting MMMs [15, 196, 231]. First of all, the presence of silica particles may increase the distance between polymer chains and limit the chain packing [232~234]. The silica particles in MMMs can be considered as physical barriers in the polymers, which affect the transport of CO_2 through membranes [235]. Furthermore, the OH groups on silica particles may interact with CO_2 polar gas, thus enhancing gas solubility inside the composite membranes [236]. It is common that the weak interaction between the silica and polymer may cause the formation of voids between inorganic and organic materials, which in turn results in an abruptly higher permeability [237]. For instance, the silica/$BPPO_{dp}$ membranes were observed with greatly enhanced CO_2 permeabilities, as compared to the pure $BPPO_{dp}$ membranes, which were ascribed to the presence of nanogaps surrounding the nanoparticles [196, 229]. The polysulfone (PSF) MMMs with high fumed silica loading showed significantly greater gas permeabilities, which was ascribed to an increase in free volume of parent polymer [237]. Sadeghi et al. reported that the CO_2 permeability and CO_2/N_2 selectivity of polybenzimidazole MMMs with 20 wt% silica nanoparticles were 3.5 and 19.4 times higher than those of plain membranes [231]. The MMMs with the addition of trimethylsilyl-modified silica showed lower CO_2 permeability when compared to those with the incorporation of unmodified silica, which was due to the decreased gas diffusivity. In addition, the CO_2/CH_4 selectivity was found almost unchanged [238].

In recent years, the use of mesoporous silica in MMMs has attracted great interest. Because of the small cross-sectional areas per chain ($\leqslant 1$ nm^2), polymer chains may penetrate into the mesoporous silica (e.g. MCM-41 or MCM-48) to form intimate composite membranes [239]. Furthermore, the ordered mesoporous silica possesses large surface areas with hydroxyl groups which could link to the polymers with aryl ether oxygen atoms, i.e. PSF, by hydrogen-bonding [240,241]. The properties of mesoporous silica, including tailorable particle shapes, sizes and pores, are useful in the design of high-permeance MMMs. As the first study on the gas transport properties of MMMs with mesoporous silica molecular sieves, Reid et al. reported that there was no strong interaction between mesoporous silica and gases, thus little change in the selectivities of membranes before and after adding MCM-41 [241]. However, a significant enhancement in permeabilities was observed, ~40% ~ 170%, for MCM-41/PSF MMMs [241]. Similar result was also reported in the study on the PSF MMMs with the addition of MCM-48 materials, showing a dramatic increase (89% ~ 308%) of gas permeabilities without

sacrificing selectivities, when compared with plain PSF [242]. The addition of smaller mesoporous particles, such as nanoparticles, could increase the polymer/particle interfacial area and develop the feasibility to fabricate homogenous MMMs with a high loading of mesoporous silica [243]. When the loading of nano-sized MCM-41 silica was 40 wt%, the gas permeability of MMMs was increased by 300% as compared with that of neat polymer membranes. In particular, the MMMs with amine-functionalized MCM-41 possessed significantly enhanced CO_2/CH_4 selectivity [243]. Zornoza and co-workers reported that the use of spherical mesoporous silica particles with a narrow size distribution in the fabrication of MMMs could minimize the particle agglomeration and enhance their interaction with polymer [239], thus superior separation performances of MMMs. The resulting MMMs with 8 wt% of 2 ~ 4 μm mesoporous silica spherical particles were observed with greater CO_2 permeabilities and selectivities (Figure 9.13) [239].

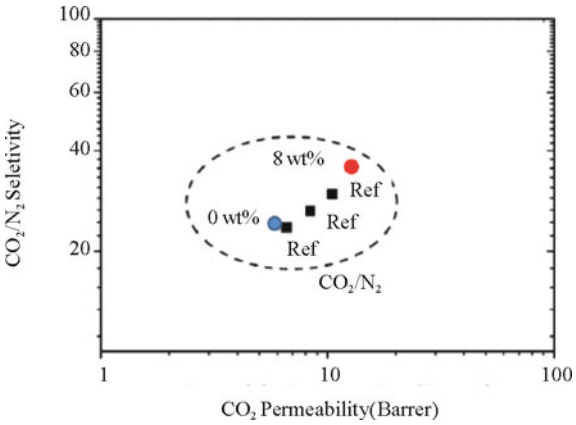

Figure 9.13 CO_2/N_2 selectivity as a function of CO_2 permeability at 35 °C for 0 and 8 wt % MCM-41/PSF MMMs (solid circles) [239]. For comparison, experimental CO_2/N_2 results in other references using 10 wt % MCM-41 [241, 243] or MCM-48 fillers [242] are shown (solid squares).

9.5.4 Other fillers

Polyhedral oligomeric silsesquioxane (POSS), which has a hybrid inorganic–organic architecture [244], was used in the fabrication of MMMs. Unfortunately, a decrease in CO_2 permeabilities was observed in either POSS-Matrimid or Zn^{2+} binding POSS-Matrimid MMMs; whereas the CO_2/CH_4 selectivities were enhanced as compared with Matrimid [245,246]. In particular, the resulting MMMs with the addition of POSS showed attractive inherent properties, such as the robustness and thermo-mechanical stability [245,246].

Metal oxide particles have been considered as important materials in the membrane-based separation, due to the presence of affinity and interaction between the surface of metal oxide and CO_2 [247]. The addition of nanoscale magnesium oxide particles into Matrimid matrix resulted in an increase of gas permeabilities. The MMMs with 40 wt% MgO loading showed highest permeability; however, the selectivity of MMMs was lower than that of neat Matrimid [247]. This was attributed to the pore sizes of MgO nanoparticles which were larger than the sizes of gas molecules [247]. Similar finding was also reported by Freeman and co-workers, that the higher loading of MgO nanoparticles increased void volumes and gas permeabilities of MMMs [248]. The CO_2 permeability of poly(1-trimethylsilyl-1-propyne) MMM with 40% MgO loading was 4.5 times higher than that of unfilled polymer [248]. Silver shows attractive inherent characteristics in relative to other metals, including electrical, antimicrobial and oxidation properties. The CO_2 permeabilities and CO_2/CH_4 selectivities of spiral-wound Ag-Pebax separation elements were ranging in 15.4 ~ 21.3 GPU and 27.8 ~ 36 in the pressure range of 1 ~ 4 MPa at 30 °C, which held promising potential in the separation of CO_2 from CH_4 [249].

In last two decades, almost all of studies have focused on the development of MMMs containing one type of inorganic fillers. In 2010, Weng et al. reported the fabrication of multilayer MMMs, consisting of poly(phenylene oxide) (PPO) and mesoporous silica SBA-15 coated onto a carbon molecular sieve (CMS)/Al_2O_3 substrate. The increasing loading of SBA-15 in PPO/SBA-15/CMS/Al_2O_3 MMMs resulted in a reduction in the gas permeabilities, but an improvement in selectivities. In particular, as compared with SBA-15/PPO MMMs, the CO_2 permeability was enhanced by 7.7% by using multi-component PPO/SBA-15/CMS/Al_2O_3 MMMs [250].

9.6 Conclusions

Global warming has been considered as one of the major environmental issues all over the world. It is difficult and impossible to completely prevent the human activities which emit CO_2 to atmosphere. However, it is feasible to limit or reduce CO_2 gas emission by separating CO_2. An ideal CO_2-selective separation membrane should possess several properties, especially high CO_2 permeability and good selectivity to other impurities, including gases and moisture.

Different classes of polymers have been studied for their use as CO_2-selective separation membranes. However, only a limited number of polymers, such as polysulfones and polyimides, have been widely and commercially used because of their good separation performances and acceptable fabrication costs. Chemical

modification or physical blending has been utilized to fabricate the membranes with improved separation performances. It is believed that the research on the development of novel polymeric materials for the fabrication of CO_2-selective separation membranes will be continuously conducted in the future. Inorganic membranes possess many advantages in CO_2 separation, such as mechanical, thermal, and chemical stability, despite higher cost than organic membranes. However, there is a need to overcome the difficulty in the fabrication of defect-free inorganic membranes with high separation performances. Mixed-matrix membranes, which combine the high selective separation properties of inorganic fillers (e.g. zeolites and carbon nanotubes) and good flexibility of polymeric membranes, have shown great potential in the commercial implementation. In particular, early modeling and experimental work has demonstrated the fast gas transport properties inside carbon nanotubes. Among carbon nanotubes, single-walled carbon nanotubes (SWCNTs) have selective pores to gas molecules, which are promising materials for CO_2 separation. However, the efficient orientation of carbon nanotubes in polymeric matrix is the key challenge in the fabrication of high performance MMMs.

Other CO_2-selective membranes have also been reported in the literature, such as supported ionic liquid membranes (SILMs) [251-253]. The CO_2 permeabilities and CO_2/N_2 separation factors for some SILMs were amlost 1000 Barrers and over 20 [251], which exceeded the Robeson's upper bound. However, the chemical stability of SILMs is expected to be further improved in the future research.

References

[1] U.K. Office of Climate Change (OCC). Stern review on the economics of climate change. 2005; Available from: http://www.hm-treasury.gov.uk/sternreview_index.htm.

[2] Pera-Titus M, Alshebani A, Nicolas C H, et al. Nanocomposite MFI−alumina membranes: High-flux hollow fibers for CO_2 capture from internal combustion vehicles. Industrial and Engineering Chemistry Research, 2009, 48(20): 9215~9223.

[3] Shekhawat D, Luebke D R, Pennline H W, A review of carbon dioxide selective membranes. National Energy Technology Laboratory, United States Department of Energy, 2003.

[4] D'Alessandro D, Smit B, Long J. Carbon dioxide capture: Prospects for new materials. Angewandte Chemie-International Edition, 2010, 49(35): 6058~6082.

[5] Alexander S S. Polymers for gas separations: the next decade. Journal of

Membrane Science, 1994, 94(1): 1~65.

[6] Sridhar S, Smitha B, Aminabhavi T M. Separation of carbon dioxide from natural gas mixtures through polymeric membranes-A review. Separation and Purification Reviews, 2007, 36(2): 113 ~ 174.

[7] Powell C E, Qiao G G. Polymeric CO_2/N_2 gas separation membranes for the capture of carbon dioxide from power plant flue gases. Journal of Membrane Science, 2006, 279(1~2): 1 ~ 49.

[8] Basu S, Khan A L, Cano-Odena A, et al. Membrane-based technologies for biogas separations. Chemical Society Reviews, 2010, 39(2): 750 ~ 768.

[9] Chung T S, Jiang L Y, Li Y, et al. Mixed matrix membranes (MMMs) comprising organic polymers with dispersed inorganic fillers for gas separation. Progress in Polymer Science, 2007, 32(4): 483 ~ 507.

[10] Chew T L, Ahmad A L, Bhatia S. Ordered mesoporous silica (OMS) as an adsorbent and membrane for separation of carbon dioxide (CO_2). Advances in Colloid and Interface Science, 2010, 153(1~2): 43 ~ 57.

[11] Scholes C A, Kentish S E, Stevens G W. Effects of minor components in carbon dioxide capture using polymeric gas separation membranes. Separation and Purification Reviews, 2009, 38(1): 1 ~ 44.

[12] Brunetti A, Scura F, Barbieri G, et al. Membrane technologies for CO_2 separation. Journal of Membrane Science, 2010, 359(1~2): 115 ~ 125.

[13] Yang H, Xu Z, Fan M, et al. Progress in carbon dioxide separation and capture: A review. Journal of Environment Science, 2008, 20(1): 14 ~ 27.

[14] Xiao Y, Low B T, Hosseini S S, et al. The strategies of molecular architecture and modification of polyimide-based membranes for CO_2 removal from natural gas-A review. Progress in Polymer Science, 2009, 34(6): 561 ~ 580.

[15] Bernardo P, Drioli E, Golemme G. Membrane gas separation: A review/ state of the art. Ind. Eng. Industrial and Engineering Chemistry Research , 2009, 48(10): 4638 ~ 4663.

[16] Baker R W, Membrane Technology and Applications. 2nd ed. West Sussex: John Wiley and Sons Ltd, 2004

[17] Robeson L M. Correlation of separation factor versus permeability for polymeric membranes. Journal of Membrane Science, 1991, 62(2): 165 ~ 185.

[18] Robeson L M. the upper bound revisited. Journal of Membrane Science, 2008, 320(1~2): 390 ~ 400.

[19] Koros W J, Mahajan R. Pushing the limits on possibilities for large scale gas separation: Which strategies? Journal of Membrane Science, 2000,

175(2): 181 ~ 196.

[20] Jansen J C, Macchione M, Drioli E. High flux asymmetric gas separation membranes of modified poly(ether ether ketone) prepared by the dry phase inversion technique. Journal of Membrane Science, 2005, 255(1~2): 167 ~ 180.

[21] Kesting R E, Fritzsche A K, Polymeric Gas Separation Membranes. New York: John Wiley and Sons. 1993

[22] Jansen J C, Buonomenna M G, Figoli A, et al. Asymmetric membranes of modified poly(ether ether ketone) with an ultra-thin skin for gas and vapour separations. Journal of Membrane Science, 2006, 272(1~2): 188 ~ 197.

[23] Hamad F, Khulbe K C, Matsuura T. Comparison of gas separation performance and morphology of homogeneous and composite PPO membranes. Journal of Membrane Science, 2005, 256(1~2): 29 ~ 37.

[24] Liang W, Martin C R. Gas transport in electronically conductive polymers. Journal of Materials Chemistry, 1991, 3(3): 390 ~ 391.

[25] Petersen J, Peinemann K V. Novel polyamide composite membranes for gas separation prepared by interfacial polycondensation. Journal of Applied Polymer Science, 1997, 63(12): 1557 ~ 1563.

[26] Zhao J, Wang Z, Wang J, et al. Influence of heat-treatment on CO_2 separation performance of novel fixed carrier composite membranes prepared by interfacial polymerization. Journal of Membrane Science, 2006, 283(1~2): 346 ~ 356.

[27] Sridhar S, Smitha B, Mayor S, et al. Gas permeation properties of polyamide membrane prepared by interfacial polymerization. Journal of Materials Chemistry, 2007, 42(22): 9392 ~ 9401.

[28] Achalpurkar M P, Kharul U K, Lohokare H R, et al. Gas permeation in amine functionalized silicon rubber membranes. Separation and Purification Reviews, 2007, 57(2): 304 ~ 313.

[29] Muñoz D M, Maya E M, de Abajo J, et al. Thermal treatment of poly(ethylene oxide)-segmented copolyimide based membranes: An effective way to improve the gas separation properties. Journal of Membrane Science, 2008, 323(1): 53 ~ 59.

[30] Xiao Y, Shao L, Chung T S, et al. Effects of thermal treatments and dendrimers chemical structures on the properties of highly surface cross-linked polyimide films. Ind. Eng. Industrial and Engineering Chemistry Research, 2005, 44(9): 3059 ~ 3067.

[31] Liu L, Chakma A, Feng X. Preparation of hollow fiber poly(ether block amide)/polysulfone composite membranes for separation of carbon dioxide

from nitrogen. Journal of Chemical Engineering, 2004, 105(1~2): 43 ~ 51.

[32] Ji P, Cao Y, Jie X, et al. Impacts of coating condition on composite membrane performance for CO_2 separation. Separation and Purification Reviews , 2010, 71(2): 160 ~ 167.

[33] Du R, Chakma A, Feng X. Interfacially formed poly(N,N-dimethylaminoethyl methacrylate)/polysulfone composite membranes for CO_2/N_2 separation. Journal of Membrane Science, 2007, 290(1~2): 19 ~ 28.

[34] Du J R, Liu L, Chakma A, et al. A study of gas transport through interfacially formed poly(N,N-dimethylaminoethyl methacrylate) membranes. Journal of Chemical Engineering, 2010, 156(1): 33 ~ 39.

[35] Du R, Feng X, Chakma A. Poly(N,N-dimethylaminoethyl methacrylate)/polysulfone composite membranes for gas separations. Journal of Membrane Science, 2006, 279(1~2): 76 ~ 85.

[36] Wallace D W, Staudt-Bickel C, Koros W J. Efficient development of effective hollow fiber membranes for gas separations from novel polymers. Journal of Membrane Science, 2006, 278(1~2): 92 ~ 104.

[37] Ding X, Cao Y, Zhao H, et al. Fabrication of high performance Matrimid/polysulfone dual-layer hollow fiber membranes for O_2/N_2 separation. Journal of Membrane Science, 2008, 323(2): 352 ~ 361.

[38] Liu R X, Qiao X Y, Chung T S. Dual-layer P84/polyethersulfone hollow fibers for pervaporation dehydration of isopropanol. Journal of Membrane Science, 2007, 294(1~2): 103 ~ 114.

[39] Puri P S. Fabrication of hollow fibre gas separation membranes. Gas Separation and Purification, 1990. 4(1): 29 ~ 36.

[40] Strathmann H. Membrane separation processes: Current relevance and future opportunities. AIChE Journal, 2001, 47(5): 1077 ~ 1087.

[41] Li Y, Chung T S, Xiao Y. Superior gas separation performance of dual-layer hollow fiber membranes with an ultrathin dense-selective layer. Journal of Membrane Science, 2008, 325(1): 23 ~ 27.

[42] Ji P, Cao Y, Zhao H, et al. Preparation of hollow fiber poly(N,N-dimethylaminoethyl methacrylate)-poly(ethylene glycol methyl ether methyl acrylate)/polysulfone composite membranes for CO_2/N_2 separation. Journal of Membrane Science, 2009, 342(1~2): 190 ~ 197.

[43] Kouketsu T, Duan S, Kai T, et al. PAMAM dendrimer composite membrane for CO_2 separation: Formation of a chitosan gutter layer. Journal of Membrane Science, 2007, 287(1): 51 ~ 59.

[44] Nunes S P, Peinemann V. Membrane Technology in the Chemical Industry// Nunes S P, Peinemann V. Membrane Materials and Membrane Preparation.

Weinheim: Wiley-VCH, 2001

[45] Sridhar S, Veerapur R S, Patil M B, et al. Matrimid polyimide membranes for the separation of carbon dioxide from methane. Journal of Applied Polymer Science, 2007, 106(3): 1585 ~ 1594.

[46] Tanaka K, Kita H, Okano M, et al. Permeability and permselectivity of gases in fluorinated and non-fluorinated polyimides. Polymer, 1992, 33(3): 585 ~ 592.

[47] Kim T H, Koros W J, Husk G R, et al. Relationship between gas separation properties and chemical structure in a series of aromatic polyimides. Journal of Membrane Science, 1988, 37(1): 45 ~ 62.

[48] Stern S A, Mi Y, Yamamoto H, et al. Structure/permeability relationships of polyimide membranes. Applications to the separation of gas mixtures. Journal of Polymer Science:Polymer Physics Edition, 1989, 27(9): 1887 ~ 1909.

[49] Qin J J, Chung T S, Cao Y. Solvent selection for manufacture of fluorinated polyimide composite membranes. Desalination, 2006, 193(1~3): 8 ~ 13.

[50] Aitken C L, Koros W J, Paul D R. Gas transport properties of biphenol polysulfones. Macromolecules, 1992, 25(14): 3651 ~ 3658.

[51] Camacho-Zuñiga C, Ruiz-Treviño F A, Hernández-López S, et al. Aromatic polysulfone copolymers for gas separation membrane applications. Journal of Membrane Science, 2009, 340(1~2): 221 ~ 226.

[52] de Abajo J, de la Campa J G, Lozano A E. Designing aromatic polyamides and polyimides for gas separation membranes. Macromolecular Symposium, 2003, 199(1): 293 ~ 306.

[53] Ulbricht M. Advanced functional polymer membranes. Polymer, 2006, 47(7): 2217 ~ 2262.

[54] Espeso J, Lozano A E, de la Campa J G, et al. Effect of substituents on the permeation properties of polyamide membranes. Journal of Membrane Science, 2006, 280(1~2): 659 ~ 665.

[55] Queiroz D P, Norberta de Pinho M. Structural characteristics and gas permeation properties of polydimethylsiloxane/poly(propylene oxide) urethane/urea bi-soft segment membranes. Polymer, 2005, 46(7): 2346 ~ 2353.

[56] Jung C H, Lee J E, Han S H, et al. Highly permeable and selective poly(benzoxazole-co-imide) membranes for gas separation. Journal of Membrane Science, 2010, 350(1~2): 301 ~ 309.

[57] Shao L, Chung T S, Goh S H, et al. Polyimide modification by a linear aliphatic diamine to enhance transport performance and plasticization

resistance. Journal of Membrane Science, 2005, 256(1~2): 46 ~ 56.

[58] Shao L, Chung T S, Goh S H, et al. the effects of 1,3-cyclohexanebis(methylamine) modification on gas transport and plasticization resistance of polyimide membranes. Journal of Membrane Science, 2005, 267(1~2): 78 ~ 89.

[59] Shao L, Liu L, Cheng S-X, et al. Comparison of diamino cross-linking in different polyimide solutions and membranes by precipitation observation and gas transport. Journal of Membrane Science, 2008, 312(1~2): 174 ~ 185.

[60] Patel N P, Hunt M A, Lin-Gibson S, et al. Tunable CO_2 transport through mixed polyether membranes. Journal of Membrane Science, 2005, 251(1~2): 51 ~ 57.

[61] Senthilkumar U, Reddy B S R. Polysiloxanes with pendent bulky groups having amino-hydroxy functionality: Structure-permeability correlation. Journal of Membrane Science, 2007, 292(1~2): 72 ~ 79.

[62] Powell C E, Duthie X J, Kentish S E, et al. Reversible diamine cross-linking of polyimide membranes. Journal of Membrane Science, 2007, 291(1~2): 199 ~ 209.

[63] Ahn S H, Seo J A, Kim J H, et al. Synthesis and gas permeation properties of amphiphilic graft copolymer membranes. Journal of Membrane Science, 2009, 345(1~2): 128 ~ 133.

[64] Hillock A M W, Koros W J. Cross-linkable polyimide membrane for natural gas purification and carbon dioxide plasticization reduction. Macromolecules, 2007, 40(3): 583 ~ 587.

[65] Kusuma V A, Freeman B D, Smith S L, et al. Influence of TRIS-based co-monomer on structure and gas transport properties of cross-linked poly(ethylene oxide). Journal of Membrane Science, 2010, 359(1~2): 25 ~ 36.

[66] Sridhar S, Aminabhavi T M, Ramakrishna M. Separation of binary mixtures of carbon dioxide and methane through sulfonated polycarbonate membranes. Journal of Applied Polymer Science, 2007, 105(4): 1749~1756.

[67] Sridhar S, Smitha B, Ramakrishna M, et al. Modified poly(phenylene oxide) membranes for the separation of carbon dioxide from methane. Journal of Membrane Science, 2006, 280(1~2): 202 ~ 209.

[68] Sen S K, Banerjee S. Gas transport properties of fluorinated poly(ether imide) films containing phthalimidine moiety in the main chain. Journal of Membrane Science, 2010, 350(1~2): 53 ~ 61.

[69] Mousavi S A, Sadeghi M, Motamed-Hashemi M M Y, et al. Study of gas

separation properties of ethylene vinyl acetate (EVA) copolymer membranes prepared via phase inversion method. Separation and Purification Reviews, 2008, 62(3): 642 ~ 647.

[70] Wang Z, Li M, Cai Y, et al. Novel CO2 selectively permeating membranes containing PETEDA dendrimer. Journal of Membrane Science, 2007, 290(1~2): 250 ~ 258.

[71] Taniguchi I, Duan S, Kazama S, et al. Facile fabrication of a novel high performance CO_2 separation membrane: Immobilization of poly(amidoamine) dendrimers in poly(ethylene glycol) networks. Journal of Membrane Science, 2008, 322(2): 277 ~ 280.

[72] Amooghin A E, Sanaeepur H, Moghadassi A, et al. Modification of ABS membrane by PEG for capturing carbon dioxide from CO_2/N_2 streams. Separation Sceince and Technology, 2010, 45(10): 1385 ~ 1394.

[73] Sadeghi M, Pourafshari C M, Rahimian M, et al. Gas permeation properties of polyvinylchloride/polyethyleneglycol blend membranes. Journal of Applied Polymer Science, 2008, 110(2): 1093 ~ 1098.

[74] Car A, Stropnik C, Yave W, et al. PEG modified poly(amide-b-ethylene oxide) membranes for CO_2 separation. Journal of Membrane Science, 2008, 307(1): 88 ~ 95.

[75] Ismail A F, David L I B. A review on the latest development of carbon membranes for gas separation. Journal of Membrane Science, 2001, 193(1): 1 ~ 18.

[76] Fuertes A B, Centeno T A. Preparation of supported asymmetric carbon molecular sieve membranes. Journal of Membrane Science, 1998, 144(1~2): 105 ~ 111.

[77] Bernardo P, Drioli E, Golemme G. Membrane gas separation: A review/ state of the art. Ind. Eng. Industrial and Engineering Chemistry Research, 2009, 48(10): 4638 ~ 4663.

[78] Tarditi A M, Lombardo E A. Influence of exchanged cations (N^{a+}, C^{s+}, Sr^{2+} and Ba^{2+}) on xylene permeation through ZSM-5/SS tubular membranes. Separation Sceince and Technology, 2008, 61(2): 136 ~ 147.

[79] Yang M, Crittenden B D, Perera S P, et al. the hindering effect of adsorbed components on the permeation of a non-adsorbing component through a microporous silicalite membrane: the potential barrier theory. Journal of Membrane Science, 1999, 156(1): 1 ~ 9.

[80] Caro J, Noack M, Kölsch P, et al. Zeolite membranes - state of their development and perspective. Microporous and Mesoporous Matevials, 2000, 38(1): 3 ~ 24.

[81] Poshusta J C, Tuan V A, Pape E A, et al. Separation of light gas mixtures using SAPO-34 membranes. AIChE Journal., 2000, 46(4): 779 ~ 789.

[82] Keizer K, Burggraaf A J, Vroon Z A E P, et al. Two component permeation through thin zeolite MFI membranes. Journal of Membrane Science, 1998, 147(2): 159 ~ 172.

[83] Lindmark J, Hedlund J. Carbon dioxide removal from synthesis gas using MFI membranes. Journal of Membrane Science, 2010, 360(1~2): 284 ~ 291.

[84] Rouleau L, Pirngruber G, Guillou F, et al. Nanocomposite MFI-alumina and FAU-alumina membranes: Synthesis, characterization and application to paraffin separation and CO_2 capture. Oil and Gas Science and Technology, 2009.

[85] Li Y, Pera-Titus M, Xiong G, et al. Nanocomposite MFI-alumina membranes via pore-plugging synthesis: Genesis of the zeolite material. Journal of Membrane Science, 2008, 325(2): 973 ~ 981.

[86] Alshebani A, Pera-Titus M, Landrivon E, et al. Nanocomposite MFI-ceramic hollow fibres: Prospects for CO_2 separation. Microporous and Mesoporous Materials, 2008, 115(1~2): 197 ~ 205.

[87] Miachon S, Ciavarella P, van Dyk L, et al. Nanocomposite MFI-alumina membranes via pore-plugging synthesis: Specific transport and separation properties. Journal of Membrane Science, 2007, 298(1~2): 71 ~ 79.

[88] Dong J, Lin Y S, Hu M Z C, et al. Template-removal-associated microstructural development of porous-ceramic-supported MFI zeolite membranes. Microporous and Mesoporous Materials, 2000, 34(3): 241 ~ 253.

[89] Hedlund J, Jareman F, Bons A-J, et al. A masking technique for high quality MFI membranes. Microporous and Mesoporous Materials, 2003, 222(1~2): 163 ~ 179.

[90] Geus E R, den Exter M J, van Bekkum H. Synthesis and characterization of zeolite (MFI) membranes on porous ceramic supports. Journal of the Chemical Society, Faraday, 1992, 88(20): 3101 ~ 3109.

[91] Yin X, Zhu G, Yang W, et al. Stainless-steel-net-supported zeolite NaA membrane with high permeance and high permselectivity of oxygen over nitrogen. Advanced Matevials, 2005, 17(16): 2006 ~ 2010.

[92] Tian Y, Fan L, Wang Z, et al. Synthesis of a SAPO-34 membrane on macroporous supports for high permeance separation of a CO_2/CH_4 mixture. Journal of Materials Chemistry, 2009, 19(41): 7698 ~ 7703.

[93] Hedlund J, Sterte J, Anthonis M, et al. High-flux MFI membranes.

Microporous and Mesoporous Materials, 2002, 52(3): 179 ~ 189.

[94] Rouleau L, Pirngruber G, Guillou F, et al. Nanocomposite MFI-alumina and FAU-alumina membranes: Synthesis, characterization and application to paraffin separation and CO_2 capture. Oil and Gas Science and Technology, 2009, 64(6): 745 ~ 758.

[95] Lin Y S, Kumakiri I, Nair B N, et al. Microporous inorganic membranes. Separ Purif Method, 2002, 31(2): 229 ~ 379.

[96] Miachon S, Landrivon E, Aouine M, et al. Nanocomposite MFI-alumina membranes via pore-plugging synthesis: Preparation and morphological characterisation. Journal of Membrane Science, 2006, 281(1~2): 228 ~ 238.

[97] Huang A, Liang F, Steinbach F, et al. Preparation and separation properties of LTA membranes by using 3-aminopropyltriethoxysilane as covalent linker. Journal of Membrane Science, 2010, 350(1~2): 5 ~ 9.

[98] Lai Z, Bonilla G, Diaz I, et al. Microstructural optimization of a zeolite membrane for organic vapor separation. Science, 2003, 300(5618): 456 ~ 460.

[99] Mintova S, Valtchev V, Engström V, et al. Growth of silicalite-1 films on gold substrates. Microporous Materials, 1997, 11(3~4): 149 ~ 160.

[100] Shin D W, Hyun S H, Cho C H, et al. Synthesis and CO_2/N_2 gas permeation characteristics of ZSM-5 zeolite membranes. Micropporous and Mesoporous Materials, 2005, 85(3): 313 ~ 323.

[101] Kanezashi M, O'Brien-Abraham Journal, Lin Y S, et al. Gas permeation through DDR-type zeolite membranes at high temperatures. AIChE J., 2008, 54(6): 1478 ~ 1486.

[102] Kanezashi M, Lin Y S. Gas permeation and diffusion characteristics of MFI-type zeolite membranes at high temperatures. Journal of Physical Chemistry C, 2009, 113(9): 3767 ~ 3774.

[103] Carreon M, Li S, Falconer J, et al. SAPO-34 seeds and membranes prepared using multiple structure directing agents. Advanced Materials, 2008, 20(4): 729 ~ 732.

[104] Li S, Fan C Q. High-flux SAPO-34 membrane for CO_2/N_2 separation. Ind. Eng. Industrial and Engineering Chemistry Research, 2010, 49(9): 4399 ~ 4404.

[105] Li S, Carreon M A, Zhang Y, et al. Scale-up of SAPO-34 membranes for CO_2/CH_4 separation. Journal of Membrane Science, 2010, 352(1~2): 7 ~ 13.

[106] Suzuki H. Composite membrane having a surface layer of an ultrathin film of cage-shaped zeolite and process for production thereof. US Patent. 1987.

[107] International Zeolite Association. http://izasc.ethz.ch/fmi/xsl/IZA-SC/ft.xsl.

[108] White J C, Dutta P K, Shqau K, et al. Synthesis of ultrathin zeolite Y membranes and their application for separation of carbon dioxide and nitrogen gases. Langmuir, 2010, 26(12): 10287 ~ 10293.

[109] Kusakabe K, Kuroda T, Uchino K, et al. Gas permeation properties of ion-exchanged faujasite-type zeolite membranes. AIChE Journal, 1999, 45(6): 1220 ~ 1226.

[110] Kusakabe K, Kuroda T, Morooka S. Separation of carbon dioxide from nitrogen using ion-exchanged faujasite-type zeolite membranes formed on porous support tubes. Journal of Membrane Science, 1998, 148(1): 13 ~ 23.

[111] Hasegawa Y, Kusakabe K, Morooka S. Effect of temperature on the gas permeation properties of NaY-type zeolite formed on the inner surface of a porous support tube. Chemical Engineering Journal, 2001, 56(14): 4273 ~ 4281.

[112] Kusakabe K, Kuroda T, Murata A, et al. Formation of a Y-type zeolite membrane on a porous α-alumina tube for gas separation. Industrial and Engineering Chemistry Research, 1997, 36(3): 649 ~ 655.

[113] Hasegawa Y, Watanabe K, Kusakabe K, et al. The separation of CO_2 using Y-type zeolite membranes ion-exchanged with alkali metal cations. Separation and Purification Reviews , 2001, 22-23: 319 ~ 325.

[114] Hasegawa Y, Watanabe K, Kusakabe K, et al. Influence of alkali cations on permeation properties of Y-type zeolite membranes. Journal of Membrane Science, 2002, 208(1~2): 415 ~ 418.

[115] Gu X, Dong J, Nenoff T M. Synthesis of defect-free FAU-type zeolite membranes and separation for dry and moist CO_2/N_2 mixtures. Industrial and Engineering Chemistry Research, 2005, 44(4): 937 ~ 944.

[116] Cheng Z, Gao E, Wan H. Novel synthesis of FAU-type zeolite membrane with high performance. Chemical Communications, 2004(15): 1718 ~ 1719.

[117] Seike T, Matsuda M, Miyake M. Preparation of FAU type zeolite membranes by electrophoretic deposition and their separation properties. Journal of Materials Chemistry, 2002, 12(2): 366 ~ 368.

[118] Guillou F, Rouleau L, Pirngruber G, et al. Synthesis of FAU-type zeolite membrane: An original in situ process focusing on the rheological control of gel-like precursor species. Microporous and Mesoporous Materials, 2009, 119(1~3): 1 ~ 8.

[119] Sebastián V, Kumakiri I, Bredesen R, et al. Zeolite membrane for CO_2 removal: Operating at high pressure. Journal of Membrane Science, 2007, 292(1~2): 92 ~ 97.

[120] Poshusta J C, Noble R D, Falconer J L. Temperature and pressure effects

on CO_2 and CH_4 permeation through MFI zeolite membranes. Journal of Membrane Science, 1999, 160(1): 115 ~ 125.

[121] Gies H. Studies on clathrasils: VII. A new clathrate compound of silica: Synthesis, crystallographic, and thermal properties. J. Incl. Phenom. Macro., 1984, 2(1): 275 ~ 278.

[122] Himeno S, Tomita T, Suzuki K, et al. Synthesis and permeation properties of a DDR-type zeolite membrane for separation of CO_2/CH_4 gaseous mixtures. Industrial and Engineering Chemistry Research, 2007, 46(21): 6989 ~ 6997.

[123] Tomita T, Nakayama K, Sakai H. Gas separation characteristics of DDR type zeolite membrane. Microporous and Mesoporous Materials, 2004, 68(1~3): 71 ~ 75.

[124] van den Bergh J, Tihaya A, Kapteijn F. High temperature permeation and separation characteristics of an all-silica DDR zeolite membrane. Microporous and Mesoporous Materials, 2010, 132(1~2): 137 ~ 147.

[125] van den Bergh J, Zhu W, Gascon J, et al. Separation and permeation characteristics of a DD3R zeolite membrane. Journal of Membrane Science, 2008, 316(1~2): 35 ~ 45.

[126] van den Bergh J, Zhu W, Kapteijn F, et al. Separation of CO_2 and CH4 by a DDR membrane. Research on Chemical Intermediates, 2008, 34: 467 ~ 474.

[127] Szostak R. Molecular Sieves - Principles of Synthesis and Identification. New York: Van Nostrand Reinhold, 1989

[128] Li S, Falconer J L, Noble R D. SAPO-34 membranes for CO_2/CH_4 separations: Effect of Si/Al ratio. Microporous and Mesoporous Materials, 2008, 110(2~3): 310 ~ 317.

[129] Li S, Martinek J G, Falconer J L, et al. High-pressure CO_2/CH_4 separation using SAPO-34 membranes. Industrial and Engineering Chemistry Research, 2005, 44(9): 3220 ~ 3228.

[130] Li S, Alvarado G, Noble R D, et al. Improved SAPO-34 membranes for CO_2/CH_4 separations. Advanced Materials, 2006, 18: 2601 ~ 2603.

[131] Hong M, Li S, Funke H F, et al. Ion-exchanged SAPO-34 membranes for light gas separations. Microporous and Mesoporous Materials, 2007, 106(1~3): 140 ~ 146.

[132] Cui Y, Kita H, Okamoto K-i. Preparation and gas separation performance of zeolite T membrane. Journal of Materials Chemistry, 2004, 14(5): 924 ~ 932.

[133] Tiscornia I, Irusta S, Téllez C, et al. Separation of propylene/propane

mixtures by titanosilicate ETS-10 membranes prepared in one-step seeded hydrothermal synthesis. Journal of Membrane Science, 2008, 311(1~2): 326 ~ 335.

[134] Tiscornia I, Irusta S, Prádanos P, et al. Preparation and characterization of titanosilicate Ag-ETS-10 for propylene and propane adsorption. Journal of Physical Chemistry C, 2007, 111(12): 4702 ~ 4709.

[135] Tiscornia I, Kumakiri I, Bredesen R, et al. Microporous titanosilicate ETS-10 membrane for high pressure CO_2 separation. Separation and Purification Reviews , 2010, 73(1): 8 ~ 12.

[136] Poshusta J C, Noble R D, Falconer J L. Characterization of SAPO-34 membranes by water adsorption. Journal of Membrane Science, 2001, 186: 25 ~ 40.

[137] Li S, Alvarado G, Noble R D, et al. Effects of impurities on CO_2/CH_4 separations through SAPO-34 membranes. Journal of Membrane Science, 2005, 251(1~2): 59 ~ 66.

[138] Ash R, Barrer R M, Lowson R T. Transport of single gases and of binary gas mixtures in a microporous carbon membrane. Journal of the Chemical Society,Faraday Transactions, 1973, 69: 2166 ~ 2178.

[139] Koresh J E, Sofer A. Molecular sieve carbon permselective membrane. Part I. Presentation of a new device for gas mixture separation. Separation Sceince and Technology, 1983, 18(8): 723 ~ 734.

[140] Koresh J E, Soffer A. Mechanism of permeation through molecular-sieve carbon membrane. Part 1.-the effect of adsorption and the dependence on pressure. Journal of the Chemical Society,Faraday Transactions, 1986, 82(7): 2057 ~ 2063.

[141] Koresh J E, Soffer A. The carbon molecular sieve membranes. General properties and the permeability of CH_4/H_2 mixture. Separation Sceince and Technology, 1987, 22(2): 973 ~ 982.

[142] Wei W, Qin G, Hu H, et al. Preparation of supported carbon molecular sieve membrane from novolac phenol-formaldehyde resin. Journal of Membrane Science, 2007, 303(1~2): 80 ~ 85.

[143] Lagorsse S, Leite A, Magalhães F D, et al. Novel carbon molecular sieve honeycomb membrane module: Configuration and membrane characterization. Carbon, 2005, 43(4): 809 ~ 819.

[144] Saufi S M, Ismail A F. Fabrication of carbon membranes for gas separation-A review. Carbon, 2004, 42(2): 241 ~ 259.

[145] Barsema J N, van der Vegt N F A, Koops G H, et al. Carbon molecular sieve membranes prepared from porous fiber precursor. Journal of Membrane

Science, 2002, 205(1~2): 239 ~ 246.

[146] Xiao Y, Dai Y, Chung T S, et al. Effects of brominating matrimid polyimide on the physical and gas transport properties of derived carbon membranes. Macromolecules, 2005, 38(24): 10042 ~ 10049.

[147] Shao L, Chung T S, Pramoda K P. the evolution of physicochemical and transport properties of 6FDA-durene toward carbon membranes; from polymer, intermediate to carbon. Microporous and Mesoporous Materials, 2005, 84(1~3): 59 ~ 68.

[148] Anderson C J, Pas S J, Arora G, et al. Effect of pyrolysis temperature and operating temperature on the performance of nanoporous carbon membranes. Journal of Membrane Science, 2008, 322(1): 19 ~ 27.

[149] Lua A C, Su J. Effects of carbonisation on pore evolution and gas permeation properties of carbon membranes from Kapton® polyimide. Carbon, 2006, 44(14): 2964 ~ 2972.

[150] Su J, Lua A C. Effects of carbonisation atmosphere on the structural characteristics and transport properties of carbon membranes prepared from Kapton® polyimide. Journal of Membrane Science, 2007, 305(1~2): 263 ~ 270.

[151] Zhang B, Shen G, Wu Y, et al. Preparation and characterization of carbon membranes derived from poly(phthalazinone ether sulfone) for gas separation. Ind. Eng. Industrial and Engineering Chemistry Research, 2009, 48(6): 2886 ~ 2890.

[152] Lee H J, Yoshimune M, Suda H, et al. Gas permeation properties of poly(2,6-dimethyl-1,4-phenylene oxide) (PPO) derived carbon membranes prepared on a tubular ceramic support. Journal of Membrane Science, 2006, 279(1~2): 372 ~ 379.

[153] Strano M S, Foley H C. Synthesis and characterization of heteropolyacid nanoporous carbon membranes. Catalysis Letters, 2001, 74(3): 177 ~ 184.

[154] Kita H, Yoshino M, Tanaka K, et al. Gas permselectivity of carbonized polypyrrolone membrane. Chemical Communications, 1997(11): 1051 ~ 1052.

[155] Kita H, Nanbu K, Hamano T, et al. Carbon molecular sieving membranes serived from lignin-based materials. Journaal of Polymers and the Environment, 2002, 10(3): 69 ~ 75.

[156] Kusakabe K, Gohgi S, Morooka S. Carbon molecular sieving membranes derived from condensed polynuclear aromatic (COPNA) resins for gas separations. Industrial and Engineering Chemistry Research, 1998, 37(11): 4262 ~ 4266.

[157] Nishiyama N, Dong Y R, Zheng T, et al. Tertiary amine-mediated synthesis of microporous carbon membranes. Journal of Membrane Science, 2006, 280(1~2): 603 ~ 609.

[158] Xiao Y, Chng M L, Chung T S, et al. Asymmetric structure and enhanced gas separation performance induced by in situ growth of silver nanoparticles in carbon membranes. Carbon, 2010, 48(2): 408 ~ 416.

[159] Fuertes A B, Nevskaia D M, Centeno T A. Carbon composite membranes from Matrimid® and Kapton® polyimides for gas separation. Microporous and Mesoporous Materials, 1999, 33(1~3): 115 ~ 125.

[160] Park H B, Kim Y K, Lee J M, et al. Relationship between chemical structure of aromatic polyimides and gas permeation properties of their carbon molecular sieve membranes. Journal of Membrane Science, 2004, 229(1~2): 117 ~ 127.

[161] Tin P S, Chung T S, Liu Y, et al. Separation of CO_2/CH_4 through carbon molecular sieve membranes derived from P84 polyimide. Carbon, 2004, 42(15): 3123 ~ 3131.

[162] Tin P S, Chung T S, Hill A J. Advanced fabrication of carbon molecular sieve membranes by nonsolvent pretreatment of precursor polymers. Ind. Eng. Industrial and Engineering Chemistry Research, 2004, 43(20): 6476 ~ 6483.

[163] Tin P S, Chung T S, Kawi S, et al. Novel approaches to fabricate carbon molecular sieve membranes based on chemical modified and solvent treated polyimides. Microporous and Mesoporous Materials, 2004, 73(3): 151 ~ 160.

[164] Kusuki Y, Shimazaki H, Tanihara N, et al. Gas permeation properties and characterization of asymmetric carbon membranes prepared by pyrolyzing asymmetric polyimide hollow fiber membrane. Journal of Membrane Science, 1997, 134(2): 245 ~ 253.

[165] Okamoto K, Kawamura S, Yoshino M, et al. Olefin/paraffin separation through carbonized membranes derived from an asymmetric polyimide hollow fiber membrane. Industrial and Engineering Chemistry Research, 1999, 38(11): 4424 ~ 4432.

[166] Kai T, Kazama S, Fujioka Y. Development of cesium-incorporated carbon membranes for CO_2 separation under humid conditions. Journal of Membrane Science, 2009, 342(1~2): 14 ~ 21.

[167] Lie J A, Hägg M B. Carbon membranes from cellulose and metal loaded cellulose. Carbon, 2005, 43(12): 2600 ~ 2607.

[168] Lie J A, Hägg M B. Carbon membranes from cellulose: Synthesis,

performance and regeneration. Journal of Membrane Science, 2006, 284(1~2): 79 ~ 86.

[169] Zhou W, Yoshino M, Kita H, et al. Carbon molecular sieve membranes derived from phenolic resin with a pendant sulfonic acid group. Industrial and Engineering Chemistry Research, 2001, 40(22): 4801 ~ 4807.

[170] Liu Q, Wang T, Liang C, et al. Zeolite married to carbon:A new family of membrane materials with excellent gas separation performance. Journal of Materials Chemistry, 2006, 18(26): 6283 ~ 6288.

[171] Rao P S, Wey M Y, Tseng H H, et al. A comparison of carbon/nanotube molecular sieve membranes with polymer blend carbon molecular sieve membranes for the gas permeation application. Microporous and Mesoporous Materials, 2008, 113(1~3): 499 ~ 510.

[172] Zhang X, Hu H, Zhu Y, et al. Carbon molecular sieve membranes derived from phenol formaldehyde novolac resin blended with poly(ethylene glycol). Journal of Membrane Science, 2007, 289(1~2): 86 ~ 91.

[173] Zhang X, Hu H, Zhu Y, et al. Effect of carbon molecular sieve on phenol formaldehyde novolac resin based carbon membranes. Separation and Purification Reviews , 2006, 52(2): 261 ~ 265.

[174] Zhang B, Wang T, Zhang S, et al. Preparation and characterization of carbon membranes made from poly(phthalazinone ether sulfone ketone). Carbon, 2006, 44(13): 2764 ~ 2769.

[175] Zhang B, Wang T, Wu Y, et al. Preparation and gas permeation of composite carbon membranes from poly(phthalazinone ether sulfone ketone). Separation and Purification Reviews , 2008, 60(3): 259 ~ 263.

[176] Lee H J, Suda H, Haraya K. Preparation of carbon membranes derived from polymer blends in the presence of a thermally labile polymer. Separation Sceince and Technology, 2007, 42(1): 59 ~ 71.

[177] Zhou Z, Yang J, Zhang Y, et al. NaA zeolite/carbon nanocomposite thin films with high permeance for CO_2/N_2 separation. Separation and Purification Reviews , 2007, 55(3): 392 ~ 395.

[178] Zhou Z H, Yang J H, Chang L F, et al. Novel preparation of NaA/carbon nanocomposite thin films with high permeance for CO_2/CH_4 separation. Chinese Chemical Letters, 2007, 18(4): 455 ~ 457.

[179] Zeng C, Zhang L, Cheng X, et al. Preparation and gas permeation of nano-sized zeolite NaA-filled carbon membranes. Separation and Purification Reviews , 2008, 63(3): 628 ~ 633.

[180] Yin X, Wang J, Chu N, et al. Zeolite L/carbon nanocomposite membranes on the porous alumina tubes and their gas separation properties. Journal of

Membrane Science, 2010, 348(1~2): 181 ~ 189.
[181] Jian X G, Dai Y, Zeng L, et al. Application of poly(phthalazinone ether sulfone ketone)s to gas membrane separation. Journal of Applied Polymer Science, 1999, 71(14): 2385 ~ 2390.
[182] Tavolaro A, Drioli E. Zeolite membranes. Advanced Materials, 1999, 11(12): 975 ~ 996.
[183] Bonhomme F, Welk M E, Nenoff T M. CO2 selectivity and lifetimes of high silica ZSM-5 membranes. Microporous and Mesoporous Materials, 2003, 66(2~3): 181 ~ 188.
[184] Merkel T C, Freeman B D, Spontak R J, et al. Ultrapermeable, reverse-selective nanocomposite membranes. Science, 2002, 296(5567): 519 ~ 522.
[185] Defontaine G, Barichard A, Letaief S, et al. Nanoporous polymer - clay hybrid membranes for gas separation. Journal of Colloid and Interface Science, 2010, 343(2): 622 ~ 627.
[186] Paul D R, Kemp D R. Diffusion time lag in polymer membraens containing adsorptive fillers. Journal of Polymer Science:Polymer Physics Edition, 1973(41): 79 ~ 93.
[187] Kulprathipanja S, Neuzil R W, Li N N. Separation of gases by means of mixed matrix membranes, U. Patent, 1992.
[188] Duval J M, Folkers B, Mulder M H V, et al. Adsorbent filled membranes for gas separation. Part 1. Improvement of the gas separation properties of polymeric membranes by incorporation of microporous adsorbents. Journal of Membrane Science, 1993, 80(1): 189 ~ 198.
[189] Jia M, Peinemann K V, Behling R D. Molecular sieving effect of the zeolite-filled silicone rubber membranes in gas permeation. Journal of Membrane Science, 1991, 57(2~3): 289 ~ 292.
[190] Süer M G, Baç N, Yilmaz L. Gas permeation characteristics of polymer-zeolite mixed matrix membranes. Journal of Membrane Science, 1994, 91(1~2): 77 ~ 86.
[191] Pechar T W, Kim S, Vaughan B, et al. Preparation and characterization of a poly(imide siloxane) and zeolite L mixed matrix membrane. Journal of Membrane Science, 2006, 277(1~2): 210 ~ 218.
[192] Yong H H, Park H C, Kang Y S, et al. Zeolite-filled polyimide membrane containing 2,4,6-triaminopyrimidine. Journal of Membrane Science, 2001, 188(2): 151 ~ 163.
[193] Jeong H-K, Krych W, Ramanan H, et al. Fabrication of polymer/selective-flake nanocomposite membranes and their use in gas separation. Journal of Materials Chemistry, 2004, 16(20): 3838 ~ 3845.

[194] Tantekin-Ersolmaz S B, Atalay-Oral Ç, TatlIer M, et al. Effect of zeolite particle size on the performance of polymer-zeolite mixed matrix membranes. Journal of Membrane Science, 2000, 175(2): 285 ~ 288.

[195] Huang Z, Li Y, Wen R, et al. Enhanced gas separation properties by using nanostructured PES-zeolite 4A mixed matrix membranes. Journal of Applied Polymer Science, 2006, 101(6): 3800 ~ 3805.

[196] Cong H, Radosz M, Towler B F, et al. Polymer-inorganic nanocomposite membranes for gas separation. Separation and Purification Reviews , 2007, 55(3): 281 ~ 291.

[197] Wang H, Holmberg B A, Yan Y. Homogeneous polymer-zeolite nanocomposite membranes by incorporating dispersible template-removed zeolite nanocrystals. Journal of Materials Chemistry, 2002, 12(12): 3640 ~ 3643.

[198] Choi S, Coronas J, Lai Z, et al. Fabrication and gas separation properties of polybenzimidazole (PBI)/nanoporous silicates hybrid membranes. Journal of Membrane Science, 2008, 316(1~2): 145 ~ 152.

[199] Choi S, Coronas J, Jordan E, et al. Layered silicates by swelling of AMH-3 and nanocomposite membranes. Angewandte Chemie-International Edition, 2008, 47(3): 552 ~ 555.

[200] Maheshwari S, Jordan E, Kumar S, et al. Layer structure preservation during swelling, pillaring, and exfoliation of a zeolite precursor. Journal of The American Chemical Society, 2008, 130(4): 1507 ~ 1516.

[201] Guseva O, Gusev A A. Finite element assessment of the potential of platelet-filled polymers for membrane gas separations. Journal of Membrane Science, 2008, 325(1): 125 ~ 129.

[202] Clarizia G, Algieri C, Drioli E. Filler-polymer combination: A route to modify gas transport properties of a polymeric membrane. Polymer, 2004, 45(16): 5671 ~ 5681.

[203] Moore T T, Koros W J. Non-ideal effects in organic-inorganic materials for gas separation membranes. Journal of Motecnlar Structure, 2005, 739(1~3): 87 ~ 98.

[204] Mahajan R, Burns R, Schaeffer M, et al. Challenges in forming successful mixed matrix membranes with rigid polymeric materials. Journal of Applied Polymer Science, 2002, 86(4): 881 ~ 890.

[205] Mahajan R, Koros W J. Mixed matrix membrane materials with glassy polymers. Part 1. Polymer Engineering and Science, 2002, 42(7): 1420 ~ 1431.

[206] Ismail A F, Kusworo T D, Mustafa A. Enhanced gas permeation

performance of polyethersulfone mixed matrix hollow fiber membranes using novel Dynasylan Ameo silane agent. Journal of Membrane Science, 2008, 319(1~2): 306 ~ 312.

[207] Duval J M, Kemperman A J B, Folkers B, et al. Preparation of zeolite filled glassy polymer membranes. Journal of Applied Polymer Science, 1994, 54(4): 409 ~ 418.

[208] Mahajan R, Koros W J. Mixed matrix membrane materials with glassy polymers. Part 2. Polymer Engineering and Science, 2002, 42(7): 1432 ~ 1441.

[209] Husain S, Koros W J. Mixed matrix hollow fiber membranes made with modified HSSZ-13 zeolite in polyetherimide polymer matrix for gas separation. Journal of Membrane Science, 2007, 288(1~2): 195 ~ 207.

[210] Vankelecom I F J, Van den broeck S, Merckx E, et al. Silylation to improve incorporation of zolites in polyimide films. Journal of Physical Chemistry, 1996, 100(9): 3753 ~ 3758.

[211] Pechar T W, Kim S, Vaughan B, et al. Fabrication and characterization of polyimide-zeolite L mixed matrix membranes for gas separations. Journal of Membrane Science, 2006, 277(1~2): 195 ~ 202.

[212] Li Y, Guan H M, Chung T S, et al. Effects of novel silane modification of zeolite surface on polymer chain rigidification and partial pore blockage in polyethersulfone (PES)-zeolite A mixed matrix membranes. Journal of Membrane Science, 2006, 275(1~2): 17 ~ 28.

[213] Li W, Wang X, Chen Z, et al. Carbon nanotube film by filtration as cathode catalyst support for proton-exchange membrane fuel cell. Langmuir, 2005, 21(21): 9386 ~ 9389.

[214] Bae T H, Liu J, Lee J S, et al. Facile high-yield solvothermal deposition of inorganic nanostructures on zeolite crystals for mixed matrix membrane fabrication. Journal of the American Chemical Society, 2009, 131(41): 14662 ~ 14663.

[215] Hudiono Y C, Carlisle T K, Bara J E, et al. A three-component mixed-matrix membrane with enhanced CO_2 separation properties based on zeolites and ionic liquid materials. Journal of Membrane Science, 2010, 350(1~2): 117 ~ 123.

[216] Vu D Q, Koros W J, Miller S J. Mixed matrix membranes using carbon molecular sieves: I. Preparation and experimental results. Journal of Membrane Science, 2003, 211(2): 311 ~ 334.

[217] Marchese J, Anson M, Ochoa N A, et al. Morphology and structure of ABS membranes filled with two different activated carbons. Journal of Chemical

Engineering, 2006, 61(16): 5448 ~ 5454.
[218] Sridhar S, Smitha B, Suryamurali R, et al. Synthesis, characterization and gas permeability of an activated carbon-loaded PEBAX 2533 membrane. Designed Monomers and Polymers, 2008, 11: 17 ~ 27.
[219] Chung T S, Chan S S, Wang R, et al. Characterization of permeability and sorption in Matrimid/C60 mixed matrix membranes. Journal of Membrane Science, 2003, 211(1): 91 ~ 99.
[220] Skoulidas A I, Ackerman D M, Johnson J K, et al. Rapid transport of gases in carbon nanotubes. Physical Review Letters, 2002, 89(18): 185901.
[221] Sokhan V P, Nicholson D, Quirke N. Fluid flow in nanopores: Accurate boundary conditions for carbon nanotubes. Journal of Membrane Science, 2002, 117: 8531 ~ 8540.
[222] Chen H, Johnson J K, Sholl D S. Transport diffusion of gases Is rapid in flexible carbon nanotubes. Journal of Physical Chemistry. B, 2006, 110(5): 1971 ~ 1975.
[223] Sholl D S, Johnson J K. Making high-flux membranes with carbon nanotubes. Science, 2006, 312(5776): 1003 ~ 1004.
[224] Verweij H, Schillo M, Li J. Fast mass transport through carbon nanotube membranes. Small, 2007, 3(12): 1996 ~ 2004.
[225] Mi W, Lin Y S, Li Y. Vertically aligned carbon nanotube membranes on macroporous alumina supports. Journal of Membrane Science, 2007, 304(1~2): 1 ~ 7.
[226] Liu T, Tong Y, Zhang W D. Preparation and characterization of carbon nanotube/polyetherimide nanocomposite films. Compos. Sci. Technol., 2007, 67(3~4): 406 ~ 412.
[227] Kim S, Jinschek J R, Chen H, et al. Scalable fabrication of carbon nanotube/polymer nanocomposite membranes for high flux gas transport. Nano Letters, 2007, 7(9): 2806 ~ 2811.
[228] Kim S, Pechar T W, Marand E. Poly(imide siloxane) and carbon nanotube mixed matrix membranes for gas separation. Desalination, 2006, 192(1~3): 330 ~ 339.
[229] Hu X, Cong H, Shen Y, et al. Nanocomposite membranes for CO2 separations: Silica/brominated poly(phenylene oxide). Industrial and Engineering Chemistry Research, 2007, 46(5): 1547 ~ 1551.
[230] Murali R S, Sridhar S, Sankarshana T, et al. Gas permeation behavior of Pebax-1657 nanocomposite membrane incorporated with multiwalled carbon nanotubes. Industrial and Engineering Chemistry Research, 2010, 49(14): 6530 ~ 6538.

[231] Sadeghi M, Semsarzadeh M A, Moadel H. Enhancement of the gas separation properties of polybenzimidazole (PBI) membrane by incorporation of silica nano particles. Journal of Membrane Science, 2009, 331(1~2): 21 ~ 30.

[232] Moaddeb M, Koros W J. Effects of colloidal silica incorporation on oxygen/nitrogen separation properties of ceramic-supported 6FDA-IPDA thin films. Journal of Membrane Science, 1996, 111(2): 283 ~ 290.

[233] Moaddeb M, Koros W J. Gas transport properties of thin polymeric membranes in the presence of silicon dioxide particles. Journal of Membrane Science, 1997, 125(1): 143 ~ 163.

[234] Kusakabe K, Ichiki K, Hayashi Ji, et al. Preparation and characterization of silica--polyimide composite membranes coated on porous tubes for CO_2 separation. Journal of Membrane Science, 1996, 115(1): 65 ~ 75.

[235] Kim J H, Lee Y M. Gas permeation properties of poly(amide-6-b-ethylene oxide)-silica hybrid membranes. Journal of Membrane Science, 2001, 193(2): 209 ~ 225.

[236] Joly C, Goizet S, Schrotter J C, et al. Sol-gel polyimide-silica composite membrane: Gas transport properties. Journal of Membrane Science, 1997, 130(1~2): 63 ~ 74.

[237] Ahn J, Chung W J, Pinnau I, et al. Polysulfone/silica nanoparticle mixed-matrix membranes for gas separation. Journal of Membrane Science, 2008, 314(1~2): 123 ~ 133.

[238] Cong H, Hu X, Radosz M, et al. Brominated poly(2,6-diphenyl-1,4-phenylene oxide) and its silica nanocomposite membranes for gas separation. ndustrial and Engineering Chemistry Research, 2007, 46(8): 2567 ~ 2575.

[239] Zornoza B, Irusta S, Téllez C, et al. Mesoporous silica sphere−Polysulfone mixed matrix membranes for gas separation. Langmuir, 2009, 25(10): 5903 ~ 5909.

[240] Kumar D, Schumacher K, du Fresne von Hohenesche C, et al. MCM-41, MCM-48 and related mesoporous adsorbents: Their synthesis and characterisation. Colloid Surface A, 2001, 187~188: 109 ~ 116.

[241] Reid B D, Ruiz-Trevino F A, Musselman I H, et al. Gas permeability properties of polysulfone membranes containing the mesoporous molecular sieve MCM-41. Journal of Materials Chemistry, 2001, 13(7): 2366 ~ 2373.

[242] Kim S, Marand E, Ida J, et al. Polysulfone and mesoporous molecular sieve MCM-48 mixed matrix membranes for gas separation. Journal of Materials Chemistry, 2006, 18(5): 1149 ~ 1155.

[243] Kim S, Marand E. High permeability nano-composite membranes based on mesoporous MCM-41 nanoparticles in a polysulfone matrix. Microporous and Mesoporous Materials, 2008, 114(1~3): 129 ~ 136.

[244] Li G, Wang L, Ni H, et al. Polyhedral oligomeric silsesquioxane (POSS) polymers and copolymers: A review. Journal of Inorganic and Organometallic Polymers, 2001, 11(3): 123 ~ 154.

[245] Li F, Li Y, Chung T S, et al. Facilitated transport by hybrid POSS®-Matrimid®-Zn^{2+} nanocomposite membranes for the separation of natural gas. Journal of Membrane Science, 2010. 356(1~2): 14 ~ 21.

[246] Iyer P, Iyer G, Coleman M. Gas transport properties of polyimide-POSS nanocomposites. Journal of Membrane Science, 2010, 358(1~2): 26 ~ 32.

[247] Hosseini S S, Li Y, Chung T S, et al. Enhanced gas separation performance of nanocomposite membranes using MgO nanoparticles. Journal of Membrane Science, 2007, 302(1~2): 207 ~ 217.

[248] Matteucci S, Kusuma V A, Kelman S D, et al. Gas transport properties of MgO filled poly(1-trimethylsilyl-1-propyne) nanocomposites. Polymer, 2008, 49(6): 1659 ~ 1675.

[249] Sridhar S, Aminabhavi T M, Mayor S J, et al. Permeation of carbon dioxide and methane gases through novel silver-incorporated thin film composite Pebax membranes. Industrial and Engineering Chemistry Research, 2007, 46(24): 8144 ~ 8151.

[250] Weng T H, Tseng H H, Wey M Y. Fabrication and characterization of poly(phenylene oxide)/SBA-15/carbon molecule sieve multilayer mixed matrix membrane for gas separation. International Journal of Hydrogen Energy, 2010, 35(13): 6971 ~ 6983.

[251] Scovazzo P, Kieft J, Finan D A, et al. Gas separations using non-hexafluorophosphate [PF6]- anion supported ionic liquid membranes. Journal of Membrane Science, 2004, 238(1~2): 57 ~ 63.

[252] Camper D, Bara J, Koval C, et al. Bulk-fluid solubility and membrane feasibility of rmim-based room-temperature ionic liquids. Industrial and Engineering Chemistry Research, 2006, 45(18): 6279 ~ 6283.

[253] Ferguson L, Scovazzo P. Solubility, diffusivity, and permeability of hases in phosphonium-nased toom temperature ionic liquids: Data and correlations. Industrial and Engineering Chemistry Research, 2007, 46(4): 1369 ~1374.